Physical and Theoretical Modelling of Wax Deposition in Thermally-Driven and Sloughing Regimes: the Effect of the Physical and Chemical Environment

Ghinwa Yaghy

Submitted in accordance with the requirements for the degree of

Doctor of Philosophy

University of Leeds

School of Chemical and Process Engineering

October 2020

The candidate confirms that the work submitted is his own, except where work which has formed part of jointly-authored publications has been included. The contribution of the candidate and the other authors to this work has been explicitly indicated below. The candidate confirms that appropriate credit has been given within the thesis where reference has been made to the work of others.

The research relating to the novel Cold Rotating Finger apparatus (Conference paper) is presented in Chapter 4. The study experimenting and modelling the wax deposition under flow regimes (Journal paper) is presented Chapter 5.

Conference paper

Yaghy, G.; Charpentier, T. V. J.; Fusi, L.; Neville, A.; Harbottle, D., *Cold Rotating Finger: Apparatus to Study Wax Deposition under Shear*. AIChE Annual Meeting, Orlando, USA, November 2019; Orlando, USA, 2019.

Journal paper

Yaghy, G.; Ali, A.; Charpentier, T. V. J.; Fusi, L.; Neville, A.; Harbottle, D., Wax deposition using a cold rotating finger: An empirical and theoretical assessment in thermally driven and sloughing regimes. *Journal of Petroleum Science and Engineering* **2020**, 108252.

Conference Presentations and poster

ChemEng Day, “The Cold Rotating Finger - A Novel Apparatus to Study Wax Deposition under Turbulent Flow“. Leeds, 27th March 2018

AIChE Annual meeting, “Measuring and modelling wax deposition kinetics in thermally driven and sloughing regimes”. Orlando, 11th November 2019

ChemEng Day, Leeds, 27th March 2018, Poster.

Scholarship

Leeds Anniversary Research Scholarship (2016)

Awards

Faculty Partnership Award (2019): Awarded to a Postgraduate researcher who is teaching or demonstrating and is based on the Faculty of Engineering level.

University Partnership Award (2019): Awarded to a Postgraduate researcher who is teaching or demonstrating and is based on the University of Leeds level.

The PhD candidate (Ghinwa Yaghy) performed all experimental work and prepared the first draft for Papers 1 and 2. For Paper 2, mathematical and modelling guidance was initially provided by Dr. Lorenzo Fusi from the Department of Mathematics in Florence University. Experimental contribution from the co-author Abdulraouf Ali should be noted especially in terms of measuring the temperature profile in the CRF system. The co-authors, Dr. Thibaut Charpentier, Prof. Anne Neville, Dr. Lorenzo Fusi and Prof. David Harbottle supervised the research and provided guidance to improve the quality of the submitted manuscripts. The authors would like to thank Michael Huggan for his technical expertise in building the Cold Rotating Finger.

To the wonderful country and its people that never let me down since I landed on September 2014, the United Kingdom.

Acknowledgment

"The second you make it all about you, is the second you've already lost." – *Chris Hill*

I would firstly like to thank Associate Professor David Harbottle, my supervisor, for putting my name forward for a PhD scholarship back in 2016 and for making that early morning call on the 10th of August to announce the award of a fully funded scholarship. A great morning and a great moment to memorise for a lifetime. Thank you, David, for that, and for being a role model to learn key skills and assets for a professional life, to mention, management, politics, courtesy and hard work. You taught me, step by step, how to elaborate my thinking as a researcher and how to communicate it verbally and on paper.

I would also like to thank Dr. Thibaut Charpentier, my co-supervisor; your warm and approachable nature is the magic paste that hold me all together when I was about to break. I remember every time you invited me to the office for a friendly chat or just to make sure I am doing well in hard times. Emotional intelligence is very rare among scientists and you are very talented in that term, you are definitely a great team player to learn from.

Professor Anne Neville, the resilient, positive, caring person; the leader who believes in her team members, cares about them as human being, before what they can bring to the worktable. Thank you for the opportunities you gave to me, for the valuable input into my project and for staying with us even in the darkest time of your life. I would repeat here what I wrote for you on the "Thank you" card after diagnosing your indefinite illness: " "If God made a charity for humans

to give up some of their lifetime and health to others, share with them some of the pain, I would definitely donate for you. Love you Anne."

I am indebted to Prof. Lorenzo Fusi for his great input into my project. I am very thankful for responding to the first email I sent to you asking about a detail in your published paper and for being positive on collaborating more with us. Visiting you in the University of Florence in Italy for a whole month has led to significant improvements to the overall project and has given the project another interesting perspective. I am definitely more friendly with mathematics than I was before.

I am also very thankful for the technicians and staff members within the Institute of Functional Surfaces (ifs), the department of Mechanical Engineering in the University of Leeds, to mention especially Mick, Jordan and Fiona, for all their technical and administrative help, all with big smile and lots of jokes!

I would like to highlight the great company I had in the Chemical Engineering Department, whether within the research group, all the Colloid group members with whom I shared my project throughout the years and I learned a lot from their work and company; my office mates, Mick, Laura, Ndidi, Peter, Tom, Stefanos, Mohamad, David, Dewi, Nancy, Faidat; and specially Abdulraouf for the valuable discussion and cooperation. The friendly technicians, Peter, Ben, Georges, Diana, Neil and Barrington, the hard working dedicated Analytical lab technician Adrian and Kare, the second floor member of staff with all the coffee and morning quick conversations; the Head of the School, Prof. Elaine and the related secretary/administration team.

Special Thanks to Dr. Nicole Hondow and Peter Dowson on their continuous encouragement, and both to put me forward for an award on my Teaching Skills as a PhD demonstrator, with many thanks to everyone who nominated me for that award.

For my best companion through all my lunch and coffee breaks, Suneela, I want to say you are a friend for life and having my scholarship after you rejected it is the greatest coincidence ever! Mojdeh (mojmoj), Svetlana (Martini), Rim (Mansaf), Maje (king), Jian (Jiejie), you made me feel home!

I sincerely thank The University of Leeds for the funding from Leeds Anniversary Research Scholarship.

I want to thank Dr. Duraid Maki and tell him that I am in debt for him to help me reach the UK for Masters. Without this step, I would never be in the UK again for a PhD.

I want to show my gratitude to my parents, my close friends and family members back home in Lebanon for their support. To mention by names who believes in me while I was just a “geek of science”, Yusra, Salam, Reina and Sonia. “Bet 3amo Atif”, I owe you lots of food!

Oliver, I cannot finish the acknowledgment without having your name. You’ve been a great company this year and you made it much less painful, indeed much joyful, with all the challenges it has. Our long walks, talks, jokes, common hobbies, great food and nice restaurants, coffee times, celebrations, shopping and all the “little things” on a daily basis made me through the lockdown

period and the last year of PhD without serious mental health problem and with memories I will carry for a lifetime.

Finally, Soha, it is hard to put words on paper when it comes to you and write details, no one can summarise his life in few words, and you are in every detail of my life…Here we go my sister, we are finally here…Cheers for a lifetime Sisterhood!

Abstract

This research considers the fundamental understanding of physical and theoretical modelling of wax deposition under dynamic conditions. The effect of physical environment i.e. the shear rate and the associated shear stress and heat transfer was investigated using a custom-built bench top Cold Rotating Finger (CRF) and a Quartz Crystal Microbalance (QCM) with heat transfer. The effect of chemical environment was studied by assessing wax deposition phenomena in the presence of wax inhibitors using the aforementioned techniques.

The CRF with an inner rotating cylinder is developed and characterised to provide the opportunity to study wax deposition on cold surfaces in the region of high fluid shear stress and laminar/transitional fluid flow. Time-dependent wax deposition study was performed at fixed operating temperatures and CRF rotational speed ranging from 0 to 700 rpm. The mass of the wax deposited was shown to decrease with the increase in the CRF rotational speed. At low rotational speeds (< 400 rpm), the reduction in the amount of deposited wax corresponded to a decrease in the bulk oil temperature (T_o) with increasing CRF rotational speed reducing therefore the overall temperature gradient driving force. The wax deposition at low rotational speeds was then described as a thermally-driven process. At higher rotational speeds (≥ 400 rpm), the change in temperature was negligible with sloughing of wax layers visually observed. The wax deposition at high rotational speeds was then described as a sloughing-driven process. A diffusive mathematical model based on molecular diffusion considering the heat transfer as governing wax deposition was elaborated assuming a linear solubility with temperature. For high CRF rotational speeds the molecular diffusion model could not accurately describe the wax deposit mass and the model was modified to include a sloughing term, described in terms of wall shear stress.

The study of formation of the first incipient wax layer on a cold surface was not possible with the CRF. Hence, a modified QCM with heat transfer across the quartz sensor was developed to enable the understanding of the crystallization of the first n-alkane wax on a cold surface as well as the effect of inhibitors on the n-alkane crystallization. The QCM was able to detect the deposition of wax crystals by analyzing the frequency shift as compared to the resistance. A large shift in the frequency (as compared to viscous frequency shift), all along with a small resistance, indicates a rigid mass load on the crystal due to the crystallization of the n-alkane on the QCM sensor.

The research considers the effect of the chemical environment on wax deposition by studying the performance of four ethylcellulose n-alkane wax inhibitors using the CRF at the static regime (0 rpm), the thermally-driven regime (100 rpm) and the sloughing regime (400 rpm). The inhibitors were characterized by 3 different degree of substitution (DS = 1, 0.6 and 0.4) and two alkyl pendant chain lengths (C22 and C18). The presence of inhibitors in a model solution of 5 wt% wax-in-dodecane/toluene (1:1) reduce the wax deposition with an inhibition that range from 10 to 35% with inhibitors efficiency depending on two main parameters: the structure of the inhibitor itself (DS and pendant alkyl chain) and the flow regime. The structure of the wax inhibitor determines its ability to interact with the n-alkane wax molecules and inhibit their deposition. A higher degree of substitution and a longer alkyl pendant chain induce a higher van der Waals interaction with wax molecules and a higher inhibitor efficiency, the inhibitor is more effective with similar carbon chain length, i.e. LMW n-alkane. A given flow regime, however, might promote the deposition of heavier or lighter molecules changing therefore the efficiency of the inhibitors as they are more effective for lighter wax.

Table of Contents

List of Figures

List of Tables

Nomenclature

A		Deposit area	m^2
C		Concentration	g/L
C_{ws}		Solubility of the wax	g/L
C_w		Volume fraction concentration of wax	dimensionless
D		Diffusivity	m^2/s
De		Pipe hydraulic diameter	m
Ea		activation energy	KJ/mol
	$\bar{F}_w$	Wax fraction in the deposit	dimensionless
F		Frequency	Hz
fr		Friction factor	dimensionless
	f_0	Fundamental mode oscillation frequency	Hz
G		Torque	dimensionless
h		Heat transfer coefficient	$W/(m^2K)$
ID		Inner diameter	m
J		Mass flux	$Kg/s^1m^2.$
k		Deposition rate constant	kg/m^2
L_v		Molecular heat of the phase change	KJ/mol
m		Mass	kg
n		Overtone number	dimensionless
PPT		Pour point temperature	K

T	Temperature	K
t	Time	s
r	Radius - Radial distance	m
r_{WD}	Rate of wax deposition	Kg/s
$r_{critical}$	Critical size of nucleus	m
R	Resistance	Ohm
S	Supersaturation ratio	Dimensionless
Sh	Sherwood number	Dimensionless
Sc	Schmidt number	Dimensionless
Z	Axial coordinate	m
ΔT	Temperature difference	K
σ	Interfacial surface tension	N/m
ρ	Density	kg/m^3
$\dot{\gamma}$	Shear rate in the fluid at the wall	s^{-1}
δ	Deposit thickness	m
ε_H	Eddy thermal diffusivity	$m^{2/}s^1$
ε_M	Eddy mass diffusivity	$m^{2/}s^1$
α_T	Thermal diffusivity of the oil	$m^{2/}s^1$
μ	Viscosity	Pa.s
Ψ	Couette friction factor	Dimensionless
u	Linear velocity	m/s
ν	Fluid kinematic viscosity	m^2/s
δ	Boundary layer thickness	m
ΔC	Concentration gradient	Kg/L

Δf	Change in frequency of oscillation	Hz
Δm	Change in mass of the system	kg
μ_q	Shear modulus of quartz	g/cm.s^2
ρ_q	Density of quartz	g/cm^3

Nomenclature associated with the mathematical model

c_p	Oil heat capacity	J/K
d	Diameter of the CRF	m
D	Wax diffusivity	m^2/s
H	Height of the CRF	cm
h	Heat transfer coefficient	W/(m^{2}K)
k_d	Thermal conductivity of the deposit	W/m.K
k_o	Thermal conductivity of the oil	W/m.K
m_T	Total mass of the deposit	g
m_d	Mass of wax fraction in the deposit	g
m_o	Mass of oil fraction in the oil	g
R_i	Radius of the inner cylinder	cm
R_o	Radius of outer cylinder	m
R_d	Radius of the wax deposit	m
R_b	Radius of the boundary layer	m
T_o	Temperature of the oil	K
T_h	Temperature T_{hot}	K
T_s	Temperature of the surface of the CRF	K
T_i	Temperature of the oil-deposit interface	K

w	Angular velocity	rpm
Re	Reynolds number	Dimensionless
Nu	Nusselt number	Dimensionless
Pr	Prandtl number	Dimensionless
Φ	Wax fraction in the deposit	Dimensionless
β	Wax solubility derivative	g/L
ρ	density	Kg/m^3
μ	Oil viscosity	Pa.s

Abbreviations

ASTM	American Society for Testing and Materials.
ATR	Attenuated Total Reflectance
(CHNS-O)	Carbon, Hydrogen, Nitrogen, Sulphur and Oxygen Analysis
C16	Crystal 16
CRF	Cold rotating finger
DE	Dielectric fluid
EA	Elemental analysis
EC	Ethylcellulose
FTIR	Fourier-transform Infrared
GC-FID	Gas Chromatography – Flame ionisation detection
HPLC	High-performance liquid chromatography
HMW	High molecular weight
LMW	Low molecular weight

HT-QCM	QCM with heat transfer
IAA	Interfacially active asphaltene
MWP	Michigan wax predictor
MA	Maleic acid
VA	Vinyl Acetate
OSPAR convention	Oslo and Paris convention
OA	Orthogonal array
PTFE	Polytetrafluoroethylene
PFPE	Perfluoropolyether
QCM	Quartz crystal microbalance
rpm	Rotation per minute
S_N	Nucleophilic substitution
SEM	Scanning electron microscopy
TGA	Thermogravimetric analysis
WAT	Wax appearance temperature
Wt%	Weight percent

Introduction

This chapter provides a brief introduction to wax deposition as a challenging flow assurance problem in crude oil recovery. Subsequently, research novelty and research objectives are highlighted, and an outline of the thesis chapters is then provided.

1.1 Background

Nowadays, oil is a primary resource for global energy consumption[1]. This versatile fossil fuel has become indispensable to the development of modern society. For transportation, around 95% of fuel energy comes from petroleum products[2, 3]. Additionally, the by-products of refined crude oil provide important petrochemical feedstocks for organic chemical products, such as plastics and synthetic fibers[4]. Human dependence on oil is overwhelming and thus far, no viable alternative has been found[1, 2, 5]. Between 2012 and 2035, global energy consumption is projected to rise by 41% based on core assumptions concerning emerging economies and demographic growth[6]. Although market shares of fossil fuels are converging, petroleum products are expected to constitute 27% of the total share by 2035, with oil demand continuing to rise by approximately 1% each year[2]. **Figure 1.1** shows the projected expected consumption of coal, oil, and natural gas by 2030.

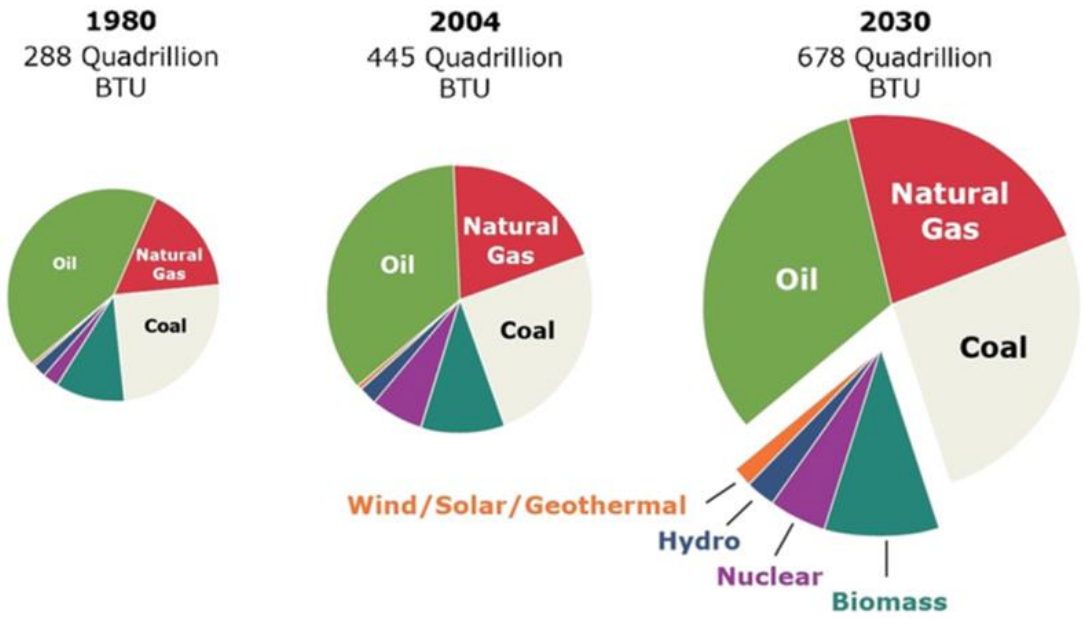

Figure 1.1 Coal, oil, and natural gas consumption by 2030 taken from Bai and Bai[6, 7].

In the January 2020 update of its Short-Term Energy Outlook (STEO), the U.S. Energy Information Administration (EIA) forecasts that U.S. crude oil production will average 13.3 million barrels per day (b/d) in 2020, a 9% increase from 2019 production levels, and 13.7 million b/d in 2021, a 3% increase from 2020[8].

However, nowadays, the world is facing the crisis of exhaustion of conventional and reachable fossil fuel. The increase in oil demand inevitably increases the demand for production. With the depletion of relatively accessible onshore and offshore reserves (shallow water), the search for oil has extended to deeper water[9, 10] (cf. **Figure 1.2**). Taking the Gulf of Mexico as an example, 20 million barrels (bbl.) (equivalent to ~3273184 cubic meters) of oil was produced from offshore deep water in 1995. This number has risen to 800 million bbl. (equivalent to ~130927392 cubic meters) in 2007 [6, 11].

Advances in upstream technologies have allowed for exploration and production in complex subsea environments. However, subsea oil recovery confronts engineers with a unique set of challenges, specifically concerning flow assurance. Flow assurance is defined as an operation that generates a reliable flow of fluids from the reservoir to the point of sale and dealing with the control of gas hydrates, wax, asphaltenes, and scales in pipelines[12]. The offshore petroleum fluids are usually transported in long-distance pipelines, which range from tens to hundreds of kilometers before they eventually reach onshore processing facilities. Hence, flow assurance challenges focus predominantly on the prevention and control of solid deposits that affect efficient transportation of hydrocarbon fluids. The operation deals with formation and deposition of gas hydrates, wax, asphaltenes, and scales that can reduce flow efficiency of oil and gas pipelines[12].

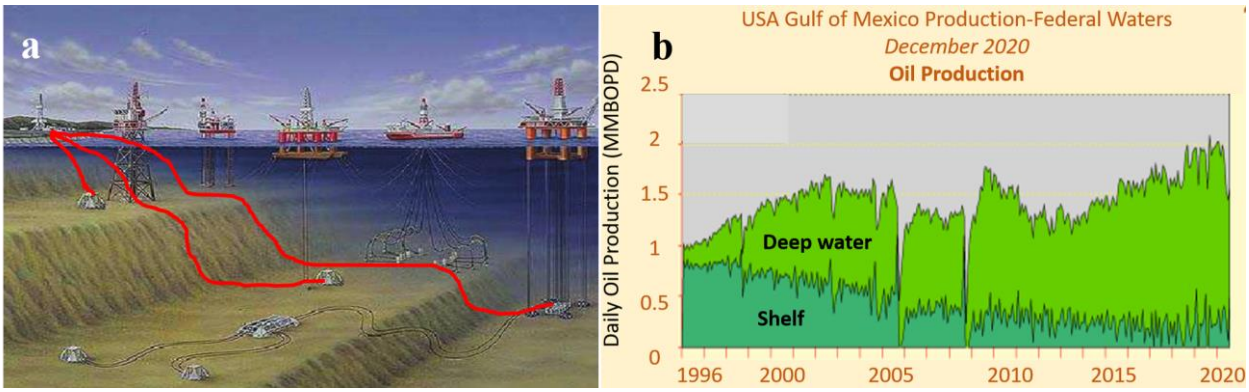

Figure 1.2. a) Schematic of the change from onshore to offshore in petroleum production in the late twentieth century adapted from Huang et al.[13], **b)** Offshore oil production in the Gulf of Mexico (GoM), adapted from The Energy Consultant Group[14].

Under cold flow conditions, the natural presence of n-alkanes (waxes) in crude oil continues to be one of the significant operational problems for subsea equipment, particularly in pipelines[15]. Accumulation of waxes may lead to production drawdown, and under severe

conditions, a risk for oil platform abandonment[16]. **Figure 1.3** shows areas reported to have wax deposition problems around the world.

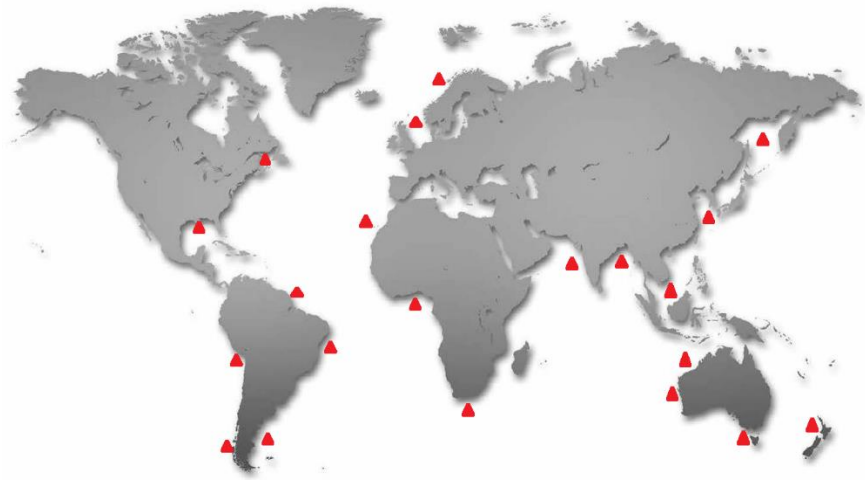

Figure 1.3. Areas reported to have wax deposition problems adapted from Huang et al.[11].

As an example, the U.S. Minerals Management Service reported 51 occurrences of severe wax-related pipeline plugging in the Gulf of Mexico between the years 1992 and 2002[17]. One of the most severe cases was reported by Elf Aquitaine (now owned by Total) in which a removal of a wax-related pipeline blockage cost as much as $5 million. The remediation of this blockage resulted in a 40-day shutdown of the pipeline, which added an additional loss of $25 million of deferred revenue[11]. The arguably most notorious incident might be from the Staffa Field, Block 3/8b, UK North Sea, in which the problem of wax deposition, after several unsuccessful attempts for remediation, eventually led to the abandonment of the field and its platform[18], leading to an estimated loss of as much as $1 billion[19].

Therefore, understanding wax deposition mechanism and working on economic solutions for the management and remediation of wax deposition remains a key factor for subsea flow

assurance strategies[11, 20, 21]. Alkane adherence to surfaces extend beyond the oil and gas sector. An abundance of analogous adhesion and deposition problems are often encountered in the food, paint, biomedical, automotive, and marine industries, as well as in nature[22]. For instance, in the energy sector, fuel derived from biomass lipids such as vegetables and animals' fat have received increasing attention as an eco-friendly alternative for conventional fossil fuel[23]. A dominant example of these biofuels is biodiesel, which is defined as a Fatty Acid Methyl Ester, a product of hydrocarbon n-alkane and other by-products. However, the use of such biodiesel pose a problematic in cold flow environment due to the high crystallization of the long chain hydrocarbon at relatively high temperature[24, 25]. Also, in food industry, the crystallisation and deposition of fatty acid derived dairy food and meat, pose a critical problem to the food processing and properties of the final product[26, 27].

1.2 Definition of Wax and Wax Deposition

Waxes are essentially mixtures of long chain hydrocarbons know as n-alkanes with carbon numbers ranging from 16 to 65[28, 29]. N-alkanes are the simplest saturated hydrocarbon having the molecular formula $C_nH_{(2n+2)}$, where *n* represents the carbon number of the n-alkane. Generally, n-alkanes are major constituents of crude oil, typically comprising 4-35 wt % of crude oil[11, 30]. Wax has a density of ~0.8 g/cm^3 and a heat capacity of ~0.140 W/(m.K). At reservoir conditions (70-150 °C and 8000-15000 psi equivalent to ~ 500-1000 bar), n-alkanes with carbon numbers less than 10 typically exist in the vapor phase in subsea oil pipelines and all other n-alkanes with carbon numbers as high as 65 will enter the pipeline in the liquid phase[20, 31]. As the crude oil leaves the reservoir and enters the pipeline, the solubility of n-alkanes drastically changes as a function of temperature[22, 32-37]. Several mechanisms for wax

deposition have been proposed in literature, among them, molecular diffusion explained in **Figure 1.4** is believed to a predominant mechanism[9, 21, 38, 39].

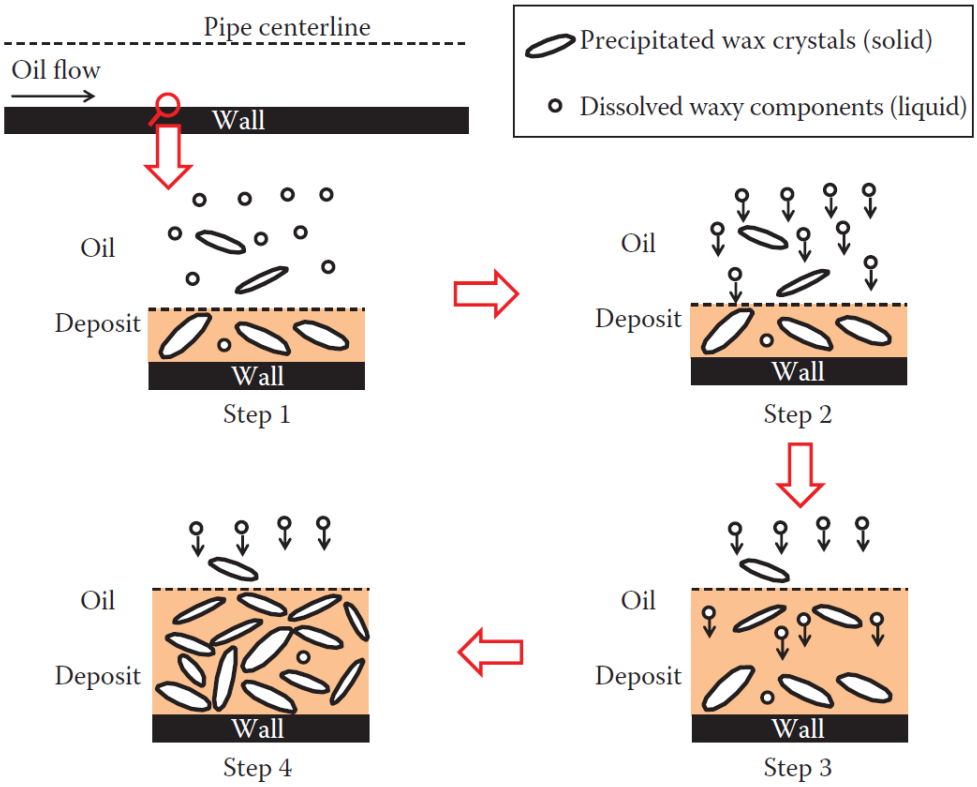

Figure 1.4. Schematic of molecular diffusion as a mechanism for wax deposition taken from Huang et al.[11].

Molecular diffusion suggests that the wax transported from the reservoir is dissolved. As the bulk fluid is subjected to a radial temperature gradient in the pipeline, crystallization of wax occurs at the pipeline wall where temperature drops below the crystallization temperature of the wax. The critical temperature at which the wax crystallizes is called the "Wax Appearance Temperature" or WAT. The crystallization of the wax results in a smaller concentration of liquid wax near to the pipeline wall in comparison to the bulk oil[9]. The subsequent concentration gradient between the bulk oil and the deposition surface induces molecular

diffusion of liquid wax from the bulk oil to the pipeline wall resulting in an incipient layer of wax deposit[11]. The mass flux of wax can be estimated by Fick's law of diffusion[9] as follows:

$$\frac{dm_m}{dt} = D_m \frac{dC}{dr} \qquad \text{Eq. 1.1}$$

where, m_{m} is the mass of wax deposit, D_{m} is diffusion coefficient of soluble wax molecules, C is the wax concentration and r is the radial coordinate. After the initial layer of wax deposit, the boundary of the bulk fluid becomes the surface for wax deposition[11]. Hence, further wax precipitation results in deposit growth. As oil is constantly pumped through subsea pipelines, liquid-phase alkanes continue to diffuse promoting the build-up of wax deposit. The wax deposit- oil interface temperature reaches the WAT due to the insulation effect of the wax, decreasing therefore the heat transfer driving force.

1.3 Research Novelty and Opportunities

Given the economic impact of wax deposition, a substantial research effort has been devoted in the literature to theoretically understand and practically model wax deposition. Researchers have studied wax deposition using simplified pilot-scale laboratory tests[11] in well controlled conditions, with an attempt to manipulate the main parameters affecting wax deposition: wax concentration, temperature gradient, flow rate, presence of impurities etc. Laboratory testing equipment is categorized as: i) flow through systems and ii) batch systems. A typical flow-through system (known as a flow loop) consists of a feed vessel, pump and pipe-loop test section which is jacketed for coolant flow. Flow-through systems can provide temperature and flow conditions similar to pipeline but are often expensive, time consuming and complicated to run and maintain. Alternatively, the batch system (commonly a cold finger test) has become a standard test method because of its small volume, good control of thermal conditions and ability to rapidly screen several parameters[11]. However, the cold finger method is often static

and does not consider the effect of flow on the wax deposition. To overcome the limitation of the cold finger, there has been various adaptations to introduce fluid shear. Some researchers induce flow in a cold finger device by using a stirring magnetic flea [40] or an impeller[41, 42]. However, while fluid flow is induced in the improved cold finger, the flow is not representative nor compared to the pipe flow environment. Other researchers[20,43,44] studied wax deposition under more realistic flow conditions by developing a cold finger with a couette flow. Wax deposition rates were shown to better represent data (comparison to the conventional cold finger method) obtained using a pilot-scale flow loop. However, the wax deposition is formed on the outer-stationary wall, in a region of low fluid shear stress.

Recognizing the test method limitation, the current study developed a novel cold finger method wherein the inner cylinder rotates (axially) and is chilled simultaneously. This set-up allows wax deposit to form in the region of high fluid shear stress and under well-defined flow conditions. The new cold finger method is called the "Cold Rotating Finger" (CRF). It has a controlled temperature gradient and well-defined hydrodynamics at the deposition surface, allowing rapid screening of test parameters, with low cost and minimal testing time.

Reviewing the literature, the effect of flow remains under-studied, which promote the need of providing greater understanding. While most researchers agreed on a decrease in the mass deposit with flow rate, they give different explanation of the underlying phenomena. Some researchers attribute the decrease in the wax deposition with flow rate to the change in the heat and mass transfer with the flow[45-47]. The heat transfer was proven to change under flow in both the cold finger and flow loop experiments. The change in heat transfer (whether by an increase in the cold surface temperature[19, 48], or a decrease in the bulk oil temperature[20, 45, 46] due to the

convective heat transfer between the cold surface and the hot fluid) leads to decrease in the thermal driven force responsible for wax deposition.

Shear removal or sloughing causing a sudden removal of a layer of the deposit is another justification for the decrease of the wax deposit with flow rate[9, 47]. Sloughing is originated from the drag force applied by the fluid to the wax particles adhering to the cold surface and it occurs when the shear stress overcomes the cohesive and adhesive forces of the alkane wax molecules to the surface[49-51]. However, to the best of our knowledge, none of the researchers was able to visualise sloughing during the wax deposition experiment.

Giving the ambiguity of the effect of flow rate on wax deposition, the CRF was a custom-built designed technique to further investigate that effect and delimitating the contribution of both the heat transfer and sloughing on wax deposition. The study was taken further to assess the effect of flow on wax inhibitors performance in the flow regimes where the wax deposition is led thermally or mechanically as well. While most studies focus on the mechanism of wax inhibitors depending on their structure or the crude oil composition, very few studies investigated the effect of shear on the performance of wax inhibitors[40, 52].

The CRF could not be used however to investigate the kinetics of wax deposition within the first minute (the first incipient layers) and the effect of inhibitors on the formation of the incipient wax layer on a cold surface. And despite the fact that wax deposition is an interfacial problem, little attention in the literature has been dedicated to the surface processes that occur in conjunction with wax deposit formation[53]. Therefore, significant uncertainty exists concerning the mechanism of incipient wax deposition at the very first stage and the deposition

of the first wax crystal on the metal surface. To allow further understanding of the mechanism of the incipient wax deposit on a metal surface and the working mechanism of inhibitors, a Quartz Crystal Microbalance (QCM) technique was developed. QCM is a surface-sensitive instrument used for assessing film properties. Researchers[53] investigated the properties of incipient wax layers using a QCM. It was proposed that the incipient wax layer is formed by a nucleation mechanism or surface adsorption. However, experimental conditions were isothermal, and therefore not representative of thermodynamic conditions associated with wax deposition in subsea pipelines[53]. To imitate heat transfer existing in a pipeline, the QCM used in this study features a heat transfer across the quartz crystal. The QCM has the unique ability to determine the mass of wax depositing layers in real time while simultaneously giving information about their viscoelastic properties.

1.4 Research Aim and Objectives

The overall aim of this research is to characterize wax deposition in different flow environments and to determine the threshold between the thermal and sloughing led regimes and assess their respective contributions.

For this purpose, two custom-built wax deposition set-ups with well-defined heat transfer and hydrodynamics were developed to simulate the temperature profile and flow in pipeline. Biodegradable wax inhibitors were also synthesized and tested using the aforementioned laboratory equipment.

The objectives of the thesis can be formulated as the following:

1- Assess experimentally and theoretically the role of flow regime in a cold rotating finger and decouple a thermally driven wax deposition regime from a shear driven wax deposition regime.

2- Evaluate the role of biodegradable wax inhibitors in wax management in the identified thermally driven and mechanically driven wax deposition regimes.

3- Provide an insight into the mechanism of incipient wax deposit formation and elucidate the role of dispersant using a Quartz Crystal Microbalance technique.

1.5 Thesis Outline

In Chapter 2, the literature review on the main parameters affecting wax deposition was summarized with an emphasis on the gaps to be addressed. The effect of flow rate was investigated and the ambiguity of the effect of flow regime/rate on the decrease in wax deposition was addressed. The mathematical models describing and predicting wax deposition based on heat and mass transfer were critically assessed as well as the models considering the effect of flow in terms of sloughing. Also, the wax management using wax inhibitors was summarized with the main commercial wax inhibitors and their performances reported.

Chapter 3 was dedicated to describe the different experimental techniques used and the specific materials and methods were described specifically in each chapter.

Chapter 4 was dedicated to the design and characterization of the CRF as a cell to study wax deposition in a dynamic system. The cell was then tested using a model solution chosen (dodecane and n-alkane wax C_{20}-C_{45}) and tested using a rapid screening and optimized

experimental matrix called Taguchi. Taguchi study was followed with more systematic test to emphasize the effect of rotational speed on wax deposition. Chapter 4 concludes by highlighting the controversial effect of the CRF rotational speed on wax deposition and introduce chapter 5 as a study fully dedicated to this subject.

Chapter 5 was dedicated to decouple the effect of flow in terms of heat transfer and sloughing on wax deposition. The CRF was operating up to a relatively high rotational speed (700 rpm) and mass deposit, wax deposit composition and temperature profile of the bulk oil were measured consequently. A mathematical model based on molecular diffusion was then elaborated to predict the mass deposit in the specific geometry of the CRF and fitted over the range of flow rates used. When the model failed to fit high rotational speeds, it was modified to introduce the sloughing mechanism at high rotational speeds.

In Chapter 6, in the same context of studying the effect of CRF rotational speed on wax deposition, screening of inhibitors at different rotational speeds was undertaken. Inhibitors synthesized out of biodegradable materials, ethylcellulose, were tested using the CRF. Both the mass and the chemical composition of the wax deposit were assessed at different rotational speeds corresponding to both thermally driven and sloughing regimes.

In Chapter 7, the wax deposition at early stages was investigated using a QCM with heat transfer across the quartz sensor. The QCM was modified to allow a coolant fluid to flow from the back of the quartz sensor and a hot fluid to circulate on the top of the sensor. Wax deposition was then studied by varying the heat transfer across the quartz crystal and comparing the frequency shift to the resistance change at different conditions. This study allows a new insight

into the understanding of the inherent interfacial phenomenon associated with wax deposit formation.

Chapter 2 Theoretical Background and Literature Review

2.1 Synopsis

In this chapter, the current literature on wax deposition experiments and modelling will be summarized. The effect of temperature and heat transfer as a main driving force for wax deposition is presented and the controversial effect of flow is also discussed. Current models based on molecular diffusion mechanism to predict wax deposition are presented with an emphasis on the sloughing models where possible. The literature also review highlights the different types of wax inhibitors as well and their mechanism.

The literature review shows a gap in the understanding of the effect of flow rate on wax deposition. While researchers agree on the decrease of the wax deposit mass with higher flow rate, they attribute this decrease to either the change in heat transfer in the system due to enhanced convection or to sloughing due to a higher wall shear stress. However, none of the researchers were able to delineate the threshold between both effects and to observe the sloughing. Mathematical modelling of such a phenomenon was therefore mostly based on heat transfer (or molecular diffusion) and few models introduce the sloughing as a contributor for wax deposition prediction. The wax management using wax inhibitor also lack the fundamental understanding of the working principle of these chemicals under flow rate.

2.2 Effect of Operating Temperatures on Wax Deposition

To begin with, it is important to distinguish between the two phenomena –precipitation and deposition. Precipitation is a necessary, but not sufficient condition for deposition.

Unfortunately, this issue seems to be a bit confused in common parlance in the oil industry. Precipitation is, sometimes, incorrectly referred to as deposition[54].

Wax precipitation is simply a thermodynamic phenomenon that is observed when the fluid temperature is reduced below the so-called WAT[55-57]. As the fluid temperature is further reduced, more waxes precipitate out of solution, possibly leading to a point where the fluid loses mobility due to gelation[29, 58].

Deposition is a result of the temperature gradient between the cold wall and the hot oil where wax crystallizes on the surface leading to a concentration gradient from the bulk to the wall. This mechanism is already explained as the molecular diffusion.

It has been shown by several researchers that two conditions must be met for wax deposition to occur. These conditions are:

1. The oil temperature near the wall must be lower than the wax appearance temperature ($T_{oil} < T_{WAT}$)

2. The wall temperature must be lower than the oil temperature ($T_{wall} < T_{oil}$)

Experiments performed with no radial heat flux ($T_{wall} = T_{oil}$) or an "inward" heat flux ($T_{wall} > T_{oil}$) have shown no deposition to occur[59].

On the other hand, the minimum size of the nucleus in wax crystallization, where it is sustainable and capable for further growth, is given by the following relation:

$$r_{critical} = \frac{2 \times \sigma \times WAT}{L_v \times \Delta T_{critical}} \quad \text{Eq. 2.1}$$

$$\text{with } \Delta T_{critical} = WAT - T \quad \text{Eq. 2.2}$$

where, L_v is the molecular heat of the phase change, σ the interfacial surface tension. As it is seen from Eq.2.1 and Eq.2.2, the temperature is a determinant factor in the reduction or the increase of the critical size of nucleus and therefore in the probability of the formation of wax crystals[60]. Besides the WAT, known also as the "could point", waxy oil is characterized by two temperatures defined as follow:

Pour point: the pour point represents the temperature of gelation under static conditions. In another words, it is the lowest temperature at which the oil or fuel will continue to flow, that's the viscosity has not increased or it has not become clogged with waxy particles[61].

Gelation temperature: the gelation temperature is the temperature at which the fuel becomes so viscous that it "gels" and will no longer flow at all by gravity nor by pumping through the oil lines. The gelation temperature is closely related to the pour point except that the gelation temperature is also function of the stress applied on the system. The pour point is the gelation temperature at a given rate for a system where no stress is applied[11, 61].

Over the past few decades, many lab-scale experimental studies have been carried out to study the effect of temperature on wax deposition. This effect was studied depending on the following operating temperatures:

- The temperature gradient between the bulk oil and the cold surface;
- The temperature of the bulk of the oil;
- The temperature of the cold surface;
- The cooling rate.

2.2.1 The Effect of the Temperature Gradient between the Bulk Oil and the Cold Surface (ΔT)

Molecular diffusion is regarded as the most prevalent deposition mechanism. In this mechanism, the mass flux of the wax molecules at the interface oil-deposit (from the oil towards the deposit) ($D_{wo,interface}\left.\frac{dC}{dr}\right|_{at\ interface}$) represents the loss of wax from the oil to form a deposit. Among the parameters in the mass flux, the concentration gradient ($\left.\frac{dC}{dr}\right|_{at\ interface}$) can be approximated by applying the chain rule and using two parameters: the radial temperature gradient ($\left.\frac{dT}{dr}\right|_{at\ interface}$) and the solubility gradient ($\frac{dC}{dT}$). The radial temperature gradient has been the focus in previous studies where the thermal driving force has been considered as the major parameter to explain the temperature effects on wax deposition[9, 62].

Some researchers believed that the overall temperature difference between the hot crude oil and the colder surrounding is the governing factor for wax deposition[20, 48, 63]. Some other researchers have proven that a higher overall temperature difference does not necessarily correlate to the extent of wax deposition. While some researchers showed the deposition rate to increase as the temperature differential increased[38, 46, 48, 64-66] other showed the opposite conclusion where the deposition rate decreases as the temperature differential increased[64, 65, 67].

To explain these contradictory results, the temperature gradient must be seen as the extent between the operating temperatures and the WAT. The larger the (WAT-T_{cold}) or the (T_{bulk}-WAT), the higher the deposition rate[64, 68, 69].

2.2.2 The Effect of the Temperature of the Hot Oil

According to Bidmus and Mehrotra's[64], the bulk temperature can be characterized by two main conditions explained below:

- Hot flow (T_{bulk} > WAT): it refers to the case where the wax-solvent mixture temperature is higher than the WAT, where the thermal driving force is not sufficient and the wax molecules are hard to crystallize in the bulk.
- Cold flow (WAT > T_{bulk} > PPT (pour point temperature)): it refers to the case where the wax-solvent mixture is at a temperature below its WAT and above its PPT. The heat transfer driving force is sufficient and the solute wax molecules crystallize. In pipelines, the crystalized wax remains suspended in the flowing oil and formed a slurry that is transported through pipelines with no deposition of solids. Under cold flow, the wax deposit mass decreases with the decreases in oil temperature.

Figure 2.1 shows schematically the proposed structures of a wax-oil mixture at the various cited temperatures.

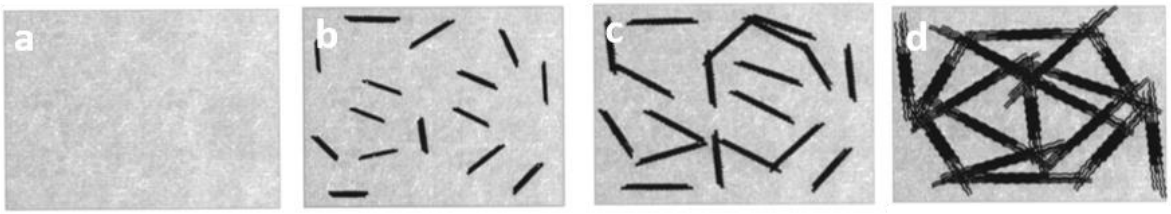

Figure 2.1. Schematic of proposed structures of a wax-oil mixture at various temperatures. **a)** Temperature is greater than the cloud point; **b)** temperature is just below the cloud point; **c)** temperature is between the cloud point and the gelation temperature; **d)** temperature is just below the gelation temperature taken from Singh et al.[32].

In hot flow conditions, where T_{bulk}> WAT and molecular diffusion is the main deposition mechanism, many researchers studied the effect of changing the bulk temperature while keeping the cold temperature constant. All results predicted a reduction of the deposition with increasing oil temperature at a constant coolant temperature (cf. **Figure 2.2**)[62, 64, 70-73].

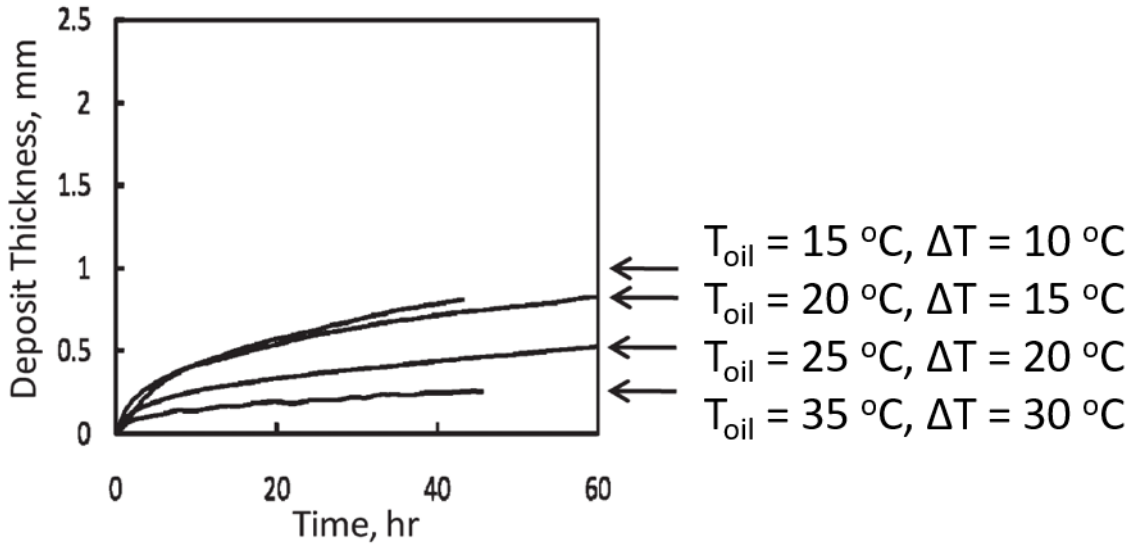

Figure 2.2. Comparison of deposit thickness as a function of oil temperature taken from Huang et al.[62].

Quan et al.[74, 75] studied the wax content and carbon number distribution in deposit under different bulk oil temperatures and constant coolant temperature. Results show that the increase in the bulk oil temperature under constant coolant temperature leads to the increase in the dissolving ability of higher carbon number components in bulk oils. Hence, the concentration of wax molecules with high carbon chain length increases in the deposit.

Many researchers investigated as well wax deposition under cold flow[56]; It has been suggested that cold flow is an alternative technology for decreasing solids deposition. Some

patents deal with the remediation of wax deposition by operating under cold flow conditions where a wax slurry is generated, precipitated wax crystals remain suspended in the flowing crude oil and will not adhere to the walls[75, 76]. Bidmus and Mehrotra[77] compare the two sets of deposition experiments cold flow and "hot flow" and showed that in hot flow, the deposit mass increased with a decrease in the mixture temperature, under hot flow. However, the deposit mass decreased with a decrease in the mixture temperature, under cold flow.

2.2.3 The Effect of Temperature of the Cold Surface

Many scholars[46, 48, 74, 75] have studied the effect of the coolant temperature under constant bulk temperature on wax deposit and carbon chain length distribution.

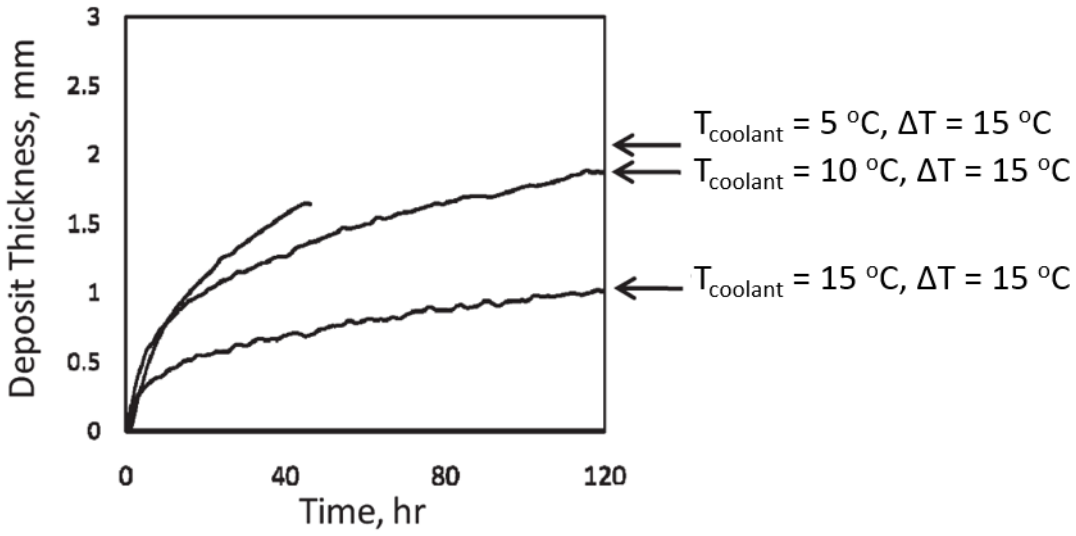

Figure 2.3. Comparison of deposit thickness as a function of coolant temperature, $T_{coolant}$, while T_{oil} was maintained constant at 20 °C taken from Huang et al.[62].

Results show that experiments with lower coolant temperature strengthens the driving force of the wax molecules diffusion from the bulk oil to the cold surface and improves of the ability of wax molecules to precipitate on the cold surface, hence, the wax deposition increases (cf.

Figure 2.3). However, the decrease in the coolant temperature allow the low molecular weight wax to crystallize. This leads to a wax deposit with high percentage of low carbon chain length wax[78-83].

2.2.4 The Effect of the Cooling Rate

The effect of cooling rate on wax deposition was studied in the literature with respect to its effect on the crystallization of the wax. First, cooling rate has a major effect on the crystal quantity, shape and size. It has been claimed that higher cooling rates result in the precipitation of smaller and highly populated wax crystals, creating a large number of nucleation (crystallisation) sites; On the other hand, the crystallisation process is believed to be slower at lower cooling rates leading to the formation of more uniformly larger wax crystal formation[84-89]. **Figure 2.4** shows the wax crystal size as a function of temperature and cooling rate of a waxy mixture, inferring that small crystals are formed at higher cooling rates.

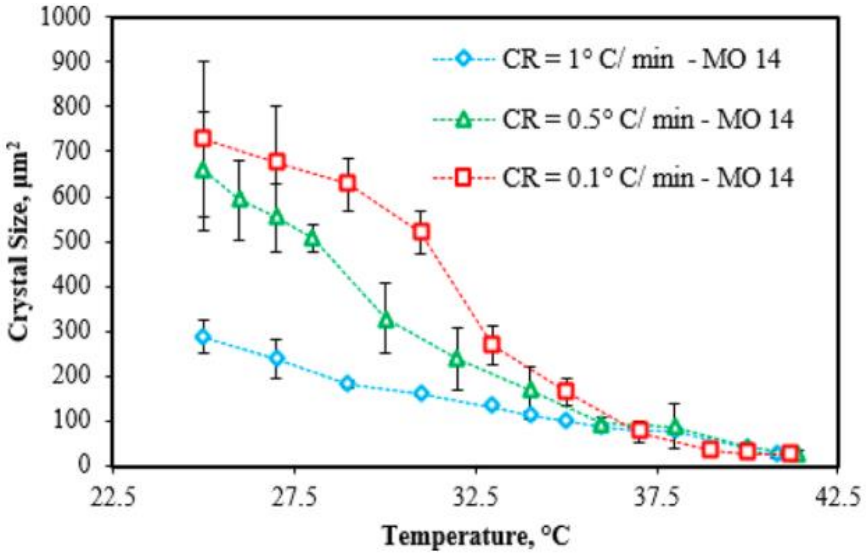

Figure 2.4. Crystal size evolution with temperature and cooling rate variations of a waxy mixture taken from Soedarmo et al.[86].

Besides, cooling rates have been discussed to have an effect on the WAT and the gelation temperature. While some researchers e.g. Singh et al.[32] claim that cooling rate does not affect the cloud point as it is a molecular phenomenon but it affects the gelation temperature of wax[32], a number of other experiments confirm that the WAT of a waxy mixture decreases with increasing the cooling rate. This change in the WAT is attributed to the effect of the cooling rate on the supersaturation of the waxy solution directly responsible of the formation of the first wax crystals[42, 90, 91].

2.3 Effect of surface on wax deposition

To perform a mechanistic study of wax deposition, cold surface properties should be investigated as a major parameter affecting wax deposition. As stated before, wax deposition requires the cold surface temperature to be less than WAT with a negative radial temperature gradient. However, the intensity of wax deposition is also highly dependent on the affinity of wax to the pipe surface[48]. Theoretically, one of the most effective method to eradicate wax deposition in subsea pipelines is to prevent conditions that promote the phenomenon on the surface itself, i.e. wax repellent surface. Hence, the niche to synthesise wax-phobic pipeline surfaces has been a target for flow assurance engineers[22]. To date, industrial efforts to identify effective anti-wax surfaces have largely focused on existing materials and surface modification techniques, and have proceeded via a trial-and-error methodology. In order to provide a current perspective of the development of wax-repellent coating materials, state-of-the-art surfaces used or tested for paraffin deposition control are summarized in the following section as well as a fundamental understanding of the adhesion mechanisms involved[22].

2.3.1 Surface materials: Adhesion theory

In the oil and gas industries, internal tubular coatings are commonly used to prevent corrosion of pipelines by carbon dioxide, hydrogen sulphide, oxygen, chloride, and acidic components. In the same perspective, an appropriately designed inner-wall coating for a pipeline can effectively reduce wax deposition without retarding oil production and causing financial losses. It is important to note however, surface materials must comply with other property requirements relating to integrity, corrosion, abrasion and chemical inertness to certify long-term operability[22]. Furthermore, pipeline surfaces need to be resistant to other deposits, for example asphaltenes and scales[22].

Researchers and industries have used a range of non-stick and anti-adhesive coatings to inhibit solid-liquid deposition phenomena. The literature survey encompasses several different types of materials, from metal surface treatments to synthesized polymers[22]. **Figure 2.5** shows the mass deposit reduction as a function of three different coatings used: epoxy, polyurethane, and Teflon PTFE.

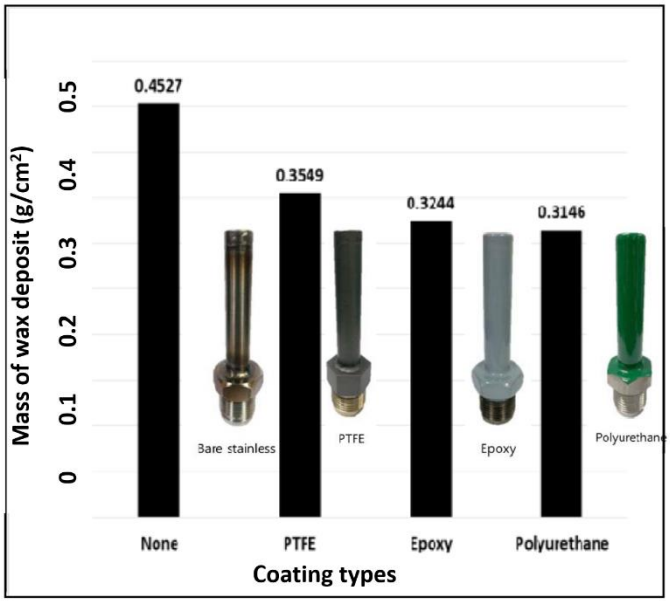

Figure 2.5. Mass of wax deposition per unit area depending on various coating of cold fingers, adapted from Juan et al[92].

Polyurethane coating, the most effective one, has a high wear resistance and also improved roughness characteristics and thermal insulation properties. It is widely used in the oil industry to control wax and scale deposition. Epoxy, is the most widely utilized coating to prevent the corrosion of pipelines and has been suggested as an effective coating to control wax deposition due to its the low free surface energy. PTFE (Polytetrafluoroethylene) Coating is expected to reduce wax deposition because it has a characteristic fluoropolymer that exhibits a low free surface energy[92-94].

The physical properties of coatings that influence wax adhesion are: surface wettability, roughness and thermal insulation[92].

2.3.2 Surface wettability

During crude oil transport and paraffin deposition on pipeline, the interaction force between crude oil and pipeline surface plays an important role in paraffin deposition and friction loss. The regular pipes, which have high free surface energy, can adsorb firmly the paraffin, asphalt, etc., in crude oil. It was postulated that the amount of wax deposition for a given temperature difference decreases with decreasing free surface energy[22, 95, 96].

In their work, Zhang et al.[95] studied the influence of several coatings, such as polyvinylidene fluoride (PVDF), silicone rubber, methyl acrylate-styrene copolymer (MAS), polyurethane (PU), epoxy resin (EP), on paraffin deposition prevention. The wettability characteristics and the contact angle between coating surface and crude oil were measured. The wetting characteristics of the surface have a significant influence on the amount of paraffin deposited. The low surface energy of fluoroethylene polymer, silicone rubber and methyl acrylate-styrene copolymer coatings, can increase the contact angle and decrease the steel surface wettability against crude oil.[95] The wettability difference of the coating would be related to their surface composition, functional group and surface density[97].

2.3.3 Surface roughness

Research suggested that the surface roughness had a pronounced effect on the amount of deposit[95]. Surface roughness refers to the extent of the fine embosses on a surface. Increasing the roughness on steel and plastic surfaces has been shown to increase wax deposition, likely resulting from the addition of heterogeneous nucleation sites as well as substrate where wax deposition can take place[92]. Results obtained from an investigation performed by Patton et al.[97] indicate that wax does not adhere to the pipe wall but is held in place by surface roughness

and/or irregularities. The smoother the surface, the more easily the embryonic deposit would be removed from the surface[97, 98].

2.3.4 Thermal conductivity

Thermal conductivity refers to the property value for the amount of thermal conduction; a low thermal conductivity for a coating can maintain the temperature of the inner wall of the pipeline throughout the whole section. This leads to a decrease in the thermal driving force between the deposition surface and the bulk oil, which is proportional to the rate of wax deposition.

Figure 2.6a shows the effect of the thermal conductivity of 4 different coating on wax deposition and **Figure 2.6**b shows a graph that presents the amount of wax deposition compared with the thickness polyurethane coating.

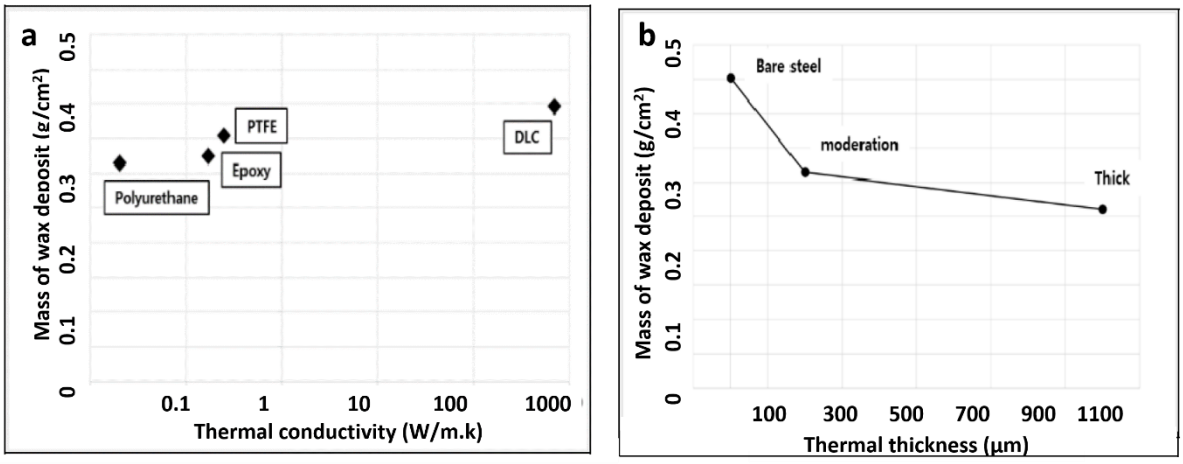

Figure 2.6. a) Mass of wax deposition per unit area depending on thermal conductivity **b)** mass of wax deposition per unit area depending on coating thickness for polyurethane taken from Jung et al.[92].

Results indicate that wax deposition reduces as coating thickness increases and thermal conductivity decreases. Jung et al. stated that thermal conductivity and coating thickness are, of all the properties of internal tubular coatings, the most influential factor in the changes relating to the amount of wax deposition[92].

2.4 Effect of Flow Rate on Wax Deposition

The effect of flow behavior on wax deposition is subject to controversial discussion between researchers at both theoretical and experimental levels. Until now, there has been no final conclusion about the mechanism by which the flow regime affect wax deposition[39].

2.4.1 The Shear Dispersion as a Deposition Mechanism

Brown et al.[99] reported that the rate of wax deposition by shear dispersion is expected to be governed by the following equation:

$$r_{WD} = kC_w\dot{\gamma}A \qquad \text{Eq. 2.3}$$

where k is the deposition rate constant, C_w is the volume fraction concentration of solid wax at the wall, A is the deposition area, and $\dot{\gamma}$ is the shear rate.

Theoretically, Eq. 2.3 has been used in the literature as a model for shear dispersion mechanism[9]. However, Azevedo & Teixeira[9] note that for oil flowing in a pipeline, the concentration of solid wax is highest at the wall and lowest in the bulk liquid phase. Thus, the natural direction for shear dispersion is away from the pipe wall.

To understand the contribution of flow on wax deposition, several studies have been conducted in wax deposition loops under zero heat flux conditions[9, 38]. In these studies, oil and wax mixtures were pumped through pipes, having inlet temperatures below the cloud point. The pipe wall was either maintained isolated or kept at the same temperature as the fluid, so as to guarantee that there would be no heat flux from the wall to the fluid. Under such conditions, it was expected that solid crystals would be present throughout the flow and available for deposition. Since the heat flux is zero, there can be no means for the molecular diffusion mechanism to act. Also, since there is no radial heat flux and, consequently, no radial diffusion of liquid wax, there will be no concentration gradient of solid particles close to the pipe wall. Under zero heat flux conditions, the deposition would only be possible due to a flow-induced mechanism, such as shear dispersion. All the experimental results available in the open literature, however, have shown no deposition under zero heat flux conditions. Researchers have then concluded that the shear dispersion is not relevant to the deposition of wax crystals but rather contributes to the decrease in the mass of the wax deposit[9].

Under similar heat flux, in most cases where multiple shear rates were studied, it was found that, contrary to Eq. 2.3 , the deposition rate decreased with increasing shear rate (cf. **Figure 2.7**)[59, 99-101]. This decrease in the wax deposition is refered to either the change in the heat transfer across the deposition surface or the effect of sloughing that remove wax layers at a relatively high shear rate. Below is an extensive summary of both phenomena reported in the literature.

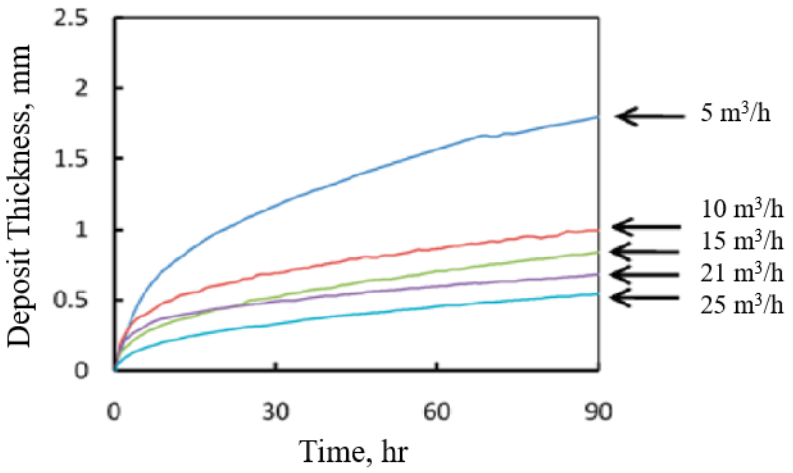

Figure 2.7. Comparison of deposit thickness as a function of the oil flow rate with constant coolant and oil temperatures taken from Lu et al.[47].

2.4.2 The Effect of Flow on Heat Transfer

Many studies intuitively attribute the decrease of wax deposition with shear to the change in the heat and mass transfer with the flow. The heat transfer was proven to change under flow in both the cold finger and flow loop experiments. For instance, to evaluate the effect of the flow on wax deposition in a cold finger device, Bidmus and Mehrotra[45] performed an investigation about the temperature change with rotational speed with several thermocouples mounted in the bulk solution. The results show that, for a fixed cold finger and bulk temperature, the temperature of the bulk decreases with increasing the shear rate due to convective heat flux from the bulk solution to the cold finger. In their studies, Jennings and Weispfennig[46] observed an increase in the heat transfer from the cold finger with stirring speed which leads to decrease in the bulk temperature. A similar trend is observed in cold disk experiments reported by Wu et al.[20]: At higher flow rate, the temperature difference between the bulk solution and the cold disk decreases. This detriment effect is responsible for the decrease in the wax deposition as the thermal driven force is weakened.

Other research groups have made similar observations with flow loop deposition tests as well[19, 48]. Fogler and co-workers developed "The Michigan Wax Predictor" (MWP) to elucidate this trend by analyzing the growth rate of the wax deposit in a series of flow loop experiments from first principles[47]. They stated that the change of the flow rate has three main effects:

Effect 1: An increase in oil flow tends to provide a smaller boundary layer and a steeper radial concentration profile, thereby increasing the mass flux (cf. **Figure 2.8**).

Effect 2: An increase in oil flow causes more hot oil to be pumped through the pipe and, thus, leads to an increase in the temperature at the deposit interface. This increase in the interfacial temperature causes the diffusivity at the interface to increase thereby increasing the mass flux.

Effect 3: An increase in oil flow results in an increase in temperature at the interface (cf. **Figure 2.9**), which leads to a higher concentration of dissolved wax molecules at the interface. This increase in interface concentration decreases the concentration difference ($C_{inlet} - C_{interface}$), thus decreasing the mass flux.

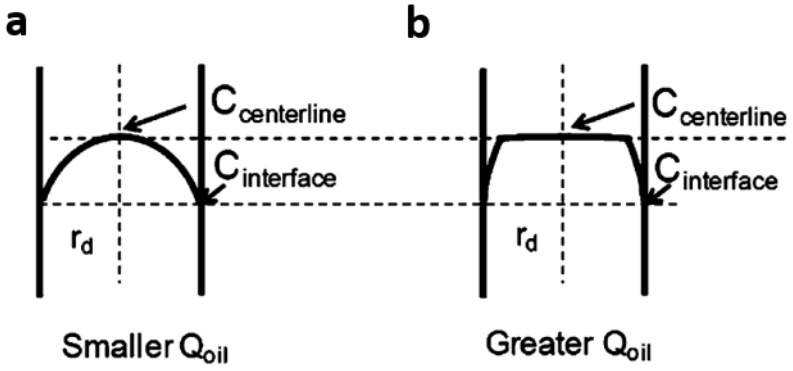

Figure 2.8. Sketches of the concentration profiles with **a)** small flow rate **b)** greater flow rate taken from Lu et al.[47].

At isothermal conditions, a faster deposition rate is observed with an increasing flow rate because only effect 1 plays a role in affecting the radial mass flux. However, in the case of wax deposition, which occurs under non-isothermal conditions, the existence of effects 2 and 3 delineates how the interaction of heat transfer and the solubility curve can alter the conclusions from isothermal conditions, which can result in the counterintuitive effects of the flow rate on the growth rate of the wax deposit.

Indeed, the rise in forced convection associated with an increase of rotation frequency contributes to a steeper temperature profile at the liquid solid interface. This has two antagonistic effects on the rate of wax deposition. First, the diffusion coefficient of alkane molecules increases which has a positive impact on deposition rate. However, the rise in temperature will increase the solubility of alkanes at the wax interface, this detrimental effect for wax deposition is often regarded as the most influential input parameter for wax deposition models[13, 47, 62].

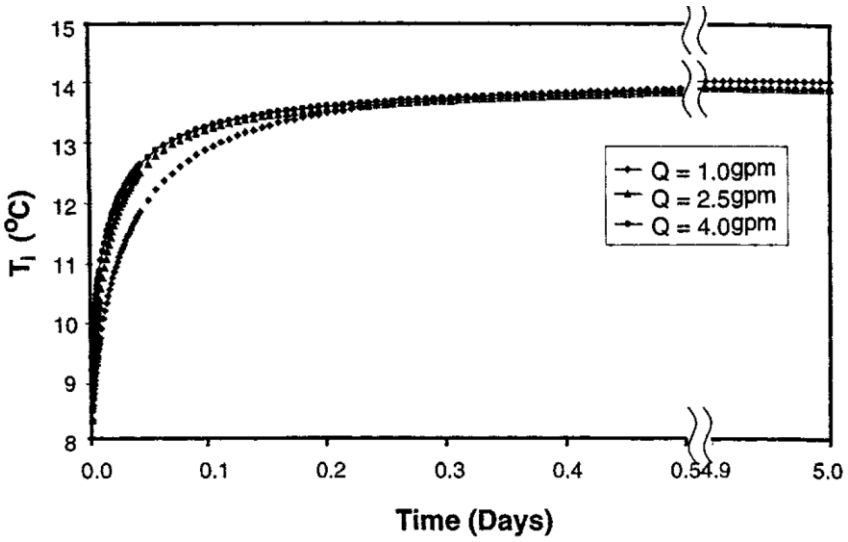

Figure 2.9. Interface temperatures as a function of time for various flow rates at mid-section of flow loop taken from Singh et al.[19].

2.4.3 The Effect of Flow on Sloughing/Wax Removal

Wax deposit is inevitably subjected to the shear forces due to the flow of the oil. While the flux from the bulk to the wall causes deposition, the sloughing effect makes part of already deposited wax to break free. Azevedo & Teixeira[9] pointed out that shear dispersion may play a role in wax deposit removal, which would affect the rate at which wax molecules accumulates. The thickness of deposit layer with sufficiently low mechanical strength can be limited by sloughing. Sloughing is originated from the drag force applied by the fluid to the wax particles that may overcome the adhesion. In particular, the removal of wax deposit by shear forces becomes significant under turbulent flow conditions compared to laminar flow off[81, 102-106].

Lu et al.[47] stated that the terminology of "shear removal" referred either to the possible continuous retardation in the build-up of the deposit by the fluid at the oil−deposit interface or to the sloughing that causes the sudden removal of a layer of the deposit, especially in the flow

regime with relatively high Reynolds numbers. The possible explanations are either that the increasing shear stress makes it more difficult for new wax molecules to adhere to the already existing wax deposit or that the shear stress removes parts of the already deposited wax [107]. If the gel is formed statically, the crystal-crystal interactions that are initially weak have the opportunity to grow in strength and eventually gel, but this formation does not happen as easily with the presence of a shear stress. In this situation, more wax crystals are needed to form the necessary interactions to form a gel, which would require a lower temperature.

Besides, sloughing is believed to occur when the shear stress overcomes the cohesive and adhesive forces of the alkane wax molecules to the surface[49-51]. Sloughing is believed to be a function of a combination between both the operating temperature and shear stress. Fong and Mehrotra[70] stated that at low temperature, the reduction rate in thickness of deposit layer would not be obvious even at a large wall shear stress. But when the oil temperature and wall temperature are increased, the wax layer was eroded in a high rate up, with a lower shear stress. For this process the temperature plays a key role in sloughing. It is possible that the results are related to the adhesion of deposit layer. With the increase of operating temperature, part of the deposit layer becomes soft and accordingly the adhesion stress declines. In this case, any soft or loose deposit layer would break down even if the shear stress at the solid–liquid interface is not too large.

2.4.4 Effect of Flow Rate on Wax Deposit Composition

Further investigation on the effect of shear rate on wax deposition was undertaken by analyzing the wax deposit carbon chain length distribution using GC-FID. GC-FID results show a change in the chemical make-up of the deposit with shear rate. Deposits obtained under

increased flow rate conditions were found to be harder, with higher solid content and lower solvent or oil content (cf. **Figure 2.10**)[19, 31, 42, 48, 70, 108-110]. Besides, as the shear rate increases, the percentage of low molecular weight wax decreases.

These results can be explained by three main scenarios:

First scenario concerns the effect of flow in terms of applying a shear stress on the deposit layer. With increasing stress, the oil liquid fraction of the deposit is squeezed out of the wax deposit reducing both the total oil content as well as the concentration of low molecular weight already dissolved in the trapped oil. Besides, the shear stress may lead to removal of wax from the wax deposit. However, this removal may be selective. The higher the wax chain length, the higher the total van der Waals intermolecular forces and the higher the wax lattice energy. Hence, with low molecular weight wax, the cohesive forces are low enough to be overcome by a shear stress at the interface of the wax layer.

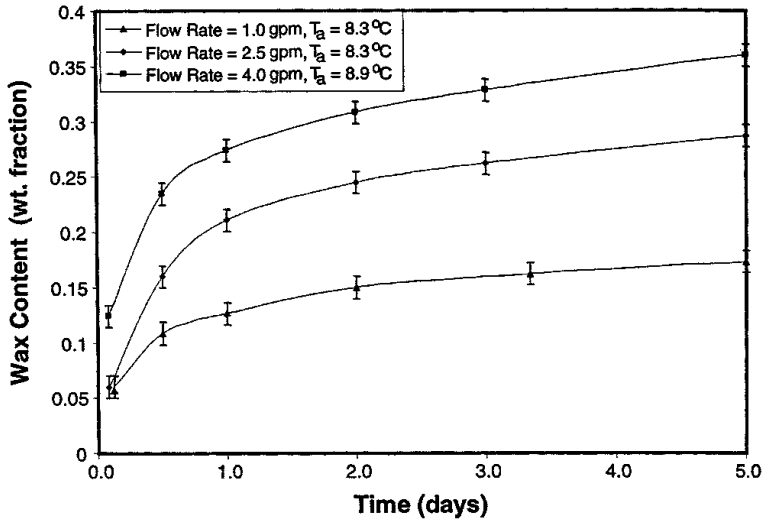

Figure 2.10. Wax content of the gel deposit as a function of time for various flow rates taken from Singh et al.[19]

The second scenario concerns the aging process that may be enhanced by the effect of flow. The change in the chemical make-up can be explained by the counter diffusion of lighter and heavier constituents within the deposit, as proposed by Singh et al[19]. With the wax deposit thickness being reduced by the flow, the temperature gradient across the wax layer increases leading to a higher counter diffusion of wax within the gel layer inducing a higher wax content.

The third scenario concerns the effect of flow on the temperature of the deposit surface. The increase in the coolant temperature increases the dissolving ability of wax molecules and the amount of low carbon number wax molecules dissolved around the cold surface increases[19, 31, 32].

2.5 Modelling Wax Deposition

A number of mathematical models has been developed in the literature to describe and predict wax deposition. These models are mostly based on molecular diffusion mechanism and have a main aim to predict the wax deposit thickness. The aim of this part of the literature review is to write a comprehensive analysis of the fundamentals of transport phenomena used to derive wax deposition models and the use of molecular diffusion mechanism as the descriptive phenomena for wax deposition.

2.5.1 Basics of Wax Deposition Models

The first two questions to answer and understand deeply before deriving a wax deposition model are questioned and answered by the pioneer group in the wax deposition modelling, Fogler group, in the University of Michigan[11]:

- What form of wax deposits?
- How wax deposits?

Wax present in the oil has two forms (cf. **Figure 2.11**): Dissolved wax and precipitated wax in suspension in the oil. Of these two types of wax, which is the source for wax deposition at the pipe wall?

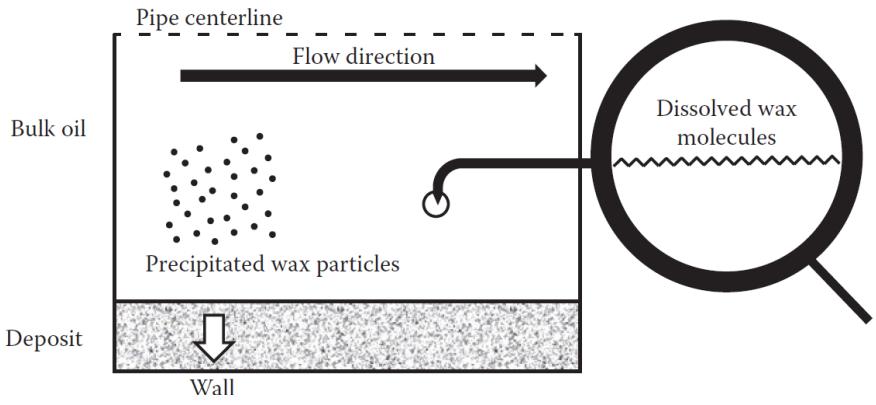

Figure 2.11. Schematic of the two types of wax that could potentially cause wax deposition taken from Huang et al.[11].

This question was intensively studied between the 1980s and 2000s. During the early stage of such investigation, the wax deposit formation mechanisms initially proposed by Burger et al.[38] and discussed earlier in the introduction, are based on the diffusion of either the dissolved wax in the bulk oil solution or the precipitated wax in suspension in the oil solution. Molecular diffusion mechanism states that wax deposition is due to the diffusion of soluble wax to the cold surface, on the other hand, shear dispersion, Brownian diffusion and gravity settling mechanisms attribute the wax deposition to the suspended wax molecules already precipitated in the solution. However, the later mechanisms based on the diffusion of precipitated wax were quickly identified to have insignificant impact on wax deposition and it was generally accepted

that the molecular diffusion, based on diffusion of dissolved wax, is the main mechanism for wax deposition. The precipitated wax crystals formed away from the wall do not seem to contribute to the formation of the wax deposit but rather flow with the oil to form a suspension in the fluid mixture. Molecular diffusion was therefore used to model wax deposition in many studies[13, 19, 111-113].

Identifying molecular diffusion as the primary mechanism for wax deposition, one can answer then the second question: how does the wax deposits based on molecular diffusion?[11]

Molecular diffusion mechanism attributes the wax deposition to the diffusion of the dissolved molecules of the waxy components toward the wall. The wax deposition depends on the magnitude of the radial diffusion of dissolved wax through the boundary layer towards the cold surface. This rate of diffusion is determined by heat and mass transfer. Besides the radial diffusion of wax, it was found that a counter diffusion phenomenon, in which wax molecules diffuse into the gel deposit and oil molecules diffuse out of the deposit, is responsible for aging as well. The aging rate of the gel deposit depends on the wall temperature of the pipeline as well as the flow rate of the oil[19].

The molecular diffusion consists of 4 steps schematized in **Figure 2.12**:

Step 1: Precipitation of dissolved wax molecules.

Step 2: Generation of radial concentration gradient of dissolved waxy components.

Step 3: Deposition of waxy components on the surface of an existing deposit.

Step 4: Internal diffusion of waxy components in the deposit[11].

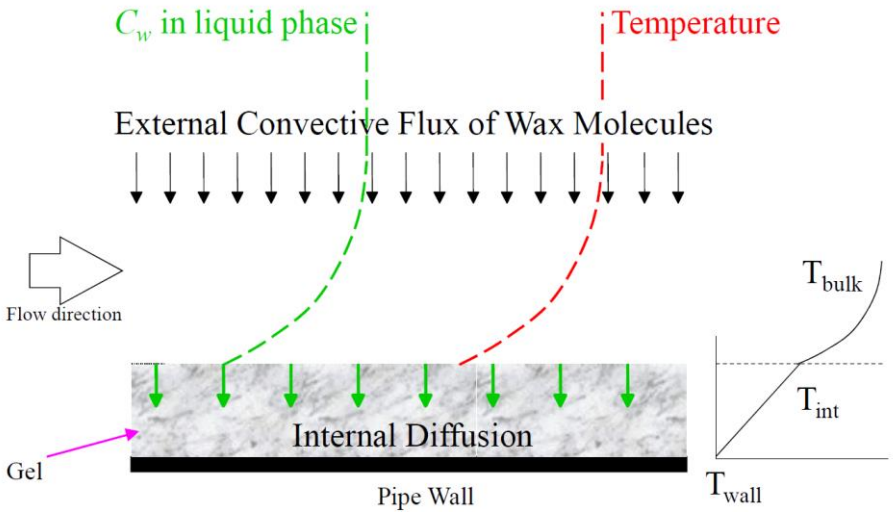

Figure 2.12. Schematic of the wax deposition process taken from Huang et al.[11].

2.5.2 Wax Deposition Algorithm

Figure 2.13 shows the general algorithm for wax deposition modelling. The algorithm is based on molecular diffusion mechanism and consists mainly of two steps: the calculation of the heat transfer and related hydrodynamics to characterize the temperature profile in the system; and the derivation of the mass growth rate through mass transfer calculations. The main input of this algorithm are the operating conditions and oil properties.

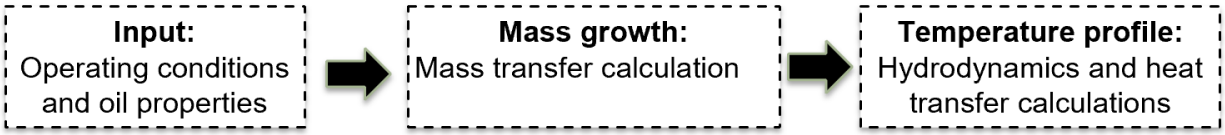

Figure 2.13. General algorithm for wax deposition model, adopted from Huang et al.[11]

Although models in the literature are based on the same algorithm scheme, however, the difference reside mainly in the approach used to calculate the heat and mass transfer and the

link between them to derive the mass growth. Three scenarios shall be considered here for wax deposition:

(1) no precipitation of wax molecules in the oil until they reach the interface;

(2) instantaneous precipitation of wax molecules;

(3) slow precipitation of wax molecules.

These three scenarios form the basis of deposition models in the Literature. Based on these 3 scenarios, 3 different approaches used to model wax deposition in the literature as well as an example of each model from the literature will be discussed. The approaches and the example models to be discussed are the following:

Scenario 1: The Chilton-Colburn analogy approach: Example: Singh el al. model for wax deposition under laminar flow in flow loop[19].

Scenario 2: The Solubility approach: Example: Venkatesan and Fogler model for wax deposition under turbulent flow in flow loop[114].

Scenario 3: The wax precipitation kinetics approach. Example: Michigan Wax predictor wax deposition modelling in flow loop under laminar and turbulent flow[115].

2.5.2.1 Balance of the Gel Layer

To calculate the heat and mass transfer, an energy and mass balance must be derived at the wax deposit interface. The convective flux of wax molecules to the gel deposit-oil interface has been formulated using the following mass and energy balances[19].

Energy balance (temperature profile):

Rate of change of temperature across the gel deposit = radial convective heat flux from the bulk to the fluid-gel interface

$$2\pi r_i h_i [T_b - T_i] = \frac{2\pi k_e [T_i - T_w]}{\ln(\frac{R}{r_i})} \quad \text{Eq. 2.4}$$

where r_i is the effective radius of a pipe, h_i the inner convective heat transfer coefficient, T_b the temperature of the bulk, T_i the temperature at the interface, T_w is the temperature on the wall, R is the radius of a pipe, k_e is the thermal conductivity of the wax deposit (cf.**Figure 2.12**)[19].

Mass balance (Growth rate):

Rate of change of wax in the gel deposit = radial convective flux of wax molecules from the bulk to the fluid-gel interface

$$(-2\pi r_i)\overline{F_w}\rho_{gel}\frac{dr_i}{dt} = 2\pi r_i k_M [C_b - C_{ws}(T_i)] \quad \text{Eq. 2.5}$$

where $\bar{F}_w$ is the wax fraction in the deposit, ρ_{gel} is the density of the wax deposit, k_M is the inner convective mass transfer coefficient, C_b is the bulk concentration of wax, C_{ws} is the solubility of the wax[19].

In order to solve these heat and mass transfer equations, the inner convective heat and mass transfer coefficient, h_i and k_M must first be calculated. The calculation of the mass and heat transfer define the approach used and its limitation.

2.5.2.2 Scenario 1: The Chilton-Colburn Analogy: Example of Singh el al. Model for Wax Deposition Model under Laminar Flow

In two articles published in the *AIChE Journal in 2000 and 2001,* Singh et al., have explored the wax deposition phenomenon using laboratory flow-loops, and developed a mathematical model to predict the deposition under the laminar flow regime[19, 31].

In order to estimate the transport rates, the famous heat-transfer analogy "Chilton-Colburn" equation was used. The Chilton-Colburn assumes an independent heat and mass transfer where the Nusselt number is equated to the Reynolds and Prandtl numbers as

$$Nu = 0.023Re^{0.8}Pr^{1/3} \quad \text{Eq. 2.6}$$

The mass transfer coefficient is calculated based on the analogy between heat and mass transfer using the analogous correlation for mass transfer below where the Pr number was replaced by the Schmidt number Sc:

$$Sh = 0.023Re^{0.8}Sc^{1/3} \quad \text{Eq. 2.7}$$

According to this analogy, the heat and mass transfer coefficients are calculated as follows with k_{oil} is the oil thermal conductivity:

Heat transfer coefficient:

$$h_h = \frac{Nu_h \times k_{oil}}{2R} \quad \text{Eq. 2.8}$$

Mass transfer coefficient, where D_{wo} is the diffusivity of the wax in the oil.

$$k_1 = \frac{Nu_m \times D_{wo}}{2R} \quad \text{Eq. 2.9}$$

Excellent agreement with the experimental data was found in the laminar flow regime where the heat and mass transfer correlations used in this model are independent of each other. This correlation for mass transfer above assumes that bulk precipitation does not occur during mass

transfer. This decoupling of the heat and mass transfer neglects the precipitation of wax molecules in the oil phase and corresponds to Scenario (1) for molecular diffusion. However, work has shown that for turbulent flow conditions this assumption is invalid. In turbulent flow conditions, the heat and mass transfer are not independent because there can be significant precipitation of wax molecules in the oil phase. The precipitated wax particles do not deposit on the pipe wall but rather flow with the oil. More importantly, the precipitation of wax reduces the amount of dissolved wax molecules in the oil that can be potentially transported to the wall and deposit. Therefore, this approach of using independent heat and mass transfer (IHMT) correlations (also known as the ‘‘Chilton–Colburn analogy") overestimates the deposition rate by assuming all the wax to be dissolved in the bulk solution and available for diffusion and deposition on the cold surface.

The Colburn analogy is a well-known analogy for predicting the heat and mass- transfer coefficients in turbulent pipe flow. However, this analogy is not applicable for predicting the mass transfer rate in turbulent flows, where the concentration field is correlated to the temperature field. During the wax deposition process, the temperature gradient is directly responsible for establishing the concentration gradient as explained earlier. Thus, these fields are not independent. The concentration boundary layer thickness is not independent of the temperature boundary layer thickness.

As a result, the heat-mass transfer analogy as described earlier is not expected to hold. Hence, an approach based on solubility to derive the mass-transfer coefficient was used later on for wax deposition modelling.

2.5.2.3 Scenario 2: The Solubility Approach: Example of Venkatesan and Fogler Model for Wax Deposition under Turbulent Flow in Flow Loop

Because heat and mass transfer occur simultaneously in the boundary layer, the wax concentration profile is strongly influenced by the temperature profile[114]. When the temperature falls below the cloud point temperature, precipitation of wax molecules occurs in the thermal boundary layer. In order to take into account of this dependency, Venkatesan and Fogler proposed[114] a solubility method to calculate convective mass transfer rate when there is a dependency between heat and mass transfer. The mass transfer is dependent on heat transfer based on the solubility of wax, $C_{ws}(T)$ as follows:

$$Nu = 0.023Re^{0.83}Pr^{0.33} \quad \text{Eq. 2.10}$$

$$Sh = Nu\left(\frac{dC_{ws}(T)}{dT}\right)|_{interface}\frac{T_{bulk}-T_{interface}}{C_{ws,bulk}(T)-C_{ws,interface}(T)} \quad \text{Eq. 2.11}$$

The term on the right hand side of Eq. 2.11 is the slope of the wax solubility curve (C vs. T) at the interface temperature (Solubility curve is shown in **Figure 2.14**). An assumption made in taking this ratio is that the system is at thermodynamic equilibrium, that is, the kinetics of alkane precipitation are much faster compared to the transport rates.

By combining the Nusselt number with the solubility of wax as shown in Eq.2.11, this approach calculates the mass transfer rate (i.e., the Sherwood number) assuming that the concentration of wax in the oil follows thermodynamic equilibrium with the precipitated solid wax particles. This assumption indicates that during radial transportation, all the super saturated wax molecules will precipitate instantaneously in the oil and form particles when they reach a region where the temperature falls below the WAT. These precipitated wax particles

will flow with the oil and no longer contribute to deposition, which corresponds to Scenario (2) as discussed in the previous section. At any time *t*, the Sherwood number can be calculated using the tangent of the solubility curve at the interface temperature multiplied by $\Delta T / \Delta C$.

However, by over predicting the precipitation rate, this ‘‘solubility method’’ underestimates the remaining dissolved wax molecules in the boundary layer of the oil. These dissolved wax molecules can eventually reach the wall and deposit. Therefore, this approach provides the lower bound of the deposit thickness[62].

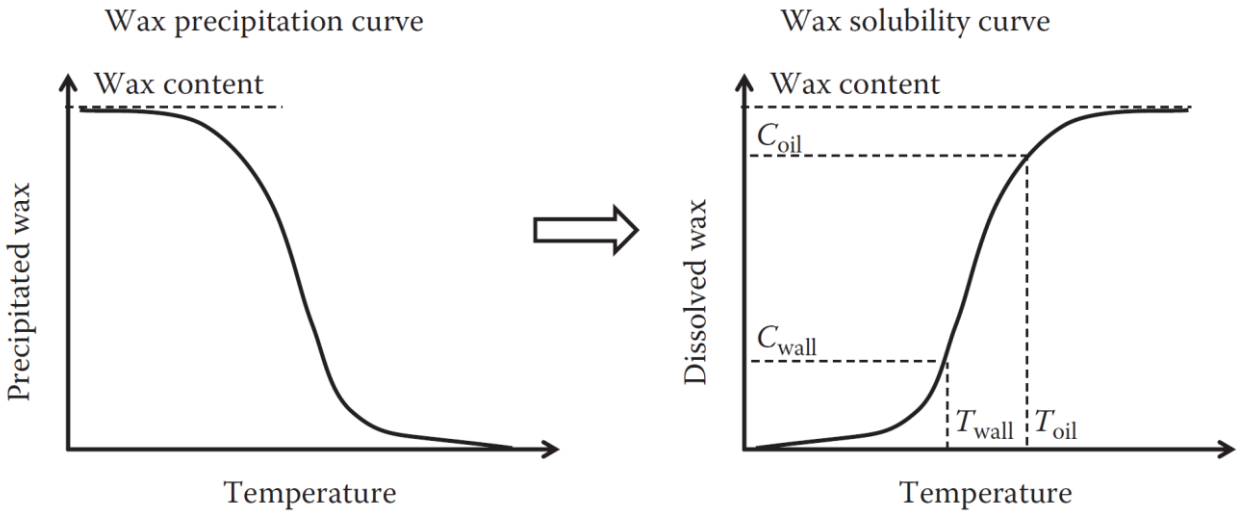

Figure 2.14. Conversion from the wax precipitation curve to the wax solubility curve taken from Huang et al.[11]

2.5.2.4 Scenario 3: The Wax Precipitation Kinetics Approach: Example of Michigan Wax Predictor Wax Deposition Modelling in Flow Loop under Laminar and Turbulent Flow.

One of the primary limitations of the previous predictive deposition models is the assumption of the complete absence of kinetic limitations in the rates of incipient gel formation and deposit build-up[116].

Given these upper bound and lower bound provide physical limits of deposition modeling, a deposition model that falls between these two bounds and accounts for the kinetics of the precipitation of wax in the oil phase (Scenario (3)) is still needed to better describe the deposition phenomena in turbulent flow conditions. Neglecting crystallization kinetics considerations may lead to predictions of wax deposition in cases where a stable gel cannot form, resulting in unnecessary capital expenditures related to alkane wax remediation and control systems.

To quantify the effect of precipitation kinetics on wax deposition an upgraded deposition model called the Michigan Wax Predictor (the MWP) was developed by Huang et al. [13, 115]. The MWP first evaluates the heat and mass transfer by solving numerically the following equations.

Heat transfer:

$$V_z \frac{\partial T}{\partial z} = \frac{1}{r}\frac{\partial}{\partial r}\left[r(\varepsilon_H + \alpha_T)\frac{\partial}{\partial r}\right] \qquad \text{Eq. 2.12}$$

where, Z is the axial coordinate, r is the radial coordinate, ε_H eddy thermal diffusivity and α_T thermal diffusivity of the oil.

Mass transfer:

$$V_z \frac{\partial C}{\partial z} = \frac{1}{r}\frac{\partial}{\partial r}\left[r(\varepsilon_M + D_w)\frac{\partial C}{\partial r}\right] - k_r\left(C - C_{ws}(T)\right) \qquad \text{Eq. 2.13}$$

where, ε_M eddy mass diffusivity.

The last term on the right-hand side of Eq. 2.13, accounts for the rate of precipitation of wax in the oil, where k_r is the precipitation rate constant.

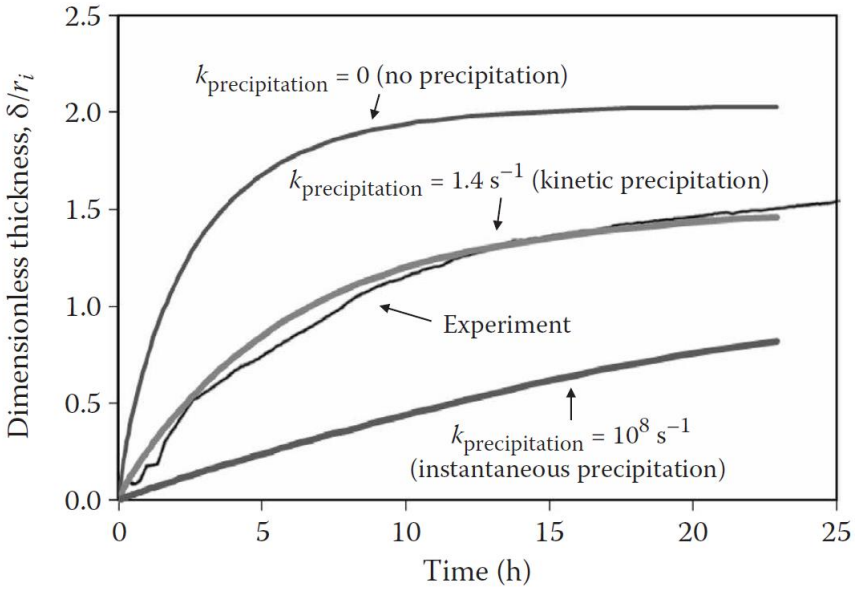

Figure 2.15 The impact of wax precipitation kinetics in the oil flow on wax deposition predicted by the MWP taken from Huang et al.[11].

It can be seen in Eq. 2.13 that the precipitation rate constant, k_r, determines the effect of precipitation of wax molecules in the bulk oil on wax deposition. It should be noted that if no precipitation of wax molecules occurs in the oil, the heat and mass transfer equations Eq. 2.12 and Eq. 2.13 are not related; thus, the model reduces to the IHMT model as the upper-bound prediction. As k_r increases and approaches infinity, the wax concentration becomes close to the thermodynamic equilibrium concentration, $C_{ws}(T)$, which represents the lower-bound

solubility model (cf. **Figure 2.15**). The precipitation rate constant k_r (or equivalently the growth rate of wax nucleus in supersaturated solution) is zero if the temperature of oil is greater than the WAT. When the oil temperature is lower than the WAT, it is assumed that nucleation occurs over a short time and the size of the nuclei quickly reaches the critical nucleus size.

2.5.3 Sloughing Modelling

There have been several attempts made to empirically estimate the shearing effect. Some of the widely cited models are listed below.

2.5.3.1 Kern and Seaton (1959)

The One of the earliest and widely used expression of shear removal modelling was based on the fouling model of Kern and Seaton (1959)[117]. Kern and Seaton suggested that rate of deposit's shear removal (mr) is proportional to the wall shear stress (τ_w) and deposit thickness (S).

$$mr = K_2\, \tau_w\, S \qquad \text{Eq. 2.14}$$

where, K_2 is a proportionality constant

2.5.3.2 Nazar Model (2001)

Nazar et al.[118] enhanced Kern and Seaton expression of fouling and proposed that the removal rate (J_r) is proportional to the deposit mass (m_t), wall shear stress (τ_w), and inversely proportional to the wax deposit strength (ψ), as follows:

$$J_r = \frac{k_c \tau_w m_t}{\psi} \qquad \text{Eq. 2.15}$$

where, k_c is a proportionality constant.

In this model, aging (internal diffusion) was considered to be directly related to the sloughing mechanism and was implicitly considered in the modelling through a parameter called (k_r)

$$k_r = \frac{k_c}{\psi} = A_1\, e^{(\frac{B_1}{\Delta T})} \qquad \text{Eq. 2.16}$$

where, A_1 and B_1 are constants which depend on the oil composition, and ΔT is the temperature difference across the wax deposit.

This model showed a good agreement with experimental data in laminar flow conditions. However, the results of the model under turbulent flow conditions was only assessed qualitatively by using some parametric studies, as no detailed experimental data is available. "k_r" was considered constant and is equal to 0.01, assuming that the sloughing effect is only a function of the flow hydrodynamics.

2.5.3.3 Tulsa Model (2004)

TUWAX was modified by Hernandez et al.[119] by adding a shear removal term to the deposition model as follows:

$$J_g = J_c\,[1 - \varphi(F_w)] - J_s \qquad \text{Eq. 2.17}$$

where, J_g is the net mass flux directed toward deposit growth, J_c is the convective mass flux from bulk fluid to the interface, J_s is the shear removal flux, φ is a function, and F_w is the wax fraction in deposit.

The shear removal term was considered to be constant with time, as the mechanism is not yet fully understood. It was recommended to better understand this term to study its dependence as a function of shear stress, Reynolds number, and fluid viscosity.

2.5.3.4 Edmonds (2007) & Pan (2009)

This model is also a modified version of kern-Seaton model.[120] incorporated the finding found by Venkatesan et al.[121] that wax gel yield stress might be proportional to the mass fraction of the wax layer raised to the power 2.3 ($\omega^{2.3}$) to the model, as follows:

$$J_{sr} = \frac{k\delta\tau_w}{\omega^{2.3}} \qquad \text{Eq. 2.18}$$

where, δ is the deposit thickness, and k is a parameter

Pan et al.[122] added a parameter (α) to Edmonds equation for a better fitting, as follows:

$$J_{sr} = \frac{k\delta\tau_w^{\alpha}}{\omega^{2.3}} \qquad \text{Eq. 2.19}$$

This model was used when wax deposition rates estimated by molecular diffusion overpredicts the experimental results, in which shear removal may not be neglected. However, tuning seems to be impossible to avoid, due to insufficient information in the literature about shear removal or sloughing mechanism.

2.5.3.5 Huang et al. Model (2014)

Wang and Huang[123, 124] have developed a unified wax deposition model suited for most of crude oils based on both theoretical analysis and the loop simulation of nine typical crude oils, which explicitly incorporated the impact of shear stress near the pipe wall (at the solid/liquid interface) on wax.

$$W = 87.1\tau_w^{-0.3008}\frac{1}{\mu}\left(\frac{dC}{dT}\right)\left(\frac{dT}{dr}\right)^{0.2737} \quad \text{Eq. 2.20}$$

where, W is the wax deposition rate, τ_w is the shear stress near the pipe wall. The shear stress of the Newtonian fluid under turbulent flow can be calculated by the following equation based on a turbulence correlation of the Darcy/Fanning fraction factor with the Reynolds number on a smooth pipe:

$$\tau_w = 4.94 \times 10^{-3} Re^{0.75}\frac{8V}{d}\mu \quad \text{Eq. 2.21}$$

If the flow is laminar, the shear stress can be expressed as:

$$\tau_w = \frac{8V}{d}\mu \quad \text{Eq. 2.22}$$

where, μ is the viscosity of the crude oil, which can be determined by interpolation for the viscosity-temperature profile.

dC/dT is the change of dissolved wax concentration with respect to temperature near the pipe wall and dT/dr is the radial temperature gradient near the pipe wall.

As stated above, molecular diffusion is indeed the key mechanism that controls wax deposition, but an accurate quantitative description of wax deposition also needs to take the effects of shear stripping into account.

Wax deposit is inevitably subjected to the shear forces due to the flow of the oil. While the flux from the bulk to the wall causes deposition, the sloughing effect makes part of already deposited wax to break free.

Simulating the wax removal by the shear forces can improve the understanding of the physics of wax deposition, thus help in the design of appropriate operation strategy and flow improving chemicals[123].

2.6 Wax Management

The petroleum industry practices several remediation strategies for managing wax deposition. These are generally based on mechanical, thermal and chemical technologies. Economic costs for executing these technologies increases dramatically with ocean depth[10]. However, these technologies must be carried out to maintain flow assurance. One of the most common methods of removing a wax deposit is through flowline pigging. This method employs a mechanical pig, which scours the pipeline walls removing wax deposit. Facilitating pigging requires significant forethought planning in the design of subsea pipelines and this strategy may force subsea operations to shut down for several days, leading to significant production losses[10].

Thermal management involves the active heating or insulation of subsea pipelines [10]. This can prevent wax from crystallizing to eliminate deposition altogether. However, this strategy is often expensive and may not be practical, especially when transporting crude oil over long distances[125]. Selecting an economically viable strategy is therefore central to subsea oil recovery. A description of the chemical technologies, relevant to my thesis, will be discussed herein in more detail.

2.6.1 Chemical Inhibitors

As a result of their intrinsic simplicity, chemical inhibitors are an attractive remediation technique for managing wax deposition in subsea systems[15]. Although these technologies may rarely eliminate the phenomenon altogether, the rate of deposition can be reduced by high percentage[10]. Improving their effectiveness further requires representative testing in conditions closely matching to those in the field.

2.6.2 Types of Wax Inhibitors

In general, chemical additives can be categorized into different groups[33, 126]:

2.6.2.1 EVA Copolymers

EVA copolymers (cf. **Figure 2.16**a) are comprised of chain of polyethylene (PE) polymers copolymerized with Vinyl Acetate (VA). The effectiveness of EVA resides in the complementary work of both the PE and the VA[127-129]. First, the non-polar alkyl chain (PE) of the inhibitor interacts with the alkane wax, then the inhibitor co crystallize with wax into long-chain alkane with a polarity moiety end tail of VA. The VA creates a steric hindrance that interferes with the alignment of new incoming wax molecules[33, 130]. Besides, VA is a polar compound consisting of 2 short alkyl groups and two active oxygen atoms. Molecular dynamic simulation displays strong van der Waals interaction between the oxygen and the wax alkane [33, 131]. This will increase the solubility of wax and reduces the WAT. Significant relevance is attributed therefore to the VA content of EVA[33, 127, 128]. At low VA contents, EVA has higher crystallinity potential and may crystallize out of the solution above the WAT acting as a nucleating agent. At high VA content, the copolymer interacts with wax through co-crystallization and/or adsorption[132, 133].

The comb-type EVA polymer consists of a polyvinyl back-bone with different pendant alkyl chains[33, 134]. Compared to EVA, the crystalline group of EVA are contained with the polymer back-bone making the comb co-polymer stronger inhibitors than EVA[20, 135].

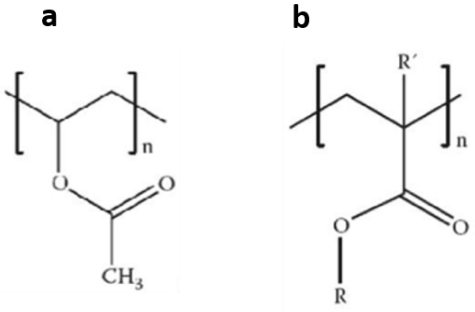

Figure 2.16. Molecular structure of **a)** EVA, **b)** MA adopted from Billy et al.[33, 126, 136].

2.6.2.2 Maleic Acid Comb Co-polymer

Comb copolymers (cf. **Figure 2.16**b) are generally synthesized from one of two classes of monomers, (meth) acrylate ester, or maleic acid or both. In those copolymers, the alkyl side chains interact with the alkane waxes while the ester group interrupts wax crystal growth. The length of the pendant chain in comb copolymer is the most crucial feature. A compatibility in length between the alkyl pendant chain and the alkane wax increases the efficacity of the wax inhibitor, a similar length achieves an optimum inhibition[33, 137-141]. The longer the length of alkyl chain, the higher the solubility of copolymer in the structure of alkane wax[33, 126, 142-146].

2.6.2.3 Crystalline-Amorphous Polymers

Crystalline amorphous inhibitors (cf. **Figure 2.17**) have polyethylene crystalline group (PE) and amorphous moieties such as polybutylene (PB) or polyethylene propylene (PEP) [147 ,33] . The presence of two non-polar groups (crystalline non-polar group and amorphous non-polar group) presents an exception case to the standard structural characteristics of the wax inhibitors[33, 136, 147, 148].

Crystalline amorphous polymers self-assemble into a micelle-like structure with a crystalline core and amorphous brushes surrounding the core. The formed micelle may interact with alkane waxes through nucleation effect and co-crystallization, resulting in more abundant albeit smaller wax crystals.

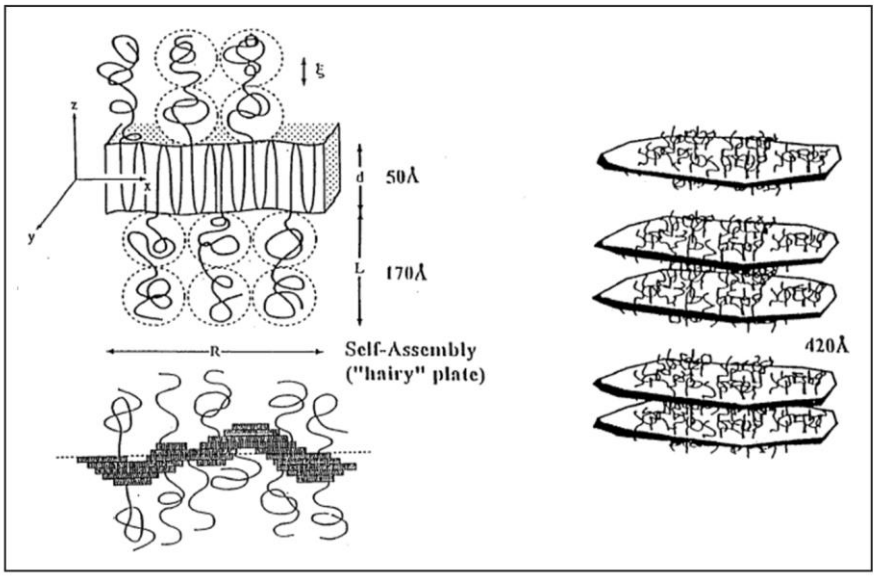

Figure 2.17. Generic structure of the polyethylene-polyethylenepropylene (PE-PEP) aggregates. The crystallization of PE forms extended platelets, while the PEP hairs form brushes on both sides taken from Lim et al.[149].

2.6.2.4 Nano Hybrids Pour Point Depressant

Nanoparticles exhibit potential applications in polymer modification due to unique size, high surface and quantum size effect. Research has been performed on the preparation of polymeric nanocomposites via dispersion of polymeric nanocomposites into polymer phase. Compared with pure polymers, nanocomposite have an enhanced effect on reducing wax deposition. The enhanced performance may be due to the following possible mechanisms: the change in nucleation (the nanoparticles serve as dispersed nucleation sites), co-crystallization (the incorporation of nanoparticles into the wax crystals hinders their growth), or the adsorption of nanoparticles on the surface of wax crystals (which modulates or hinders the growth of wax crystals). In the presence of nanoparticles, the crystallized wax was found smaller and more dispersed[149].

2.6.2.5 Surfactant

The conventional surfactants are also known as wax dispersant. Similar mechanism between surfactants and polymeric inhibitors are shown in many studies[150 ,33]. Basically, the adsorption of the wax dispersant molecules to the growing wax crystals impeded the agglomeration of wax crystals and the formation of a tri-dimensional structure of wax. The hydrophobic chain is responsible for the interaction between the surfactant and the wax chain and the hydrophilic moieties hinder the crystal growth. The effectiveness of the surfactant increases with the increase in the hydrophobic chain length.

2.6.3 Mechanism of Wax Inhibitors

The mechanism of wax inhibitors was extensively explored in various studies[33, 126, 138]. The wax inhibitors are widely recognized for interfering with the crystallization process of the wax

(cf. **Figure 2.18**). A combination of interactions between the wax inhibitors and alkane waxes involving nucleation, adsorption and solubilization are relevant.

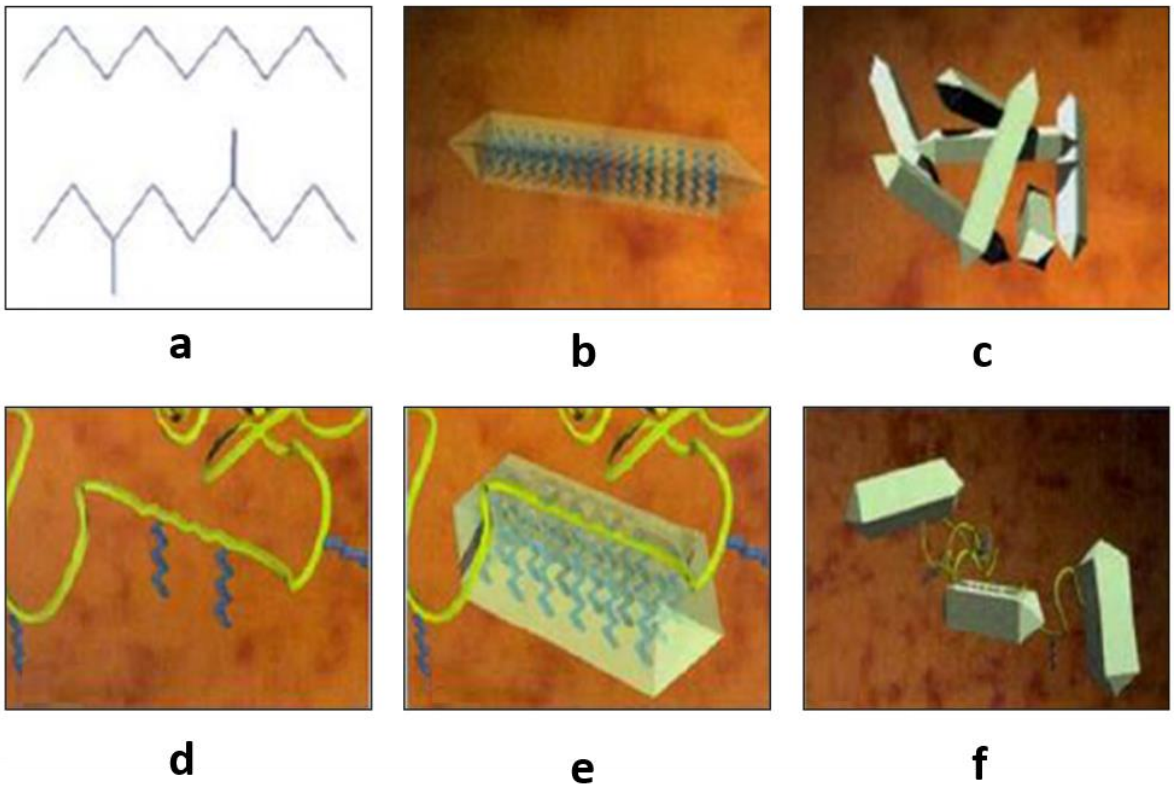

Figure 2.18. Modification process of the paraffin crystal with the polymeric wax inhibitor, **a)** chemical structure of wax, **b)** crystal shape of wax structure, **c)** crystal structure of growing wax lattice, **d)** polymeric wax inhibitors with wax-like components, **e)** co-crystallization of wax inhibitor, and **f)** sterically hindered wax structure taken from Lim et al.[149].

Despite the fact these additives clearly work, there is an incomplete understanding regarding the mechanisms which underpin their functionality. Dependent on the temperature of the medium, the following mechanism may interfere.

2.6.3.1 Nucleation

The molecules of both wax and inhibitors undergo the nucleation process. The wax molecules precipitate out from the oil phase below, which form crystalline nucleus (of a critical size); thus, prompting the formation of a larger compound, specifically the wax crystal. Meanwhile, the high molecular weight of the inhibitor propels the crystalline nucleus to self-assemble into a micelle-like aggregate exhibiting a crystalline core and soluble hairy brushes surrounding the core. This eventually creates more subcritical nuclei, which reduce supersaturation and prompt the formation of smaller wax crystals that remain stable in the oil phase[126, 148, 151].

2.6.3.2 Adsorption (co-crystallization)

The inhibitor co-crystallizes with wax molecules or adsorb on growing surfaces of precipitated wax crystals. Adsorption of the inhibitor into wax crystals disturbs crystal growth of the wax crystals or alter the morphology of growing crystals and delays the formation of three-dimensional crystals[33, 134, 135, 152-156].

2.6.3.3 Solubilization

The van der Waals interaction between the polymeric chain and the wax increases the solubility of wax in the crude oil, improves the dispersion of tiny wax crystals and eventually reduces the WAT[33, 126, 145, 154].

2.7 Conclusions

This chapter was dedicated to summarize and present the state-of-the art research on wax deposition in production pipeline. The focus was mainly on the effect of operating parameters such as temperature of the bulk oil, the cold surface and the cooling rate. The controversial effect of flow regimes on wax deposition was emphasized as well, stating therefore the gaps in the literature to be addressed. Wax deposition modelling was summarized with a focus on the molecular diffusion models as it is believed to be the main governing mechanism for wax deposition. A listing of the sloughing models and their progress through literature was undertaken. Finally, wax inhibitors were described with their types and mechanisms.

From the literature review, the effect of temperature operating conditions is well established, where generally, the increase in the hot oil temperature or the cold surface temperature decreases the deposition rate. The temperature gradient is the main driving force for wax deposition, and it can be seen either as the extent between the hot and cold temperature or the extent between the WAT and the hot or cold temperature. Both temperature gradients should be taken into consideration while analyzing temperature effect on wax deposition. The cooling rate was found to affect mainly the crystallization process, making it slower or faster and therefore affecting significantly the crystal size and the appearance of the first wax crystal in the oil and the WAT.

The effect of surface was also evaluated in terms of three main parameters: surface wettability, roughness and thermal conductivity. It has been demonstrated that high surface free energy promotes wax deposition by increasing the adhesion forces between wax molecules and the surface. Roughness on the other and provides sites of nucleation for wax to strongly

adhere to the surface. Thermal conductivity was evaluated as a crucial characteristic of the surface as it controls the temperature driving force at the surface and the cooling of the bulk of the oil.

The effect of flow regime and flow rate on wax deposition was studied with conclusions stating mainly the decrease in the wax deposition with the increase of the flow rate. However, the mechanism underlying the change in the wax deposition with the change in flow is poorly understood. While some researchers attribute the decrease in mass deposition to the increase in the heat transfer in the deposition system with an increase in the solubility of the wax at the deposition interface, others attribute the decrease in the mass deposition to sloughing due to the removal of wax layers by shear stress applied on the deposition surface by the shearing fluid. None was able to detect or show a sloughing effect though.

For the modelling of wax deposition, the focus was on the summary of wax deposition model based on molecular diffusion. The models consider either an independent heat and mass transfer and succeed to predict wax deposition in the laminar flow regime or consider a dependent heat and mass transfer for the prediction of wax deposition in the turbulent flow regime. Models in the literature were further improved by applying the kinetic of wax precipitation in the deposition model all along with the solubility curve. The effect of sloughing was introduced in some models as well.

Wax inhibitors were described as a mean for wax management. Literature shows that most wax inhibitors contain a non-polar moiety and a polar moiety. The non-polar moiety is an alkyl chain that co-crystallize with the alkane wax, while the polar moiety alters the morphology and

the growth of the wax crystal. Prior to selection of a wax inhibitor, it is necessary to analyze the carbon chain length and the molecular weight of both long-chain saturated alkane and selected inhibitor considering that most polymeric inhibitors emphasis on their compatibility with these alkane chain. Moreover, it is imperative to critically explore the selectivity of the inhibitor depending on the composition of the crude oil is also recommended to seek for a cleaner with smaller molecules or non-toxic, biodegradable inhibitors.

Chapter 3 Experimental techniques

This chapter introduces the many experimental techniques used throughout the study to characterise waxy model solution, the wax deposit and the synthesis and performance study of wax inhibitors. The chapter is designed to provide theoretical background on the techniques used while further specific details on the experimental methods set-up, reproducibility are provided in the relevant materials and methods of each results chapter.

3.1.1 Avantium Crystal 16

A turbidimetric technique was undertaken to measure the WAT using Avantium Crystal 16 system. Avantium Crystal 16 is a multiple variable temperature reactors of 1 mL scale and applied the turbidimetric technique to detect cloudy and clear points of a solution associated with crystallization and dissolution phenomenon (cf**. Figure 3.1**). As seen in **Figure 3.1**a, this automatic crystallisation equipment can hold 16 (4 x 4) standard HPLC glass vials (11.5 mm diameter, flat bottomed, 1.5 mL volume). It has 4 parallel units containing 4 individually heated aluminium reactor blocks. Each unit can be heated and cooled electrically by a combination of Peltier elements and a heater. Crystallisation and dissolution temperatures were analysed according to the solution turbidity profile as the temperature at which the transmission deviates from 100 % due to the appearance of first crystals or the transmission starts to increase from 0% to 100 % meaning the dissolution of solids. The Crystal16™ operating software can be used to program and run each reactor block individually at specific operating conditions[157].

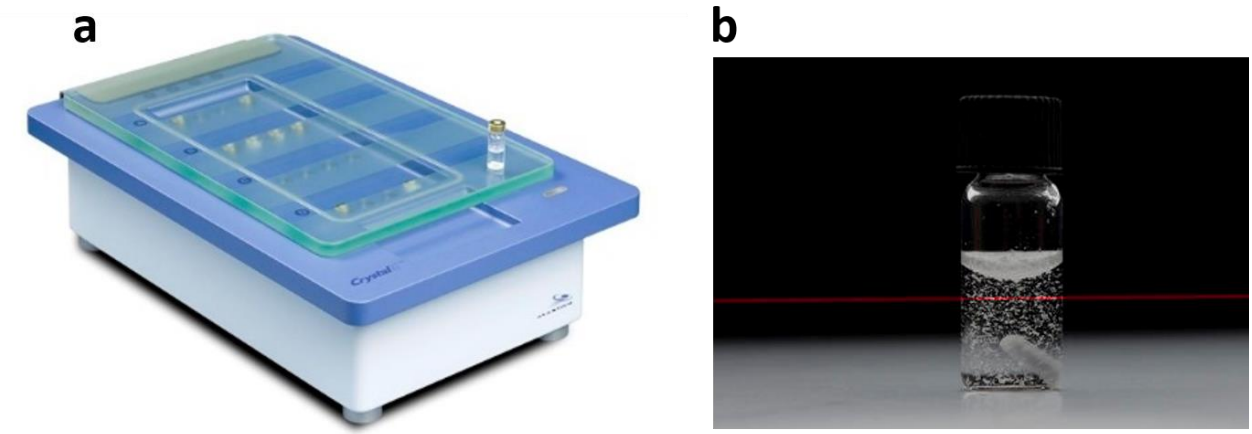

Figure 3.1. a) Apparatus of the Avantium Crystal 16, **b)** C16 vial with laser beam detecting turbidity of the solution. Specification of the Crystal 16: Temperature range -15 to 150 (°C), with temperature accuracy of 0.1 °C, heating/cooling of 0 - 20 °C/min and stirring speed of 0 – 1250 rpm taken from Technobis Crystallization Systems website[157].

The experimental procedure consists of preparing 16 samples of 4 different concentrations of wax and dodecane. The prepared solutions were then induced in the 1 mL scale transparent vials with mini magnetic stirrers. The prepared vials were set in the C16 vials in a way to have 4 different concentration on each block. A poly-thermal heating segment is then programmed to detect the onset temperatures of dissolution and crystallisation by heating up and cooling down the process. As an example, in this experiment, the heating cycle was first increased to 60 ^{o}C, above the expected dissolution temperature and then decreased to 0 ^{o}C which is below the expected crystallization temperature. Additionally, constant holding was applied to the top and bottom temperature for an hour to ensure complete homogenization of the solution. The four heating and cooling rates used were 0.5, 1, 2 and 5 ^{o}C/min for 4 model solutions with 3 sequences of cycle repeats to obtain repeatable quality data. It should be noted that constant stirring was applied to all vials at a speed of 700 rpm. This stirring was found to give good and repeatable data on this specific equipment. A typical profile as obtained from Crystal 16 using

poly-thermal method is displayed in **Figure 3.2** highlighting the heating/cooling cycle (temperature profile) and the transmission percentage (Turbidity). The temperature at which the transmission falls from 100 % is considered as the crystallization temperature and the temperature at which the transmission is above 0% is considered as the dissolution temperature.

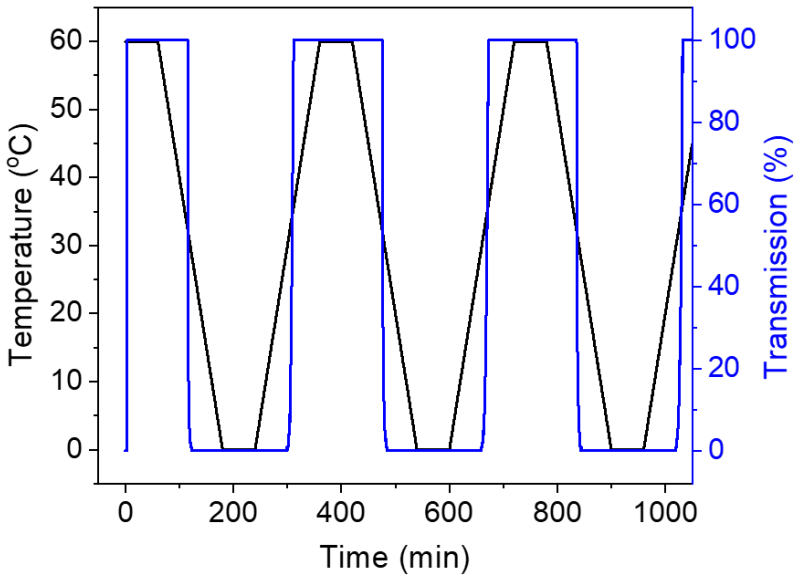

Figure 3.2. Poly-thermal profile for temperature and transmission against the time for measuring the cloud and clear points of the solution.

3.1.2 PE Clarus 500 GC/FID

Gas chromatography/flame ionisation detection (GC/FID) is a powerful technique for separating, identification and quantification of the components in a mixture. It is used for analysis of organic liquid samples. This GC is fitted with an on-column injector and high temperature column. It is set up to perform a number of standard liquid fuel tests including carbon number analysis, simulated distillation, gasoline in engine oil and glycerol and glycerides in biodiesel.

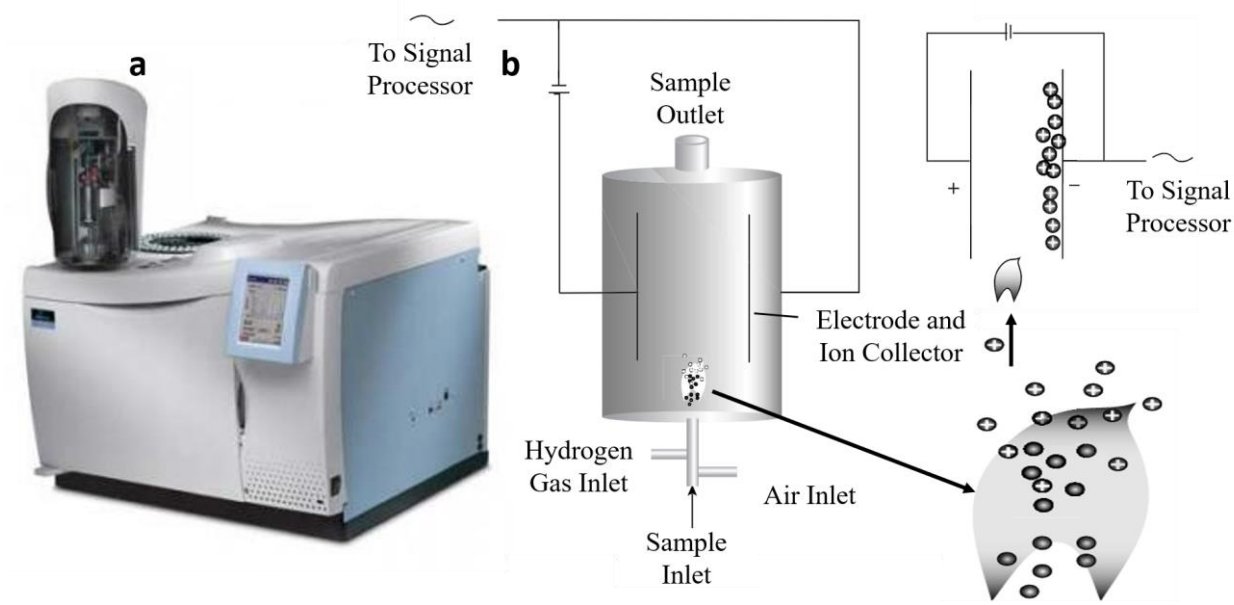

Figure 3.3. a) GC/FID - Perkin Elmer Clarus 500 On-Col equipment **b)** Diagram of the FID measuring principle adopted from British Standards Institute[158]. Instrument: Perkin Elmer Clarus 500, column: Perkin Elmer Elite PS1 HT, column length: 15m * 0.53 i.d., 0.15 µm film thickness, Carrier gas: Helium, Flow rate: 12 mL/min. Temperature: 35 ^{o}C, heat at 20 ^{o}C/min to 350 ^{o}C. Sampling rate: 1.5625 pts/s.

The measurement utilized by the FID is the ionization of organically bound carbon atoms in a hydrogen flame. The ionization current measured by the FID depends on the number of C-atoms of organic compounds burning in the fuel gas flame, the form of bonding (straight chain or branched chain) and of bonding partners. The response factor is a function of the specific design of the detector and the adjusted operating conditions. The main advantage of the FID is that it responds strongly to organic carbon containing components and less to other inorganic flue gas components (such as CO, CO_2, NO, H_2O). This technique also has a very good limit of detection (parts-per-billion to low parts-per-million level).

Figure 3.3 shows the operational principle of FIDs. FIDs are comprised of a sample inlet, hydrogen fuel inlet, combustion chamber, and electrodes that provide the electric field and act as an ion collector. The decomposed sample is vented through a chimney exhaust. The FID measures electric current generated by the ions. Samples can be introduced into an FID either directly or through a GC column. Hydrogen, air, and sample vapor are mixed in the combustion chamber and burned. Because of the high temperature of the hydrogen-rich flame, organic substances in the vapor are decomposed to hydrocarbon fragments and undergo a series of reactions including thermal fragmentation, chemi-ionization, and ionic molecule and free radical reactions to produce the charged species or ions. The quantity of ions produced is proportional to the number of reduced carbon atoms present in the flame and hence the number of molecules. The ions move along the electrical field toward the electrodes where current is produced when the ions hit them. This signal is then sent to the electronic signal processor[158, 159].

Following the standard test method, ASTM D2887, the calibration was performed by injecting known mixtures of *n*-alkanes (Supelco 04070-1ML, C8-C20; Supelco 04071-1ML, C21-C40) to find the retention times, which are used by the data processing method to split the chromatogram into timed carbon number 'segments' (cf.**Figure 3.4**) The area under each segment is found and calculated as a percentage of the total area of all the identified segments to give the carbon chain length distribution of the sample.

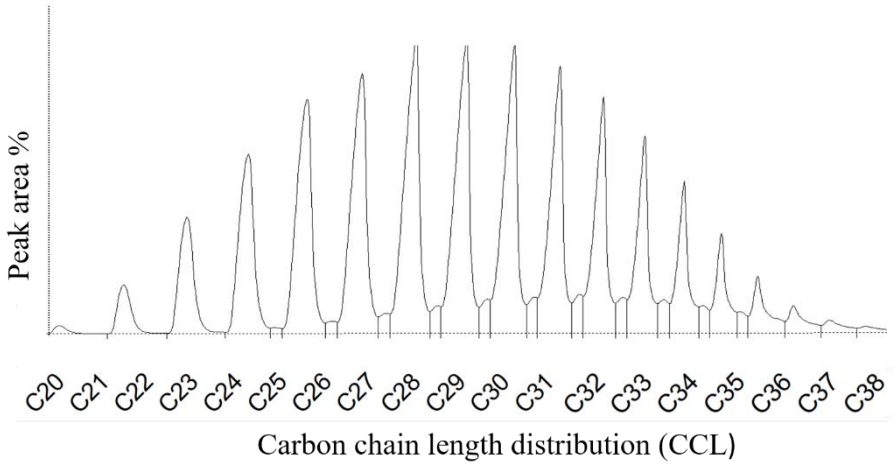

CCL	Start time	End time
C20	12.6	13.44
C21	13.45	14.39
C22	14.40	15.19
C23	15.20	16.09
C24	16.10	16.79
C25	16.80	17.49
C26	17.50	18.19
C27	18.20	18.84
C28	18.85	19.55
C29	19.56	20.32
C30	20.33	20.89
C31	20.80	21.30
C32	21.31	21.95
C33	21.96	22.40
C34	22.40	23.10
C35	23.11	23.60
C36	23.61	24.00
C37	24.01	24.50
C38	24.51	24.90

Figure 3.4. Example of wax Chromatogram indicating graphically retention times and timed segments of Carbon followed by a table for retention time for Carbon chain length presented in chromatogram.

3.1.3 Rheometery

Discovery Hybrid HR-2, manufactured by TA instruments is a rotational shear rheometer used in this study to determine the flow properties (viscosity versus temperature) of the model solution and its WAT under flow experiment.

Viscosity is the mechanical property of fluids which depends on the interaction between molecules tending to resist flow. Fluids with viscosity independent of shear rate are called Newtonian fluid such as water and solutions of single phase low molecular weight. Fluids with viscosity strongly depends on the shear rate are categorised as non-Newtonian and the study of their behavior is called rheology[160, 161].

Hence, rheology is the study of flow and deformation of materials. Deformation and flow are referred to as strain or strain rate, respectively, and indicate the distance over which a body moves under the influence of an external force, or stress[162].

A rheometer is a precision instrument that contains the material of interest in a geometric configuration, controls the environment around it, and applies and measures wide ranges of stress, strain, and strain rate[162]. The rheometer and the geometry used in this study can be seen in **Figure 3.5**. All the tests have been carried out using a Peltier Concentric Cylinder temperature system with DIN rotor and standard cup geometries.

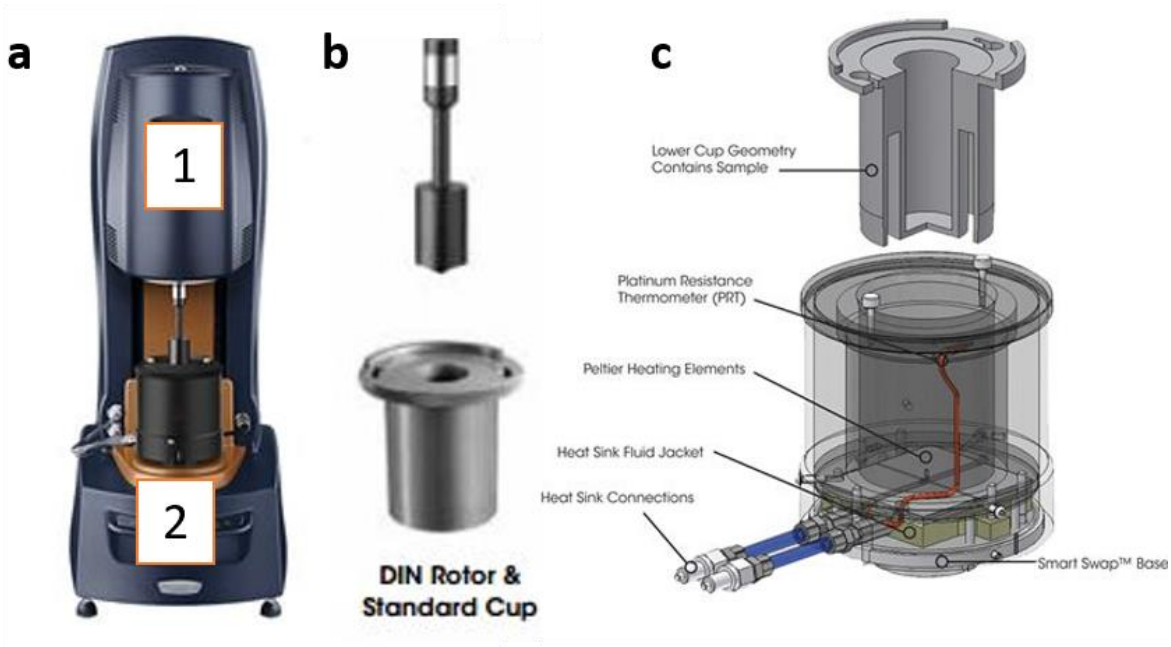

Figure 3.5. a) The TA rheometer used in the current study with (1) the rotational equipment containing all the mechanical parts including the force transducer, and (2) Peltier element for temperature control; it accommodates the housing for the rotating part (i.e., inner cylinder); **b)** DIN standard bob geometry and a standard cup and **c)** a close-up of the Peltier Concentric Cylinder temperature system taken from TA instruments website[162].

Concentric Cylinder geometries are commonly used for testing low viscosity fluids, dispersions or any liquids that are pourable into a cup. The concentric cylinders geometry is a Couette flow geometry where the inner part is rotating while the outer housing is kept stationary. TC geometry was chosen to conduct this study because of the following:

- It provides a large surface area to detect and measure low to medium viscosity of the waxy model solution at high temperature.
- While the Vane and cup geometry provides larger surface area and higher sensitivity to low viscosities, it may create a secondary flow that interfere with the measurement.
- The TC geometry provide a good host for the waxy solution especially at temperatures below the WAT, where wax crystallize, and the solution exhibit a change in phase. With a cone and plate geometry, the crystallizing wax may get out of the geometry leading to errors in measurements.
- It is capable to generate a heating/cooling to the solution with minimal evaporation and loss of light component due to the use of sealing on the top.

The viscosity of model solution as a function of temperature can be described using the following Arrhenius-type equation:

$$\mu = Ae^{Ea/RT} \qquad \text{Eq. 3.1}$$

where μ is the viscosity, A is around 1-5 × 10^{-3}, Ea is the activation energy typically in the range of 10-30 KJ/mol, R is the universal gas constant and T is the temperature [36]. The model solution exhibits a Newtonian behaviour above the WAT and a non-Newtonian behaviour below the WAT due to the precipitation of wax.

The rheometer is able to delineate the temperature at which the model solution deviate from the Newtonian behaviour depending on change in viscosity as seen in **Figure 3.6**. The WAT is a function of the wax composition, the cooling rate and the presence of additives[36, 61].

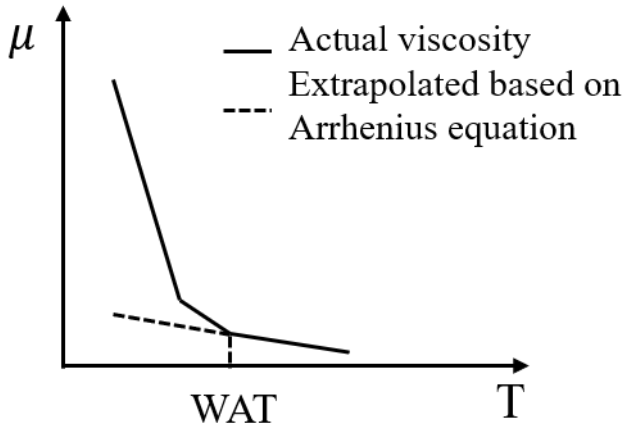

Figure 3.6. WAT measurement using the rheometer and Arrhenius equation adapted from Huang et al.[11].

Using a rheometer, the model solution is cooled from T > WAT to T < WAT using a constant cooling rate between of 0.5 and 1°C/min and under constant rotation per reciprocal second[36]. The first deviation in the viscosity-temperature curve is considered as the WAT.

The rheometer requires a sufficient amount of wax (~0.3–0.4 wt%) to crystallize in order for the heat effect to be detectable. Besides that, the change in the slope is a function of the composition of the wax. A narrow range of carbon number will crystallize in a narrow temperature range and give a sharp slope. However, a broader range of carbon number is likely to give a gradual slope[11].

3.1.4 FTIR Thermo iS10

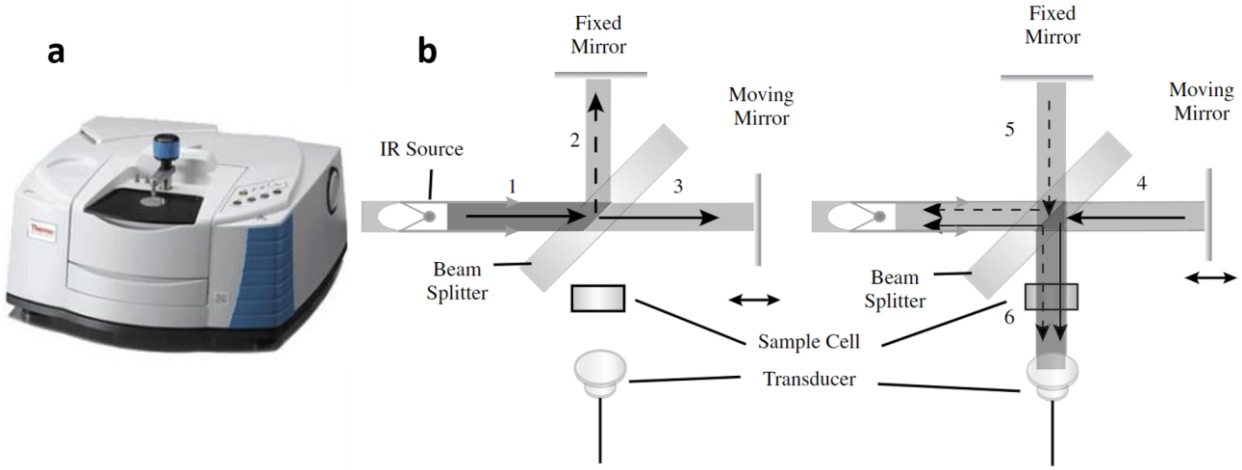

Figure 3.7. a) FTIR - Thermo iS10 **b)** schematic of interferometer taken from Sun, Y.[159].

Fourier-transform infrared (FT-ir) spectrometry Thermo iS10 shown in **Figure 3.7**a is a technique that allows the analyst to investigate the functional groups present in a sample. The attenuated total reflectance (ATR) sampling accessory is used for performing most analyses quickly and easily without involved sample preparation of KBr disc. The technique is relatively quick and straightforward to perform but the interpretation of IR spectra is a science in itself. Generally, both quantitative and qualitative analyses can be conducted using IR spectrometry. In our study, FTIR was used to verify the etherification of the ethylcelullose by identifying the presence of a new alkyl group in the ethylcellulose molecule.

The technique involves placing a sample on top of a diamond crystal (which has a high refractive index) embedded in a stainless-steel disk, called the DuraDisk. An infrared beam from the spectrometer passes through the crystal and penetrates slightly into the sample to permit analysis of strong infrared absorbing solutions. Ideally, when the targeted chemical is

present in the sample, IR absorption at characteristic wavelengths occurs. The intensity of IR absorption for those wavelengths changes according to the concentration of the targeted chemical. Signals are sent to the central processor for chemical identification and/or concentration determination (cf. **Figure 3.7**b).

Organic molecules are composed of various atoms and function groups that are connected to each other through different types of bonds. Each of these bonds vibrates in a specific manner at a certain frequency that fall within the IR region. When exposed to radiation in the infrared region of the electro-magnetic spectrum, chemical bonds may undergo a number of transitions such as stretching, rotation and vibration. **Figure 3.8**a illustrates some of these vibration modes, including stretching, in-plane bending, and out-of-plane bending.

In various chemicals, the same characteristic function group vibrates in the same fashion and absorbs IR radiation of same frequency. For example, when the C-C bond vibrates in the stretching fashion, it absorbs IR of 2800 to 3000 cm^{-1}. This range is called the group frequency region. Different structures, however, may affect the vibration frequency of the characteristic function group, resulting in different absorption characteristics.

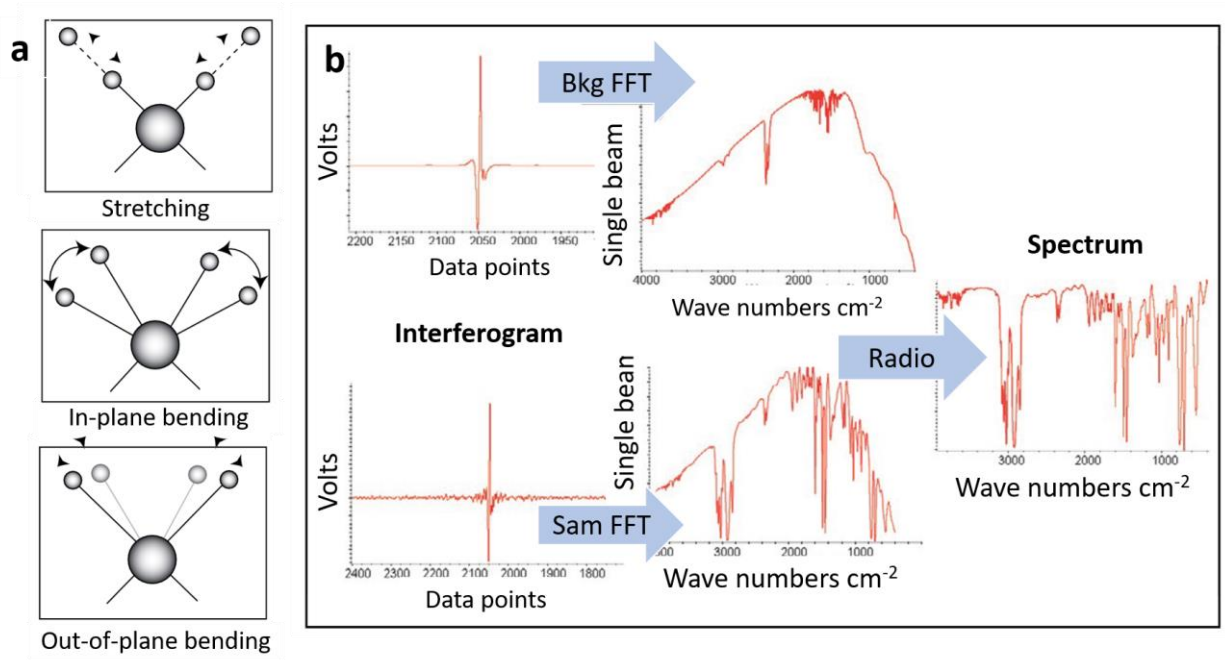

Figure 3.8. a) example of molecular vibration model taken from Sun, Y.[159] **b)** the process of collecting an infrared spectrum in an FT-IR spectrometer (where Sam refers to sample and bkg refers to background) taken from Thermofisher website[163].

This feature makes it possible to identify the function groups in a molecule based on the frequencies absorbed by the molecule when scanned through the entire IR spectrum by plotting a spectrum of the amount of radiation absorbed against the wavelength. However, before placing any sample for scanning through IR, a background should first be taken on a clean diamond (without any sample placed) in order to eliminate the interference of air and moisture into the final spectrum. The identification of a substance and its structure can be determined through matching its IR absorption spectrum with spectra from the databases (cf. **Figure 3.8**b)[164].

3.1.5 Scanning Electron Microscopy (SEM)

Scanning electron microscopy (SEM) is a highly versatile non-destructive methodologies for 2D and 3D materials characterization. SEM is a type of electron microscope that scatters electrons onto a target surface and produces an image allowing the examination of the morphologies (size and shape) of all samples (organic and inorganic materials) on a high spatial resolution from nano- to microscale. SEM is composed mainly of lens system, electron gun, electron collector, visual and recording cathode ray tubes and electronics associated with them (cf. **Figure 3.9**)[165].

The basic principles underpinning the use of electron microscopy lies on the fact that the solid sample is bombarded with electron beam generated by an electron gun located at the top of the microscope. The beam travels down a vacuum zone, passes through electromagnetic lenses and hit the sample, resulting in energy loss as characteristic X-rays, backscattered, secondary electrons and some other photons of various energies. The ejected signals (secondary electrons, backscattered and X-rays) from the sample are collected by detectors thereafter and are converted into a signal to produce a final image with a magnification and resolution of SEM depend mainly on the working distance between the detector and the sample[165].

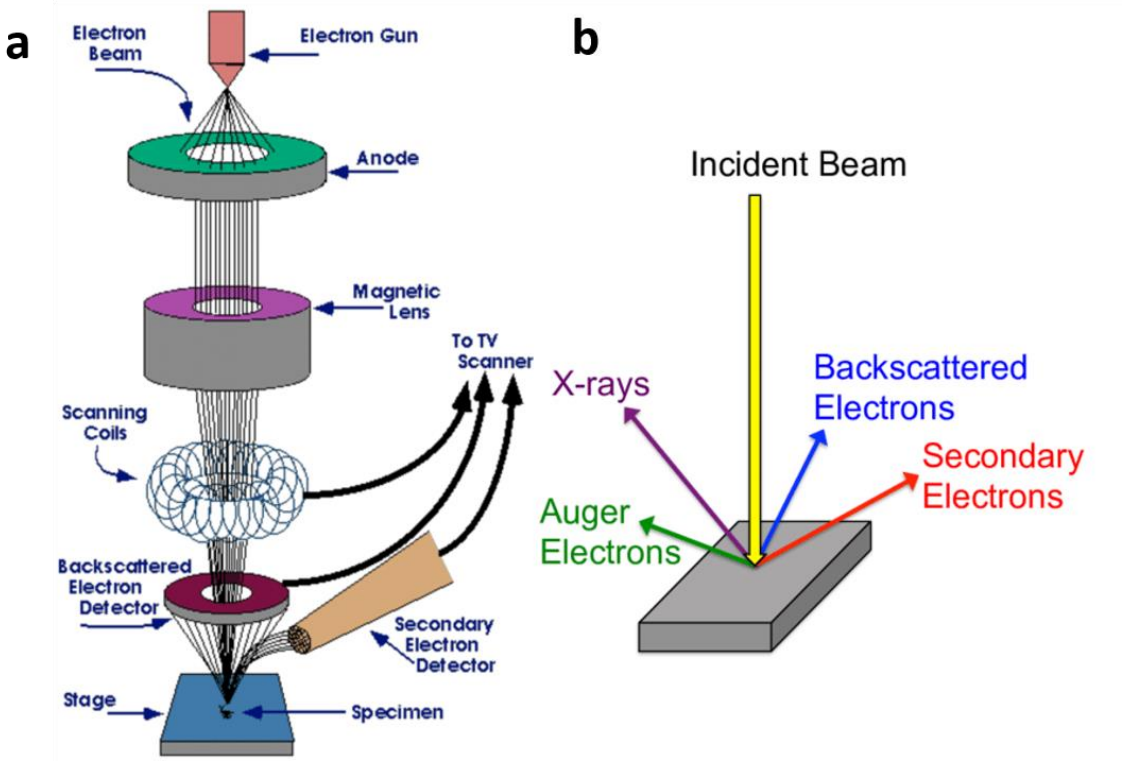

Figure 3.9. Schematic drawing of **a)** the typical Scanning Electron Microscope (SEM) column, and **b)** sample-beam interactions within a SEM taken from Walock[166].

The morphology and surface structure of the wax deposit samples was characterised using a high-performance cold field emission scanning electron microscope shown in **Figure 3.10**. It consists of a Helios G4 CX DualBeam SEM made by Thermofisher (formally FEI) with a FIB attached to it and a PP3010T cryo-SEM system by Quorum Technologies allowing to take images under cryogenic conditions. The details of the sample preparation and experimental procedure are detailed in chapter 4.

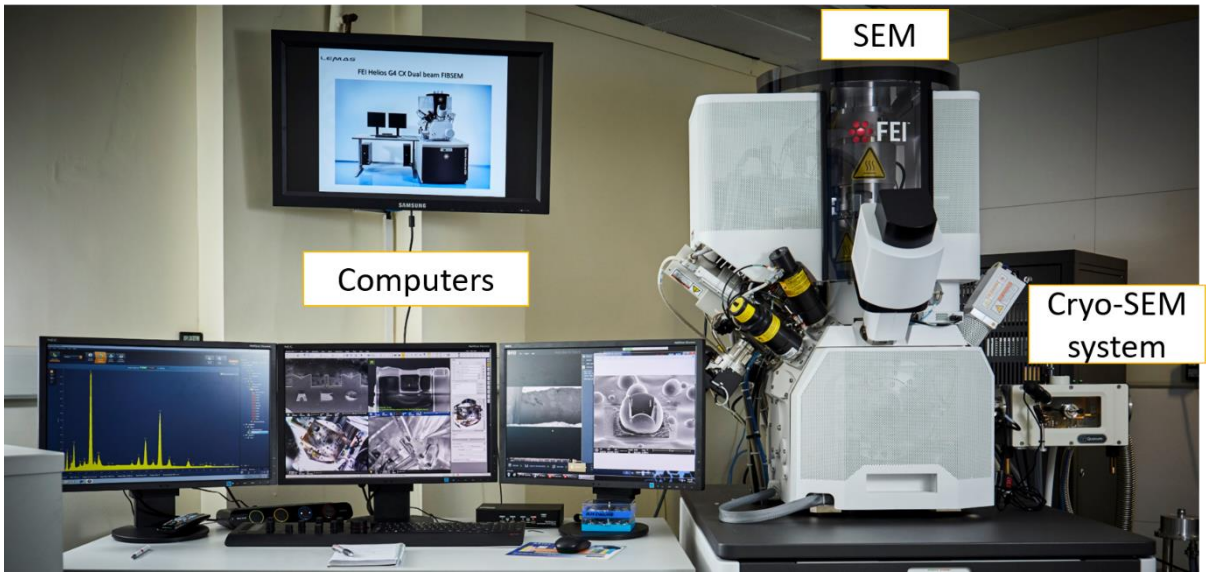

Figure 3.10. Helios G4 CX DualBeam SEM along with PP3010T cryo-SEM system.

3.1.6 Elemental Analysis: Carbon, Hydrogen, Nitrogen, Sulphur and Oxygen Analysis (CHNS-O)

CHNS-O, a process also commonly known as elemental or ultimate analysis is used to quantify the percentage of elements in a sample. The principle of this technique is based on the Pregl-Dumas method. All CHNS samples are weighted into soft tin capsules and oxygen analysis samples are weighted into silver capsules. The capsules are folded and gently crushed to fully encapsulate the sample and remove air, then loaded onto the instrument auto-sampler.

The Thermo Scientific Flash EA2000 elemental analyser shown in **Figure 3.11** is able to determine carbon, hydrogen, nitrogen and sulfur (CHNS) in suitable samples to percentage-levels using the combustion method. The sample is dropped into a furnace at 900 ^{o}C in a continual flow of helium. Pure oxygen is added for a few seconds and the sample burns. The combustion products pass through an oxidation/reduction reactor to ensure they are in the

correct form (CO_2, H_2O, N_2 and SO_2) to be separated using a gas chromatography column, then detected using thermal conductivity.

Figure 3.11. Thermo Scientific Flash EA2000 elemental analyser.

The Flash EA2000 is also able to determine the oxygen content. It does this by pyrolyzing the sample at 1060 ^oC under helium to release oxygen from the matrix. The oxygen passes over carbon impregnated with a catalyst and is reduced to form carbon monoxide, which is then separated using gas chromatography and detected[167, 168].

The combustion products are removed from the combustion chamber using helium as an inert gas and they are separated using a chromatographic column and are detected on the thermal conductivity detector (TCD) as an output signal. These signals are proportional to the

concentration of the individual components in the mixture. The EA 2400 Data Manager, which is SQL-based software, was used for data manipulating and exporting the results.

3.1.7 Thermogravimetric Analysis (TGA 4 - Shimadzu TGA 50):

Thermal analysis is a group of analytical techniques that gives valuable insights into the physical and chemical properties of a sample. Thermogravimetric analysis (TGA) is a thermal analysis in which the sample weight is monitored continuously against time and temperature using microbalance in a controlled atmosphere under inert or reactive gases such as such as nitrogen, argon, air and carbon dioxide. This technique can be used to characterise any materials (liquids or solids) that exhibit a weight change (loss or gain) with temperature as a result of decomposition, dehydration, desorption, reduction and oxidation. TGA 4 - Shimadzu TGA 50 was employed in this work to analyse the thermal stability of wax inhibitors. **Figure 3.12**a illustrates the schematic diagram of the TGA used, which consists of a balance control unit, mass flow controller unit, furnace, loading/unloading samples (pan), and a temperature programming facility connected with thermocouples. Samples typically 1-100 mg are inserted into an empty crucible in a size approximately 3 to 8 mm and loaded. The crucible is then positioned inside a furnace and a heating cycle (s) is applied. The temperature programme consists of one or more ramp (s) from the initial temperature (minimum of 30 ^{o}C) to the final temperature (maximum of 1600 ^{o}C) with a typical heating rates of 5-25 ^{o}C/min with hold period to be added if required.

The output data is plotted as mass of the sample with respect to time/temperature as seen in the example in **Figure 3.12**b the analysis of the data can give the measurement of weight change between given times or temperature, measurement of the temperature or time at a given

weight change or determination of the onset, end set mid-point and inflection point of weight change.

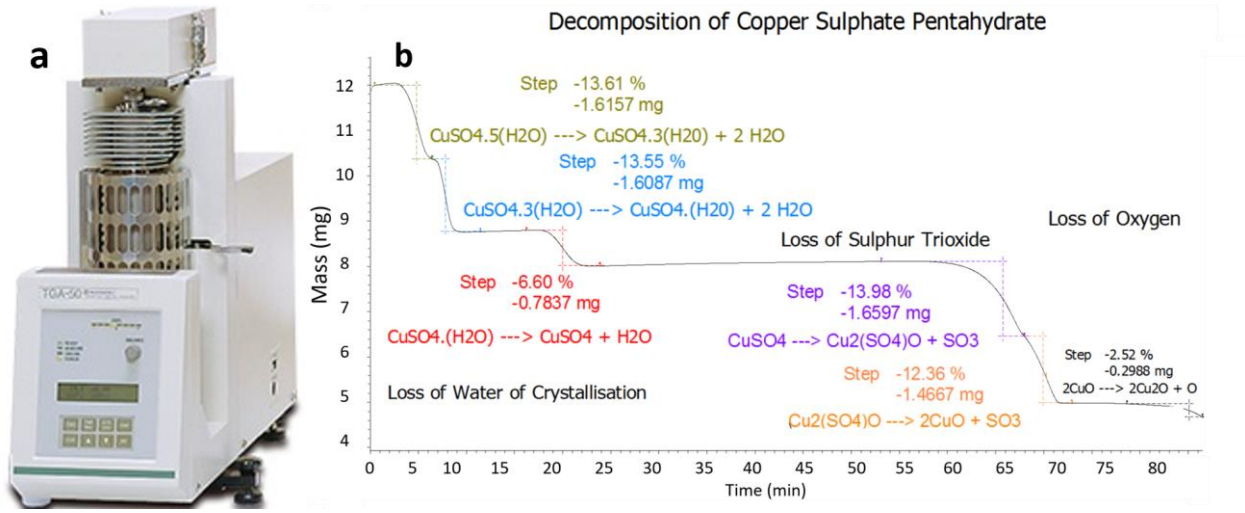

Figure 3.12. a) TGA instrument **b)** and example proximate analysis of TGA of the decomposition of copper sulphate pentahydrate.

3.1.8 Thermal Imaging

Thermal imaging is the production of images by detecting, measuring, and recording the thermal (infrared) radiation emitted by objects[169]. The infrared ray is a form of an electromagnetic wave as well as a visual light or a radio wave. The wavelength band is 0.78 to 1000 μm that is longer than visual light yet shorter than radio wave, and the wavelengths are classified from the near infrared to the far infrared region. The infrared ray is also energy radiated by motions of atoms and molecules on the surface of object, in case the temperature of the object is more than absolute zero degree. Thermal imaging relies on the infrared energy emitted from the measured object due to the motion of atoms and molecules and converted into

an electrical signal by the imaging sensor (microbolometer) and displayed as a color or black & white thermal image.

Infrared camera can detect thermal radiation and produce colour images, termed as thermograms. A thermogram contains temperature data, and allows to visualise temperature differences across the object captured, using colour differences that are related to a colour-temperature scale. **Figure 3.13** shows AVIO's R300SR Series (R301W2-NNU-C01) a high resolution, multi-purpose thermal imaging camera used to visualise the temperature gradient across wax deposition in the CRF. The camera has an operating temperature range between − 40 and + 500 °C, frame rate of 60 Hz, 640 × 480 pixel infrared resolution, a spectral range of 8–14 μm, and an accuracy of ± 1 °C[169-171].

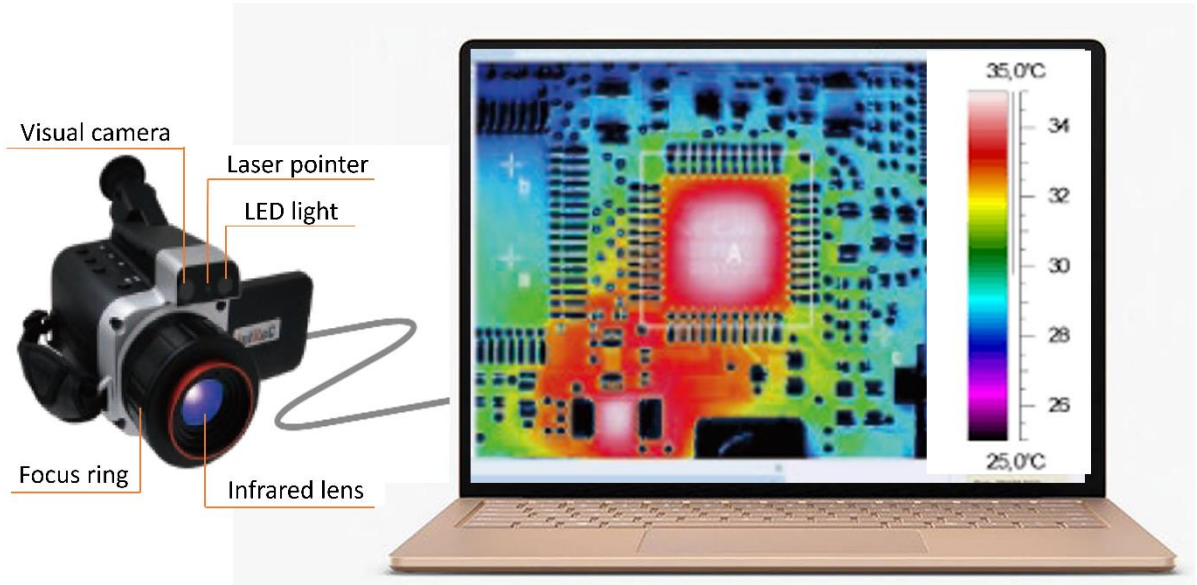

Figure 3.13. AVIO's R300SR Series camera with a thermogram adopted from Avio website[172].

The method is non-invasive and non-destructive, and does not require contact with the object examined. The acquisition of the infrared images is quick and easy to perform; however, various protocols, guidelines and checklist must be followed, for instance, attention should be paid to the position of the camera, distance of the camera from the object captured[170]. **Figure 3.14** shows the field of view of AVIO's R300SR thermal camera used at different distance.

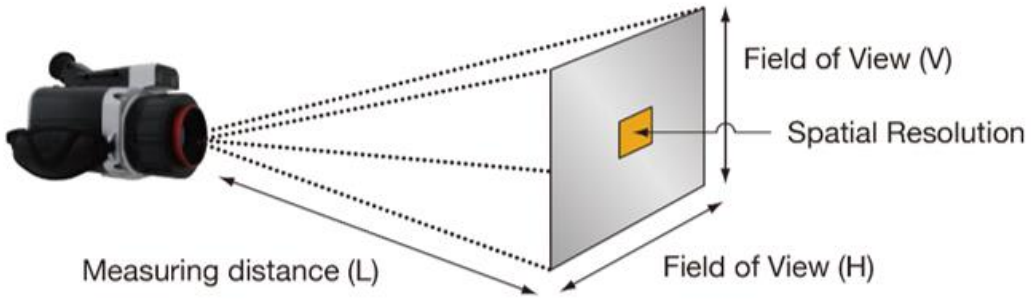

Measuring distance (m)	Minimum detectable Size (H × V mm)	Horizontal range (m)	Vertical range (m)
0.1	0.12×0.12	0.038	0.029
1.0	1.21×1.21	0.38	0.29
10	12×12	3.8	2.9
100	121×121	38	29

Figure 3.14. Measuring spatial resolution depending on the measuring distance adopted from Avio website[172].

Real-time Image acquisition were occurring during wax deposition, while the camera is positioned on a tripod, at a fixed location of 10 cm, with an angle of 45 degree to the CRF. The development of the image processing procedure was performed using the software InfReC Analyzer NS9500 Professional.

Chapter 4 Design and Test of a New Cold Rotating Finger: Apparatus to Study Wax Deposition under Shear

4.1 Synopsis

A bench-top Cold Rotating Finger (CRF) was developed to study the effect of fluid shear on wax deposition. An inner rotating cylinder provides opportunity to study wax deposition on surfaces in the region of high fluid shear stress (and laminar/transitional flows). A model system of linear n-alkane (C20 to C45) dissolved in dodecane was used for the deposition tests and an experimental matrix was elaborated using Taguchi statistical method to test the functionality of the CRF against the main parameters affecting wax deposition. The CRF results shows that wax deposit mass decreased with a decrease in the wax wt%, an increase in the rotational speed, and an increase in the cold surface and hot oil temperatures. The kinetic of wax deposition was non-linear, with an initial rapid deposition (approximately linear) followed by a slower rate as the deposit mass tends to steady-state within 30 min. The wax deposit mass becomes limited by thermal insulation of the cold surface and not wax depletion. The wax deposit morphology was studied by cryo-scanning electron microscopy with the static deposit showing a layered structure (ridges) which diminished at 200 rpm, confirming a denser, less porous deposit.

4.2 Introduction

Flow restriction in pipes by depositing wax on cold surfaces remains a significant problem in petroleum production, with the mechanism of wax deposition dependent on numerous

physicochemical parameters. One parameter that is not always represented in lab-scale testing is fluid flow and its influence on wax deposition. Flow-through systems can provide such conditions but are often more complicated to use and rapid screening is not viable. A typical flow-through system consists of a feed vessel, pump and pipe-loop test section which is jacketed for coolant flow. Alternatively, the cold finger method has become an industry standard because of its small volume, good control of thermal conditions and ability to rapidly screen chemicals[11]. However, the method is often static and does not consider the effect of fluid hydrodynamics and shear on the wax deposit. To overcome this limitation there has been various adaptations to introduce fluid shear. Jenning and Weispefennig combined the cold finger and gentle fluid motion by stirring with a magnetic flea[46]. Higher shear stress and the transition from laminar to turbulent flow has been achieved by mixing with impellers[41, 42]. While fluid flow is induced, the fluid stresses are highest at the impeller edges and not the depositing surface, the latter best representing the pipe flow environment.

Wu et al. developed a cold disk method to attain high shear stresses at the wax deposit-oil interface[20]. The cold disk was positioned in the outer cylinder wall, with fluid flow induced by a 2-paddle mixer. While the effect of flow velocity on wax deposit mass was studied, the flow pattern in the mixing vessel induced by a 2-paddle mixer is not known. Nigo et al.[173] modified the cold-disc method and proposed a spinning-disc method to study fouling by fat deposits. The spinning-disc method provided a well-defined flow condition but only attained laminar flow and a shear stress that varied along the radius of the spinning-disc.

Zougari et al.[43] developed an "Organic Solids Deposition and Control System" to study wax deposition under realistic production and transportation conditions. The method consisted of a rotating cylinder submerged in a cold fluid chilled by an outer cylinder and could mimic

production conditions in terms of Reynold number (*Re*) and wall shear stress. Wax deposition rates were shown to better represent data (comparison to the cold finger method) obtained using a pilot-scale flow loop. However, the wax deposition is formed on the outer-stationary wall, in a region of low fluid shear stress.

Recognizing some test method limitations, the current study developed a cold finger method wherein the inner cylinder rotates (axially) and is simultaneously chilled. This set-up allows wax deposits to form in the region of high fluid shear stress and under well-defined flow conditions. The new cold finger technique is termed the Cold Rotating Finger (CRF).

While developing the CRF, emphasis was placed on designing and testing an experimental setup that could meet the following key design criteria:

(1) Accurate temperature control, to ensure testing under well-defined thermal conditions;

(2) Well-defined hydrodynamics, to allow testing under controlled flow conditions;

(3) Controlled shear at the wall, to enable the study of the effect of flow/shear stress on wax deposition;

(4) Accuracy and precision of wax deposition measurement and characterisation, to ensure generation of reproducible and reliable data;

(5) Small sample volume;

(6) Ability to rapidly screen chemical inhibitor performance.

4.3 Cold Rotating Finger: Description and Design of the Technique

The CRF as shown in **Figure 4.1** was designed and developed to study and quantify the deposition process at different temperatures and rotational speeds. The CRF is an advanced version of the cold finger where both heat transfer and fluid dynamics are well defined and

controlled. The CRF is based on a Couette flow; the cell comprises of a central rotating cylinder and an outer stationary cylinder with the process fluid occupying the annular space. The rotation of the inner cylinder is amenable to precise control and reproducible experimental boundary conditions[174].

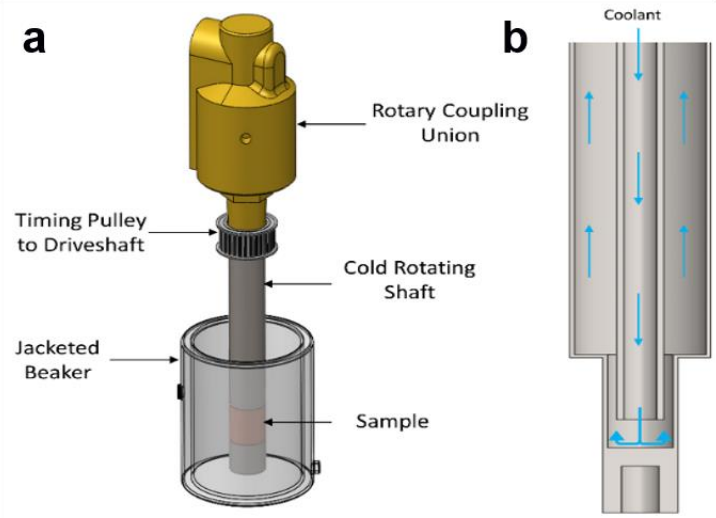

Figure 4.1. Schematic of the **a)** CRF with the rotary coupling providing effective rotary seal and **b)** coolant circulation path inside the rotating shaft.

To replicate subsea conditions in terms of the heat transfer, a temperature gradient between the inner and the outer cylinder is controlled. The outer wall of the sample cylinder is heated and the wall of the inner cylinder is chilled to act as the wax deposition surface. This design was based on two factors: i) for a Couette flow with an inner cylinder rotating, the flow in the boundary layer of the deposition surface is very well defined; and ii) the wall shear stress, which is a parameter influencing wax deposition is highest at the inner rotating cylinder interface, thus giving an increased range of operating conditions.

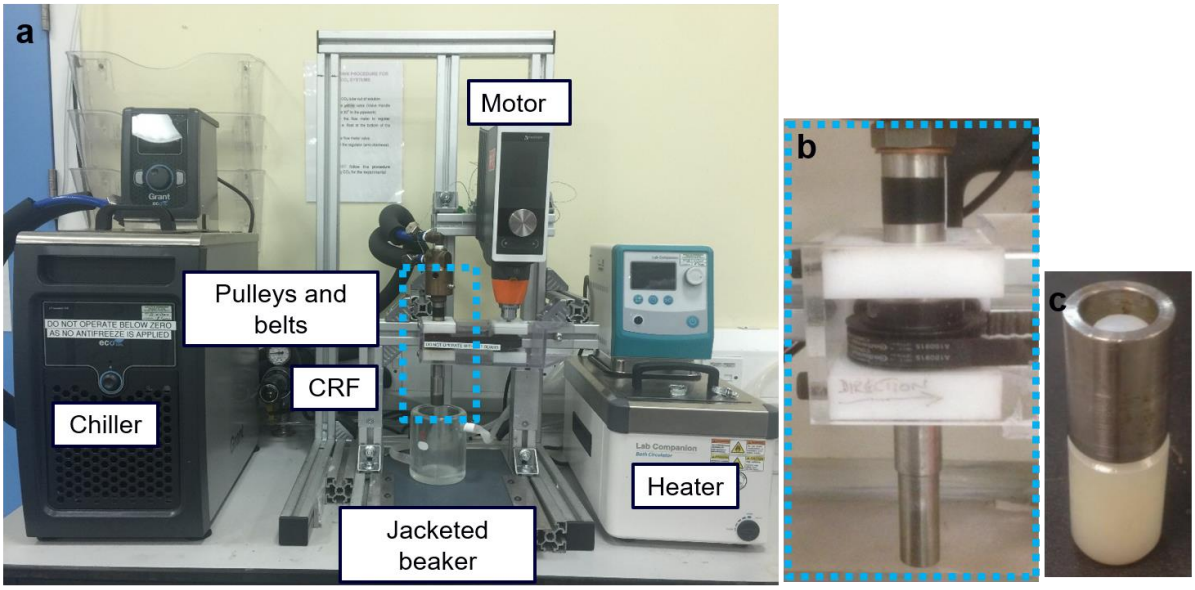

Figure 4.2. a) Image of the CRF experimental set-up; **b)** close up of the CRF; **c)** close up of the wax deposit sample.

Table 4-1. Dimensions of the inner cylinder test cell and the outer jacketed beaker.

Inner cylinder test cell	
Outer diameter	20 mm
Wall thickness	3 mm
Length	28 mm
Area	1759 mm^2
Outer jacketed beaker	
Inner Diameter	66 mm
Height	21 mm
Volume	300 mL

A doubled jacketed beaker was used to regulate the temperature of the outer cylinder using a heating bath (CW3-10, Jeio tech. Inc. Lab companion, temperature range 5-150^{o}C). However, controlling the temperature of the inner cylinder was more complicated because of the rotating cylinder. In the CRF, a rotary union and a set of timing pulleys were used to achieve surface

cooling and rotation. To enable rotation, the inner cylinder and the motor were connected through a belt and pulley mechanism. A set of two-timing pulleys and a belt were fastened by a driveshaft to an overhead stirrer (Hei-TORQUE Value 100), to precisely control the CRF rotational speed between 0 and 700 rpm. The pulleys were tightened against the driveshaft and the rotating finger by grub screws to limit geometry slip. This setup allowed the inner cylinder to rotate. Connecting a rotary union to the end of the inner cylinder, fluid can flow in and out of the rotating cylinder as shown in **Figure 4.2**. A Deublin Series (55-655-094) rotary union was chosen to provide a seal as coolant is pumped via a refrigeration unit. A stationary supply pipe was attached inside the rotary union to channel pumped coolant down the rotating finger as shown in **Figure 4.2** (length: 150mm, O.D.: 6.35mm). Due to exposure to a range of solvents, the rotating finger was made out of 316L stainless-steel; providing good corrosion resistance. Using a lathe tool, the diameter of the cylinder was stepped down twice; 20-16 mm and 16-11.5 mm. The first reduction in diameter was to prevent the shaft from moving axially by choosing a diameter for the inner dimension of the two stabilizing bearings. The second step improved heat transfer on the deposit sample. A cylindrical deposit surface was formed from stainless steel 316L. An X65 carbon steel collar was screwed onto the bottom of the shaft to lock in place the deposit surface. By designing a removable deposit surface, it allowed for easy mass measurement and characterisation of the wax deposit. Dimensions of the deposit sample are shown in **Table 4-1**. A refrigeration unit (Grant LT ecoccol 100, temperature range -25 to 150^{o}C) was used to control the inlet temperature of the rotating shaft. This was chosen based on its 20 L capacity and 18 L/min flow rate; ensuring reliable thermal stability in experiments (±0.1°C). The coolant was a 1:1 mixture of inhibited ethylene glycol and distilled water.

4.4 Characterisation of the CRF

Characterising the temperature profile when using the CRF and the flow conditions was undertaken as a first step before testing the CRF for wax deposition. The aim of the characterisation was to better define the operating conditions of the CRF.

4.4.1 Temperature Characterisation of the CRF

Wax deposition is a function of the temperature gradient between the hot oil and the cold surface. The CRF was designed to mimic this temperature gradient by chilling the CRF surface and by heating the bulk oil. As stated before, the CRF was chilled using a refrigeration unit that circulate a water/glycol mixture in the inner pipe of the CRF allowing the outer surface of the CRF to be chilled by conduction. On the other hand, the bulk oil is maintained hot in a jacketed beaker sat at the desired hot temperature using a heater. However, setting the chiller and the heater at the precise temperatures, does not necessarily lead to the same desired temperature on the deposition surface of the CRF neither in the bulk oil and this is due to the heat transfer the hot oil and the cold surface and the heat loss to the environment through the circulating systems. In order to have an understanding of the temperature profile in the CRF, a series of experiments were undertaken to measure, where possible, the temperature of the CRF and the bulk oil. **Figure 4.3**a shows a sketch of the temperature profile in the CRF and below is the definition of each temperature.

T_{hot}: the temperature as set on the heater.

T_{oil}: the temperature of the bulk oil.

T_{cold}: the temperature as set on the chiller.

$T_{surface}$: the temperature on the outer surface of the CRF.

$T_{interface}$: the temperature of the interface of the cold surface and the hot oil.

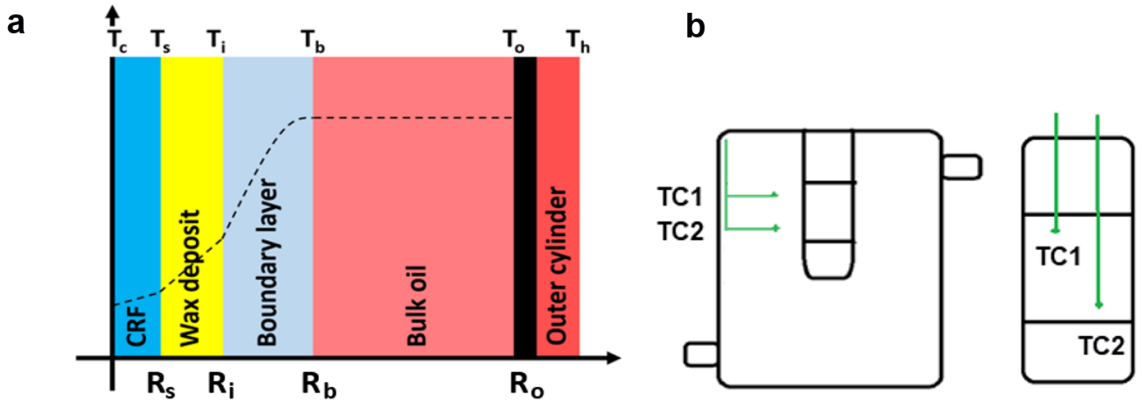

Figure 4.3. Schematic of **a)** the temperature profile in the CRF, **b)** thermocouples position in the bulk oil at a height of 5 and 20 mm from the top of the removable sample and at a distance 10 mm from the CRF towards the bulk and **c)** thermocouples position on the cold finger surface at a height of 5 and 20 mm from the top of the removable sample.

A series of characterisation experiments were performed on a blank system with pure dodecane (the choice of the solvent will be justified in the materials section) in the absence of alkane wax to prevent any change in the temperature profile due to wax deposition. The characterisation method consists of introducing a type K thermocouples (TC) probe (The SE027 TC from Pico Technology is a PTFE insulated, 0.2mm twisted pair conductor, 1.5mm tip diameter, tip temperature measurement range from -75°C to +250°C with a tolerance of ±1.5 °C), used with Pico Technology TC-08 thermocouple data logger. Tow TCs positioned inside the bulk oil at the same height at a radial distance of 10 mm from the cylindrical deposition sample (cf. **Figure 4.3**b), and another 2 TCs positioned at the top and bottom of the CRF deposit sample at a distance of 5 and 20 mm from the top of the sample (cf. **Figure 4.3**b). Changes in $T_{surface}$ and T_{oil} were monitored with time at three different operating conditions until steady state:

1- Static conditions (0 rpm), fixed T_{cold} and variable T_{hot}.

2- Static conditions (0rpm), fixed T_{hot} and variable T_{cold}.

3- Dynamic conditions, fixed T_{cold} and T_{hot}. Perhaps, only T_{oil} was measured due to challenges associated with inserting a TC on a rotating surface.

In an attempt to visualise the temperature gradient in the whole CRF system, and recognising the difficulties to insert TC on the CRF while rotating, TC measurements were coupled with thermal imaging technique. Thermal imaging consists of taking an overview thermal image of the CRF at precise operating conditions using R300SR Thermal Camera (320 x 240, -40 to 500°C, 60Hz) and analysing the data using InfReC Analyzer NS9500 Pro Program (details of the camera specifications, mode of operation and data analysis are found in methodology section).

4.4.1.1 Time dependent temperature measurement of $T_{surface}$ and T_{oil} at static conditions, for a fixed T_{cold} and a changing T_{hot}

The first characterisation experiment consists of measuring $T_{surface}$ and T_{oil} for T_{cold} = 5 ^{o}C and varying bulk temperature T_{hot} = 40, 45, 50 and 55 ^{o}C at 0 rpm as initial conditions. Time-dependent temperature measurement results are shown in **Figure 4.4** and steady state temperatures are shown in **Table 4-2**.

Results show that, initially, before immersing the CRF in the bulk oil, $T_{surface}$ (measured in the air) was equal to ~7 ^{o}C, which show a slight increase from the set temperature T_{cold} due to heat loss to the surrounding environment and conduction through the CRF wall. At time 0 s, as soon as the CRF is immersed in the hot oil, $T_{surface}$ increases significantly to 15.2, 16.2, 18.1 and 20.6 ^{o}C within the first 30 s then $T_{surface}$ starts to decrease slightly until it reaches the steady state temperature of 12.5, 13.8, 15.5 and 17.8 ^{o}C respectively for T_{hot}= 40, 45, 50 and 55 ^{o}C

within 10 min. The increase of $T_{surface}$ in the first 30 s is due to the heat transfer from the hot oil to the cold surface due to natural convection. This heat transfer is initially large due to the large difference between the hot stream and the cold stream; however, it takes a relatively long time for the final temperatures to be established. The change in $T_{surface}$ after 30 s is mainly due to the change in the T_{oil} with time. As discussed later in this paragraph, T_{oil} decreases when the CRF is immersed in the hot oil, this decrease in T_{oil} induces respectively a decrease in $T_{surface}$ until the system reaches steady state.

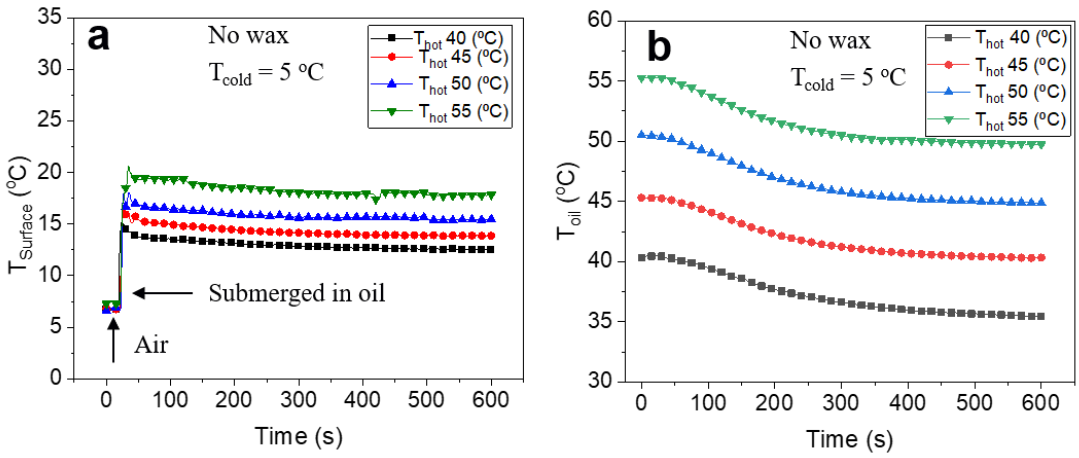

Figure 4.4. Time-dependent temperature profile of (a) $T_{surface}$ of the CRF and (b) T_{oil} (Average TC1 and TC2) with T_{cold} = 5 °C and varying bulk temperature T_{hot}= 40, 45, 50 and 55 °C at 0 rpm.

Table 4-2. Steady state temperatures of T_{oil} and $T_{surface}$ at 0rpm.

T_{cold} (°C)	T_{hot} (°C)	$T_{surface}$ (°C)	T_{oil} (°C)
5	40	12.5	35.5
5	45	13.8	38.5
5	50	15.5	44.9
5	55	17.8	49.7

On the other hand, **Figure 4.4**b shows that, initially, T_{oil} was equal to the set temperature T_{hot} because the bulk oil was heated up on a separate hot plate to the desired temperature before being poured into the jacketed beaker. At time 0 s, as soon as the CRF is immersed into the hot oil, T_{oil} decreases consistently, at the same cooling rate, for all T_{hot} conditions and the decrease in temperature is not as sharp as $T_{surface}$. The relatively slow decrease in T_{oil} is due to the large volume of the bulk oil compared to the surface area of the cold immersed surface and to the TC being positioned on a distance of 10 mm from the CRF. The steady state temperature is reached within less the 10 min for all the set temperatures.

4.4.1.2 Temperature dependent measurement of $T_{surface}$ and T_{oil} measured at static conditions, for a fixed T_{hot} and a changing T_{cold}.

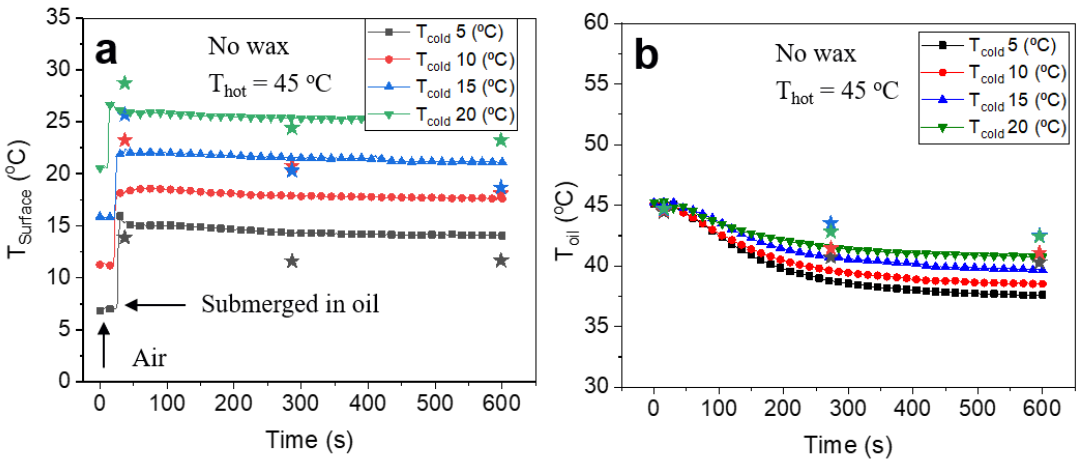

Figure 4.5. Time-dependent temperature profile of **a)** $T_{surface}$ and **b)** T_{oil} at operating conditions corresponding to T_{hot} = 45 ºC and varying T_{cold}= 5, 10, 15 and 20 ºC at 0 rpm. Symbol star show values measured by thermal imaging at the same conditions.

Table 4-3. Steady state temperatures of T_{oil} and $T_{surface}$ at 0rpm.

T_{hot} (ºC)	T_{cold} (ºC)	$T_{surface}$ (ºC)	T_{oil} (ºC)
45	5	13.8	37.8
45	10	17.6	38.5
45	15	21.2	39.7
45	20	25.2	40.7

The second characterisation experiment consists of measuring $T_{surface}$ and T_{oil} for T_{hot} = 45 ºC and varying T_{cold} = 5, 10, 12 and 20 ºC at 0 rpm as initial conditions. Time-dependent temperature measurement results are shown in **Figure 4.5** and steady state temperatures are shown in **Table 4-3**. Results show that, initially, before immersing the CRF in the bulk oil, $T_{surface}$ (measured in the air) was equal to 6.8, 11.3, 15.9 and 20.6 ºC, which shows a slight increase from the set temperature T_{cold} due to heat loss to the environment. However, the loss

seems to be more significant with lower set value of T_{cold}. Increasing the temperature difference between the surrounding environment and the set cold temperature enhances the heat transfer by natural convection between the cold surface and the air and increases initial $T_{surface}$. At time 0 s, as soon as the CRF is immersed into the hot oil, $T_{surface}$ increases significantly to 15.9, 18.6, 22.1 and 25.9 ^{o}C within the first 60 s then $T_{surface}$ starts to decrease very slightly until it reaches the steady state temperatures of 13.8, 17.6 and 21.2 and 25.2 ^{o}C respectively for T_{cold} = 5, 10, 15 and 20 ^{o}C within 10 min. Again, for constant T_{oil} (45 ^{o}C), $T_{surface}$ doesn't change consistently. At steady state a difference of 7, 6.3, 5.3 and 4.6 ^{o}C between steady state and initial temperature of $T_{surface}$ is observed respectively for $T_{surface}$ (air) 6.8, 11.3, 15.9 and 20.6 ^{o}C. Hence, the larger the temperature difference between the hot oil and initial $T_{surface}$, the greater the heat transfer and the deviation of $T_{surface}$ from initial conditions.

Regarding T_{oil}, **Figure 4.5**b shows that, initially, T_{oil} was equal to the set temperature T_{hot} because the bulk oil was heated up on a hot plate to the desired temperature before inserting it into the jacketed beaker. At time 0 s, as soon as the CRF is immersed into the hot oil, T_{oil} starts decreasing, however, this decrease occurs at the different cooling rates depending on the corresponding $T_{surface}$. Lower $T_{surface}$ induces a higher cooling rate, a lower final steady state and a longer time to reach steady state. Hence, again, this is due to a higher heat transfer rate due to the larger temperature difference between the hot and the cold streams.

The star signs in **Figure 4.5** show the measurements taken and analysed using thermal imaging camera at the same conditions. The thermal imaging data are in good agreement with the TC measurement data in terms of trends, however, they show a slight decrease in $T_{surface}$ and a slight increase in T_{oil}, however, these differences are within the range of tolerance of both measurement techniques and the error of the experimental procedure as well. One should note

that the thermal imaging takes the temperature of the surface of the oil and the CRF in contact with the air, therefore, the temperature would not be consistent with the one measured by TC at a depth of few millimetres from the surface.

A comparison between **Figure 4.4** and **Figure 4.5** shows the effect of changing T_{oil} on $T_{surface}$ and the effect of changing $T_{surface}$ on T_{oil}. A calculation of the average change in T_{oil} by increasing $T_{surface}$ shows a change of 0.96 ºC for every increment of 5 ºC in $T_{surface}$. However, the calculated average of $T_{surface}$ change is 1.6 ºC for every increment of 5 ºC in T_{oil}. This comparison allows to conclude that, in the CRF system, the change in bulk temperature has a greater effect on the heat transfer and therefore on wax deposition. This is due to the relatively large volume of the bulk oil with respect to the deposition sample surface area.

4.4.1.3 Temperature dependent measurement of $T_{surface}$ and T_{oil} at dynamic conditions, at fixed T_{cold} and T_{hot}

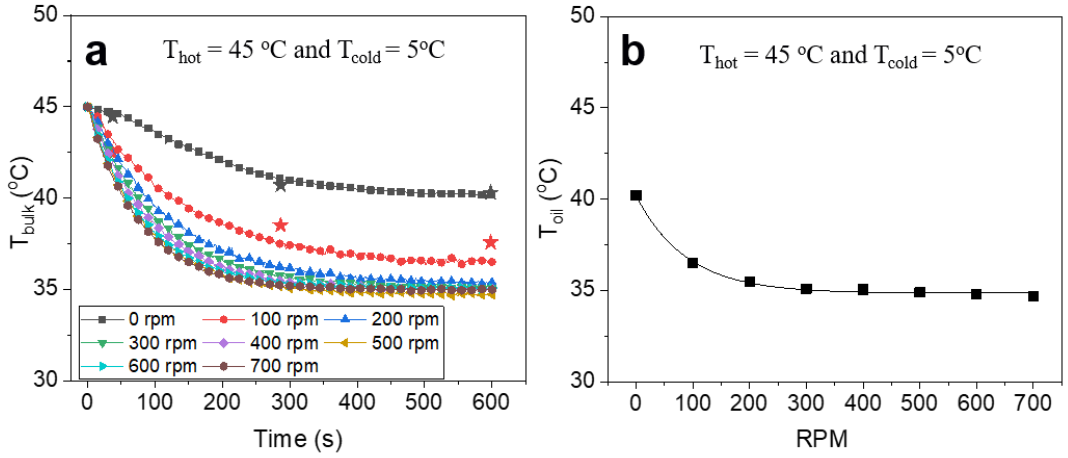

Figure 4.6. a) Time-dependent temperature profile of T_{oil} with T_{hot} = 45 ºC and T_{cold} = 5ºC, for varying rotational speeds between 0 and 700 rpm. Symbol star show values measured by thermal imaging at the same conditions, **b)** Steady state temperatures of T_{oil} with T_{hot} = 45 ºC and T_{cold} = 5ºC, for varying rotational speeds between 0 and 700 rpm. Line is to guide the eye and takes the form, $y = y_0 + Ae^{(Bx)}$ with y_o = 34.85, A = 5.32 and B = -0.011.

The effect of the rotational speed on the heat-mass transfer in our CRF system was also measured in n-dodecane in the absence of alkane wax. Results confirmed a reduction in T_{oil} with increasing rotational speed and an increase in the cooling rate with rotational speed. **Figure 4.6**b shows that at 0 rpm, T_{oil} decreased to ~40°C (~10 min to attain steady-state values). At 100 rpm, T_{oil} decreased to ~36.5°C (~8 min) and above 400 rpm, T_{oil} decreased to ~35°C (~5 min) for all rpm. Unfortunately, $T_{surface}$ could not be directly measured with TC due to challenges associated with attaching a TC on a rotating surface.

The star signs in **Figure 4.6**a show the measurements taken and analysed using thermal imaging camera at the same conditions. The thermal imaging data are in good agreement with the TC measurement data in terms of trends, however, they show slight differences which are again within the range of tolerance of both measurement techniques and the error of the experimental procedure as well. Thermal imaging data of **Figure 4.6**a were taken by analysing thermal images presented in **Figure 4.7**. **Figure 4.7** shows on scale of colour/temperature ranging from 45 to 5 °C (pink to blue colour) the change in the CRF temperature with time for 0 and 100 rpm at the same T_{cold} and T_{hot}. The images show a change in the bulk solution colour from pink at 1 min to light red at 0 rpm and dark red at 100 rpm at 10 min reflecting therefore the decrease in the temperature with rotation. A careful examination of the thermal image of 100 rpm, 1 min, shows that, in a bulk of hot oil (pink colour), there are waves of dark colour released from the side of the CRF. These waves show the increase in the heat transfer with the rotational speed by forced convection from the cold surface into the bulk oil. The fluid motion enhances heat transfer and the higher the RPM, the higher the heat transfer rate. However, after a critical RPM (400 rpm in our CRF operating conditions), the heat transfer is less affected by the RPM and the temperature profile seems to have a similar trend steady state temperature.

The temperature profile of the CRF was characterised and T_{oil} and $T_{surface}$ were identified to be different from the set temperature T_{hot} and T_{cold}. This difference depends on the hydrodynamics of the CRF and the difference between the T_{hot} and T_{cold}. It is very challenging therefore to design our experiments at well-defined and precise T_{oil} and $T_{surface}$ and therefore, all our experiments are going to be designed on the basis of T_{hot} and T_{cold} keeping in mind the temperature profiles of $T_{surface}$ and T_{oil} for data analysis.

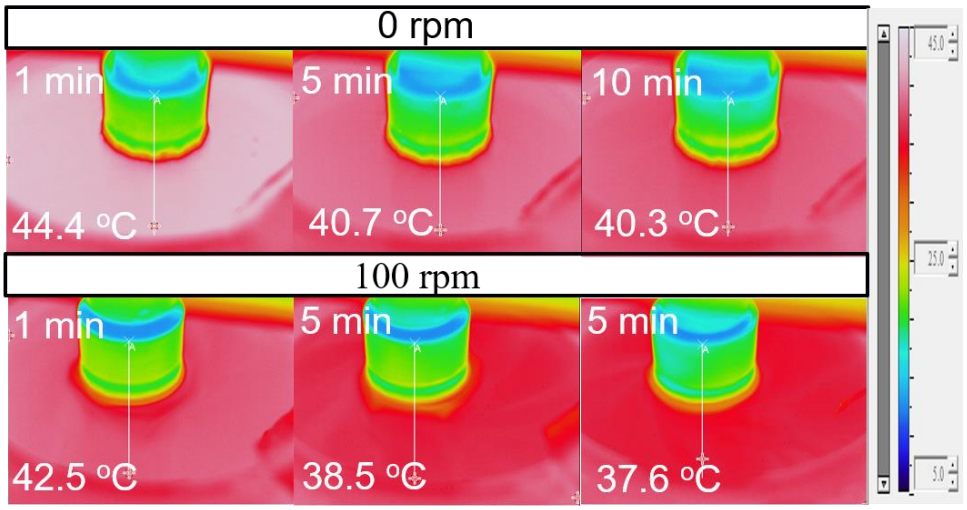

Figure 4.7. Thermal imaging of the CRF immersed in dodecane oil with T_{hot} = 45 °C and T_{cold}= 5°C at 0 and 100 rpm.

4.4.2 Hydrodynamic and Flow characterisation of the CRF

The CRF flow field is Couette flow type (azimuthal flow between two cylinders) with a certain degree of axial circulation. While different from pipe flow, similarity between Couette flow and pipe flow has been demonstrated in the literature[43, 44, 175]. Fluid dynamics research has shown that the boundary layer, where wax deposition is taking place, shares common characteristics in most internal flows. Ostilla-Monico et al.[176] conducted Direct Numerical Simulations (DNS) for a variety of internal flows and observed a great similarity between their

respective boundary layers. **Figure 4.8** illustrates the dimensionless coordinates in wall units for these systems. **Table 4-4** compares key flow parameters for Couette flow and pipe flow processes and shows the similarities in both types of flow[43].

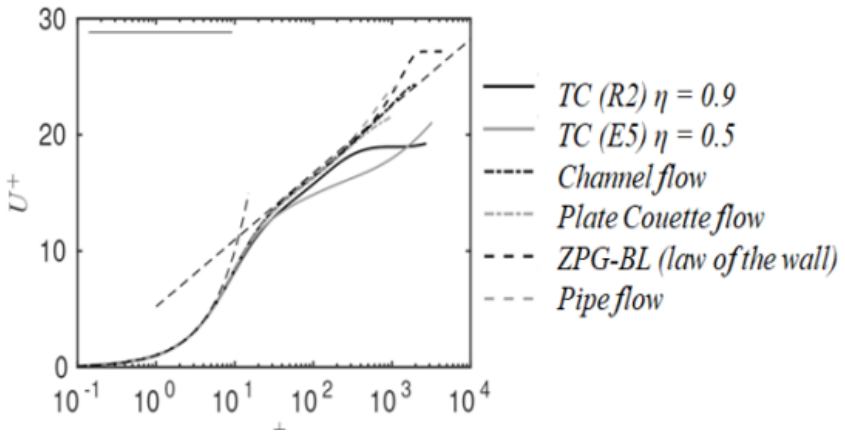

Figure 4.8. Azimuthal velocity near the wall, in wall units (U+, r+) obtained from DNS studies taken from Ostilla-Mónico et al.[176].

Table 4-4. Similitude between Couette flow and pipe flows adopted from Zougari et al.[43].

Parameter	Pipe	Couette flow
Reynolds number	$Re = \frac{uD_e}{v}$	$Re = \frac{u(r_o - r_i)}{v}$
Wall shear stress	$\tau_w = \frac{1}{8}\rho f u^2$	$\tau_w = \frac{1}{8}\rho \Psi\, u^{1.8}$
Friction factor	$\frac{1}{\sqrt{f_r}} = C_1 \log\left(Re\sqrt{f_r}\right) + C_2$	$\frac{1}{\sqrt{f_r}} = C'_1 \log\left(Re\sqrt{f_r}\right) + C'_2$
Hydrodynamic boundary layer	$\delta_p = 91 D_e \frac{\ln(Re)}{Re}$	$\delta_{CT} = 3.8(r_o - r_i)\frac{\ln(Re)}{Re^{0.8}}$

Where, Ψ, the friction factor Re is the Reynolds number, De the pipe hydraulic diameter, fr the friction factor, u the linear fluid velocity, F the fluid density, ν the fluid kinematic viscosity,

Ψ the CT friction factor, δ the boundary layer thickness, r_o the radius of the Couette flow cell stationary deposition surface and r_i the radius of Couette flow cell.

It should be noted that the CRF has a limitation in replicating exactly the amount of wax depositing for the given heat transfer. In fact, the centrifugal forces arising from the spinning cylinder direct the wax away from the cold finger. The mass deposited can be then referred to an apparent mass. This limitation, however, doesn't have an effect on the functionality of the CRF as a convenient apparatus to study wax deposition as the CRF is meant to analyse the trends of wax deposit mass at various flow rates rather than quantifying the wax deposit mass and compare to field results or pilot-scale equipment.

4.5 Materials and Experimental Methods

4.5.1 Wax Properties

A model waxy oil composed of low (C_{20}-C_{40} [manufacturer quoted distribution, Merck, UK], melting point 58-62°C) and high (melting point 65-71°C, Fisher Scientific, UK) molecular weight solid n-alkanes, and dodecane (Acros Organics, UK) with a boiling point of 170-195°C and density of 0.751 g/cm^3 was used throughout the study. The carbon chain length distribution as measured by GC-FID is shown in **Figure 4.9**. Blending low and high molecular weight waxes produced a carbon chain length distribution representative of that found in crude oils[34].

Figure 4.9 shows the carbon chain length distribution of the LMW and HMW waxes as well as their average. The mixture of LMW and HMW was chosen in the purpose of having a broad range of carbon chain length distribution close to the composition of wax in crude oil. In crude oil, wax is essentially a mixture of long chain hydrocarbons with carbon numbers ranging

from 18 to 65 and n- alkanes are generally the major constituents. The wax mixture already covers a broad range of wax and it is within our GC-FID limits of detection (C10-C41) (more information about the GC-FID working principles, analysis and limitations are found in methodology section). On the other hand, several solvents (heptane, decane, dodecane, isopar, mineral oil) of different carbon chain length and viscosities were experimented to choose the most suitable one for our model solution.

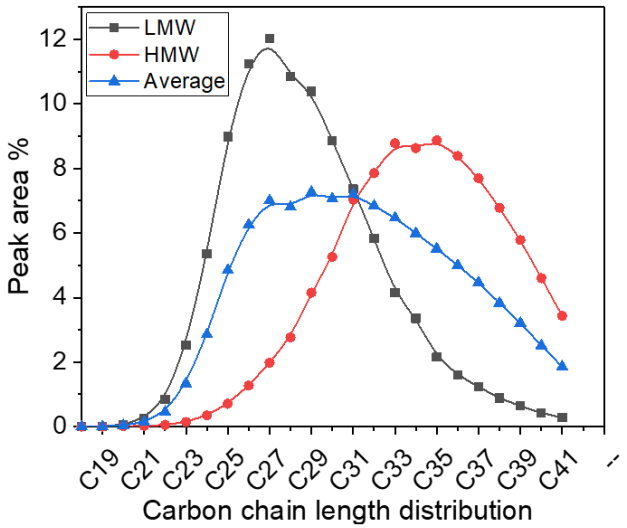

Figure 4.9. Carbon chain length distribution of the Low Molecular Weight (LMW) and High Molecular Weight (HMW) waxes used throughout the study.

Dodecane was chosen because it has a relatively high boiling point, reducing its evaporation during experiments, it has a carbon chain length C_{12} much smaller than the alkane wax used which helps to identify solvent peaks and wax peaks in the GC-FID spectrum. Dodecane is cheap, available and already used in peer-reviewed published papers[110]. Besides, in the range of temperature operating conditions (0 and 60 ^{o}C), dodecane shows a good wax deposition data that are quantifiable, measurable and with a deposit thickness that wouldn't change the dimensions and the configuration of the CRF.

4.5.2 Wax Appearance Temperature measured by Light Transmission

The wax appearance temperatures (WAT) of 4.7, 9, 13 and 16.6 wt% n- alkane -in-dodecane (1:1 mass basis for low and high molecular weight wax) were measured by turbidity measurement performed at different cooling rates using a Crystal 16 apparatus (Technobis). The Crystal 16 comprises sixteen sample wells split into four blocks. Each block is independently temperature-controlled and enables a range of cooling rates to be studied simultaneously. Samples were added to 1 mL glass vials. The solution turbidity (transmission %) is measured as a function of temperature. Each test began by heating the samples to 60°C and held at that temperature for 30 min to ensure thermal equilibrium. Then the samples were cooled at 0.5, 1, 2 and 3°C /min to 0°C while stirred using a magnetic flea at 700 rpm. The WAT is taken to be the temperature at a light transmission of 90% (100% is transparent).

4.5.3 Wax Appearance Temperature measured by Rheology

The wax appearance temperatures (WAT) of 4.7, 9, 13 and 16.6 wt% n- alkane -in-dodecane (1:1 mass basis for low and high molecular weight wax) were identified by viscosity measurement performed at different cooling rates using a TA DHR-II rheometer with concentric cylinders temperature system. A DIN standard bob geometry and a standard cup with Peltier temperature control for fast heating and cooling Peltier were used. Prior to loading, the sample and the measuring geometry were maintained at 60 ^{o}C to assure wax is completely dissolved in dodecane. 18 mL of the sample is then loaded in the grooved cup and kept for until the temperature of the cup is stable at 60 ^{o}C. All rheology WAT measurements were carried out using on flow mode and temperature ramp from 60°C to 10°C, at a frequency of 50 rad/s and a ramp rate of 0.5 and 1 ^{o}C/min.

4.5.4 Gas Chromatography-Flame Ionization Detection (GC-FID)

GC/FID (Perkin Elmer Clarus 500 GC), with hydrogen flame and kerosene as a reference, was used for the analysis of the wax deposit. The GC-FID included an Elite M1 column of length 15 m, inner diameter (ID) of 0.53 mm and a temperature range of -60 to 340/360^{o}C. Approximately 0.2 g of the wax deposit was taken by cutting a slice of the wax deposit from the top to the bottom of the deposit sample. The wax sample was inserted into a Thermo Scientific 11 mm non-assembled amber crump top autosampler vial and stored at 4^{o}C until the GC experiment was performed. On the experiment day, approximately 1 mL of carbon disulphide was added to the vial to dissolve completely the wax before entering the GC column.

4.5.5 Cryo-scanning Electron Microscope (Cryo-SEM)

Cryo-SEM was used to study the morphology of wax deposits. Wax deposits were carefully removed from the cylindrical test sample using a clean scalpel. To avoid damaging the structure of the wax deposit, two vertical lines of ~10mm were cut from the edge of the sample and the scalpel slid between the sample and deposit surface to remove the wax layer. The wax layer was placed in a freezing rivet and the sample frozen in slushed nitrogen before transferring to the SEM under vacuum. To study cross-section of the wax layer, the sample was fractured using a chilled knife. The samples was sputter coated with Iridium and imaged using 2 kV at 0.1 nA.

4.5.6 Wax Deposition Tests

Solutions of 4.7, 9, 13 and 16.6 wax wt% n- alkane-in-dodecane were used for deposition tests. To prepare the wax solution, an equal amount of low and high molecular weight alkane wax was added to n-dodecane at 60°C and held at temperature for 1 h until all the wax had

dissolved (visual assessment). The solution was then cooled to the desired T_{hot} to begin the wax deposition test. Deposition tests were conducted in a 300 mL Pyrex jacketed beaker which maintained the wax solution at the desired T_{hot} (under static condition) and monitored using a K-type thermocouple (± 0.5°C). The coolant fluid at the desired T_{cold} was pumped through the CRF to chill the outer surface of the CRF and initiate wax deposition. The mass of the wax deposit on the cylindrical test sample was assessed by gravimetric measurement. Following each experiment, a scalpel was used to remove wax external to the cylindrical test sample. Mass deposited was taken to be the difference in mass between the cylindrical test sample in the absence and presence of wax. All wax deposition tests were run in triplicate.

4.5.6.1 Understand the Parameter Space of the CRF: Taguchi experimental approach

As a first attempt to test the functionality of the CRF for wax deposition studies, a screening experimental matrix was designed based on four key parameters affecting wax deposition. Those parameters were chosen based on their major contribution to wax deposition phenomena as reported in the literature. The 4 parameters and their related operating conditions are presented in **Table 4-5** below where factors refer to "parameters" and Level refers to "parameter value".

Table 4-5. Taguchi experimental matrix of factors affecting wax deposition.

Factors	Level 1	Level 2	Level 3	Level 4
T_{cold} (◦C)	5	10	15	20
T_{hot} (◦C)	40	45	50	55
Wax (wt %)	4.7	9	13	16.6
RPM	0	50	100	150

The operating conditions of T_{hot} and T_{cold} were chosen depending on the WAT of the wax wt% and chosen to have a $T_{hot} > T_{WAT}$ and $T_{cold} < T_{WAT}$. An increment of 5 ^{o}C between the different values of T_{hot} and T_{cold} is chosen for consistency and for achieving mass deposit results that are not within the experimental error, with a deposit mass deviation higher than 10%. T_{hot} and T_{cold} were taken instead of T_{oil} and $T_{surface}$ because the characterisation of the temperature profile in the CRF shows that the former temperatures are not easily controlled nor defined at different operating conditions. They may change greatly depending on the RPM and the operating conditions of the chiller and the heater. As a starting point to test the functionality of the CRF, taking fixed T_{hot} and T_{cold} is simpler to work with.

The selection of the wax weight percentages was made according to real field data given in the literature (wax % causing wax deposition problems in crude oil is between 2 and 20wt% [11]). Rotational speeds were varied from static to 150 rpm to study the effect of rotational speed on wax deposition.

The study of the individual effect of the 4 key variables and their effects through traditional statistical method will lead to the following number of experiments to be conducted:

$$4^4 = 256\ experiments$$

To reduce the number of experiments and maintain the quality of data collection, an optimization approach called Taguchi Method was chosen. Taguchi Method is an optimization approach used to statistically plan and design an experimental robust matrix that reduce the number of experiments, allow the study on the effects of multiple variables simultaneously while maintaining the quality of data collection. Taguchi Method was used as a rapid screening

on the main factors affecting wax deposition with a small number of experiments for optimizing future studies on wax deposition. Taguchi's key concepts and the steps to build up the experimental matrix are explained in the appendix section. **Table 4-6** presents the final experimental matrix designed by Taguchi method.

Table 4-6. Taguchi experimental matrix of wax deposition using CRF.

Run	T_{cold} (°C)	T_{hot} (°C)	Wax wt%	RPM
1	5	40	4.7	0
2	5	45	9	50
3	5	50	13	100
4	5	55	16.6	150
5	10	40	9	100
6	10	45	4.7	150
7	10	50	16.6	0
8	10	55	13	50
9	15	40	13	150
10	15	45	16.6	100
11	15	50	4.7	50
12	15	55	9	0
13	20	40	16.6	50
14	20	45	13	0
15	20	50	9	150
16	20	55	4.7	100

The experimental matrix presents 16 experiments. Each row of the matrix represents a run (or an experiment) at specified operating conditions. **Table 4-7** below shows the deposit mass results for each experiment in triplicate. 30 min was chosen to be the experiment duration based on temperature profile screening, where temperature steady state and deposition are believed to be already achieved by that time.

Table 4-7. Wax mass deposit after 30 min for Taguchi experimental matrix.

Run	Test 1 (g)	Test 2 (g)	Test 3 (g)	Av. mass	Error (± g)
1	2.6	2.3	2.2	2.4	0.5
2	2.8	2.6	2.7	2.7	0.2
3	1.7	1.7	1.7	1.7	0.0
4	1.3	1.2	1.3	1.2	0.1
5	3.0	3.4	2.7	3.0	0.7
6	0.5	0.5	0.6	0.5	0.0
7	3.4	3.2	3.2	3.3	0.3
8	1.3	1.2	1.3	1.3	0.1
9	4.4	4.2	4.1	4.2	0.3
10	3.8	3.6	3.2	3.6	0.6
11	0.4	0.4	0.4	0.4	0.1
12	0.6	0.7	0.8	0.7	0.1
13	9.6	9.6	9.6	9.6	0.0
14	2.4	2.8	2.6	2.6	0.3
15	0.4	0.4	0.5	0.4	0.0
16	0.0	0.0	0.0	0.0	0.0

4.6 Results and Discussion

4.6.1 Wax Appearance Temperature

As the temperature of the oil decreases at a controlled and specified cooling rate, the wax starts to precipitate and form solid crystals. The highest temperature at which the first crystals are observed and starts to drop out in the liquid bulk solution is called the WAT. Various experimental techniques have been developed to assess the WAT based on the change in the physical properties of the waxy solution during the formation of wax crystals, however, none of the available techniques are able to detect the very first wax crystals. Precipitated wax

crystals can be detected in different size, quantity and form. Crystal 16 and rheometer are the two techniques used in this study to determine the WAT.

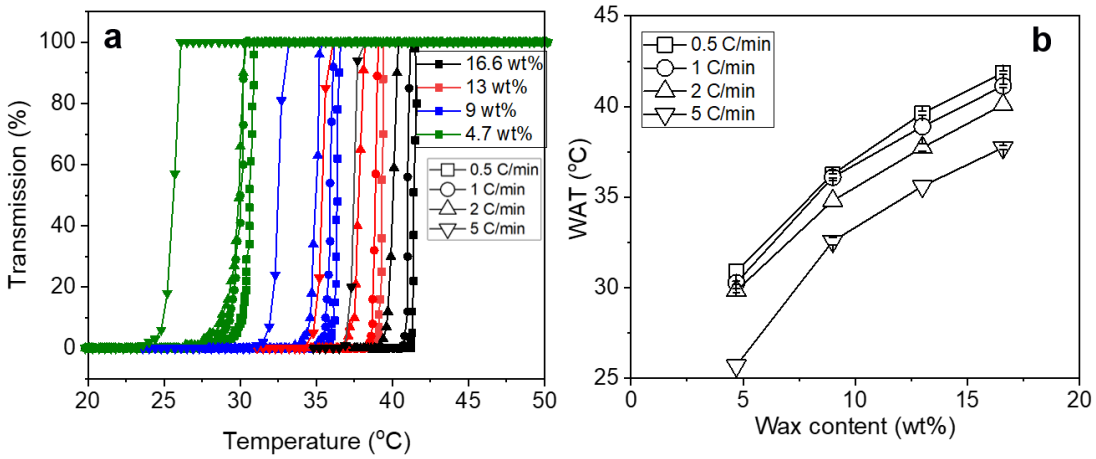

Figure 4.10. a) Light transmission % (turbidity) of alkane wax-in-dodecane as a function of temperature and wax content at different cooling rates. The WAT is the temperature when the light transmission is 90%. **b)** Comparison of WAT as a function of the alkane concentrations cooling rate and wax content.

The Crystal 16 is a turbidimetric method to detect the cloudy points by measuring the transmission of a laser beam through a solution under heating/cooling cycles. This technique was chosen because it has a high resolution to detect crystal in nano size. **Figure 4.10**a shows data obtained from Crystal 16 for 4.7, 9, 13 and 16.6 wt% wax-in-dodecane cooled at rates between 0.5 and 5°C/min from 60 °C to 10 °C (graph shows only 50 to 20 °C for a better resolution of the graph). The WAT is taken at the temperature when the transmission is 90% and **Figure 4.10**b compares the WAT of all wax wt% as a function of cooling rate.

The measurement of the WAT in crystal 16 was compared to the WAT measured by a rheometer which relies on the change of the viscosity during the cooling process. Above the

WAT, the crude oil behaves as a Newtonian fluid, and the viscosity of oil is independent of the temperature change. As temperature is lowered below the WAT, the wax precipitates, and the precipitated solids remain suspended in the bulk liquid. The suspended wax particles change the viscosity.

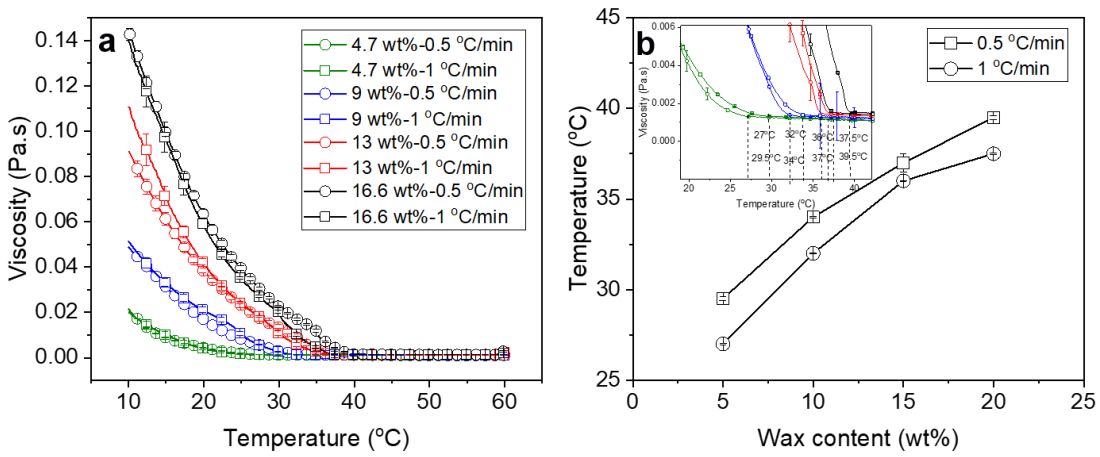

Figure 4.11. a) Viscosity of wax solution as a function of temperature for 4.7, 9, 13 and 16.6 wt% alkane wax-in-dodecane during cooling from 60 °C to 0 °C at cooling rates of 0.5 °C/min and 1°C/min. The WAT is the temperature when the viscosity plateau deviates (Viscosity increases), **b)** Comparison of WAT as a function of alkane wax content and cooling rates. Shear rate is fixed at 50 rad/s corresponding to 63 s^{-1}.

Determination of the WAT based on viscometry utilizes the change in the slope in the viscosity vs. temperature curve. In a typical viscosity-temperature experimental measurement (cf. **Figure 4.11**), the oil sample is cooled from 60°C to 10°C at a rate of 0.5°C and 1°C/min. The change of viscosity as a function of temperature is measured under a constant frequency of 50 rad/s. Extrapolation from the Newtonian region is performed to determine the WAT. Depending on the composition of the precipitating n-alkane, the change in the slope of the viscosity–temperature curve near the WAT can be either sharp or gradual. If the precipitating n-alkane only containing a narrow range of carbon chain length, the change in the slope is

likely to be sharp because n-alkanes precipitate in a narrow temperature range. Contrarily, if the precipitating n-alkane covers a wide range of carbon numbers, as the case of our model solution, the change in the slope is likely to be gradual as the n-alkanes precipitate over a wider temperature range.

Sometimes, the change in the slope can become difficult to identify when very little wax is precipitating, which will cause a significant underestimation of the WAT.

As seen in **Figure 4.10** and **Figure 4.11**, the WAT is a great function of the wax concentration and the cooling rate. The higher the wax concentration, the higher is the WAT; for the same cooling rate of 0.5 ^{o}C/min, the WAT measured by C16 was shown to decrease from 41.8 °C (16.6 wt%) to 36.2 °C (4.7 wt%) and the WAT measured by Rheometer decreases from 39.5 °C (16.6 wt%) to 29.5 °C (4.7 wt%). To understand this effect, one should understand the supersaturation which is the main driving force of crystallisation. The supersaturation is described in terms of concentration driving force ($\Delta C = C - C_e$) or relative supersaturation ratio ($S = \frac{C}{C_e}$), where C is the solution concentration at a specific temperature and C_e is the concentration at equilibrium with that temperature. Therefore, the increase in the solution concentration increases the supersaturation which is an essential stage to form the nucleation and the crystallisation process. With increasing cooling rates, the WAT was shown to decrease as well. The dependence of WAT on cooling rate is due to differences in crystal growth rate with temperature, with larger crystals formed at low cooling rates influencing solution transmission or viscosity more than small crystals formed at high cooling rates. Besides, low cooling rates allow more time for the equipment to detect any change in the solution transmission or viscosity. Wax crystallisation is also a time-dependent function, while being at or below the WAT, the crystallisation starts and the growth of the wax crystals continue even

at a constant temperature, therefore, more wax crystals are expected to form in the time-being of low cooling rates.

4.6.1.1 Comparison between WAT Measurements

Table 4-8 summarizes WAT measured by rheometer and turbidity testing as a function of wax contents and cooling rates. Due to the low size detection limit of the C16 method, it is likely that C16 provides the most conservative measure of the WAT among the two methods. The sensitivity of the rheometer technique is lower than C16. In most cases, an amount of 0.3–0.4 wt% solid material needs to have precipitated in order to cause a detectable deviation in the viscosity of the solution, whereas the wax crystals only need to grow to ~1 μm to be detectable by C16, corresponding to ~0.1 wt% solid material in the liquid[11]. Therefore, the WAT determined based on viscosity measurements is lower than the values determined by C16.

Table 4-8. Comparison of WAT measured by rheometer and turbidity testing as a function of wax content and cooling rate.

	Rheometer				**Tubidimeter**			
Wt%	4.7	9	13	16.6	4.7	9	13	16.6
0.5°C/min	29.5	34	37	39.5	30.9	36.2	39.6	41.8
1°C/min	27	32	36	37.5	30.2	36.1	38.9	41.1

4.6.2 Results of Taguchi Method to Assess the Parameter Space

The analysis of Taguchi results is based on calculating the mean of wax deposit mass for each factor at every level by considering all the runs when this factor/level appears. Taking T_{cold} factor and level 1 (5^{o}C) as an example, the mean value of the wax deposit mass at every experiment run at this factor/level is calculated by averaging the mass deposit of experiments

where this factor/level appears (run 1, 2 , 3 and 4 in this case). The mean values of each factor's levels are then plot in **Figure 4.12**. This figure shows the change in the wax deposit mass as a function of 4 factors: wax wt%, RPM, T_{hot} and T_{cold}.

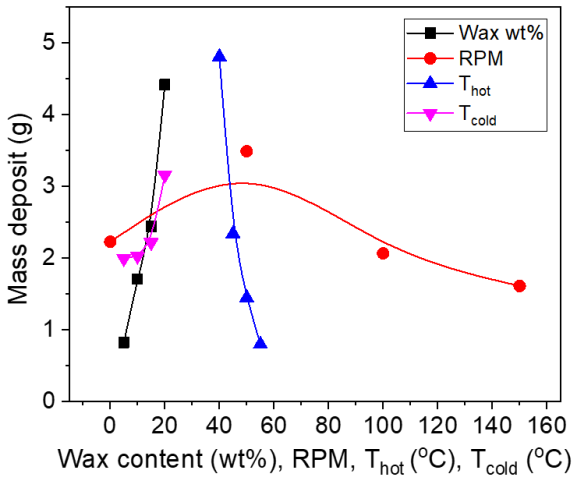

Figure 4.12. Summary of test runs based on the proposed Taguchi method.

One should note that the data in **Figure 4.12** needs to be analysed qualitatively rather than quantitatively. In fact, for quantitative measurements, the experiments are usually performed by varying only one parameter. In Taguchi, this consistency is missed, for instance, the study of the factor T_{cold} at different levels, T_{hot}, wax wt% and RPM needs to be fixed in systematic studies, but they are not in Taguchi matrix, as shown in **Table 4-6**. This reduce Taguchi method to a preliminary qualitative tool to assess the functionality of the CRF and to screen rapidly the weight of each factor chosen on wax deposition.

4.6.2.1 Effect of Wax Content

Figure 4.12 shows the change in the mass deposit with wax wt% and the significant increase in the mass deposit with the wax wt%. The higher the concentration of wax, the higher is the

wax available for deposition. Besides, related back to the supersaturation concept explained in the WAT measurements, the increase in the wax wt% increases the supersaturation driving force for crystallisation and enhances crystallisation at higher temperatures. The wax is able to crystallise up to a higher temperature when the concentration is higher. Hence, while the wax deposit on the cold surface and $T_{interface}$ is increasing due to the insulation of the wax layer, a higher wax concentration with higher WAT requires a thicker layer of wax in order for the $T_{interface}$ to reach the WAT. Taguchi results shows that the increase in the mass deposit is consistent between 4.7, 9, 13 wt% then becomes sharp with 16.6 wt%. This inconsistency may be due to run number 13 (at 16.6 wt%) that shows the highest wax deposit mass in the 16 runs. At run 13, the oil temperature is within the WAT range of 16.6 wt% wax-in-dodecane solution ($T_{hot} \sim 40\ ^{o}C$), which maximise the wax deposition. This wasn't the case for the remaining runs.

4.6.2.2 Effect of CRF Rotational Speed

Figure 4.12 shows the change in the mass deposit with rotational speed. The mass deposit seems to increase while changing the RPM from 0 to 50 rpm, then decreases for 100 and 150 rpm. The change in the mass deposit with rotational speed is already well studied in the literature but not very well understood. Few researchers reported an increase in the mass deposit at low rotational speed (or laminar flow). Cole and Jessen (1960) states that the wax deposition increases with the increase of flow rate in laminar flow due to the availability of more particles at the surface for deposition. When the flow regime becomes turbulent, the shear flow mechanism becomes more prevalent and the wax deposition decreases. Howell and Jessen (1958) reported that the amount of wax deposited for flow in a turbulent regime was lower than that obtained for a laminar regime[177-179]. This trend can be compared to deposition under isothermal conditions where a faster deposition rate is observed with an increasing flow rate because only advection plays a role in affecting the radial mass flux[47]. However, in the case of

wax deposition, which occurs under non-isothermal conditions, the heat and mass transfer are dependent especially in turbulent flow[114] which can result in different effect of flow on the wax deposition. Indeed, most flow studies show that the wax deposit mass decreases with increasing flow rate. Some researchers attribute the mass reduction to the effect of sloughing (physical removal of wax) due to the increase of the wall shear stress, or densification of the wax deposit as oil is squeezed from the deposit when sheared[46, 48, 124] while others consider the effects of flow on heat and mass transfer[47]. In the presence of flow, the boundary layer thickness decreased (with increasing fluid shear), and the heat transfer between the hot and cold temperatures is enhanced which alter the thermal gradient and consequently the concentration gradient of wax. Depending on the geometry, the flow may either increase the temperature at the interface reducing therefore the deposition as in flow loop[19, 47] or decreasing the thermal gradient between the hot and cold temperature which lead to lower wax deposition as in cold finger apparatus[20, 45, 46].

4.6.2.3 Effect of T_{cold}

Regarding the effect of operating temperatures on the wax deposition, the analysis of **Figure 4.12** shows that the increase in T_{cold} increases the mass deposit. This result is in complete contradiction with the mechanism of wax deposition. Research confirmed that the decrease in the T_{cold} is the main driving force of wax deposition, therefore increasing T_{cold} should lead to a decrease in the wax deposition. The increase in T_{cold} increases the wax solubility at the interface deposit-oil and decreases the crystallisation of wax molecules. Results from literature show that experiments with lower coolant temperature strengthens the driving force of the wax molecules diffusion from the bulk oil to the cold surface and improves of the ability wax molecules to precipitate on the cold surface, hence, the wax deposition increases[65, 75].

To explain the contradictory results of Taguchi in terms of the effect of the cold temperature on wax deposition, a systematic analysis of the effect of the cold temperature on wax deposition was made. In this analysis, the increase in the cold temperature was only considered with experiments having the same temperature gradient between the hot and cold temperatures.

The effect of T_{cold} was analysed for the same wax wt% and similar ΔT (between the hot and cold temperature). Taking for instance 4.7 wt% wax solution and comparing experiments 1, 6, 11 and 16, having T_c= 5, 10, 15 and 20 ^oC respectively and operating all at ΔT = 35 ^oC, the mass of the wax deposit is 2.4, 0.5, 0.4 and 0 g respectively. These results are in line with the literature and prove that the increase in the cold temperature leads to a decrease in the mass deposit wax. Similar example can be taken for 9 wt% where experiments 2 and 12 are operating at T_c= 5 and 15 ^oC with ΔT= 40 ^oC and the mass deposit is equal to 2.7 and 0.7 g respectively.

4.6.2.4 Effect of T_{hot}

On the other hand, Taguchi results show that the increase in T_{hot} leads to a decrease in the wax deposition, which is already confirmed in the literature. For the same reason, increasing T_{hot} increases the solubility of the wax molecules in the bulk and increase $T_{surface}$ as shown in the T profile characterization of the CRF (cf. **Figure 4.8**), leading to less crystallization and deposition of wax molecules on the CRF.

4.6.3 Further Assessment of the Effect of Operating Temperatures on Wax Deposition

As the analysis of Taguchi results were not always consistent with the literature nor was the mechanism of wax deposition, a rearrangement of the results was made for further analysis. For instance, the effect of operating temperatures was taken as a function of the extent between

the WAT and the hot or cold operating temperatures, on the basis of ΔT_{hot} ($\Delta T_{hot} = T_{hot} - T_{WAT}$) and ΔT_{cold} ($\Delta T_{cold} = T_{WAT} - T_{cold}$) instead of T_{cold} and T_{hot}[64, 68, 69]. Based on that, the larger (WAT-T_{cold}) and the smaller (T_{hot}-WAT) lead to higher deposition rate. Below, for each run, ΔT_{hot} and ΔT_{cold} were calculated and the runs were rearranged on an increasing ΔT_{hot} and ΔT_{cold} basis as seen in **Table 4-9**. Calculations are based on the temperature operating conditions for each run and the WAT presented in **Table 4-8**.

Table 4-9. Taguchi experimental matrix considered as a function of ΔT_{hot} and ΔT_{cold}.

Run	ΔT_{hot} (°C)	Mass (g)	Run	ΔT_{cold} (°C)	Mass (g)
13	0.5	9.6	16	9.5	0.0
9	3	4.2	15	14	0.4
10	5.5	3.6	11	14.5	0.4
5	6	3.0	14	17	2.6
14	8	2.6	12	19	0.7
1	10.5	3.3	13	19.5	9.6
7	10.5	2.4	6	19.5	0.5
2	11	2.7	9	22	4.2
3	13	1.7	5	24	3.0
4	15.5	1.2	1	24.5	3.6
6	15.5	0.5	10	24.5	2.4
15	16	0.4	8	27	1.3
8	18	1.3	2	29	2.7
11	20.5	0.4	7	29.5	3.3
12	21	0.7	3	32	1.7
16	25.5	0.0	4	34.5	1.2

A plot of **Table 4-7** results is shown in **Figure 4.13**.

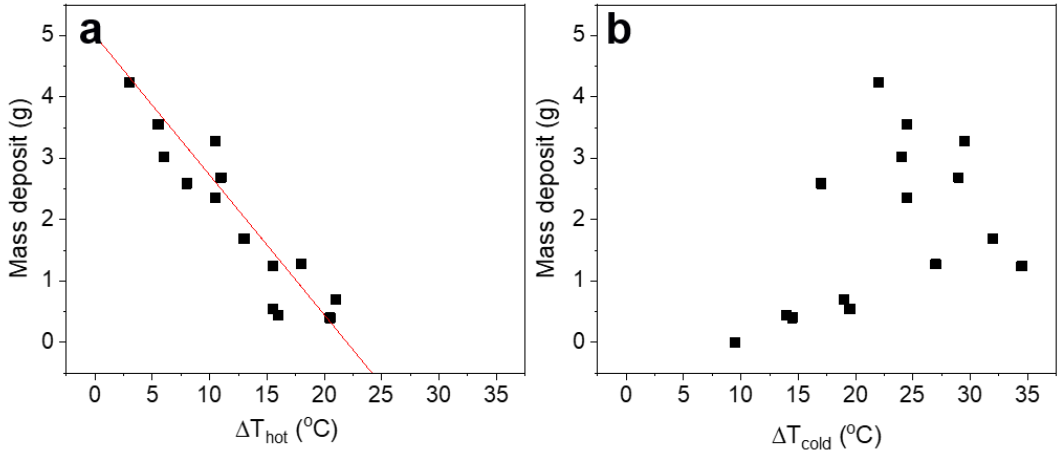

Figure 4.13. Taguchi results showing the change in the mass gain as a function of **a)** the ΔT_{cold} and **b)** ΔT_{hot}. Line on figure a is to guide the eye and takes the form, $y = ax + b$. Values of the constants are in **Table 4-10**.

Table 4-10. Values of the fitting curves constants of **Figure 4.13**.

$y = ax + b$	
a	5
b	-0.22758

Figure 4.13 shows the effect of ΔT_{cold} and ΔT_{hot} on the mass deposit as a function of the extent of T_{hot} and T_{cold} from the WAT. **Figure 4.13**a shows a linear relationship between the mass deposit and ΔT_{hot} with negative slope showing a decreasing function of the mass with the respective increase in ΔT_{hot}. The decrease is sharp and match the results found earlier in the previous analysis. **Figure 4.13**b shows however a more complex relationship between the mass deposit and ΔT_{cold}. While the trend looks like linear with a positive slope at $\Delta T_{cold} < 20$ °C, the mass deposit trend starts to change after that, suggesting an exponential trend between 20 and 30 °C with an unexplained decrease in the mass gain $\Delta T_{cold} \geq 30$ °C. Although **Figure 4.13**b doesn't show a clear trend of the mass deposit, however, it denies the results found by the first

analysis of Taguchi where the mass deposit was a decreasing function of increasing ΔT_{cold}. Analysing Taguchi results based on ΔT decrease the number of varying parameters per run. In fact, when analysing the effect of T_{cold} with Taguchi, T_{hot}, wt% and RPM are already changing simultaneously, therefore, the reliability of the data is low. While re-analysing following ΔT, the changing in wax wt% is eliminated, which has already a great effect on the mass deposit. Nevertheless, T_{hot} and the RPM are still changing which may still induce a great error in the analysis.

4.6.3.1 Effect of ΔT_{cold} and ΔT_{hot} on chemical composition

To highlight changes in the wax carbon chain length distribution of deposit samples with ΔT_{cold} and ΔT_{hot}, two sets of 3 runs each were chosen with an increasing ΔT_{cold} and ΔT_{hot} and compared in terms of wax composition. The set of runs are presented in **Table 4-11** and the chemical compositions of the wax deposits are presented in **Figure 4.14**. The mass fractions of C20-C41 *n*-alkanes were normalized on a solvent-free basis then compared to those in the original wax mixture composition represented in dash lines.

Table 4-11. Taguchi runs rearranged by increasing ΔT_{hot} and ΔT_{cold} and comparison to wax deposit chain length distribution.

	ΔT_{hot} (°C)	**Run**		**ΔT_{cold} (°C)**	**Run**
ΔT_{hot1}	0.5	13	ΔT_{cold1}	14	15
ΔT_{hot2}	13	3	ΔT_{cold2}	22	9
ΔT_{hot3}	21	12	ΔT_{cold3}	29.5	7

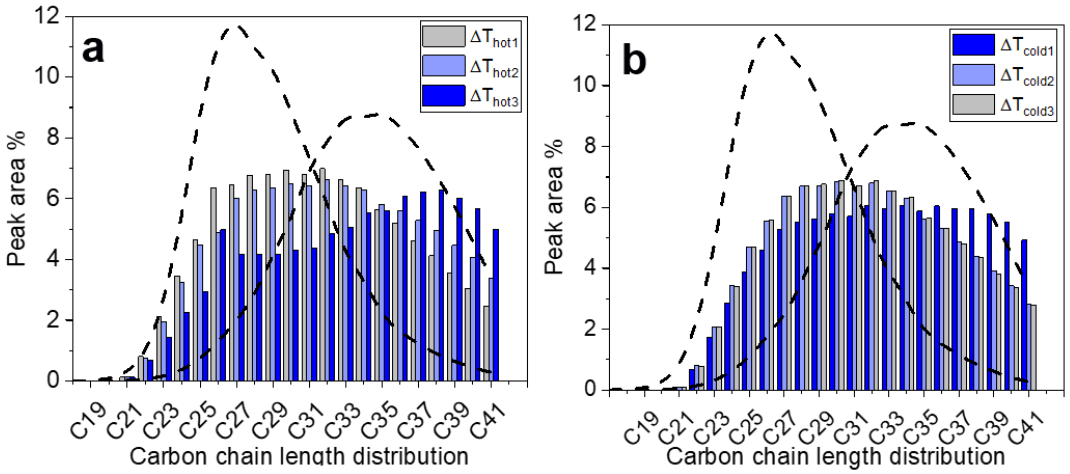

Figure 4.14. Carbon chain length distribution of deposited wax as a function of **a)** ΔT_{hot} **b)** ΔT_{cold}.

Figure 4.14a shows the effect of increasing ΔT_{hot} on the chemical composition of the deposit wax. While increasing ΔT_{hot}, a large shift towards the HMW wax is observed. With ΔT_{hot1} nearly at the WAT (a negligible difference of 0.5 ^{o}C), all the wax carbon chain length crystallizes at the deposit-oil interface leading to a deposit chemical composition similar to the initial wax composition used in the model solution. With increasing ΔT_{hot} to a large extent (ΔT_{hot3}= 21 ^{o}C), the LMW wax are readily soluble and hardly crystallize in the wax deposit. This effect leads to a wax deposit with large amount of HMW wax.

Figure 4.14b shows the effect of increasing ΔT_{cold} and study the effect of coolant temperature on the wax deposit chemical composition. Results show that a shift towards the HMW wax is achieved with a decrease in ΔT_{cold}. The increase in the coolant temperature with respect to the WAT increases the dissolving ability of wax molecules and the amount of LMW wax molecules dissolved around the cold surface increases. This leads to a wax deposit with low percent of LMW wax.

A comparison between the effect of ΔT_{hot} and ΔT_{cold} on the wax deposit chemical composition shows that clearly the change is more significant with an increase in T_{hot}. Taking the same magnitude of ΔT (ΔT_{hot3} = 21 ^{o}C and ΔT_{cold2} = 22 ^{o}C) and comparing their effect on the carbon chain length of the wax deposit, one can see that for ΔT_{cold2} = 22 ^{o}C, the carbon chain length distribution is still within the average distribution of the initial wax. However, with ΔT_{hot3} = 21 ^{o}C, there is a great shift in the chemical composition of the wax deposit towards HMW wax. If this is related back to the temperature characterisation of the CRF, this trend can be justified by the fact that the change in T_{hot} induces a higher effect on $T_{surface}$ than the change in T_{cold} does on T_{oil} mainly due to the large volume of the bulk oil with the relatively small surface area of the CRF.

Fixing ΔT_{hot} and ΔT_{cold} to study the effect of RPM on mass gain: Figure 4.15a showed the results for the change in the mass deposit as a function of the RPM with a nearly constant ΔT_{hot} and ΔT_{cold}. With a constant ΔT_{hot} and ΔT_{cold}, the factors of T_{hot}, T_{cold} and wax wt% are constants making therefore the comparison as a function of RPM more reliable. The mass deposit decreases with an increase in the RPM, which is a trend already widely observed in the literature. This decrease is generally attributed to the change in the heat and mass transfer in the system or to sloughing. A more comprehensive test is presented later in the chapter to discuss this result (cf. **4.6.5.**)

Table 4-12. Taguchi matrix rearranged by an increasing RPM of the CRF.

RPM	ΔT_{cold} (°C)	ΔT_{hot} (°C)	Mass deposit (g)	Run
0	10.5	29.5	3.3	7
50	11	29	2.7	2
100	13	32	1.7	3

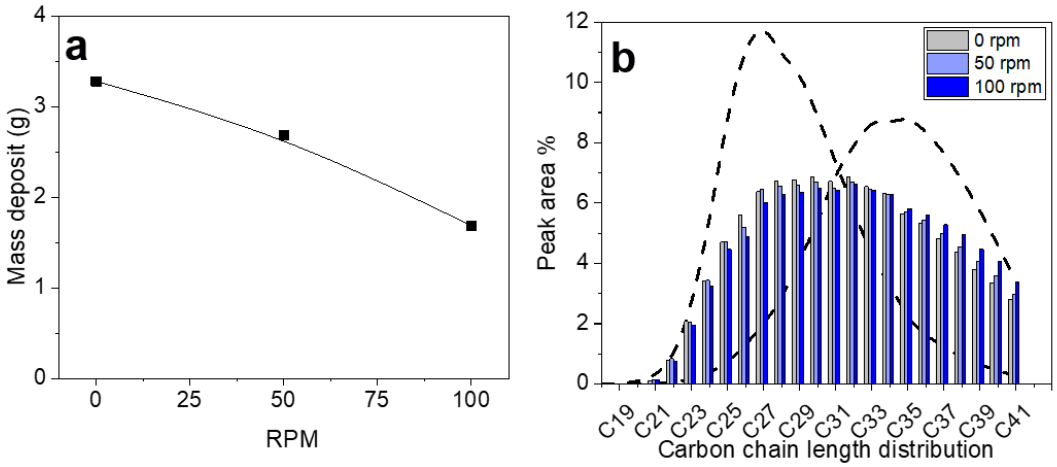

Figure 4.15. a) The change in deposit mass as a function of the CRF RPM, **b)** carbon chain length distribution of deposited wax as a function of RPM.

While an interesting trend is observed for the mass deposit with the change in RPM, the chemical composition of the wax deposit seems to stay within the average range of the initial wax used with a slight shift towards the HMW with increasing RPM to 100 rpm. However, this shift is still within the error and not considered significant. Increasing the RPM up to 100 rpm doesn't seem to change the chemical composition of the wax deposit, although the temperature characterisation of the CRF still suggest a great change in the temperature profile in the system with increasing RPM up to 100 rpm. Further systematic investigations on the effect of RPM on the chemical composition is needed in order to make a clear analysis.

As Taguchi was a qualitative tool for a preliminary assessment of wax deposition, further robust and reliable experiments were needed to study the effect of temperature and RPM on wax deposition.

4.6.4 Systematic study to confirm the effect of ΔT_{cold} and ΔT_{hot} on wax deposition at static condition

Results from Taguchi suggest that the effect of T_{cold} and T_{hot} on wax deposition should be seen relatively to the WAT of the wax solution and the magnitude of ΔT_{hot} and ΔT_{cold}. An increase in ΔT_{cold} and a decrease in ΔT_{hot} induce higher wax deposition. One can make the hypothesis then that, at a fixed ΔT_{cold} and ΔT_{hot}, wax deposits at the same rate and magnitude regardless the set T_{cold} and T_{hot} and the wax wt%. To verify this hypothesis, an experiment was conducted on the CRF, where for two wax wt% (9 and 13 wt%), deposition experiments were conducted at the same ΔT_{cold} and ΔT_{hot}. **Figure 4.16**b shows that for 13 wt% (WAT= 39.6 ^oC), operating at T_{cold} = 5 ^oC and T_{hot} = 45 ^oC result in ΔT_{cold} = 34.6 ^oC and ΔT_{hot} = 5.4 ^oC. To compare with 9 wt% (WAT= 36.6 ^oC), operating at the same temperatures T_{cold} = 5 ^oC and T_{hot} = 45 ^oC doesn't lead to the same magnitude of ΔT_{cold} = 31.6 ^oC and ΔT_{hot} = 8.4 ^oC. To do so, 9 wt% wax solution experiment is performed at same ΔT_{cold} and ΔT_{hot} as 13 wt% with different operating temperatures (T_{cold} = 2 ^oC and T_{hot} = 42 ^oC).

To sum up, three experiments were performed as following:

Experiment A: 13 wt%, T_{cold} = 5 ^oC and T_{hot} = 45 ^oC (ΔT_{cold} = 34.6 ^oC and ΔT_{hot} = 5.4 ^oC).

Experiment B: 9 wt%, T_{cold} = 5 ^oC and T_{hot} = 45 ^oC (ΔT_{cold} = 31.6 ^oC and ΔT_{hot} = 8.4 ^oC).

Experiment C: 9 wt%, T_{cold} = 2 ^oC and T_{hot} = 42 ^oC (ΔT_{cold} = 34.6 ^oC and ΔT_{hot} = 5.4 ^oC).

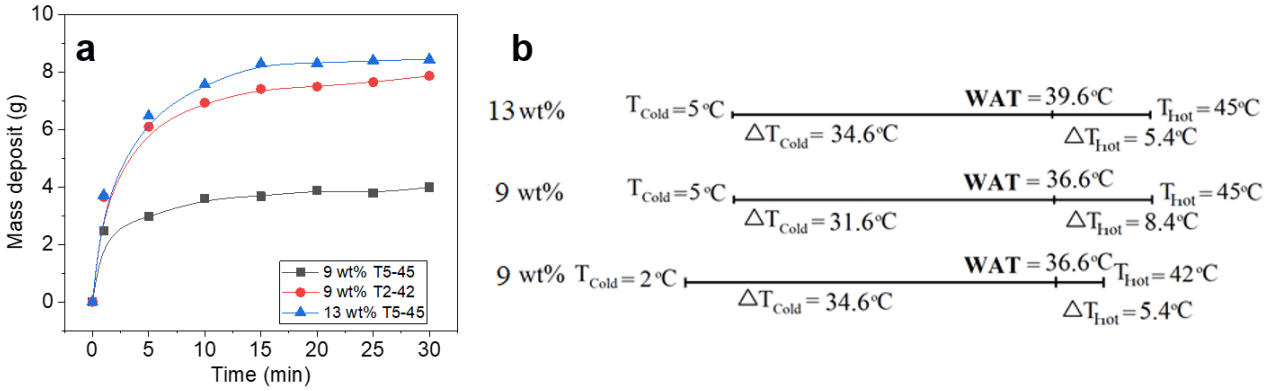

Figure 4.16. a) Time-dependent wax deposition for 9 and 13 wt% wax-in-dodecane at T_{cold} = 5 °C and T_{hot} = 45 °C at 0 rpm. Also included is 9 wt% wax-in-dodecane at T_{cold} = 2.4 °C and T_{hot} = 42.4 °C. While $\Delta T_{hot\text{-}cold}$ is constant, reducing T_{cold} to account for the lower WAT at 9 wt% compared to 13 wt% wax results in a similar deposition profile, **b)** schematic of ΔT_{hot} and ΔT_{cold} corresponding to the abovementioned deposition experiments.

Figure 4.16a shows the time-dependent mass deposit of the 3 experiments. Results show that the mass deposit of experiment A and B (9 and 13 wt% wax-in-dodecane at the same operating temperatures (T_{cold} = 5 °C and T_{hot} = 45 °C)) give a large difference in the deposit mass, with an increase of 70% for 13 wt% at steady state. This large increase in the mass is usually attributed to the higher concentration of wax in the 13 wt% wax solution and therefore a higher availability of wax molecules to deposit. However, results of experiment C show a very close mass deposit to experiment A while operating with a 9 wt% wax instead of 13 wt%. Experiment C shows that the amount of wax available has less impact on wax deposition when compared to the magnitude of ΔT_{cold} and ΔT_{hot}. Operating at the same wax concentration with a lower cold temperature with respect to the WAT allow more wax to crystallise on the surface of the CRF and need larger thickness for the $T_{interface}$ to reach the WAT. Operating at higher T_{hot} with respect to the WAT increases the solubility of the wax in solution.

4.6.5 Kinetic and Dynamic Studies of Wax deposition

Further experiments were performed to study the kinetic of the wax deposition under varying RPM. For : 9 wt% alkane wax-in-dodecane, T_c = 5°C and T_h = 45°C and rotational speeds of 0, 100, 200 and 500 rpm, wax deposits were collected at 1, 3, 5, 10, 15, 20, 25 and 30 min to study the kinetics of deposition. Dynamic conditions at 0, 25, 50, 100, 150, 200, 250, 300 and 500 rpm were compared at 30 min.

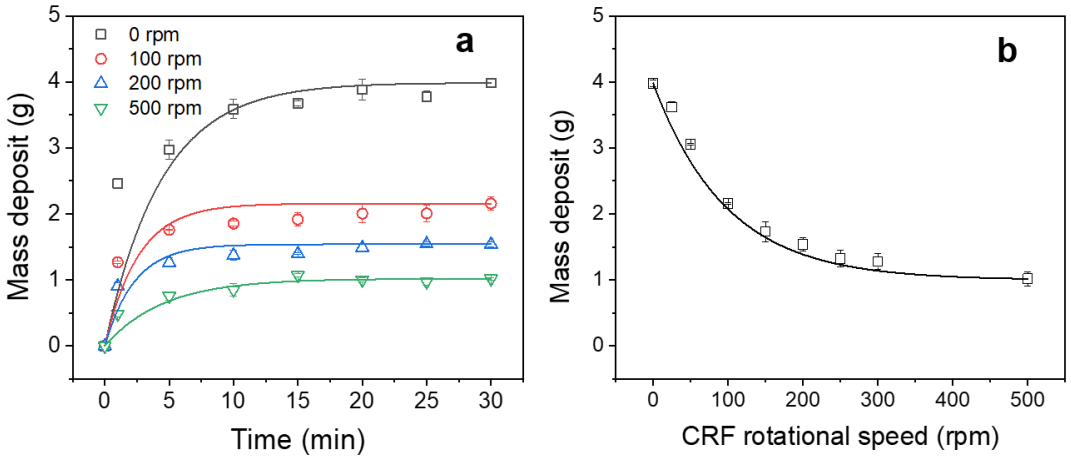

Figure 4.17. a) Time-dependent wax deposition as a function of CRF rotational speed. Experimental conditions: 9 wt% alkane wax-in-dodecane, T_c = 5°C and T_h = 45°C. Lines are to guide the eye and takes the form, $y = y_0 + Ae^{(R_o x)}$. **b)** Mass of wax deposited at 30 min as a function of the CRF rotational speed. Experimental conditions: 9 wt% alkane wax-in-dodecane, T_{cold} = 5°C and T_{hot} = 45°C. Lines are to guide the eye and takes the form, $y = y_0 + Ae^{-R_o x}$. Values of the constants are in **Table 4-13**.

Table 4-13. Values of the fitting curves constants of **Figure 4.17**.

	Fig 4.17a				Fig 4.17b
Constants	**0 rpm**	**100 rpm**	**200 rpm**	**500 rpm**	
y_o	3.99	2.16	1.54	1.02	0.99
A	-3.99	2.16	-1.54	-1.02	2.98
R_o	-0.23	-0.38	-0.43	-0.22	-0.01

4.6.5.1 Wax Deposition Kinetics at Different CRF Rotational Speeds

Figure 4.17a shows the wax deposit mass as a function of time and at rotational speeds of 0, 100, 200 and 500 rpm. For all tests, > 50% of the deposited wax (of the mass deposit at 30 min) occurred within 1 min. The initial rate of wax deposition is rapid and can be approximated by a linear rate. Due to the experimental method, data at t < 1 min could not be attained with good reproducibility. At t > 1 min the wax deposit rate is non-linear, and the deposited mass approaches a steady-state value at t = 30 min. Between t = 5 min and 30 min, the deposited mass increased by ~25%, ~18%, ~19% and ~25% for 0, 100, 200 and 500 rpm, respectively. Under static condition (0 rpm), the wax deposited at 24 h (4.9 g) confirmed the wax deposit continue to grow, although at negligible rates.

The wax deposition rate is attributed to the change in temperature at the wax deposit-oil interface. Based on the molecular diffusion mechanism, wax deposition depends on radial diffusion of wax molecules from the bulk fluid to the wax deposit-oil interface. Radial diffusion is induced by a temperature difference between the bulk oil (T > WAT) and the wax deposit-oil interface (T < WAT). While the temperature difference is initially high (reflecting the rapid increase in wax deposit), the temperature difference decreases with more wax deposited,

thermally insulating the cold surface to the point when the temperature at the wax deposit-oil interface is equal to WAT and further wax deposition cease[123]. Alternatively, wax deposition can cease if the wax in the bulk fluid is depleted. Based on the 9 wt% wax-in-dodecane, the initial mass of wax in solution is 22.5 g. For 0 rpm, the mass deposited at 30 min was 3.9 g, thus 83% of the initial wax content remains in solution and wax depletion cannot be attributed to the decrease in wax deposition rate.

4.6.5.2 Wax Deposition Dynamics

Figure 4.17b compares the wax deposit mass at 30 min as a function of the CRF rotational speed between 0 and 500 rpm (the shear rate at 500 rpm is 750 s^{-1} based on a fluid viscosity of 0.00119 Pa.s, 9 wt% alkane wax-in-dodecane at 45°C). The wax deposit mass decreases with increasing rotational speed, possibly attaining a minimum mass deposit at higher rotational speeds (where the mass deposit is independent of rotational speed), although higher rotational speeds have not yet been considered.

A decrease in wax deposit with increasing fluid flow is commonly observed and the reduction in deposit mass is found at all flow conditions. The reduction in mass deposit is often considered to result from a decrease in the thermal gradient between the fluid and cold surface in flow and/or the effect of fluid shear stress on the wax deposit that removes wax[11, 47, 62].

4.6.5.2.1 Heat Transfer Effect

An increase in rotational speed increases the heat transfer between the hot fluid and cold surface, reducing the temperature difference between the hot and the cold temperatures. In the CRF, the temperature of n-dodecane in the absence and presence of 9 wt% alkane wax was measured at different rotational speeds. With T_{cold} = 5°C and T_{hot} = 45°C (initial condition

before CRF is submerged in the test fluid), 3 thermocouples positioned at the top, centre and bottom and at a radial distance of 10 mm from the cylindrical test sample, confirmed a reduction in fluid temperature with increasing rotational speed. For 0 rpm, T_{oil} decreased to ~40°C (~10 min to attain steady-state values) and ~43.5°C (~10 min) in the absence and presence of wax. At 100 rpm, T_{oil} decreased to ~36°C (~8 min, no wax) and ~42.5°C (~3 min, wax) and at 700 rpm, T_{oil} decreased to ~34°C (~5 min, no wax) and ~ 42°C (~1 min, wax). The decrease in the oil temperature induce a decrease in the thermal gradient temperature between the hot and cold temperatures reducing the wax deposit.

The change in heat transfer due to the rotational speed is not linear, with a significant reduction between 0 and 100 rpm and then an almost independence at ≥ 500 rpm. At rpm ≥ 500, the decrease in wax deposit mass is not due heat transfer (since T_{oil} and $T_{surface}$ are less independent of rpm) and may indicate that the further reduction in wax deposit mass at 500 rpm compared to 300 rpm likely results from another factor.

4.6.5.2.2 Shear Removal

Shear removal describes either the retardation of continuous wax deposition (wax molecules adhere less on the wax deposit) or sloughing (the removal of wax from the wax deposit). Sloughing is thought to occur when the fluid shear stress exceeds the wax yield stress causing deformation of the wax layer and ablation of wax from the deposited layer.

For the CRF, sloughing as a function of rotational speed was studied on wax deposits formed under static conditions for 30 min (the wax deposits were thick and retained ~85 vol% solvent). After wax deposition, the CRF was submerged in pure n-dodecane (no wax dissolved) and the wax deposit rotated at 100, 200, 300 and 500 rpm for 10 min. To minimize dissolution of wax

T_{oil} was set to 32°C (below the WAT). GC-FID analysis of the n-dodecane after the CRF was submerged in pure dodecane for 30 min (no rotation) revealed only trace amounts of C20-C25, and therefore the contribution of dissolution to changing wax deposit mass is considered negligible.

Figure 4.18 shows the wax deposit after rotating the cylindrical test sample for 10 min at increasing rotational speeds. While the wax deposit at 100 rpm shows slight deformation of the deposit (following the standard protocol), the wax deposit mass was within ~95% of the static wax deposit, hence no measurable mass loss. With increasing rotational speed, the wax deposit is visually deformed, and undulations were observed throughout the wax deposit at 500 rpm, with the mass loss increasing by ~15%, ~20% and ~30% for 200, 300 and 500 rpm, respectively.

While these results confirm the potential of sloughing, it should be noted that these measurements were all conducted on wax deposits formed at 0 rpm. It is not clear if sloughing is a contributing factor when depositing at higher rotational speeds. While the wax deposit layer is thinner at higher rotational speeds.

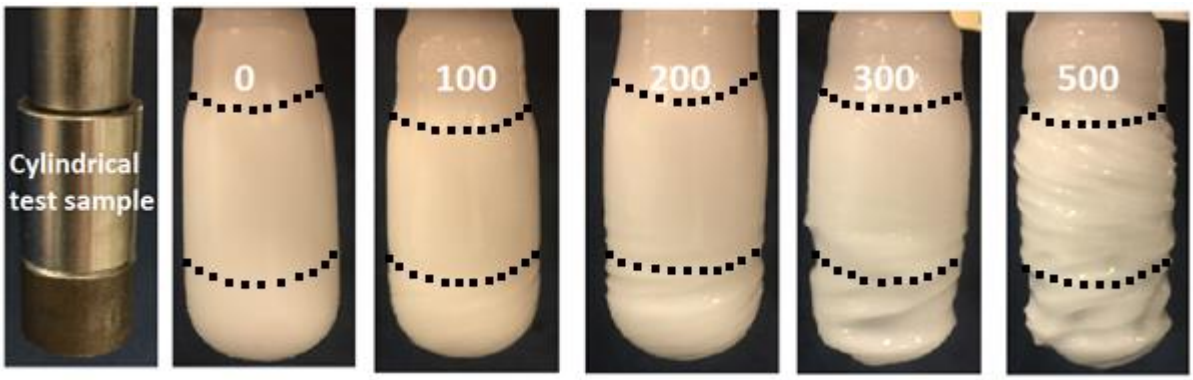

Figure 4.18. 9 wt% alkane wax-in-dodecane deposited on the CRF at 0 rpm for 30 min. With the wax deposit formed, the sample is transferred to pure dodecane and rotated at 100, 200, 300 and 500 rpm for 10 min.

4.6.5.3 Wax Deposit Structure

Cryo-SEM images of wax deposits formed under static (0 rpm) and dynamic (200 rpm) conditions are shown in **Figure 4.19**. For static deposition (**Figure 4.19**a), the wax deposit reveals an arrangement of thin sheets of alkane stacked together in parallel multi-layers with space in between where the solvent is occluded in the deposit. The layer can be described as a semi-solid (composite of alkane wax and oil), with stepped morphology of wax layers that result in ridges throughout the wax deposit. At 200 rpm, the stepped morphology of wax layers is less visible with negligible porosity throughout the wax layer (based on the uniformity of the wax layer), indicating a denser wax deposit. In the absence of shear, alkane crystallizes in layers which consist of wax molecules having planar zigzag conformations, and this results in the stepped morphology. In shear, wax crystals are found to be smaller and have a tendency to aggregate, which in the bulk fluid can lead to stronger networks [180, 181]. In **Figure 4.19**b the wax deposit is visibly different to that formed under static condition and shows reduced stepped morphology. The different morphology may be influenced by the fluid shear during wax deposition and formation (rearrangement of wax crystals), and/or densification of the wax deposit layer through continued shear.

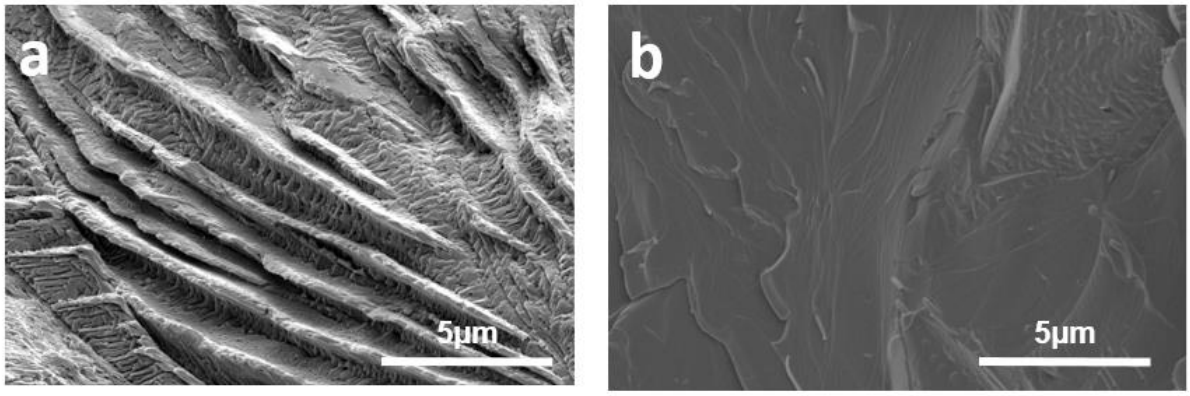

Figure 4.19. Cryo-SEM images of wax deposits formed after 30 min under **a)** 0 rpm and **b)** 200 rpm.

4.6.5.4 Wax Deposit Chemical Composition

The analysis of the chemical composition of the wax deposit at different rotational speeds in a systematic experimental procedure fixing all the operating conditions and varying only the rotational speed is presented in **Figure 4.20**. **Figure 4.20**a, b, c and d shows the kinetic change in the chemical composition of 0, 100, 200 and 500 rpm at times 1, 15 and 30 min, while **Figure 4.21** shows the chemical composition of the wax deposit at steady state (30 min) for the range of RPM as previously.

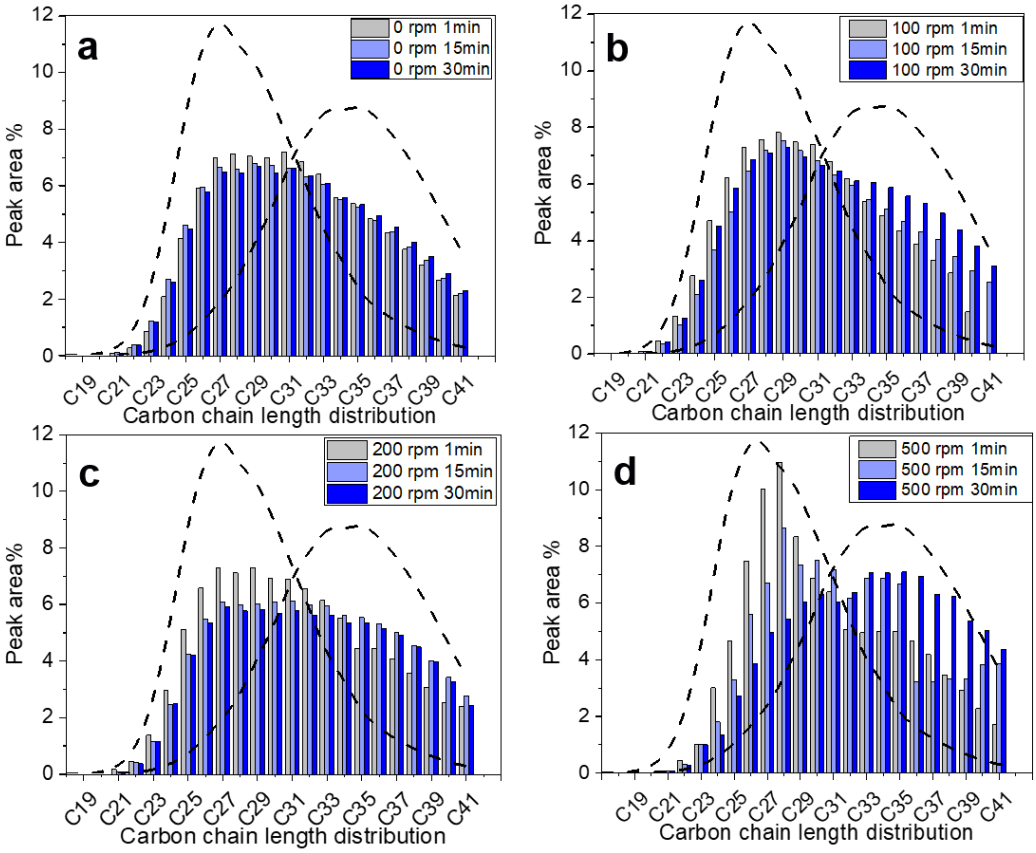

Figure 4.20. The carbon chain length distribution of deposited wax as a function of time at **a)** 0 rpm **b)** 100 rpm **c)** 200 rpm **d)** 500 rpm. Comparison of carbon chain length distributions as a function of RPM at 30 min. Wax content 9 wt%.

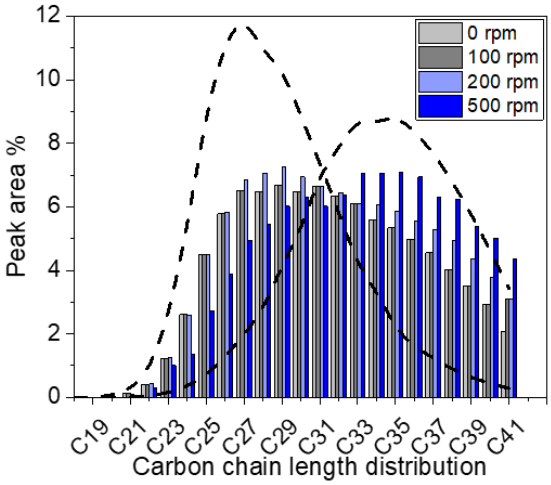

Figure 4.21. Comparison of carbon chain length distributions as a function of RPM at 30 min. Wax content 9 wt%.

Figure 4.20 shows that at time 1 min, the chemical composition of the all the wax deposits fall within the average of the initial wax used in the model solution, however, only at 500 rpm the carbon chain length falls within the LMW wax. At late time of 15 min and up to the steady state at 30 min, the chemical composition starts to shift gradually to HMW wax, this shift is negligible at 0 rpm, more prevalent at 100 rpm and very significant at 200 and 500 rpm. The description of the carbon chain length distribution with the rotational speed allow us to define three regimes for the change of the chemical composition with time and RPM. A first regime (0 rpm), where the carbon chain length stays within the average composition with time, a second regime (100 and 200 rpm), where the wax deposit is within the average composition at early stages of wax deposition, then start to shift to the HMW wax with a critical time, accelerated by the increase in the RPM (30 min for 100 rpm and 15 min for 200 rpm) and a third regime where the wax composition falls within the LMW wax at early times then shift towards the HMW wax later on. In the first regime, all the wax carbon chain lengths are able to crystallise as long as the temperature at the interface is below the WAT. As the rotational speed increases, the deposition starts to be preferential to HMW after a critical time. Probably, at early stage of the deposition, the temperature of the CRF is relatively low, allowing all the wax to crystallise but also exhibiting a high van der Waals force between the wax molecules. As the wax build up, the temperature at the interface deposit-oil increases and the LMW having low van der Waals forces are less likely to adhere to the wax deposit. Besides, aging, which is the counter diffusion of the oil and the wax molecules within the wax deposit, is enhanced by the rotational speed, allowing the oil to be squeezed out of the wax bed taking out some soluble LMW wax with it. In the third regime however, there is a different trend of preferential adherence of LMW wax at time 1 min and a preferential adherence of the HMW at time 30 minutes. While the shift towards HMW with time can be explained by the aging process, and

most probably the drag forces engendered by the rotational speed preventing the LMW wax to deposit due to their weak interaction with similar molecules, the preferential deposition of the LMW wax at time 1 min is exceptional. Most probably, the LMW wax molecules are more easily pushed towards the inner cylinder by advection due to their small size and the high intensity of the rotational speed. At time 1 min when the temperature of the CRF is low enough for them to adhere to the cold wall, they will be predominant in the wax bed due to their relatively high concentration at the vicinity of the CRF. With the temperature at the deposit-oil interface increases, the LMW wax find it hard to adhere to the deposit at high wall shear stress.

The change in the chemical composition with rotational speed was further investigated with an experiment that aims mainly to check whether the shift towards the HMW wax with rotational speed is due to the depletion (lower availability) of the LMW wax after 15 min of wax deposition or to the change in the temperature profile in the system that leads to a higher solubility or low adhesion force of LMW wax. To do so, an experiment was conducted consisting of depositing wax using a solution of 9 wt% wax-in-dodecane at 250 rpm for 20 min while the CRF is half-immersed in the wax-in-dodecane solution. After 20 min, the full CRF was then immersed in the solution for a further 10 min at same operating conditions. The chemical composition of the lower and upper halves of the CRF were compared.

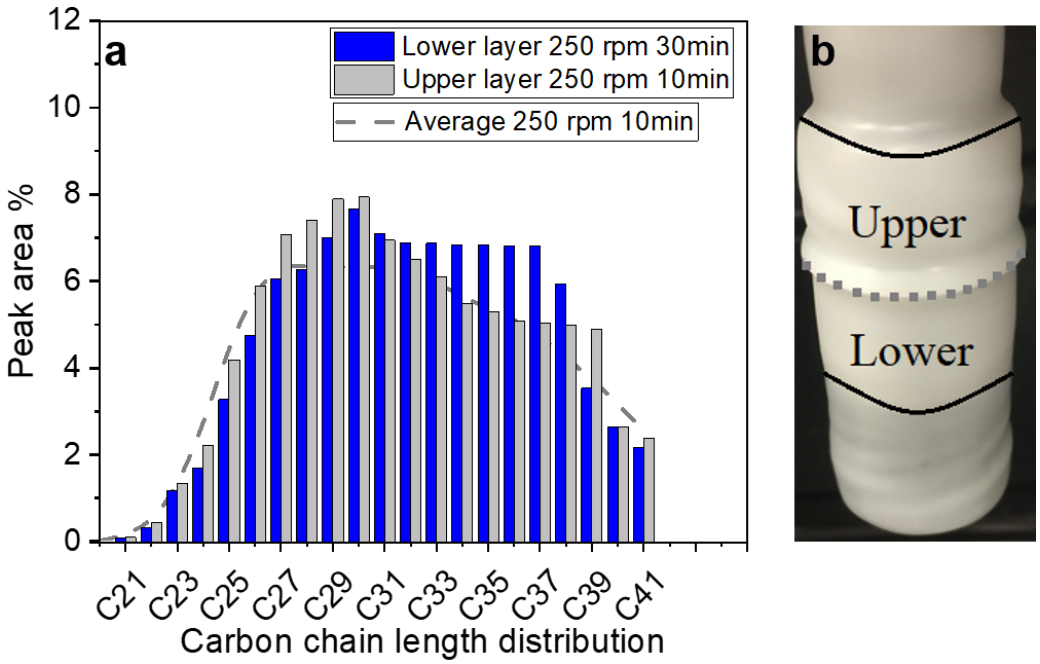

Figure 4.22. a) The carbon chain length distribution of the lower and upper layers of the deposited wax. A comparison, in dash line, is made to the average chain length distribution of deposit wax layer at 10 min 250 rpm, **b)** a picture of the lower and the upper layers.

The chemical composition of the lower half of the CRF was expected to be the same as the standard chemical composition of a wax deposit at the same operating conditions. However, after 20 min, if the LMW wax deplete, when immersing the full CRF, the chemical composition of the new wax deposit would be also shifted towards the HMW. **Figure 4.22**b shows a picture of the CRF after the experiment. The black solid lines delimitate the CRF deposition sample and the dash grey line in the middle shows the limit between the half immersed initially and the half immersed after 20 min. Using a scalpel, a wax layer was taken from the upper black line to the dash line for the analysis of the upper part of the wax deposit and a wax layer from the dash line to the bottom black line was taken for the analysis of the composition of the lower part of the wax deposit. **Figure 4.22**a shows the carbon chain length distribution of the upper and lower layers compared to a standard chemical composition of a wax deposit at 250 rpm,

10 min at the same operating conditions as the suggested experiment. Results in **Figure 4.22**a shows that for the lower part of the CRF, a shift towards the HMW is observed and this is in harmony with the results previously obtained while increasing the rotational speed of the CRF. The upper layer, instead of exhibiting the same composition as the lower layer, shows a composition that is within the standard composition of a wax deposit at 250 rpm at 10 min with the same operating conditions. This result suggests that the shift towards HMW after a critical time (15 min in our operating conditions) is not due to the depletion of LMW wax but to the increase in the temperature at deposit-oil interface leading to a higher solubility wax or lower van der Walls attraction forces of the LMW to the deposit.

Further investigation on the effect of forced convection induced by the rotational speed on wax deposition was conducted. The experiment aims to investigate the aim of the rotational speed on the final deposit mass and thickness. As shown previously, a clearly lower mass deposit and smaller wax deposit thickness deposits at higher rotational speed. One can assume then that, while rotating, the $T_{interface}$ reach the WAT (Steady state) at smaller wax thickness. One can suggest then that the wax composition at higher rotational speed has a higher insulation effect due to the change in the composition of the wax deposit with RPM. Or, that the temperature in the system is changing with the rotational speed and leading to a less driving for wax deposition. An experiment was then suggested to be performed to further emphasis the effect of rotational speed on wax deposition. The experiment consists of performing a wax deposition with 9 wt% of wax-in-dodecane at 200 rpm for 30 min (T_{cold} = 5 ^{o}C and T_{hot}= 45 ^{o}C), then stop rotation while the CRF is still immersed in the wax solution and allow deposition at the same operating conditions for another 15 min, then measure the wax deposit mass at the end of the experiment (after 45 min). The experiment was chosen to be performed at 200 rpm because previous investigations suggest that there is no sloughing at this rotational speed. 30

min was chosen because it is the time needed for the system to reach steady state and the rate of wax deposition is very low after. Therefore, when the rotation stops, any major change to the deposit mass is solely due to the changing in the hydrodynamics in the system. The temperature of the bulk was monitored as well all along the experiment.

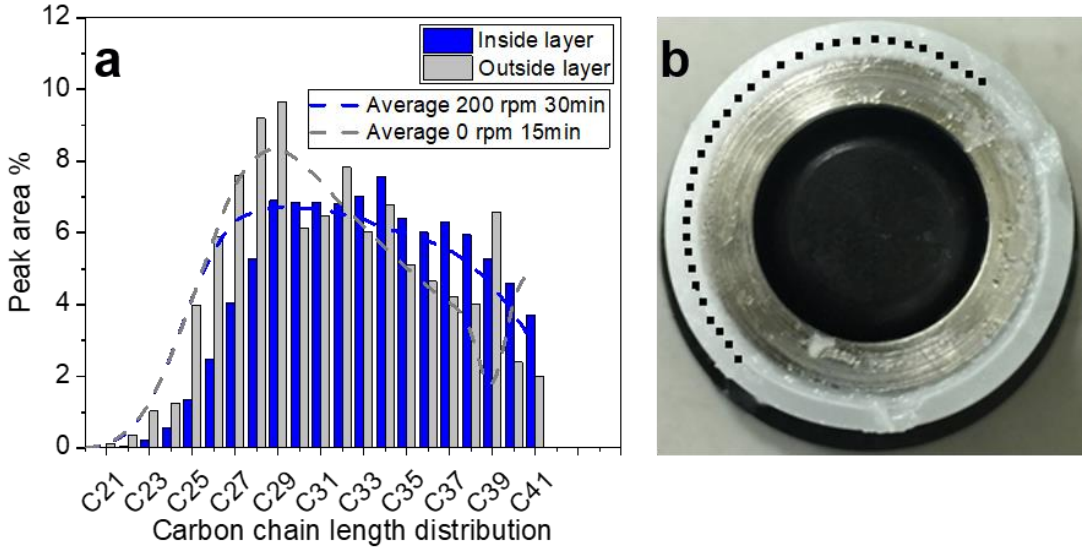

Figure 4.23. a) The carbon chain length distribution of the inside and outside of the deposited wax layers as described in **Figure 4.21** and compared to the carbon chain length distributions of a deposit wax at 200 rpm, 30 min and 0 rpm 15 min, **b)** a picture of the wax deposit with dash line separating the inside and outside layers.

Results shows that the wax deposit at 200 rpm reach a mass gain of ~ 1.5 g after 30 min and when the rotation stops, a rapid wax crystallisation build up on the deposit interface leads to a final mass of 4.8 g after 15 min. **Figure 4.23**b shows clearly the boundaries between the wax deposit formed at 200 rpm and the further build-up at 0 rpm. Besides, the temperature in the bulk solution shows a decrease with rotational speeds to 42 ^{o}C at 200 rpm and then a rapid increase in the bulk oil was observed after stopping the rotational speed to 44 ^{o}C. This

experiment suggests that the change in the temperature profile with rotational speed is the main driving force for less deposition at low rotational speeds.

A characterisation of the deposit composition by GC-FID was performed as well. At the end the experiment, a scalpel was used to carefully cut a layer of the wax deposit formed at 0 rpm from the "outside layer" first; the layer was cut to be the farther possible from the edge between the two depositions and afterwards, the scalpel was used to remove any wax deposited at 0 rpm and reach the inside layer deposited at 200 rpm to take another sample for analysis. As stated before, the sample is taken in a longitudinal way to cover the whole deposit sample from the top to the bottom. **Figure 4.23**a shows the carbon chain length distribution of inside and outside layers and their comparison with the carbon chain length distribution of a wax deposit formed at the same operating conditions: dashed black line for a wax deposit formed at 200 rpm, 30 min and the dashed grey line for a wax deposit formed at 0 rpm, 15 min. Results in **Figure 4.23**a show that the composition of the wax deposit formed at 200 rpm, followed by deposition at 0 rpm exhibit a similar trend of similar deposition experiments performed previously. At 200 rpm, the shift towards the HMW wax is therefore again proved to not be due to the depletion of the LMW but to the change in the temperature profile in the system that makes the LMW wax more soluble and less adhesive at higher rotational speeds.

4.7 Conclusions

A novel Cold Rotating Finger representing a Couette flow has been developed to study wax deposition. The CRF displays innovative success, which stems from its ability to provide fairly controlled flow conditions and heat transfer profiles, all along with rapid and economic screening of different parameters affecting wax deposition. The design is validated through preliminary testing using a screening and optimization method called Taguchi. The

experimental matrix has demonstrated rig functionality to study the main factors affecting wax deposition: wax wt%, RPM, T_{hot} and T_{cold}. Taguchi showed some general trends with good agreement with the mechanism of wax deposition and with the literature, however, more systematic experiments were needed and both kinetic and dynamic studies at well-defined operating conditions were considered then. The kinetic study showed an initial high deposition rate (within 1 min) followed by a secondary slower deposition rate as the wax deposits approached steady-state values (~30 min). Wax deposition kinetics are shown to be governed by the temperature gradient between the bulk fluid and the wax-oil interface. Initially, the temperature gradient is large and promotes a high deposition rate of wax. As the wax deposit thickness increases the temperature gradient decreases and this results from the increased thermal resistance of the wax deposit layer. The wax deposit approaches a steady-state value (deposit mass) as the wax-oil interface temperature approaches the WAT. Dynamic studies showed a decrease in the wax deposit mass with increasing rotational speed of the CRF. While the reduction in mass can be attributed to a heat transfer and/or shear removal effect, in the current study, the reduction in wax deposit mass is attributed to a predominantly heat transfer effect. Increasing the rotational speed decreases T_{oil} and therefore decreases the thermal gradient between the hot and cold temperatures, thus decreasing the thermal diffusivity of wax molecules. While this phenomenon describes behaviour at low rotational speeds, at 500 rpm the fluid shear was shown to strongly deform and decrease the deposit mass of a wax layer formed at 0 rpm. This introduces the possibility of shear removal (sloughing) at higher RPM. The analysis of the chemical composition of the wax deposit at different rotational speeds shows the kinetic change in the chemical composition While initially, at time 1 min, the chemical composition of all the wax deposits fall within the average of the initial wax used in the model solution, with time progressing, the chemical composition shift towards HMW with increasing rotational speed. This behaviour may be attributed to an enhanced aging process due

to the wall shear stress or a preferential wax deposition of the HMW wax due to their high intermolecular interactions at high temperatures. Deposit at 500 rpm shows a different trend though, bouncing between a composition falling within the LMW wax carbon chain length at time 1 min and a composition within the HMW wax carbon chain length at steady state. This great change in the composition is attributed to the co-existence of two effects: the advection due to high drag forces enhancing the diffusion of LMW wax to the deposition wall initially and the wall shear stress overcoming the adhesion forces of the LMW wax and stripping them off with the increase of the deposit-oil interface temperature.

Chapter 5 Wax Deposition using a Cold Rotating Finger: An Empirical and Theoretical Assessment in Thermally Driven and Sloughing Regimes

5.1 Synopsis

Time-dependent wax deposition on a rotating stainless-steel surface was studied using a newly-built laboratory-scale Cold Rotating Finger (CRF). The CRF includes a chilled (T_{cold} = 5°C) rotating inner cylinder and a jacketed beaker to heat the oil phase (T_{hot} = 45°C). Wax deposition rates and pseudo-steady state deposit mass values were shown to depend on the CRF rotational speed. Relative to the static test (0 rpm), the wax deposit mass decreased with increasing rotational speed, reducing by 54% at 100 rpm and 82% at 700 rpm. At low rotational speeds, the reduction in deposited wax corresponded to changes in the bulk oil (T_o) and wax interface (T_i) temperatures with increasing CRF rotational speed. Such behavior was well described by a diffusive model to account for the fluid motion in the CRF. The model described the temperature profile in the boundary layer by considering the heat transfer coefficient as a function of the CRF rotational speed, with heat transfer governing wax deposition. Mass transfer was described by Fick's law assuming a linear solubility with temperature, and constant diffusivity determined from experimental data at the reference CRF rotational speed of 100 rpm. The change in heat transfer governed the mass deposited, with wax deposition at low rotational speeds described by a thermally-driven process. At higher rotational speeds, T_o was independent of CRF rotation, although the wax deposit mass continued to decrease. Visual assessment of the CRF test revealed sloughing at CRF rotational speeds of ≥ 400 rpm. For high CRF rotational speeds the molecular diffusion model could not accurately describe the wax deposit mass and was modified to include a sloughing term, $\dot{S}(t)$,

described in terms of the wall shear stress, deposit radius and θ, which was taken to be an adjustable parameter to describe the sloughing intensity.

5.2 Introduction

Crude oil is a complex mixture of saturates, aromatics, resins and asphaltenes. Waxes in crude oil are particularly problematic due to their solubility decreasing as the crude oil cools[114]. At temperatures below the wax appearance temperature (WAT), and dependent on surface properties and fluid mechanics, wax deposits can restrict flow and eventually plug a pipeline[11, 114].

Researchers often consider the effect of a temperature gradient on wax deposition[46, 48, 60, 64-67, 72], yet few studies consider the effect of flow on wax deposition rates and wax deposit properties, see **Table 5-1** for a summary of published data. With few published pipeline tests, due to challenges in construction, operation and an inability to rapidly test samples, the static cold finger method has been ubiquitously adopted as a standard test method, consequently, the effects of flow are rarely considered.

Most flow studies show the wax deposit mass decreases with increasing flow rate, attributing mass reduction to the effects of sloughing (physical removal of wax), or densification of the wax deposit as oil is squeezed from the deposit when sheared[46, 48, 124]. Mehrotra and co-workers[71, 110, 182] studied wax deposition in flow and concluded that wax deposition is primarily thermally driven in both laminar and turbulent flows. The steady state deposit-layer thickness (or mass) corresponded to the thermal driving force and thermal resistance of the liquid phase and deposit layer. Lu et al. observed reduced deposit thickness

with increasing flow rate and considered the effects of heat and mass transfer with deposition time[47]. In the presence of flow, the boundary layer thickness decreased (with increasing fluid shear) and the wax deposit interface temperature increased. While the reduced boundary layer thickness led to a higher radial concentration gradient, and increased mass flux, the increased flow rate also led to higher wax interface temperature due to an increased thermal load, with the latter reducing mass transfer.

Molecular diffusion is often considered the dominant mechanism responsible for wax deposition[11, 38, 114], describing wax molecules diffusing towards a cold surface. A radial concentration gradient of dissolved wax molecules exists before the system attains steady state, when the temperature of the wax deposit interface equals the WAT[11, 38]. Several studies have developed mathematical models, solving for both heat and mass transfer, to describe wax deposition based on molecular diffusion theory[11, 13, 19, 38, 111, 114]. However, studying wax deposition under a zero or slightly negative thermal gradient (bulk oil temperature equal or lower than the coolant temperature), Yang et al. measured wax deposits on the pipe invert in flow[183]. The authors attributed the wax deposition to an accumulation of precipitated wax particles which deposit on the pipe invert and form a yield strength deposit when the yield stress exceeds the local fluid shear stress. The authors comment that molecular diffusion alone cannot fully describe the observed behavior.

Singh et al. developed a comprehensive model to predict wax deposition and deposit thickness in laminar flow[114]. Good agreement between experiments and the model were found when heat and mass transfer correlations were independent of one another. Such an approach was only valid for laminar flow and assumed the wax concentration gradient to be maximum in the boundary layer. The approach of independent heat and mass transfer correlations (also

known as the ‘‘Chilton–Colburn analogy") over predicts mass deposition in turbulent flow and represented the upper-bound of the deposit thickness, considering all wax to be dissolved and able to deposit on a surface[11, 13, 62, 114]. For turbulent flows, a solubility approach was considered by Venkatesan and Fogler to account for the effect of heat transfer on mass transfer[114]. Since both heat and mass transfer occur simultaneously in the boundary layer, the wax concentration profile was strongly influenced by the temperature profile. As the temperature decreased below the WAT, wax precipitates in the thermal boundary layer, thus, the concentration of the dissolved wax in the boundary layer depends on the temperature profile. Based on the solubility approach, the system is assumed to be at thermodynamic equilibrium, that is, the kinetics of wax precipitation is instantaneous and much faster than the diffusion rate of wax molecules. The solubility approach underestimates the amount of dissolved wax in the boundary layer and represents the lower-bound of the deposit thickness.

.

Researchers have attempted to include precipitation kinetics into their deposition models. For example, the TUWAX model includes an additional kinetic precipitation-step at the wax deposit interface. Unlike previous models which assumed the wax concentration at the deposit interface to be the equilibrium-wax concentration at the interface temperature, the TUWAX kinetic model introduced a different condition such that the wax concentration at the deposit interface is not necessarily at thermodynamic equilibrium and follows a kinetic concentration profile[111]. Huang et al. developed the *Michigan Wax Predictor* which describes the kinetics of wax precipitation and applied it to the boundary layer of the fluid instead of the pipe wall where the oil is expected to experience drastic cooling while flowing in the pipeline[11, 13], with the model applicable to both lab- and field-scale tests. These more advanced models are all a variant of a deposition model where only the effects of flow on coupled heat and mass transfer was studied.

Wax deposits are subjected to shear forces when formed in a flowing pipeline. Under such conditions wax can be removed from the deposit via sloughing. Azevedo and Teixeira showed shear dispersion to influence wax deposit removal, and thus the rate of wax deposit formation[9]. One of the earliest and most widely used expressions for shear removal was based on the fouling model of Kern and Seaton (1959)[117]. The authors suggested that the rate of wax deposit removal was proportional to the wall shear stress and deposit thickness. This expression was then developed further to better predict wax removal, including other properties such as the deposit wax volume fraction[112, 121].

The current study considered CRF tests in static and dynamic conditions. Using a model waxy oil, the deposition rates and pseudo-steady state wax deposit masses were revealed as the flow transitioned from static, laminar to secondary flow. The experimental data was fitted using a deposition model based on molecular diffusion theory which accounted for the flow in the CRF and modified to describe sloughing at high CRF rotational speeds.

Table 5-1. Wax deposition studies in flow.

Study	Experiment	Deposition conditions	Sample	Summary of flow on wax deposition
Ji et al.[184]	Couette apparatus. Outer cylinder rotating, cooled inner cylinder stationary.	0 – 250 rpm. Laminar flow	Puyang crude oil, 15.36 wt% wax.	Wax deposition studied in laminar flow. Increased rotational speed reduced the wax deposition rate. Assumed the effect of rotation on temperature gradients to be negligible.
Tinsley and Prud'homme[185]	Parallel plate channel flow for small sample volumes.	Re, 160 and 320. Wall shear stress, 5 – 60 Pa.	C_{20}-C_{48} wax in Norpar 12 solvent at 3 wt%.	High shear stress led to initial rapid growth of the wax deposit which plateaued in ~30 min. Low shear stress led to slower growth of the wax deposit but thicker wax layers. Wax content increased with aging time and composition shifted to higher carbon chain lengths.
Zougari and co-workers[43, 44]	Shear cell based on Couette flow. Inner cylinder rotating and outer cylinder stationary and cooled.	Cylinder rotation 25 to 100 s^{-1}. Shear stress at the deposit wall, 5 to 49 Pa.	Light crude oil, 34° API, 2.7 wt% wax.	Trend of decreasing wax deposition with increasing wall shear stress. Test of live crude oil at constant rotational speed confirmed a non-linear deposition profile attributed to depletion of wax. Differences in deposition dynamics attributed to fluid viscosity variation. Wax deposition reduced at higher pressures.
Lu et al.[47]	Flow loop: chilled test section 5.5 m length, 0.053 m ID.	Re, 9942 – 49710. Wall shear stress, 1.93 – 26.64 Pa.	North Sea oil, 4.5 wt% wax.	Experimental and modelling approach confirmed a reduction in wax deposit thickness with increasing oil flow rate. Accounted for 3 effects with increasing flow rate: i) reduced boundary layer thickness increases mass transfer; ii) increased heat loading increased T_i and diffusivity from the bulk to the interface; iii) increased T_i leads to a higher dissolved wax concentration at the interface. Effects 1 and 2 increase growth rate, while effect 3 decreases growth rate.
Hoffman and Amundsen[107]	Flow loop: chilled test section 5.5 m length, 0.053 m ID.	Volumetric flow rate, 5 – 25 m^3/h. Shear stress, 5 – 89 Pa.	North Sea waxy condensate, 4.5 wt% wax.	Higher flowrates led to thinner wax deposits after 50 h tests. Wax deposit thickness strongly dependent on the surface temperature. Composition of the wax deposit was sensitive to the surface temperature, with heavier fractions preferentially depositing at higher surface temperatures, contributing to changing deposit hardness. Calculating the pure wax thickness showed an increase and decrease with increasing flow rates. The decrease was suggested to relate to the effect of shear stress on wax molecule adhesion or removal of wax from the deposit.
Mehrotra and co-workers[109, 182]	Flow loop: chilled test section 0.1016 m length, 0.0254 m ID.	Re, 9000 – 31000.	Norpar 13 solvent (C_{10}-C_{16}) and Parowax (C_{19}-C_{60}) at 7, 10, 15 wt% wax.	Wax deposit thickness increased asymptotically with time but overall the wax deposit mass decreased and deposit wax content (soluble and insoluble wax) increased with increasing Re. Thermal steady state was attained within 30 mins as the wax deposit interface temperature and WAT were almost equivalent. Extended flow tests revealed negligible change to the wax deposit mass but an aging effect on deposit wax content.
Creek et al.[48]	Flow loop: chilled test section 50 m length, 0.0434 m ID.	Flow rates between 8 and 320 m^3/day.	Gulf of Mexico crude oil. 35° API. WAT = 48.9 °C.	Wax deposition rate decreased with increasing flow rate. Deposition in turbulent flow significantly less than laminar flows, with deposits formed in turbulent flows found to be harder with a lower oil content. Aging effects observed in turbulent flows which was attributed to an effect analogous to Ostwald ripening of small wax crystals.

5.3 Materials and Experimental Methods

A model waxy oil composed of low (C_{20}-C_{40} [manufacturer quoted distribution, Merck, UK], melting point 58-62°C) and high (melting point 65-71°C, Fisher Scientific, UK) molecular weight solid paraffin waxes, and dodecane (Acros Organics, UK) with a boiling point of 170-195°C and density of 0.751 g/cm^3 was used throughout the study. The carbon chain length distribution as measured by GC-FID is shown in Fig. 4. Blending low and high molecular weight waxes produced a carbon chain length distribution representative of that found in crude oils[34].

5.3.1 WAT measured by Crystal 16

The WAT of 13 wt% n-alkane-in-dodecane (composed of 1:1 mass basis for low and high molecular weight waxes) was measured by turbidity performed at different cooling rates using the Crystal 16 apparatus (Technobis). The Crystal 16 comprises of sixteen sample wells split into four blocks. Each block is independently temperature-controlled and enables a range of cooling rates to be studied simultaneously. Samples were added to 1 mL glass vials. The solution turbidity (transmission %) was measured as a function of temperature. Each test began by heating the samples to 60°C and held at temperature for 30 min to ensure thermal equilibrium. Then the samples were cooled at 0.5, 1, 2 and 5°C /min to 0°C while stirred using a magnetic flea. The WAT was taken to be the temperature at a light transmission value of 90% (fully transparent sample = 100%).

5.3.2 CRF Wax Deposition

Waxy model oils of 13 wt% n-alkane-in-dodecane were used for all tests. The wax content was selected as being the optimal to achieve reliable and repeatable mass deposit measurements and to

ensure the WAT remained within the temperature range of the CRF. To prepare the waxy oil, an equal amount of low and high molecular weight n-alkane wax was added to n-dodecane at 60°C and held at temperature for 1 h until all the wax dissolved (visual assessment). The solution was then cooled to 45°C to begin the wax deposition test. Deposition tests were conducted using a 300 mL Pyrex jacketed beaker with the circulating oil maintained at T_{hot} = 45°C. The temperature of the waxy oil, T_o, was monitored using a K-type thermocouple (± 0.5°C). The cold side (circulating coolant fluid) was maintained at T_{cold} = 5°C. Wax deposition was measured at CRF rotational speeds of 0, 100, 200, 300, 400, 500, 600 and 700 rpm, and wax deposits were collected at 1, 3, 5, 10, 15, 20, 25, 30 and 60 min to study the kinetics of deposition. Following each test, a scalpel was used to cut the wax deposit at the base and top of the cylindrical test sample, with the mass difference between the blank and wax deposited test sample determining the mass of wax. All wax deposition tests were repeated in triplicate.

5.3.3 Gas Chromatography-Flame Ionization Detection (GC-FID)

The composition of the wax deposit was measured by GC/FID (Perkin Elmer Clarus 500 GC) using a hydrogen flame and kerosene as a reference. The GC-FID included an Elite M1 column of length 15 m, inner diameter (ID) 0.53 mm and a temperature range of −60 to 360°C. Approximately 0.2 g of the wax deposit was removed in the form of a slice that spanned the top and bottom of the cylindrical test sample. After sample removal and prior to measurement, the sample was stored at 4°C in a sealed glass vial to mitigate the loss of any light-ends. The wax sample was placed in a Thermo Scientific 11 mm non-assembled amber crump top autosampler vial with ~1 mL carbon disulphide to completely dissolve the wax. The composition of the wax deposit was determined on a solvent-free basis where the GC-FID analyses were normalized by omitting peak areas below C_{17}.

5.4 Wax Deposition Modelling

A mathematical model was developed to predict wax deposition in the CRF. The model was based on the molecular diffusion mechanism occurring in the thermal boundary layer adjacent to the deposit. The diffusion rate was determined by writing the heat and mass balances, and optimum configurations of the adjustable parameters were identified. The following assumptions were considered: i) all the main variables depend only on the radial coordinate r and on time t, and variations along the longitudinal coordinate z (CRF axis) are negligible; ii) the wax solubility was derived from an empirical equation developed by Singh et al.[19]; iii) hydrodynamics calculations were based on empirical equations fitted to the 100 rpm experimental data; iv) wax was treated as a single component; v) wax diffusivity was considered a constant tuning parameter; vi) the latent heat of crystallization was neglected; vii) the oil and wax were taken to have the same density, 800 kg/m^3; viii) the wax deposit was formed by wax and oil with the wax fraction assumed independent of time; and viii) the lateral external wall of the outer cylinder is adiabatic (zero heat flux).

Mass growth is expressed as:

$$\frac{dm}{dt} = D\frac{\partial C}{\partial r}\Big|_{R_i} = D\frac{dC}{dT}.\frac{\partial T}{\partial r}\Big|_{R_i} \qquad \text{Eq. 5.1}$$

where m is the mass deposited, D the wax diffusivity, C the concentration of dissolved wax in the boundary layer, r the radial coordinate and R_i the wax deposit layer thickness. The steady state temperature in the three zones defined in **Figure 5.2**b is given by:

Wax deposit (D_p):

$$T(r,t) = T_s + \frac{T_i(t) - T_s}{\ln\left({R_i}/{R_s}\right)} \ln\left(\frac{r}{R_s}\right) \quad \text{Eq. 5.2}$$

Boundary layer (BL):

$$T(r,t) = T_i(t) + \frac{T_b(t) - T_i(t)}{\ln\left({R_b}/{R_i}\right)} \ln\left(\frac{r}{R_i}\right) \quad \text{Eq. 5.3}$$

Bulk oil (B):

$$T(r,t) = T_b(t). \quad \text{Eq. 5.4}$$

where, t is the time, T_s, T_i, T_b are the temperatures of the CRF surface, wax deposit-oil interface and boundary layer-bulk oil interface, respectively. R_s and R_b are the radii of the CRF and the boundary layer, respectively.

Imposing thermal flux balance at the interface R_i:

$$k_d \frac{T_i(t) - T_s}{\ln\left({R_i}/{R_s}\right)} \frac{1}{R_i} = k_o \frac{T_b(t) - T_i(t)}{\ln\left({R_b}/{R_i}\right)} \frac{1}{R_i} \quad \text{Eq. 5.5}$$

where k_d and k_o are the thermal conductivities of the wax deposit and oil, respectively. The heat flux at the interface R_i is assumed to be proportional to the temperature drop in the boundary layer so that:

$$k_d \frac{(T_i - T_s)}{\ln\left(\frac{R_i}{R_s}\right)} \frac{1}{R_i} = h\,(T_b - T_i) \quad \text{Eq. 5.6}$$

where h is the heat transfer coefficient. Hence,

$$T_i = \frac{T_b\alpha + T_s}{1+\alpha} \quad \text{Eq. 5.7}$$

$$\alpha(t) = \frac{hR_i(t)}{k_d} \ln\left(\frac{R_i(t)}{R_s}\right) \quad \text{Eq. 5.8}$$

Thermal balance at $r = R_b$ yields:

$$\frac{d}{dt}\int_{R_b}^{R_o} \rho c_p T_b dr = -k_o \left.\frac{\partial T}{\partial r}\right|_{R_b} \quad \text{Eq. 5.9}$$

where R_o is the radius of the CRF outer cylinder, c_p the heat capacity of oil and ρ the density of the oil. Assuming the variation in the thickness of the wax deposit plus the boundary layer is negligible ($R_s \approx R_i \approx R_b$):

$$\rho c_p \dot{T}_b (R_o - R_s) = -k_o \frac{(T_b - T_i)}{\ln\left({R_b}/{R_i}\right)} \frac{1}{R_i} \quad \text{Eq. 5.10}$$

where zero flux at $r = R_o$ Is assumed. Combining Eqs. (5.1), (5.2), (5.6):

$$\dot{T}_b = -C_1 \frac{(T_b - T_s)}{(1+\alpha)} \quad \text{Eq. 5.11}$$

where,

$$C_1 = \frac{h}{\Delta R \rho c_p} \quad \text{Eq. 5.12}$$

with $\Delta R = (R_o - R_s)$. Integration of the above with $T_b(0) = T_h$ (the constant temperature of the circulating hot fluid) provides:

$$T_b(t) = T_s + (T_h - T_s)\exp\{-C_1 g(t)\} \quad \text{Eq. 5.13}$$

where,

$$g(t) = \int_0^t \frac{1}{1+\alpha(t)}\,dt \quad \text{Eq. 5.14}$$

then,

$$\frac{\partial T_b}{\partial t} = -(T_h - T_s)\exp\left\{-\frac{h}{\Delta R \rho c_p}\int_o^t \frac{1}{1+\alpha}\,dt\right\}\frac{1}{1+\alpha(t;h)}\frac{h}{\Delta R \rho c_p} < 0 \quad \text{Eq. 5.15}$$

proving that T_b decreases with time. Also,

$$\frac{\partial T_b}{\partial h} = (T_h - T_s)\exp\left\{-\frac{h}{\Delta R \rho c_p}\int_o^t \frac{1}{1+\alpha}\,dt\right\}\frac{\partial}{\partial h}\left\{-\frac{h}{\Delta R \rho c_p}\int_0^t \frac{1}{1+\alpha}\,dt\right\} < 0 \quad \text{Eq. 5.16}$$

implying that T_b decreases as the heat transfer (and hence the CRF rotational speed) increases. Following Singh et al.,[19] the solubility gradient is supposed constant and given by the empirical relation:

$$\frac{dC}{dT} = \beta = ab(T_s + 17.8)^{(d^{-1})} \quad \text{Eq. 5.17}$$

where, a, b and d are constants and equal to $4.9.10^{-7}$, 297.95 and 5.98 respectively. Recalling Eq. 5.1, the mass growth rate is expressed as:

$$\frac{dm}{dt} = \frac{D\beta h}{k_o}\left(T_b(t) - T_i(t)\right) \quad \text{Eq. 5.18}$$

where $T_b(t), T_i(t)$ are given by Eqs. (5.7) and (5.13).

The heat transfer coefficient is calculated using the Nusselt number:

$$Nu = LR_e^m P_r^n = \frac{hR_o}{k_o} \quad \text{Eq. 5.19}$$

where, Re is the Reynolds number ($Re = \frac{\rho\omega R_s^2}{\mu}$), Pr the Prandtl number ($Pr = \frac{\mu c_p}{k_o}$), with constants L, m and n determined by fitting the wax deposition data at 100 rpm.

5.5 Results and Discussion

5.5.1 Wax appearance temperature

Figure 5.1a shows data obtained using Crystal 16 for 13 wt% n-alkane wax-in-dodecane cooled at rates between 0.5 and 5°C/min. The WAT was taken at the temperature when the transmission equalled 90%. **Figure 5.1**b compares the WAT as a function of the cooling rate. With increasing cooling rate the WAT was shown to decrease from 39.6°C to 35.6°C. The dependence of WAT on cooling rate was due to i) differences in the crystal growth rate, with larger crystals formed at low cooling rates affecting solution transmission more than smaller crystals formed at higher cooling rates[91, 186], and ii) thermal-lag, which describes the relative rates of wax precipitation and cooling (heat transfer), with lower cooling rates exhibiting reduced thermal-lag[90]. Fitting a polynomial to

the cooling rate-dependent WAT values and extrapolating the fit to an infinitely slow cooling rate (dT/dt ~ 0) the WAT was 40.4°C. For all CRF experiments with T_{hot} = 45°C and T_{cold} = 5°C, T_o remained above the WAT (**Figure 5.2**d, solid lines), hence wax precipitation in the bulk oil was not expected and not observed. While light transmission was used to determine the WAT, rheology and a changing fluid viscosity is often used to measure the WAT in crude oils. Such an approach was also considered in the current study and the WAT was found to be ~2.5 °C lower than that measured by light transmission. This difference is understandable given that light transmission is sensitive to incipient wax precipitation, and rheology is sensitive to an abundance of precipitated wax.

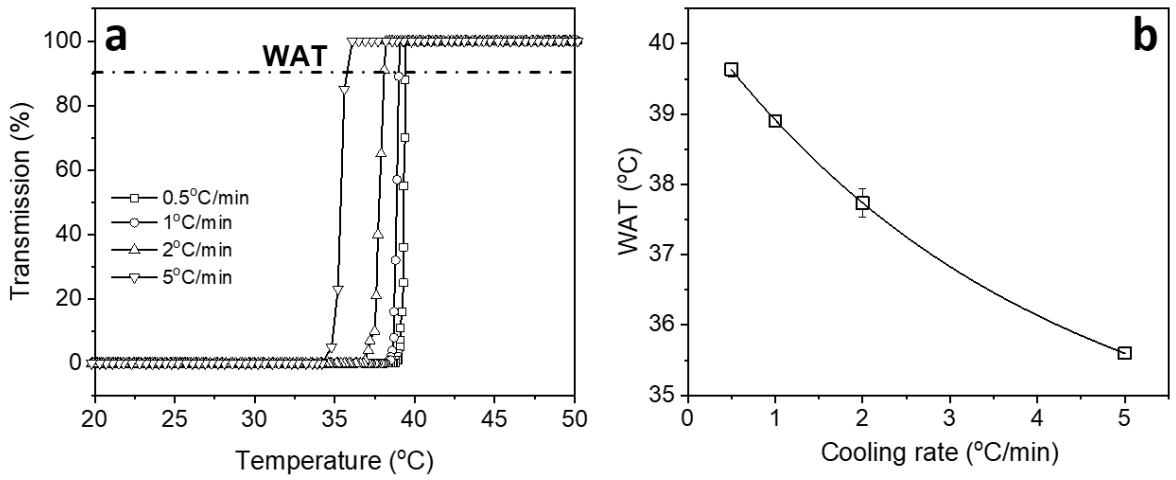

Figure 5.1. a) Light transmission % (turbidity) as a function of temperature for 13 wt% n-alkane wax-in-dodecane during cooling from 50°C to 20°C at different cooling rates. The WAT was taken at the temperature when the light transmission equalled 90%. **b)** Comparison of WAT as a function of cooling rate with the data fitted using a third-order polynomial. The thermodynamic WAT was 40.4 °C.

5.5.2 Wax Deposition

Figure 5.2a compares the rate of wax deposition as a function of CRF rotational speed between 0 and 700 rpm. For all tests, more than 50% of the total wax deposited occurred within 1 min of the 60 min test, and the initial rate (within 1 min) of wax deposition can be linearly approximated. At t > 1 min the rate of wax deposition became non-linear, and the deposited mass approached a pseudo-steady state value at t ~60 min. Between t = 5 min and 60 min, the wax deposit mass increased by ~25% at all CRF rotational speeds. While the mass of wax deposited decreased with increasing CRF rotational speeds, significant reductions in the wax deposit mass occurred between 0-100 rpm and 100-200 rpm (**Figure 5.2**b). Thereafter, smaller incremental reductions in the wax deposit mass were measured with slight differences still measured at high RPMs. Fitting an exponential decay (**Figure 5.2**c, $y = y_0 + Ae^{-\frac{x}{B}}$), good agreement to the fit is observed when the CRF rotational speed $\leq$ 300 rpm, with the mass of wax deposited diverging from the simple fit at higher rotational speeds.

For all experimental conditions (CRF RPM $\leq$ 700; apparent Re $\leq$ 4893, and apparent wall shear stress $\leq$ 0.19 Pa), the amount of wax deposited did not become independent of the CRF rotational speed. The continued decrease in deposited wax with increasing fluid shear has been observed in several studies (cf. **Table 5-1**), and this behaviour is attributed to i) heat transfer effect: changing thermal gradient between the wax interface and bulk fluid temperature, and ii) sloughing effect: mechanical removal of wax[11, 47, 62].

To understand the heat transfer effect, a typical temperature profile for the CRF is schematically shown in **Figure 5.2**b, where T_{cold}, T_s, T_i, T_b, T_o, T_{hot} describe the temperatures at the cold side (T_{cold} = 5°C), CRF surface, wax-oil interface, boundary layer-bulk oil interface, bulk oil and initial

bulk fluid temperature, taken to equal T_{hot} = 45°C. Four zones can be identified: i) ΔT between T_{cold} and T_s which describes heat transfer through the CRF test sample; ii) ΔT between T_s and T_i which represents the wax deposit; iii) ΔT between T_i and T_b which represents boundary layer; and iv) ΔT between T_b and T_o which represents the bulk fluid temperature which is considered to be radially constant. The system is considered adiabatic at the outer wall of the jacketed beaker. Based on the molecular diffusion model, radial mass diffusion occurs only within the boundary layer [R_i , R_b]. Hence at t = 0, $T_i = T_s$ (no wax deposit) and the mass diffusion effect is strongest, promoting fast wax deposition. As the wax layer builds up, the insulating effect of the wax layer leads to an increase in T_i, hence mass diffusion is weakened and the mass of wax deposited begins to plateau as T_i = WAT[123]. It should be noted that the pseudo-steady state values for wax deposited are not a result of wax depletion with 73% of the initial wax content remaining in solution after 60 min for CRF = 0 rpm.

While T_s and T_i could not be accurately measured during CRF rotation, T_o was measured in the absence and presence of wax (13 wt% n-alkane wax-in-dodecane) as a function of the CRF rotational speed (**Figure 5.2**d). T_b was measured by averaging two temperatures, with thermocouples positioned at the top and base of the cylindrical test section and at a radial distance 10 mm from the test section surface (cf. **Figure 5.2**d inset). The test protocol involved attaining steady baseline temperatures for T_{cold} and T_{hot} before submerging the CRF in the jacketed beaker. This protocol led to a drift in T_o until a new thermal equilibrium was achieved (**Figure 5.2**d). The decrease in T_o to a new equilibrium temperature would lower the rate of molecular diffusion, and this effect was enhanced by the increased fluid mixing at higher CRF rotational speeds.

With wax added to n-dodecane, and the insulating effect on T_s as the wax layer deposits, the effect of CRF rotational speed on T_o was considered to be negligible, cf. **Figure 5.2**d. It should be noted that during wax deposition, T_o remained above WAT (WAT = 40.4°C) thus no wax precipitation was observed in the bulk fluid.

Moreover, the wax deposit mass continued to decrease with increasing CRF rotational speed (**Figure 5.2**c), and attempts to measure the density of the wax deposit at 60 min deposition showed little variation with CRF rotational speed, 775 $\pm$ 20 kg/m^3. Therefore, a thinner wax deposit at higher CRF rotational speed is assumed to be less insulating and T_i would decrease. Relative to one another, T_o-T_i should be larger at 700 rpm compared to 500 rpm, and thus the mass transfer from the bulk fluid to the wax interface should be greater. However, the mass of wax deposited was less, hence, mass diffusion alone cannot completely describe the wax deposition kinetics.

Shear removal considers both the retardation of wax deposition, as wax molecules adhere less to the wax deposit, and sloughing which describes the physical removal of wax from a deposit[123]. While sloughing of the wax deposit could not be quantified, visual assessment of the CRF test revealed wax particles being agitated in the CRF test beaker at CRF rotational speeds of 400 rpm and higher (see Supplementary Information Video; 13 wt% n-alkane wax-in-dodecane, T_{cold} = 5°C and T_{hot} = 45°C, 500 rpm at 3 min 30 s). Since T_o exceeded the WAT at all rotational speeds, such observations were attributed to the onset of sloughing.

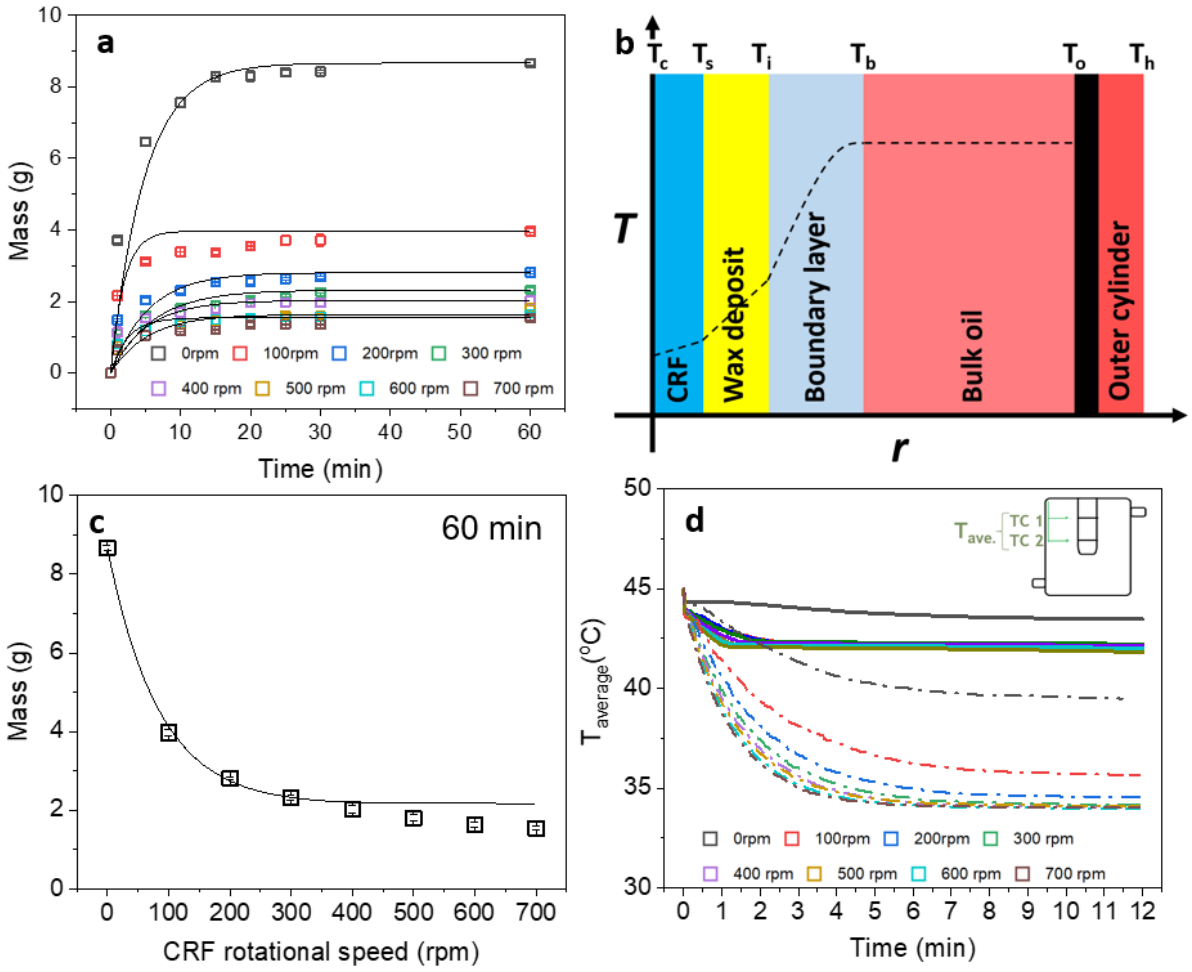

Figure 5.2. a) Time-dependent wax deposition as a function of CRF rotational speed. Experimental conditions: 13 wt% n-alkane wax-in-dodecane, T_{cold} = 5°C and T_{hot} = 45°C. Lines are to guide the eye and take the form, $y = y_0 + Ae^{-x/t}$. **b)** Schematic of the temperature profile in the CRF. **c)** Mass of wax deposited at 60 min as a function of the CRF rotational speed. Line is to guide the eye and takes the form, $y = y_0 + Ae^{-\frac{x}{B}}$. **d)** Time-dependent temperature profiles of T_o in the absence and presence of wax with T_{hot} = 45 °C and T_{cold} = 5°C and the CRF rotational speed is varied betwen 0 and 700 rpm. Thermocouples TC1 and TC2 are positioned in the bulk oil at a height of 5 and 20 mm from the top of the removable sample and at a distance 10 mm from the CRF test surface. Dash and solid lines represent the temperature profile of pure dodecane oil and 13 wt% wax-in-dodecane, respectively.

GC-FID was used to measure the composition of the wax deposit as a function of time and CRF rotational speed. A typical composition of the wax deposit included strong signals for carbon chain lengths between C_{20}-C_{41} and weak signals for carbon chain lengths between C_{42}-C_{45} (only trace amounts), hence the latter was neglected in further analysis. **Figure 5.3**a shows the composition of the deposited wax to be partly time-dependent, with the effect enhanced at higher CRF rotational speed (700 rpm). The dashed lines in **Figure 5.3**a represent the carbon chain length distributions of the low and high molecular weight waxes used in the model oil. At 700 rpm, the carbon chain length distribution of the deposited wax is seen to shift towards the higher carbon chain length distribution with the effect progressively observed at 10 and 60 min. While there may be a similar effect at lower CRF rotational speeds, the difference between carbon chain length distributions at the 3-time intervals is less apparent.

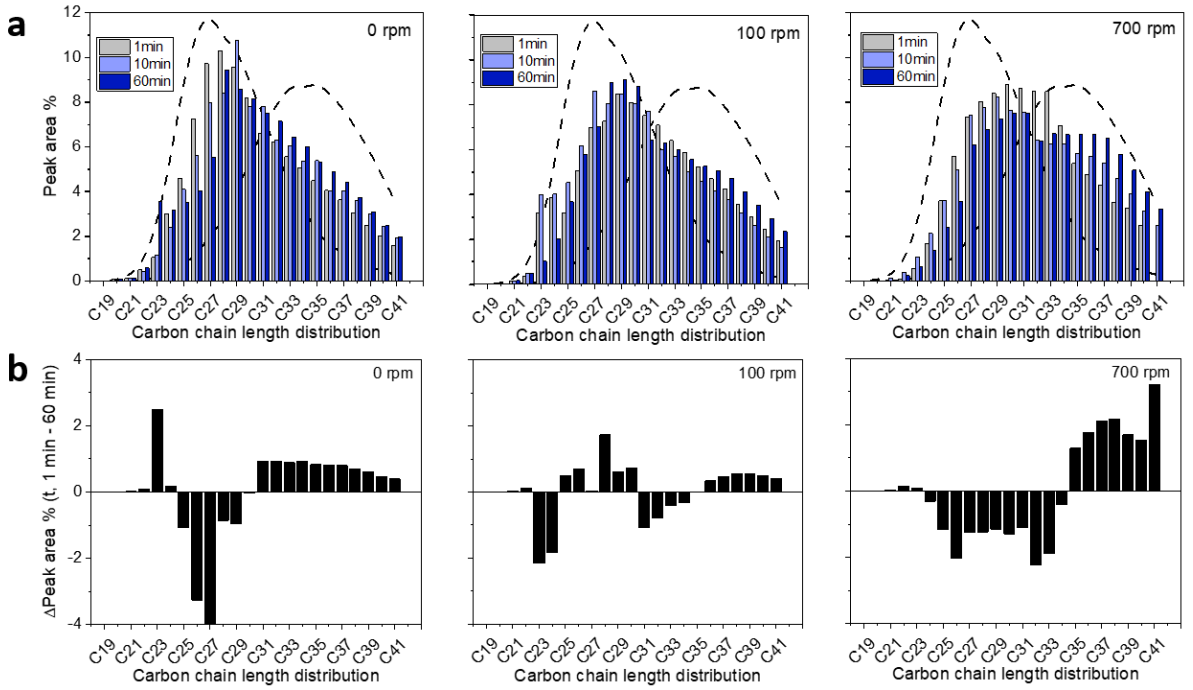

Figure 5.3. a) Carbon chain length distribution of the wax deposit as a function of time at 0, 100 and 700 rpm. The dashed lines represent the carbon chain length distributions of the low and higher molecular weight wax fractions. **b)** Relative change in the carbon chain length distribution with time (between 1 and 60 min) at 0, 100 and 700 rpm.

The wax deposit aging effect has previously been observed and discussed by Singh et al.[19] and Fong and Mehrotra[182] when studying wax deposition in pipe flow. When a wax network forms a gel, the gel is composed of both wax molecules (both precipitated and soluble) and oil molecules. During the initial deposit formation, the wax content of the deposit is low (significant oil fraction within the deposit), and with time oil is displaced and the wax content of the deposit increases. The gradual increase in wax content results from soluble wax molecules diffusing into the wax network and precipitating on the wax surface, thus displacing oil. The precipitating wax is governed by the wax solubility in the oil, with lower molecular weight waxes being more soluble than higher molecular weight waxes. The difference in solubility leads to the low molecular weight wax molecules being expelled with the oil, hence not only does the wax content of the deposit

increase, but the composition shifts to the higher molecular weight fraction. Differentiating between wax molecules that remain soluble and those that precipitate is described by the critical carbon number (CCN). In the current study, **Figure 5.3**b shows the relative change (from 1 to 60 min) in the carbon chain length distribution with time at 0, 100 and 700 rpm. Based on the shift in carbon chain length distribution, the CCN was approximated by the critical carbon length which shows a significantly higher peak area (%) at 60 min relative to 1 min. With increasing CRF rotational speed, the CCN shifted slightly towards a higher carbon chain length with CCN equal to C35 at 700 rpm. Since the effect is less significant at 0 and 100 rpm, the significant shift in carbon chain length distribution at higher CRF rotational speed is likely attributed to the effect shear removal, with high shear preferentially removing the low molecular weight fraction due to weakened van der Waals forces and reduced cohesion within the deposit[123].

5.6 CRF Wax Deposition Model

The newly developed CRF deposition model was compared to experimental data at different CRF rotational speeds. As shown in **Figure 5.4**, the model reasonably describes the pseudo-steady state wax deposit mass up to 300 rpm. A slight over prediction of the deposited wax at short times (200 and 300 rpm) is due to the assumption that wax solubility varies linearly with temperature, which is a reasonable simplification in the range of temperatures considered. Increasing the CRF rotational speed changes the heat transfer in the boundary layer where wax diffusion and deposition occurs. While the model considers wax diffusivity as a constant and independent of temperature (which is a reasonable assumption based on the more significant effect of the thermal gradient[47]), and wax solubility is taken to be a linear function of temperature; changes in wax deposited mass are only influenced by the changing heat transfer coefficient, *h*, which increases

with increasing CRF rotational speed. The increase in *h* leads to a decrease in T_b, as described by Eq. 5.16, and decreases the thermal gradient, $\Delta T_{b\text{-}i} = T_b\text{-}T_i$.

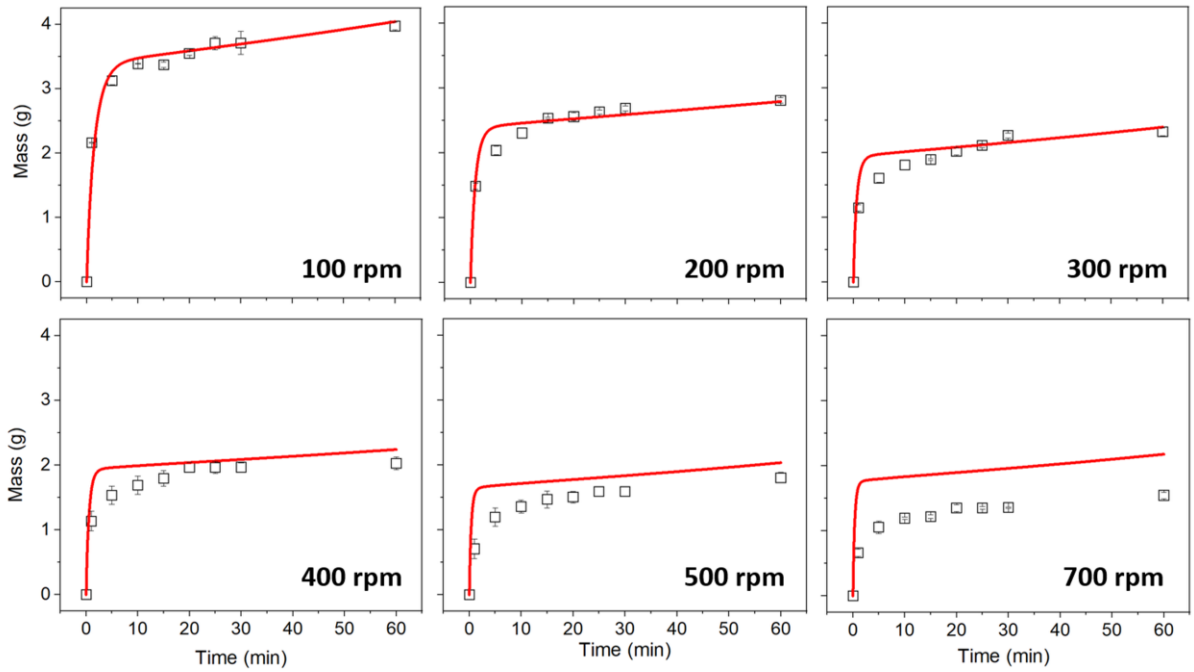

Figure 5.4. Time-dependent wax deposition as a function of CRF rotational speed. Experimental conditions: 13 wt% n-alkane wax-in-dodecane, T_{cold} = 5°C and T_{hot} = 45°C. Data fitted using the molecular diffusion model (Eq. 5.18).

At CRF rotational speeds ≥ 400 rpm, the pseudo-steady state wax deposition cannot be predicted by adjusting the heat transfer coefficient in the molecular diffusion model (Eq. 5.18), likely confirming the increasing contribution of shear removal, and in good agreement with experimental observations, cf. **Figure 5.2**c. To account for these effects, the model was modified by introducing a shear removal term, $\dot{S}(t)$. This term considered shear removal to be a function of the changing wax deposit thickness and the temperature/viscosity of the wax deposit-oil interface as a function of time. An increase in wax deposit thickness (R_i) with time increases the sloughing

rate $\dot{S}(t)$ as described in Eq. 5.25, where the magnitude of R_i is proportional to the magnitude of sloughing. Moreover, an increase in the temperature of the wax deposit-oil interface (T_i) with time decreases the sloughing rate by decreasing the wall shear stress. The magnitude of these opposed effects governs the degree of sloughing during wax deposition.

Contribution of Sloughing: In order to account for sloughing, the model was modified to include a sloughing term $\dot{S}(t)$ as follows:

$$\dot{m}(t) = \dot{D}(t) - \dot{S}(t) \qquad \text{Eq. 5.20}$$

where, $\dot{D}(t)$ is the deposition rate (Eq. 5.18) and $\dot{S}(t)$ is the sloughing rate:

$$\dot{S}(t) = -\theta|\tau|_{R_i} R_i \qquad \text{Eq. 5.21}$$

where θ is a fitting parameter describing the sloughing intensity, $|\tau|$ the wall shear stress ($|\tau| = (\frac{2\mu R_o^2 \omega}{R_o^2 - R_i^2})$, with ω the angular velocity), and R_i the radius of the wax deposit.

$$m(t) = \int_0^t \dot{D}(\delta) d\delta - \int_0^t \frac{2R_o^2}{R_o^2 - R_i^2} [\theta \mu(T_i(\delta)).w.R_i] d\delta \qquad \text{Eq. 5.22}$$

where the viscosity, $\mu = \mu(T)$, and is a decreasing function of temperature (with γ being a constant):

$$\mu = \frac{\gamma}{T_i(t)} \qquad \text{Eq. 5.23}$$

So that,

$$m(t) = \int_0^t \dot{D}(\delta)d\delta - \int_o^t \left(\frac{2R_o^2 w}{R_o^2 - R_i^2}\right)\frac{\theta\gamma R_i}{T_i(\tau)}\,d\delta \qquad \text{Eq. 5.24}$$

$$m(t) = \int_0^t \dot{D}(\delta)d\delta - \int_o^t C_2\,\frac{wR_i}{T_i(t)}\,d\delta \qquad \text{Eq. 5.25}$$

where, $C_2 = \theta\gamma\left(\frac{2R_o^2}{R_o^2 - R_i^2}\right)$ and is a fitting parameter.

Accounting for the sloughing effect, $\dot{S}(t)$, the modified wax deposition model was able to reasonably predict the wax deposition kinetics at CRF rotational speeds of 400, 500 and 700 rpm. While the same value of C_2 was used for 400 and 500 rpm, the value was adjusted slightly at 700 rpm to fit the experimental data, suggesting that the linear model for sloughing could not reliably predict wax deposition at very high CRF rotational speeds, possibly due to non-linearity at large wall shear stress values.

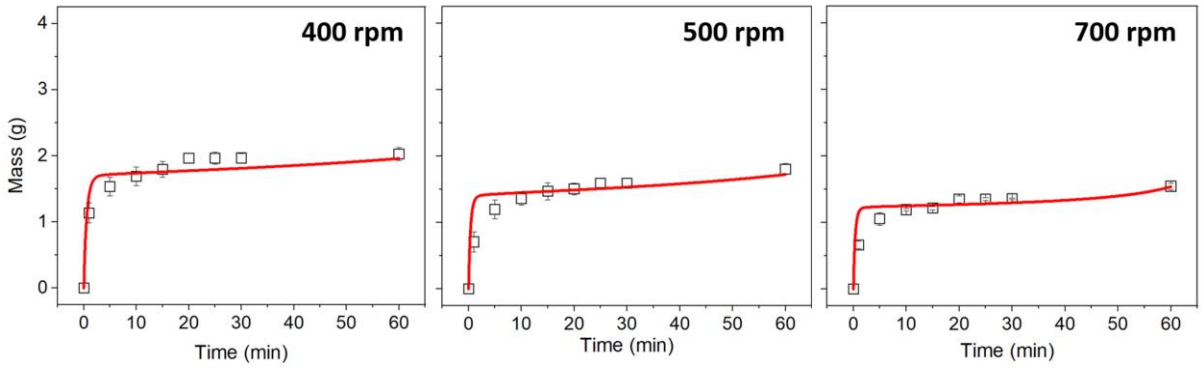

Figure 5.5. Time-dependent wax deposition as a function of CRF rotational speed. Experimental conditions: 13 wt% n-alkane wax-in-dodecane, T_{cold} = 5°C and T_{hot} = 45°C. Data fitted using the molecular diffusion + sloughing model (Eq. 5.25).

5.7 Conclusions

A cold rotating finger (CRF) testing device was built to study wax deposition in Couette flow. Using a model waxy oil composed of a blend of low and high molecular weight n-alkane wax-in-dodecane, the kinetics of wax deposition were shown to be consistent at all CRF rotational speeds, with an initial fast wax deposition rate followed by a secondary slower deposition rate, attaining pseudo-steady state after 60 min. The mass of wax deposited (at 60 min) was shown to decrease with increasing CRF rotational speeds, with the relative change in mass of deposited wax more significant at lower CRF rotational speeds. Such data was suitably described by a molecular diffusion model with the CRF rotational speed being an adjustable parameter. The diminishing thermal driving force at higher CRF rotational speeds meant the continual decrease in the mass of wax deposited was attributed to a secondary sloughing effect. While difficult to quantitatively measure, sloughing was observed at CRF rotational speeds $\geq$ 400 rpm. Such observations corresponded to conditions when the molecular diffusion model failed to predict the pseudo-steady state wax deposited. The wax deposition model was modified to include a sloughing term based on the wall shear stress, deposit radius and a fitting parameter to describe the sloughing intensity. With inclusion of the sloughing term, wax deposition kinetics could be predicted at higher CRF rotational speeds. The study demonstrated the application of the CRF which meets the desirable features of a standard cold finger, but provides additional capability to study wax deposition in flow, with the high rotational speeds of the CRF accessing the sloughing regime.

Chapter 6 Performance of Ethylcellulose–based Inhibitors in Wax Management at Different Flow Regimes

6.1 Synopsis

Four inhibitors based on biodegradable ethylcellulose with various pendant chain sizes (C18 and C22) and degree of substitution were synthesised and then characterized by Fourier transform infrared spectroscopy, elemental analysis and thermogravimetric analysis to confirm their structure, degree of substitution and thermal stability. The inhibitors were tested using a model solution of 5wt% n-alkanes wax-in-dodecane/toluene (1:1) and the CRF at 30 min for 50 and 500 ppm inhibitor's concentrations and at static regime (0rpm), thermally-driven regime (100 rpm) and sloughing regime (400 rpm). Results showed that all inhibitors exhibit an efficiency that depends on their structure as compared to the chemical composition of the wax deposit; The inhibitors having a higher degree of substitution and longer alkyl pendant chain (C22) exhibit the best performance reducing wax deposition up to 35% at static regime. This is due to a higher van der Waals interaction between the inhibitor and the n-alkane wax. Besides, inhibitors show a preferential inhibition for LMW wax due to similarities between their chain lengths. The efficiency was shown to decline with the increase of the rotational speed due to the change in the chemical composition of the wax deposit with less LMW wax depositing at higher rotational speeds. Besides, the incorporation of the ethylcellulose inhibitor in the wax deposit make it stiffer and more resilient to shear stress, decreasing therefore the sloughing effect in the sloughing regime.

6.2 Introduction

Mitigation of wax deposition problem is often in the form of mechanical, or chemical treatments and economics are the main driving force on whether to employ a mechanical solution or chemical

solution[6]. Mechanical pigging is the most widely used method to control wax deposition, however, it requires significant forethought planning in the design of subsea pipelines and may force subsea operations to shut down for several days, leading to significant production losses [125]. Therefore, if the economic returns of reduced pigging frequency and decreased production downtime is substantial, then the use of alkane inhibitors will outweigh pigging. In cases where pigging cannot be deployed, chemical solutions may be the only economical solution left to control alkane deposition[187].

On the other hand, chemical inhibitors are considered an attractive remediation technique for managing wax deposition in subsea systems[15]. Although these technologies may rarely eliminate the phenomenon altogether, the rate of deposition can be reduced significantly. From conceptual standpoint, the alkane inhibitors are designed to interfere with the wax nucleation and crystallisation process[188]. They are commonly used to stop the growth of wax crystals by co-crystallizing with the native alkane wax in the crude to deform the crystal morphology. These chemicals have a polymeric structure that typically contain (1) a hydrophobic portion that can co-crystallize with the crude oil's wax forming components and (2) a hydrophilic portion that can restrict the degree of co-crystallisation and thus sterically hinder the growth of the crystals, preventing further agglomeration, network formation or deposition. The conventional chemical inhibitors used in the industry include, but are not limited to, ethylene vinyl acetate (EVA) copolymers, polyalkyl acrylates/methacrylates and maleic anhydride polyolefin copolymers[188, 189]
.

Chemical solutions however face a major two challenges: First, the performance of wax inhibitors under pipeline conditions i.e. flow is poorly understood, and second most inhibitors used

are synthetics and faced with more restrictions and increased awareness associated with the chemical hazard and risk management of the use of chemicals in Oil & Gas industry.

While few studies consider the effect of flow on the performance of wax inhibitors, some results are also contradictories or not well explained. Ridzuan et al. [69] performed a research on the performance of 4 commercial wax inhibitors in the cold finger, at static, 400 and 600 rpm. The inhibitors showed best performance on 400 rpm with respect to static and 600 rpm with no clear explanation[69]. Tinsley et al.[52] stated that the presence of inhibitors in the wax gel layer influence its yield stress and its ability to be limited by mechanical erosion. Jenning et al.[40] performed more detailed experiment in that term and they observed, using the cold finger and working at different shear rates, that the percent inhibition of the amount of total deposit weight (deposited wax with entrained crude oil) did not always increase with increasing shear though- even decreasing in many cases. This is not related to a reduction of inhibitor performance but rather due to variation in the untreated deposit reference with shear. As the amount of entrained crude oil in a deposit decreases with increasing shear, the percent change on the total deposit weight (deposited wax plus entrained crude oil) will vary for a paraffin inhibitor's effect on a fixed amount of deposited wax species[40]. These experiments leave a lot of room for further investigations into the wax inhibitors performance under flow.

On the other hand, the Convention for the Protection of the Marine Environment of the North-East Atlantic OSPAR Convention[*], which is the current legislative instrument regulating

[*] The OSPAR Convention was concluded at Paris on 22 September 1992. It combines and up-dates the 1972 Oslo Convention on dumping waste at sea and the 1974 Paris Convention on land-based sources of marine pollution. The name is likewise a combination of "Oslo" and "Paris".

international cooperation on environmental protection in the North-East Atlantic, have adopted a wide range of programmes and measures to reduce pollution from all phases of offshore oil and gas activities. Within the OSPR, the Harmonised Mandatory Control Scheme (HMCS) for offshore chemicals implemented in 2001 has the intention to enable the end-user to justify his selection of chemicals based on their environmental performance, hence, to actively promote the continuous shift toward the use of less hazardous products. The general view point was that the focus of the environmental impact should be on the replacement chemical but that it is important to consider how it compares against the replaced candidate for substitution. Compliance with these regulatory requirements has required the offshore suppliers to develop new and innovative chemistries to meet the increasingly stringent environmental requirements[190].

Within this perspective, Green chemistry approach is growing rapidly and the replacement of petroleum derived materials with bio-based materials is greatly enhanced with a special attention given to polysaccharides polymers, a renewable and almost inexhaustible source of raw material. Polysaccharides polymers (guar gum, starch, cellulose derivatives etc.) can be modified into various derivatives by substituting the reactive hydrogen from free hydroxyl groups along the macromolecular backbone with different reactive functional groups. Modification of polysaccharides polymers and its derivatives can provide a significant method to alter its physical and chemical properties for a specific end use while maintaining its biodegradibility[191-193].

OSPAR Commission, which is made up of representatives of the Governments of the 15 signatory nations, and representatives of the European Commission, representing the European Union.

Polysaccharides polymers and its derivatives find great importance in a wide range of applications in the petroleum industry due to their low toxicity and characteristics. They were reported previously as important components in drilling fluids, they are used as components in several formulations for corrosion inhibition, enhanced oil recovery, viscosity improvers and dispersant formulations[193-195]. Cellulose derivatives are used especially as demulsifier to break up W/O emulsions[196], as a viscosifier in fluids[87] and crystallisation inhibitors[197].

In this research, ethylcellulose polymer, a cellulose derivative with enhanced solubility in organic solvents, was modified to accommodate alkyl chain that can interact with wax. Wax control additives were then evaluated by measuring the mass of the wax deposit in the CRF at different inhibitor concentrations and degree of alkyl substitution. The performance of the EC based inhibitor was then compared in different flow regimes, static (0rpm), thermally-driven (100 rpm) and sloughing driven (400 rpm) regimes.

6.3 Theory of Cellulose Modification: Williamson Ether Synthesis

The modification of ethylcellulose (EC) was performed using a bimolecular nucleophilic substitution (S_N2) reaction with alkyl bromide. The reaction is shown schematically in **Figure 6.1**. As the hydroxyl groups react with alkyl bromide in the presence of sodium hydroxide, the oxygens of EC are first deprotonated to O^- ions by sodium hydroxide, and then these react with alkyl bromide by S_N2 reaction in one step.

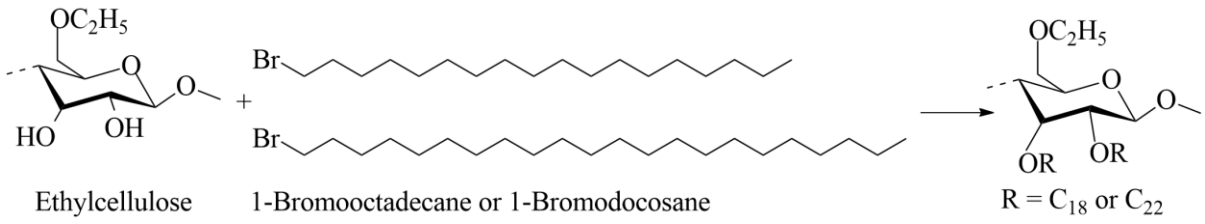

Figure 6.1. Alkylation of EC using a bimolecular nucleophilic substitution (S_N2) reaction with alkyl bromide.

6.4 Materials and Experimental Methods

6.4.1 Synthesis and Characterisation of Inhibitors

Ethylcellulose (EC) 4cp (Sigma-Aldrich Co.) with a mean particle size of 20 μm was used as a backbone chain polymer, 1-Bromooctadecane (C18) and 1-Bromodocosane (Sigma-Aldrich Co.) were used as alkylating agents for the modification of EC. N, N-dimethylacetamide DMAc (VWR) as a solvent and lithium chloride LiCl (>98%, Alfa Aesar), as a salt were used in order to obtain clear cellulose solutions. NaOH pillets (Duksan,Korea) were used for making the cellulose solutions alkaline.

6.4.2 Preparation of Alkyl Ether Cellulose

2 g of EC were suspended in 90mL of DMAc with stirring for 2 h at 120 °C. The EC/DMAc suspension was then cooled to 80 °C. After adding 3.6 g of well-dried LiCl as a salt, the suspension was stirred with cooling to room temperature overnight. The addition of 6 g of finely ground NaOH powder was carried out under a nitrogen atmosphere, and the solution was stirred for 1 h at room temperature.

For a high degree of alkylation, excess volume of Alkyl bromide as alkylating agent, was added to the suspension in 2 steps. In the first step, 5mL of alkyl bromide was added using a syringe with stirring at room temperature. After 2 h, 2 mL of alkyl bromide was added, and the temperature was increased to about 70 ^{o}C and stirred for 10 h. The reaction was then left to cool overnight and the suspension was precipitated in methanol, filtered 2 times with methanol. The obtained samples were dried at room temperature for 3 days, then soaked in water for few hours and filtered in vacuum until the PH of the water reach 7-8. The samples were then dried in vacuo overnight at 60 ^{o}C. For lower degree of alkylation, a stoichiometric volume of 5 mL of alkyl bromide was added on 2 steps, 4 mL then 1 mL.

To distinguish chemisorption from physisorption, octane and dodecane were applied as control reagents. The same procedure for the reaction was performed with octadecane, and the FTIR spectra also be obtained with no specific changed peaks, meaning that the substitution reaction was not successfully performed with alkane reactant. (Stoichiometric calculations are in appendix of Chapter 6).

6.4.3 Fourier-transform Infrared (FTIR) Spectrometry

ATR-FTIR spectroscopy Thermo iS10 was used to confirm the structure of the synthesised inhibitors. The etherification of the ethylcelullose was verified by identifying the presence of a new alkyl group in the EC molecule spectra. The technique involves placing the EC sample on top of a diamond crystal (which has a high refractive index) embedded in a stainless-steel disk, called the DuraDisk. An infrared beam from the spectrometer passes through the crystal and penetrates

slightly into the EC sample to permit analysis of strong infrared absorbing solutions. Ideally, when the targeted chemical is present in the sample, IR absorption at characteristic wavelengths occurs. FTIR spectra of EC and the modified EC are presented in **Figure 6.4**.

6.4.4 Carbon, Hydrogen, Nitrogen, Sulphur and Oxygen Analysis (CHNS-O)

To quantify the percentage of substitution in the modified cellulose, CNHS and O were quantified before and after the substitution reaction. The modified and original EC were weighted into soft tin capsules (for CHNS content) or silver capsules (for O content). The capsules were folded and gently crushed to fully encapsulate the sample and remove air, then loaded onto the instrument auto-sampler. For CHNS content, the sample was dropped into a furnace at 900 ^{o}C in a continual flow of helium. Pure oxygen is added for a few seconds and the sample burns. The combustion products pass through an oxidation/reduction reactor to ensure they are in the correct form (CO_2, H_2O, N_2 and SO_2) to be separated using a gas chromatography column, then detected using thermal conductivity. For O quantification, the sample was pyrolyzed at 1060 ^{o}C under helium to release oxygen from the matrix. The oxygen passes over carbon impregnated with a catalyst and is reduced to form carbon monoxide, which is then separated using gas chromatography and detected [167, 168]. The combustion products are removed from the combustion chamber using helium as an inert gas and they are separated using a chromatographic column and are detected on the thermal conductivity detector (TCD) as an output signal. These signals are proportional to the concentration of the individual components in the mixture. The EA 2400 Data Manager, which is SQL-based software, was used for data manipulating and exporting the results. Results are analysed and presented in **Table 6-1**.

6.4.5 Thermogravimetric Analysis (TGA)

TGA 4 - Shimadzu TGA 50 was employed to analyse the thermal stability of wax inhibitors. Samples typically ~10 mg mg were inserted into an empty alumina crucible. The crucible is then positioned inside a furnace with nitrogen flow at 50 mL/min. The temperature programme consists of one ramp from the initial temperature (30 ^{o}C) to the final temperature (500 ^{o}C) with a heating rate of 10 ^{o}C/min with no hold period added. The output data is plotted as mass of the sample with respect to temperature as seen in **Figure 6.5**.

6.4.6 Testing of the Performance of Wax Inhibitors

All experiments were carried out with prepared mixtures of alkane waxes in a petroleum solvent. Solid alkane wax of low (C_{20}-C_{40} [manufacturer quoted distribution, Merck, UK], melting point 58-62°C) and high (melting point 65-71°C, Fisher Scientific, UK) molecular weight solid paraffin waxes, dodecane (Acros Organics, UK) with a boiling point of 170-195°C and density of 0.751 g/cm^3, and toluene (Fisher scientific) with a boiling point of 111°C (purity 99+%) and density of 0.865 g/cm^3 were used throughout the study. All chemicals were used without further purification.

6.4.6.1 WAT Measurements using Light Transmission

The WAT of 5 wt% wax-in-dodecane and toluene (composed of 1:1 mass basis for low and high molecular weight waxes) was measured by turbidity using the Crystal 16 apparatus (Technobis). The solution turbidity (transmission %) was measured as a function of temperature. Two solutions were prepared with the first being a neat n-alkane-in-dodecane solution without any additives, the second containing a 500 ppm of EC-1. Each test began by heating the samples to

60°C and held at temperature for 30 min to ensure thermal equilibrium. Then the samples were cooled at 0.5 °C /min to 0°C while stirred using a magnetic flea. The plot of the crystallizing and dissolution curves are presented in **Figure 6.6**.

6.4.6.2 CRF Deposition Test

Model solution: 5wt% wax model solution was used for the CRF tests. Model solution was chosen based on a good solubility of the wax inhibitors and quantifiable and measurable wax deposition mass data. The introduction of toluene in the model solution was to enhance the solubility of the EC. Solubility test of 500 ppm EC in 25:75, 50:50, 60:40 and 75:25 dodecane:toluene mixture was performed at room temperature as seen in **Figure 6.2** and EC shows a good solubility with a toluene percentage > 50%.

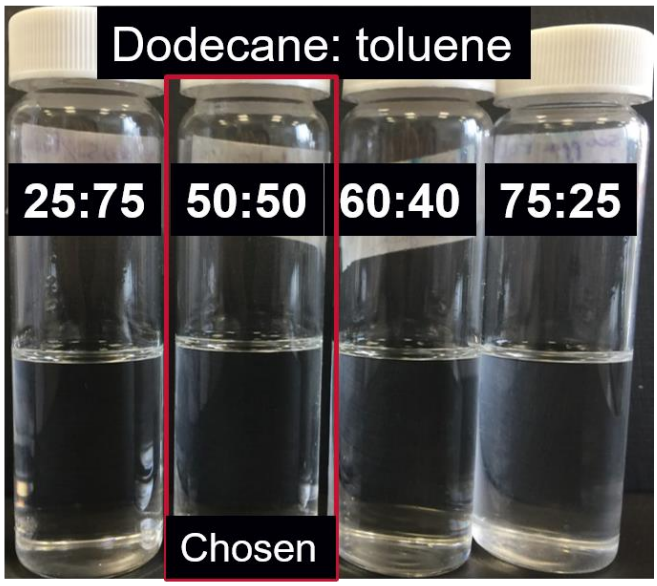

Figure 6.2. Solubility test of 500 ppm EC in 25:75, 50:50, 60:40 and 75:25 dodecane:toluene mixture at room temperature.

CRF Test matrix: The CRF equipment was used to evaluate the wax inhibition of the polymers. In total, four wax inhibitors (EC-1, EC-2, EC-3 and EC-4), and two concentrations (50 and 500 ppm) were used. The procedure consists of dissolving the amount of inhibitor needed in 5mL toluene by heat and sonication in a sonication bath (100 W) for 10 min. The inhibitor is then transferred to the sample solution and stirred at 500 rpm at 45 ^{o}C for two hours until the solution becomes clear. Neat or treated model solution is then transferred in a jacketed beaker of 300 mL set at 35^{o}C (>WAT= 24 ^{o}C). The CRF, which is set at -5^{o}C is then immersed in the waxy solution for 30 minutes (-5^{o}C was chosen to produce a thick layer of wax with repeatable data).The CRF was then raised and the wax deposit sample is weighted before and after deposition. The wax inhibition was calculated by comparing the wax deposit weight of the blank waxy solution (without wax inhibitors) to the treated waxy solution (with wax inhibitor) using the following equation:

$$\%\ Inhibition\ (mass\ reduction\ \%) = \frac{Wt\ of\ wax\ deposit\ without\ additive - Wt\ of\ wax\ deposit\ with\ additive}{Wt\ of\ wax\ deposit\ without\ additive} \times 100\%$$

6.4.6.3 Gas Chromatography-Flame Ionization Detection (GC-FID)

GC/FID (Perkin Elmer Clarus 500 GC), with hydrogen flame and kerosene as a reference, was used for the analysis of the wax deposit. The GC-FID included an Elite M1 column of length 15 m, inner diameter (ID) of 0.53 mm and a temperature range of -60 to 340/360^{o}C. Approximately 0.2 g of the wax deposit was taken by cutting a slice of the wax deposit from the top to the bottom of the deposit sample. The wax sample was inserted into a Thermo Scientific 11 mm non-assembled amber crump top autosampler vial and stored at 4^{o}C until the GC experiment was

performed. On the experiment day, approximately 1 mL of carbon disulphide was added to the vial to dissolve completely the wax before entering the GC column.

6.5 Results and Discussion

6.5.1 Synthesis of EC Inhibitors

In total 4 EC-based inhibitors were successfully synthesised using a bimolecular nucleophilic substitution (S_N2) reaction with alkyl bromide. The polymers differed in the length of the alkyl chains attached to a central backbone and the degree of substitution of the alkyl chain to each polymer. **Figure 6.3** shows a schematic representation of the two polymers. As the alkyl pendant chain is outside the EC backbones, the inhibitor is classified as comb-shape inhibitor[126].

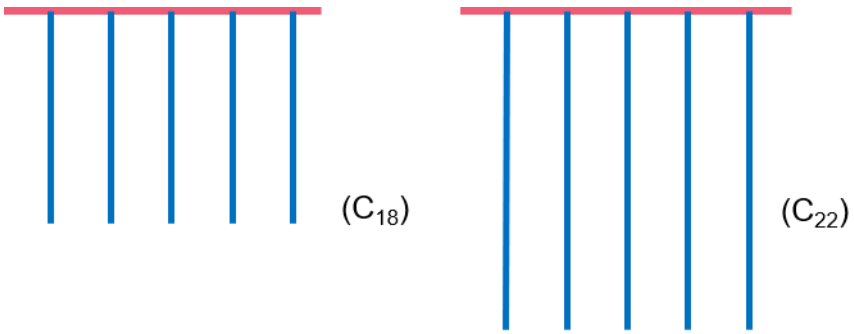

Figure 6.3. Schematic representation of the comb-shape EC inhibitors with varied alkyl pendant chain.

The chemical structures of the inhibitors were identified using Fourier transform infrared, the degree of substitution was calculated by elemental analysis and thermal stability of inhibitors with

respect to EC was studied using TGA. Below, **Table 6-1** shows the name and the specification of each inhibitor.

Table 6-1. Name, type and degree of substitution (DS) of the inhibitors synthesized.

Name	Inhibitor type	DS
EC-1	High DS C22 EC	1
EC-2	Low DS C22 EC	0.6
EC-3	High DS C18 EC	0.6
EC-4	Low DS C18 EC	0.4

6.5.2 Fourier-Transform Infrared (FTIR) Spectrometry

FTIR was used as a mean to confirm the substitution reaction and the modification of the EC by mainly identifying and confirming the presence of the alkyl group peak. **Figure 6.4** shows the EC spectrum as compared to EC-1, EC-2, EC-3 and EC-4.

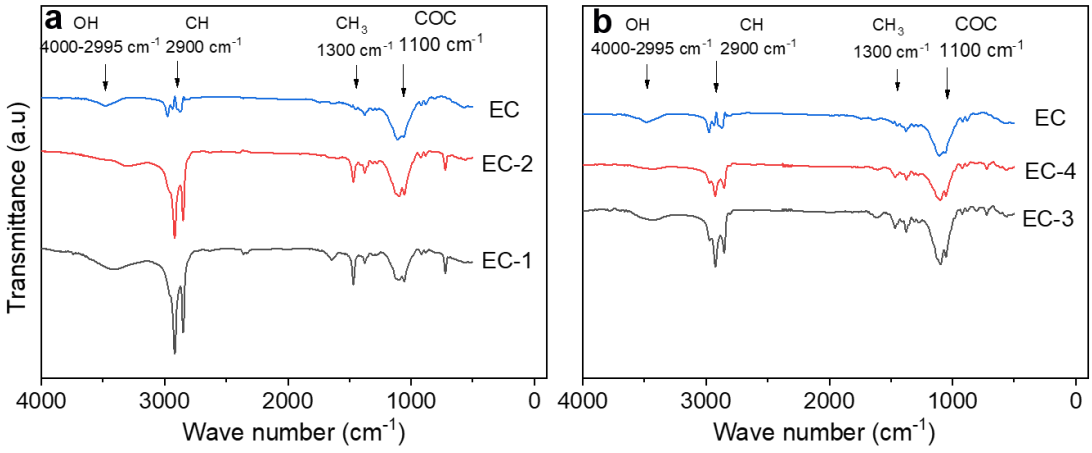

Figure 6.4. FTIR spectrum of **a)** EC, EC-1 and EC-2, **b)** EC, EC-3 and EC4.

The EC structure, used as a reference in the both FTIR spectrums, is characterised mainly by the hydroxyl (OH) and the ethyl group. The OH peak at 3700 cm^{-1} resulting from the ~50% of the initial cellulose backbone OH content (Ethylcellulose is characterised by 49% etherification of the initial OH present in the cellulose). The ethyl groups correspond to the sp3 C-H stretching vibration at ~2900 cm^{-1}, CH_3 in-plane bending at ~1300 cm^{-1}, CH_2 bending at ~1470 cm^{-1} and CH_2 rocking at 720 cm^{-1}.

All the inhibitors exhibit a change in the main 2 peaks, the OH and CH peaks characteristic of the initial EC. The OH content of EC is etherified and replaced by a long alkyl group. The alkyl group length and concentration are proportional to the intensity of the C-H stretching. Hence, the spectrum shows a sharp absorption at ~2900 cm^{-1} with an intensity order of EC-1>EC-2>EC-3>EC-4. This result is in accordance with the chemical structure of each inhibitor where EC-1 has the higher degree of substitution with the higher chain length (C22), while EC-4 has the lower degree of substitution with the low chain length (C18). The interpretation of the OH group is more complicated. For EC-2 and EC-4, corresponding to the low degree of substitution for each chain length, there is a decrease in the OH absorbance peak due to the decrease in the OH concentration. EC-1 and EC-3 however, shows a broad large absorbance peak for the OH group and a shift in the peak towards lower absorbance. This increase in the absorbance is not a result of an increase in the OH group because the alkyl group characterised by a C-H absorbance 2900 cm^{-1} is present in the IR spectrum with a larger peak corresponding to a higher degree of alkylation than EC-2 and EC-4. The increase in the intensity of the OH group and its shift can be explained by a lower H-bonding resulting in a more absorbance of the OH group. Hydrogen bonding weakens the O-H bond and its absorption frequency will be lower then. The high degree of alkylation results in less OH groups and lower degree of H bonding. The association band is broad because the hydroxyl

groups are associated in aggregates of various sizes and shapes depending on the OH environment. This produces a spectrum of closely spaced O-H absorption frequencies[198].

6.5.3 Elemental analysis: Carbon, Hydrogen, Nitrogen, Sulphur and Oxygen Analysis (CHNS-O)

Although alkyl substitution presence can be judged from FTIR spectra, accurate percentage of alkyl group in each EC monomer would be determined by elemental analysis. Listed in **Table 6-2** the wt% of C, H and O in each of EC and the four EC inhibitors with their degree of substitution.

Table 6-2. The wt% of C, H and O in EC, EC-1, EC-2, EC-3 and EC-4 with their degree of substitution as given and analysed by the CHNS-O analysis.

Sample name	C (wt %)	H (wt %)	Oxygen (wt %)	DS
EC	52.9	7.9	39.2	0.0
EC	53.8	8.0	38.3	0.0
EC-1	74.9	12.1	13.1	1.0
EC-1	74.4	12.6	13.1	1.0
EC-2	70.7	11.6	17.6	0.6
EC-2	70.9	11.8	17.4	0.6
EC-3	68.3	11.5	20.2	0.6
EC-3	68.0	11.8	20.2	0.6
EC-4	65.6	11.2	23.2	0.4
EC-4	64.2	11.6	24.2	0.4

The degree of substitution (DS) of alkylated EC was calculated from the % [O] and % [C] values determined by elemental. Below is an explanation with a sample example of DS calculation. The Ethylcellulose monomer with a degree of ethyl substitution of (~49% assumed 50%), has the following number of atoms: 5 Oxygens, A total of 9 Carbons (6 Carbons in the main molecule and assuming a substitution of half the OH group by an ethyl group, then it will have an extra 3

carbons), and a total of 16 H (7 H from the main backbone, 1.5 H from the remaining non substituted OH and 7.5 from the ethyl substituted group).

Therefore, a molecule of EC has the following atoms and mass percentages:

Table 6-3. Analysis of the number of atoms, their mass and weight percent in EC molecule.

EC molecule	Number of atoms	Mass of atoms	Wt% of atoms
O	5	80	39.2
C	9	108	52.9
H	16	16	7.8
Total		204	100

The degree of alkyl substitution of C18/C22 should be zero for an EC and the maximum degree of substitution can reach 1.5 because only 1.5 OH are free to react in an EC monomer.

The degree of substitution was calculated following the steps below, taking EC-1 as an example:

Step 1: Use the Oxygen percentage in the sample to calculate the percentage of C in the EC backbone (without any substitution)

For one EC molecule, for each 39.2 wt% O, there is a corresponding 52.9 wt% C.

Therefore, for 13.1 wt% O, there is

$$\%C\ (in\ EC\ backbone) = \frac{\%\ \mathrm{O}\ \times \%\mathrm{C}\ (\text{in EC molecule})}{\%O\ (in\ EC\ molecule)} = \frac{13.1 \times 52.9}{39.2} = 17.6\ \%$$

Step 2: Calculate the percentage of C of the substitution groups:

$$\%C\ for\ substitutions = \ Total\ \%C - \%C\ (in\ EC\ backbone) = 74.8 - 17.6 = 57.2\ \%$$

Step 3: Calculate the total number of the C18/C22 substitutions:

Each substitution has either 22 carbons or 18 carbons. For C22 substitution:

$$Total\ number\ of\ subsitutions = \frac{\%C\ for\ subsitutions}{22} = 2.6\ substitutions$$

Step 4: Calculate the total number of EC backbone monomers

Each EC unit has 5 O, therefore, the number of EC units is:

$$Toatl\ number\ of\ EC\ backbone\ monomer = \%O/5 = 13.1/5 = 2.6\ \ units$$

Step 5: Calculate the degree of substitutions is equal to the number of substitutions divided by the number of EC monomers.

$$DS = \frac{Total\ number\ of\ substitutions}{Total\ number\ of\ EC\ units} = \frac{2.6}{2.6} = 1$$

The synthesised inhibitors with different degree of substitution will allow to assess both the effect of the length of alkyl chain substitution as well as the percentage of alkyl substitution on inhibition.

6.5.4 Thermogravimetric Analysis

The thermal stability of EC, EC-1, EC-2, EC3 and EC-4 is necessary in determining their temperature range of use and thermal degradation. It gives information about their chemical composition as well confirming the chemical structure of each inhibitor. **Figure 6.5** presents the TGA experimental data for EC, EC-1, EC-2, EC3 and EC-4 where the measurement of weight

change is given as a function of temperature. The temperatures of the maximum rates of thermal degradation (Tmax) and weight loss percentage are given in **Table 6-4**.

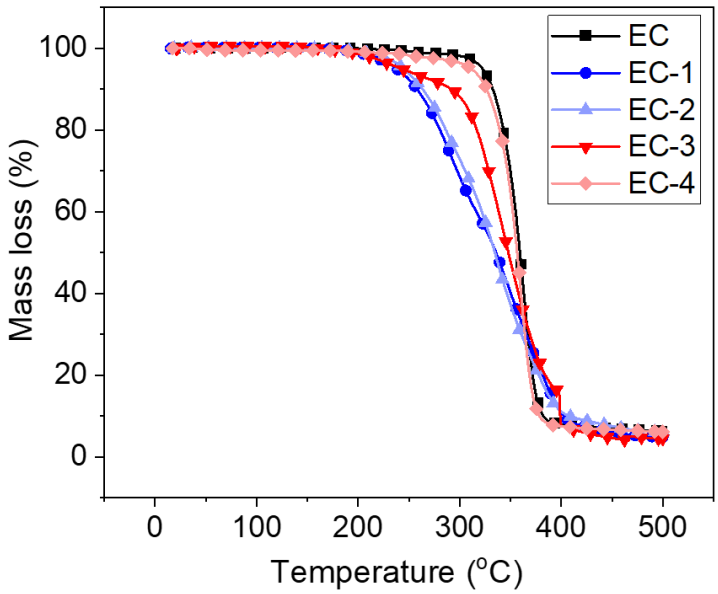

Figure 6.5. TGA Thermal analysis curves representing mass loss (%) as a function of temperature for EC, EC-1, EC-2, EC3 and EC-4.

Results from TGA show that all inhibitors are thermally stable below 220 °C which allow the use of the inhibitors in the production wellbore where the temperature reaches 130 °C[199] without exhibiting any degradation at these conditions. Besides, they show that the addition of the alkyl chain decreases the thermal stability of the inhibitor due to the change in the chemical structures. EC undergoes one thermal degradation cycle with a peak at 360 °C and a residue of 17%. With the addition of an alkyl chain, the inhibitors show perhaps two thermal degradation cycles due to independent degradation steps corresponding to the alkyl chain degradation first and the ethylcellulose backbone second.

Table 6-4. Temperatures of the maximum rates of thermal degradation and weight loss percentage for EC, EC-1, EC-2, EC3 and EC-4.

	T^1max (°C)	Weight loss (%)	T^2max	Weight loss (%)
EC	360.66	93.41	-	-
EC-1	293.55	40.93	345.36	54.18
EC-2	289.76	26.69	336.38	67.28
EC-3	242.57	15.50	355.96	77.2
EC-4	229.81	8.312	341.6	85.81

While **Figure 6.5** shows that EC-4 has the closest thermal degradation behaviour to the original EC with high stability and EC-1 the first to degrade, **Table 6-4** shows however that EC-4 is the less stable with degradation of the alkyl chain starting at ~230 °C while EC-1 is the most stable with the thermal degradation starting at ~290 °C. EC-4 has a low degree of substitution of C18, the degradation of C18 results only in the loss of ~8% of the total mass of the inhibitors, therefore, the thermal degradation curve of EC-4 is very similar to EC. EC-3 having a slightly higher degree of substitution starts the degradation process at ~240 °C with a mass low of 15%. On the other hand, EC-1, with the highest degree of substitution and the higher chain length number C22 exhibit the highest resistance to temperature due to more heat required to degrade C22 than C18 chain, however, the high percentage of alkyl chain in the inhibitor leads to a remarkable mass loss of ~40% of the inhibitor weight making the EC-1 TGA curve significantly different from EC. Similarly EC-2 shows a weight loss of ~27% at a similar temperature of degradation[191 198].

6.5.5 Light Transmission: Crystallisation and Dissolution Curves

The WAT of 5 wt% paraffin wax-in-dodecane/toluene was obtained using Crystal 16 with a cooling rate of 0.5°C/min. **Figure 6.6**a shows the crystallization and dissolution curves of neat and

treated solution in the presence of EC-1. The WAT taken at the temperature when the transmission equalled 90% shows a WAT~ 24 °C with and without the presence of EC additive, demonstrating that EC doesn't act as nucleating inhibitor, or a nucleating agent precipitated before the wax crystals.

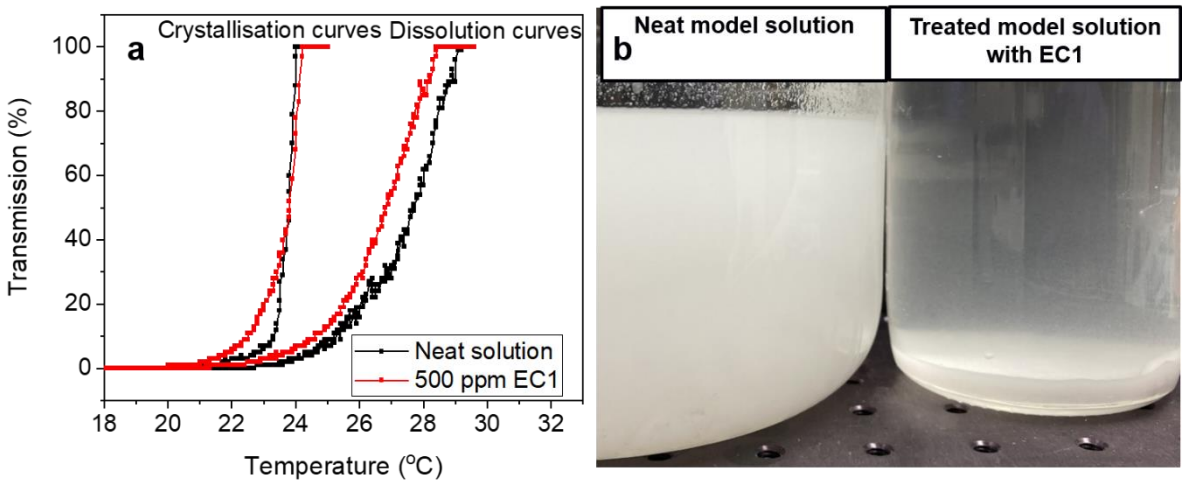

Figure 6.6. a) Crystallisation and dissolution curves as a function of temperature for 5 wt% alkane wax-in-dodecane/toluene (1:1) with and without 500 ppm EC-1 during cooling/heating from 60°C to 0°C at 0.5 °C/min, **b)** 5wt% wax-in-dodecane and toluene neat and treated with EC-1. The solutions were prepared, heated up to 45 °C for 4 hours to dissolve all wax and inhibitor, then left over night to cool down.

The WAT measurement in the presence of inhibitors is used by some researchers in the literature to assess the effect of inhibitors on wax deposition. A decrease in the WAT would induce a decrease in the wax deposit and an increase in the efficacity of the wax inhibitor[33, 154, 200]. However, some other researchers[90, 126, 201] found that the assessment of inhibitors is not restricted to the WAT. Trasi et al.[197] studied the effect of cellulosic polymers on the nucleation behaviour of supersaturated acetaminophen using Crystal 16 combined with Crystalline Particle Viewer/image analysis. While the induction time (time taken for the first particulates to be detected by the camera

corresponding to the WAT in our case) is similar to that observed for blank solution, the rate of increase in the number of particles, and the total particle count observed is much lower. Cellulosic polymers were clearly the best polymer for decreasing nucleation kinetics. The impact of a polymer on the supersaturation profile depends not only on its effect on nucleation, but also on its ability to suppress crystal growth once nuclei have formed. Pedersen et al.[202] used 12 different wax inhibitor chemicals, to survey the effects of wax inhibitor on viscosity, WAT and PPT. The researcher found that the chemicals used to inhibit waxes in the waxy crude oil had insignificant effect on the wax appearance temperature. In contrary, evident changes were observed on viscosity and pour point temperature of the crude oil. The inhibitors to some extent hindered the wax crystals from forming network structure with oil entrapped within[203].

To gain better understanding of action mechanism of the EC inhibitors, the analysis of the rate of crystallisation and rate of dissolution with and without the presence of EC-1 suggests that the inhibitor retard the precipitation of waxes undergoing cooling conditions affecting therefore the rate of precipitation and the pour point temperature. Besides, the dissolution temperature of the treated solution was slightly lower (by ~1 ^{o}C) and faster, suggesting that the EC-1 inhibitor hindered the wax crystals from forming a solid network structure.

To investigate the effect of the EC-1 on the viscosity of the model solution, two model solutions were prepared similarly with one treated with 500 ppm EC-1. Both solutions were stirred and heated at 45 ^{o}C for 3 hours and then left to cool down overnight. The solutions viscosities were compared by visual inspection as seen in **Figure 6.6**b. **Figure 6.6**b shows a clear difference between the neat and the treated solution in terms of viscosity. While in the neat solution, wax was forming a rigid wax crystal network inducing a high viscous solution with large crystals. The

treated solution was almost clear of wax crystals with a small amount of small shattered crystals precipitated at the bottom of the jar. The presence of EC-1 inhibitor resulted in smaller structure of waxes crystals, with a lower tendency of the nucleus of the waxes to combine together forming a gel[203].

Yang et al.[126] explain this effect by the co-crystallization process when the wax inhibitor molecules disrupt the crystallization process and modify the growth of wax crystals. The paraffin wax molecules adsorb on the surface of inhibitors with similar chemical structure, which are then bound together and subsequently form a wax crystal lattice structure in the crude oil. This alters the morphology of growing wax crystals and delays the formation of three-dimensional crystals. Tiny spherical-like crystals (altered in shape from large plate-like crystals) are expected to increase the flowability[204, 205].

6.5.6 CRF Test Results

The total mass deposit as well as the percentage of mass reduction as a function of inhibitor type (EC-1, EC-2, EC-2 and EC3), inhibitor concentrations (50 and 500 ppm) and CRF rotational speeds are reported in **Figure 6.7**. **Figure 6.7** shows that a general trend of decrease in the total mass deposit is observed with the presence of inhibitors at all conditions, and the order of wax inhibitor performance is in the following sequence in descending order: EC-1>EC-2>EC-3>EC-4. The reduction in mass varies according to the inhibitor type, concentration and flow conditions.

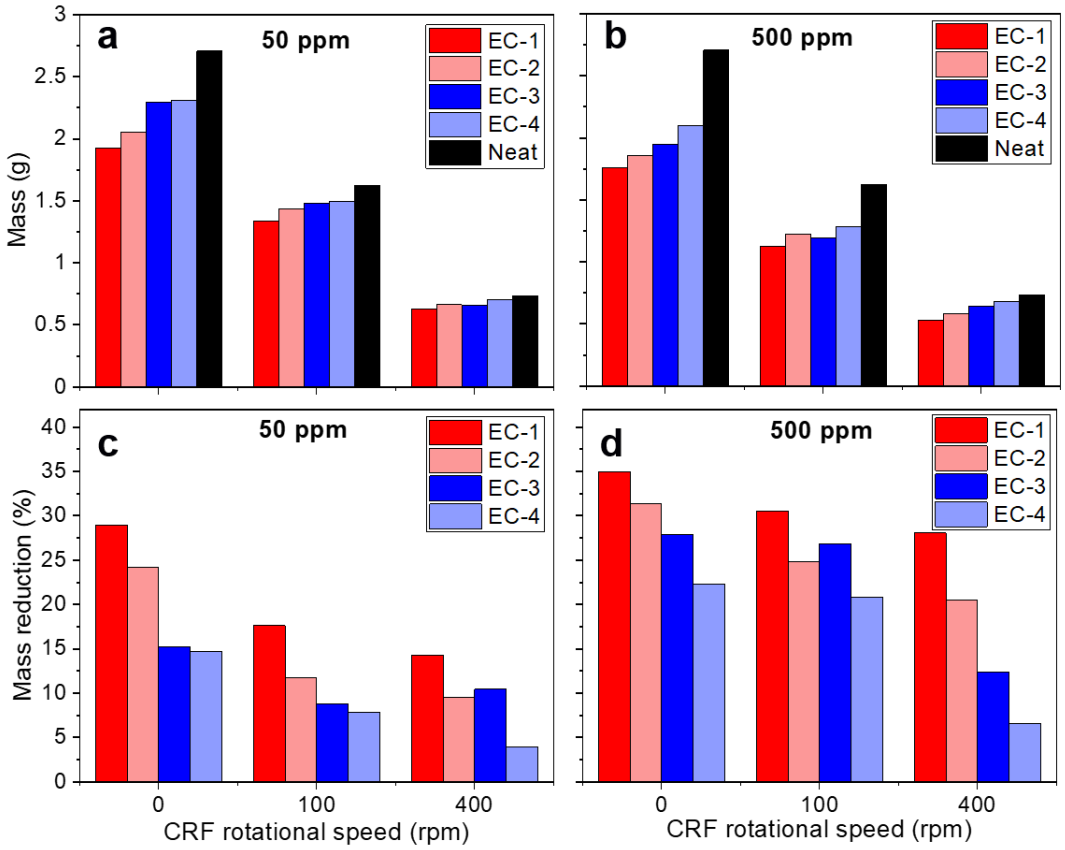

Figure 6.7. Mass of the wax deposit and mass reduction percentage as a function of inhibitor type, the CRF rotational speed and the inhibitor concentration (**a** and **c** 50 ppm, **b** and **d** 500 ppm). Experimental conditions: 5 wt% alkane wax-in-toluene and dodecane, T_{cold} = -5°C and T_{hot} = 35°C.

Table 6-5. Mass of the wax deposition and the calculated mass reduction percentage as a function of inhibitor type and the CRF rotational speed. Experimental conditions: 50 ppm inhibitor, 5 wt% alkane wax-in-toluene and dodecane, T_{cold} = -5°C and T_{hot} = 35°C.

50 ppm	**Mass (g)**			**Mass reduction (%)**		
	0 rpm	**100 rpm**	**400 rpm**	**0 rpm**	**100 rpm**	**400 rpm**
EC-1	1.92	1.3	0.62	28.94	17.60	14.29
EC-2	2.05	1.43	0.66	24.20	11.77	9.54
EC-3	2.29	1.48	0.65	15.249	8.81	10.45
EC-4	2.30	1.49	0.70	14.66	7.86	3.91
Neat	2.71	1.63	0.73	0	0	0

Table 6-6. Mass of the wax deposit and the calculated mass reduction percentage as a function of inhibitor type and the CRF rotational speed. Experimental conditions: 500 ppm inhibitor, 5 wt% alkane wax-in-toluene and dodecane, T_{cold} = -5°C and T_{hot} = 35°C.

500 ppm	Mass (g)			Mass reduction (%)		
	0 rpm	100 rpm	400 rpm	0 rpm	100 rpm	400 rpm
EC-1	1.76	1.13	0.53	35.01	30.57	28.09
EC-2	1.86	1.22	0.58	31.39	24.87	20.54
EC-3	1.95	1.19	0.64	27.90	26.85	12.41
EC-4	2.10	1.29	0.68	22.34	20.83	6.59
Neat	2.70	1.63	0.73	0	0	0

The difference in the wax inhibitors' performance is related to the difference in their chemical structures mainly with the degree of substitution of the EC backbone and the length of the alkyl chain substitution. Results shows that the higher degree of substitution and the longer the alkyl pendant chain leads to higher performance. For instance, EC-1 with the highest degree of substitution and alkyl pendant chain (DS=1 and alkyl chain = C22) shows an inhibition that goes up to 35% whereas EC-4 with the lowest degree of substitution and alkyl pendant chain (DS=0.4 and alkyl chain = C18) inhibits up to 22% only. The performance of the wax inhibitor depends greatly on their ability to interact with wax molecules. This interaction is driven by van der Waals attraction between the alkyl pendant chain and the wax molecule. The longer the alkyl pendant chain and the more abundant, the stronger is the van der Waals interaction between the inhibitor and the wax molecules. Previous studies have revealed that pendant chains of polymers play a distinct role in enhancing the performance of wax inhibitors. The higher similarity between the pendant chain structure and wax constituents results in the better performance[139, 201]. Relating back to the wax carbon chain length distribution of the model solution (cf. **Figure 4.9**), C22 has a greater

similarity to the alkane composition that C18 and is expected, therefore, to interact better with n-alkane in the solution or the deposit.

Besides, for the same size of pendant chain group, in this case EC-1 and EC-2, increasing the proportion of the pendant chain improves the performance of the additive. This effect is expected, given that the n-alkane in the solution or in the wax deposit tend to interact with Alkyl side chains while EC backbone interrupt wax crystal growth.

Results show that the increase in the wax inhibitor concentration induces a higher reduction in the mass of the wax deposit. For instance, EC-1 shows a reduction of 10%, 29% and 35% in the mass deposit at 5, 50 and 500 ppm respectively at 0 rpm. However, the decrease in the mass deposit doesn't correspond to the magnitude of change in wax concentration. While the concentration increases by 10 folds between 50 and 500 ppm, the wax deposit reduces by 6% only. An optimum wax inhibitor concentration should be therefore worked out between 50 and 500 ppm. Literature reports different results from the effect of inhibitor concentration on inhibition performance, with most of results showing inhibitors to perform better at higher concentrations[69, 201], while others show little difference or lower performance at higher inhibitor concentrations[40, 201].

The variance in flow regime between static, thermally-driven and sloughing regimes plays a vital role in the inhibitor performance as well. While inhibitors show the best performance at static conditions (35-22% for 500 ppm and 29-14% for 50 ppm), the performance of the inhibitors decreases with the increase of the CRF rotational speed in both thermally-driven regime (100 rpm with a maximum inhibition of 30%) and sloughing regime (400 rpm with a maximum inhibition of 28%). In dynamic flow, the performance of the inhibitors is affected by two main parameters,

the temperature change in the CRF system with the rotational speed, and the change in the chemical composition of the wax deposit with the change of the CRF the rotational speed. As shown in chapter 4 (**Figure 4.3**), at 100 rpm, the temperature of the bulk oil dropped significantly between 0 and 100 rpm. This drop in the temperature may reduce the solubility of the inhibitors in the solution making them less effective. In literature, the performance of a chemical inhibitor is reported to be temperature-dependent[206]. The paraffin inhibitors were effective at high temperature and became insignificant at lower temperatures. The cooling rate also significantly influences the effectiveness of wax inhibitors: increasing cooling rate (at higher rotational speed) may weaken the interactions between the wax inhibitor and paraffin waxes, thus reducing the effectiveness of inhibitor[126].

Besides, previous results reported in chapter 4 (cf. **Figure 5.3**) show that the rotational speed has a great impact on the chemical composition of the wax deposit with a shift towards the high molecular weight wax. The inhibitor with alkyl pendant chain of C18 and C22 are more likely to interact with low molecular weight wax due to higher similarity in chain length than the high molecular weight wax making them less efficient with inhibiting wax deposition in dynamic conditions. Similar observations in the literature are reported where the inhibitors were also observed to be ineffective for higher molecular weight paraffin contents with higher carbon numbers (C34 and above). However, the inhibitor had an effect on smaller carbon contents in paraffin and on the total amount of deposited waxes[207].

In the sloughing regime, the effect of wax inhibitors is controversial in the literature depending on the type of inhibitor itself and the operating conditions. Some researchers[126] found that shear results in a decline of the effectiveness of the inhibitor. The result may be understood in the context

of crystal–crystal bonds, which when ruptured by forced shearing do not reform. Hence, shear-stabilized waxy oil doesn't show a benefit from chemically treated environment. Other researchers[40, 52] concluded that the inhibition effectiveness of wax inhibitors increases consistently with increasing shear. Paraffin inhibitors are chemicals that incorporate into wax deposit structures and alter the deposit's ability to cohesively adhere to surfaces or itself. Ideally, the inhibitor weakens the deposit allowing removal of the deposit by shear forces present in flow streams[40]. In our particular case, the wax deposit is less likely to be sloughed with the incorporation of cellulose which is considered to be a superior material for reinforcement due to its rigidity and stiffness [208].

It should be noted that the percentage of wax deposit inhibition reported in **Table 6-5** and **Table 6-6** is calculated based on the amount of total deposit weight (deposited wax with entrained crude oil). This calculation does not give any exact percentage of the wax deposition reduction. Jennings et al.[40] reported that the inhibitor performance did not always increase with increasing shear, even decreasing in many cases. This is not related to a reduction of inhibitor performance but rather due to variation in the untreated deposit reference with shear. As the amount of entrained crude oil in a deposit decreases with increasing shear, the percent change on the total deposit weight (deposited wax plus entrained crude oil) will vary for a paraffin inhibitor's effect on a fixed amount of deposited wax species[40]. In our case, looking at **Figure 6.8** that shows the wax deposit at 0rpm in neat conditions and in the presence of 500 ppm EC-1, the images show clearly the high porosity of the wax deposit in the presence of the EC-1 inhibitor suggesting a higher amount of oil entrapped and less wax percentage. Therefore, our study should be carefully taken to further investigations into the exact amount of alkane wax (without oil) change with the presence of inhibitor at all flow regimes.

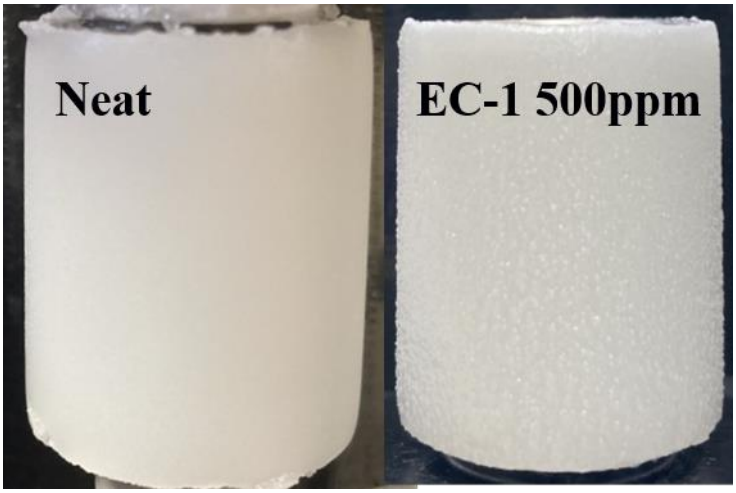

Figure 6.8. Images of wax deposits formed after 30 min under Neat condition and in the presence of 500 ppm EC-1.

6.5.7 Deposit Chemical Composition (GC-FID)

GC-FID was used to measure the composition of the wax deposit as a function of inhibitor type, inhibitor concentration and CRF rotational speed. A typical composition of the wax deposit included strong signals for carbon chain lengths between C_{20}-C_{41} and weak signals for carbon chain lengths between C_{42}-C_{45} (only trace amounts), hence the latter was neglected in further analysis. It should be noted that the composition of the wax deposit was determined on a solvent-free basis where the GC-FID analyses were normalized by omitting peak areas below C_{17}. The analysis doesn't account therefore for the change in the oil percentage at the different operating conditions.

Figure 6.9 shows the composition of the deposited wax in a neat solution as a function of CRF rotational speeds at 0, 100 and 400 rpm. The dashed lines represent the carbon chain length distributions of the low and high molecular weight waxes used in the model oil. As discussed previously, the carbon chain length distribution of the deposited wax is seen to shift towards the

higher carbon chain length distribution when the CRF change from static to dynamic regime (100 rpm) and the shift becomes more significant at 400 rpm. The change in the chemical composition is mainly due to aging accelerated by the flow which implies displacement of the oil outside the wax deposit by the force of shear stress. The expelled oil contains soluble LMW n-alkane which enrich the wax deposit with HMW n-alkane (cf. **Figure 5.3**). **Figure 6.9** is to be compared to **Figure 6.10** representing the change in the chemical composition of the wax deposit in the presence of the 4 wax inhibitors at 500 ppm.

Figure 6.10 shows that the presence of the inhibitors has an impact on the chemical composition of the wax deposit. At 0 and 100 rpm, the neat solution shows a high percentage of LMW n-alkane in its spectrum, this percentage decreases in the presence of the wax inhibitors with the lowest percentage of LMW n-alkane found in the wax deposit of EC-1. This result confirms that the wax inhibitor is selective for LMW n-alkane and less effective for the higher n-alkane chain length. As discussed previously, the alkyl pendant chain of the inhibitor shows optimum performance when it is compatible with the length of the n-alkane in solution. This result suggest as well that the wax inhibitor interact with the wax molecules mostly in solution, preventing them from depositing rather than co-crystallizing with the n-alkane in the wax deposit and cause steric hindrance. The change in the percentage of LMW n-alkane in the wax deposit is proportional to the degree of substitution with maximum inhibition for EC-1 (DS=1), similar inhibition for EC-2 and EC-3 (DS=0.6) and low inhibition for EC-4 (DS=0.4).

At 400 rpm, EC-1, EC-2, EC-3 shows minimal presence of the LMW alkane and the wax deposit falls mainly within the HMW alkane composition. This result is due to the presence of a small concentration of LMW n-alkane that can deposit at 400 rpm (as seen from the neat deposit)

and the inhibitors EC-1, EC-2 and EC-3 prevent them all from depositing. These results show that the decrease in the wax inhibition percent at higher CRF rotational speed is due to the change in the chemical composition of the wax deposit itself. Being rich in HMW alkane, the inhibitors are less effective in preventing the HMW wax from depositing on the cold surface.

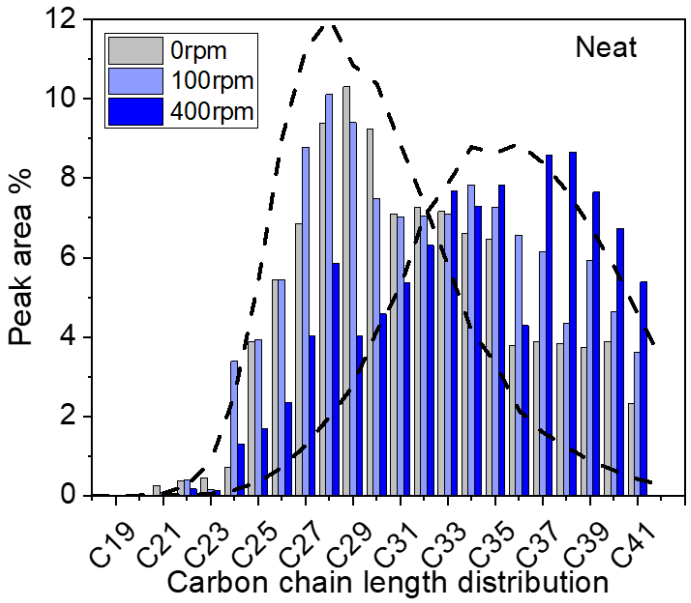

Figure 6.9. a) Carbon chain length distribution of the wax deposit of the neat solution at 0, 100 and 400 rpm. The dashed lines represent the carbon chain length distributions of the low and higher molecular weight wax fractions.

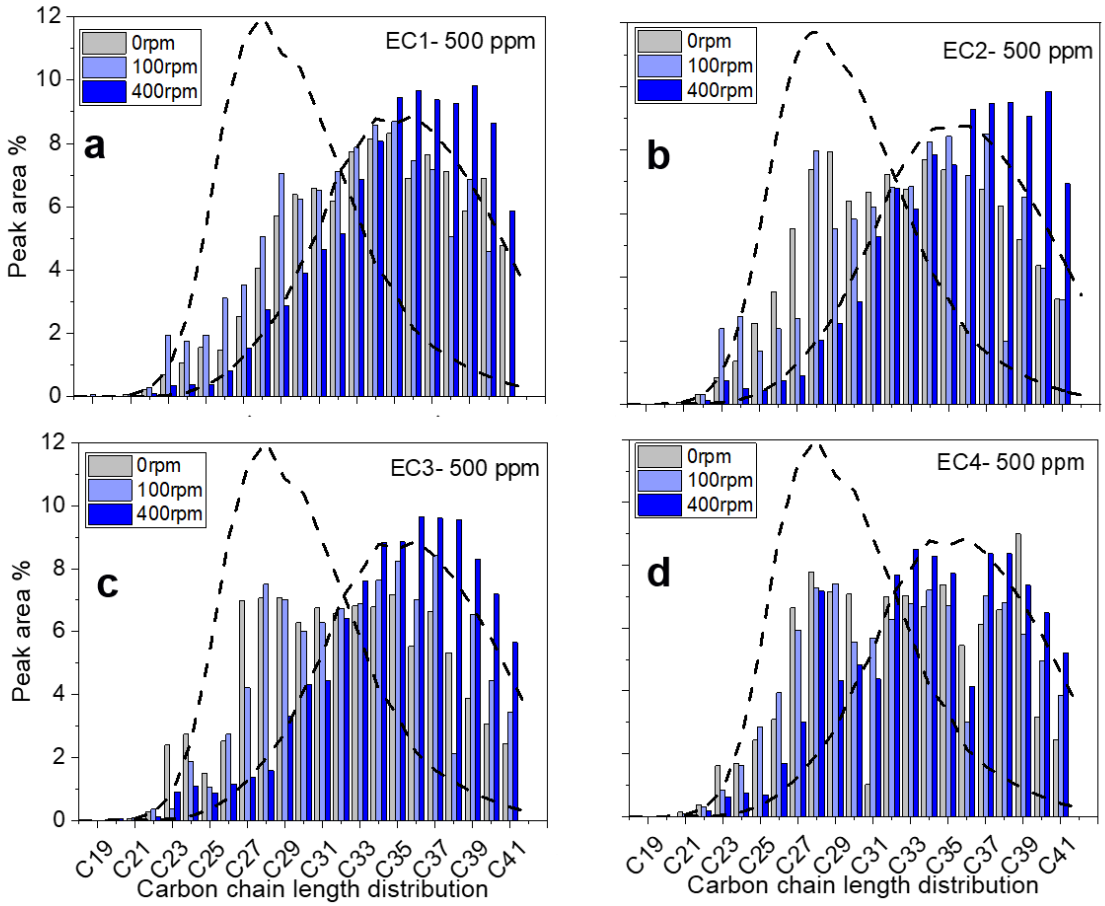

Figure 6.10. Carbon chain length distribution of the wax deposit as a function of inhibitor type (500 ppm) at 0, 100 and 400 rpm. The dashed lines represent the carbon chain length distributions of the low and higher molecular weight wax fractions, **a)** EC-1 **b)** EC-2 **c)** EC-3 **a)** EC-4.

Figure 6.11 shows the effect of the concentration of 50 and 500 ppm EC-1 on the chemical composition of the wax deposit at 0, 100 and 400 rpm. Results show that at 0 rpm, the inhibitor concentration has a great effect on the wax deposit composition. The higher the inhibitor concentration, the lower is the concentration of LMW n-alkane. This observation is similar but less expressed for 100 rpm. However, at 400 rpm, the concentration of the wax inhibitor has a minimal effect on the composition of the wax deposit as already only a low percentage of LMW wax may deposit.

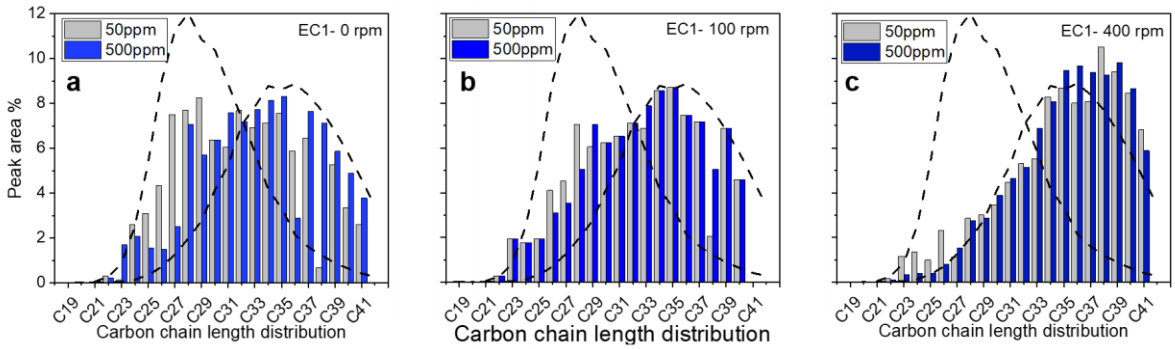

Figure 6.11. Carbon chain length distribution of the wax deposit in the presence of EC-1 at two concentrations: 50 and 500 ppm **a)** 0rpm **b)** 100 rpm **c)** 400 rpm. The dashed lines represent the carbon chain length distributions of the low and higher molecular weight wax fractions.

6.6 Conclusions

Four ethylcellulose derivative wax deposition inhibitors were synthesized with variant length of the alkyl pendant chains (C18 and C22) and variant degree of substitution. The inhibitors' chemical structures and thermal stability were confirmed by FTIR spectroscopy, Elemental analysis and TGA. Using a model waxy oil composed of a blend of low and high molecular weight paraffin wax-in-dodecane/toluene (1:1), the WAT of the solution was measured with and without the presence of inhibitor and the mass of wax deposition was tested using the CRF for a test of 30 minutes at 0, 100 and 400 rpm using 50 and 500 ppm of each inhibitor. The WAT does not change in the presence of inhibitor, however, the crystallisation kinetic was faster in the neat solution and the inhibitor accelerated the dissolution of the wax in the solution. On the CRF, all four polymeric additives exhibit good efficiency as wax deposition reducer at all flow regimes, however the chemical structure of the inhibitor and the flow regimes were significant parameters influencing the efficiency of the wax inhibitor. With respect to the inhibitor chemical structure, the best

performance was attributed to the inhibitor with the highest degree of substitution and longer pendant chain (C22) EC-1 with inhibition of 35% at 0rpm compared to 22% only for EC-4. This is can be related to a better interaction of the polymer additive EC-1 with the n-alkane molecules through the long and abundant alkyl pendant chains. The wax inhibitor with a shorter pendant chain and lower degree of substitution EC-4 exhibits a weaker van der Waals bond with the wax in the solution. According to the flow regimes, the inhibitors efficiency was the highest at 0 rpm and decrease gradually with 100 and 400 rpm. This decrease in efficiency is related to the change in the chemical composition of the wax deposit at different flow regimes. At 0 rpm, the wax deposit is rich with LMW n-alkane, therefore, the wax inhibitor is highly efficient preventing these LMW n-alkane from depositing. The chemical composition of the wax deposit at 0 rpm in the absence as compared to the neat solution, shows a shift towards the HMW n-alkane. At higher CRF speed, the shift towards HMW n-alkane in the presence of the inhibitor is less significant as already, in the neat wax deposit, the amount of LMW n-alkane is small. The GC-FID results show that the reduction in the inhibitor efficiency is due to the decrease of the potential concentration of LMW n-alkane that may deposit in the dynamic regime.

Chapter 7 The Study of the Formation of Incipient Wax Deposit using a QCM with Heat Transfer

7.1 Synopsis

The formation of the incipient wax deposit on a cold surface was studied using a quartz crystal microbalance with heat transfer across the crystal (HT-QCM) and a model system of linear n-alkane (C20 to C40) dissolved in dodecane to 0.5 wt% set to room temperature. The mechanism of wax adsorption was studied by varying the temperature of the cooling fluid to T_{room}, 10, 0, -10 and -20°C and measuring the frequency and resistance changes. Results show that the decrease in the coolant temperature gives a smaller induction time for wax crystallisation attributed to a higher supersaturation at higher cooling rates. Besides, the frequency shift decreases significantly with relatively small change in the resistance, evidencing a solid mass adsorbing on the QCM crystal.

7.2 Introduction

The mechanism of incipient wax deposition in non-isothermal system and the first stage of wax crystal formation on a cold surface is not very well investigated experimnetally[53, 209].

Various hypothesis are often proposed in the literature, concerning the incipient wax deposition mechanism. The first hypothesis postulates that waxes initially adsorb onto a metal deposition surface. The adsorbed organic layer then establishes a hydrophobic surface for the co-crystallization of waxes from solution. The second hypothesis postulates that the incipient wax

deposits form as a gel, which adhere to the deposition surface. A third hypothesis states that wax crystals become mechanically entrapped by the roughness of the inner pipe wall surface. Concurrently, growing paraffin crystals in the bulk fluid near the interface agglomerate and form a coherent gel together with the crystals entrapped at the metal surface[53, 209]. To date, wax deposition investigations have not been able to confirm either of these hypothesized mechanisms. Because of the lack of fundamental knowledge of the incipient paraffin deposition mechanism, forecasts for whether paraffin deposition will occur in a given pipeline are often poor[183].

Experimental evidences of alkane adsorption at solid-liquid interfaces using scanning tunnelling microscopy (STM), neutron diffraction, and sum frequency generation spectrometry techniques indicate that linear alkane molecules adsorb from liquid solution unto various solids, including gold, graphite, quartz, WS_2, and MoS_2, suggesting that an adsorption mechanism is feasible[210, 211]. A number of molecular simulation investigations have demonstrated that paraffin molecules adsorb to solid interfaces as well[212]. However, delineating the competing hypothesis based on these findings is challenging because the techniques mentioned were operated at isothermal conditions different to wax deposition thermal condition. More experimental evidences based on a surface technique capable of isolating the interfacial wax layer at non isothermal conditions are required.

On the other hand, the CRF operating at different rotational speeds, coupled with GC-FID analysis, emphasised the change in the mechanical properties and the shear modulus of the wax deposit layer in the different flow regimes and their behavior at different flow shear stress, however, there was no mean in our laboratory or in the literature to measure the viscoelastic properties of the wax deposit layer *in situ*, while the wax layer is forming and rheological proprieties were mostly investigated in bulk[30, 50, 61].

Herein comes a technique that could be useful in order to investigate the wax deposition on surface and the properties of the viscoelastic wax deposition layer, the Quartz Crystal Microbalance (QCM). The QCM is essentially an ultrasensitive mass balance that consists of a dip probe which contains a thin AT-cut quartz sheet with two electrodes plated onto it. When an alternating current is passed through the two electrodes, the crystal oscillates at a characteristic frequency. When the crystal sensor is exposed to a new medium of different physical properties, it experiences a shift in its resonance that is proportional to the properties of the new medium. Traditionally the QCM has been used as a quartz-based device for measuring small 'micro' masses per unit area as its name suggests, however the device since had its use extended to include measurements in liquid environments where the shift in crystal resonance was found to be proportional to the product of the viscosity and density for a non-adsorbing Newtonian fluid[213].

The quartz crystal microbalance (QCM) was chosen as a potential candidate because of its unique ability to determine the mass of wax depositing layers in real time while simultaneously giving information about their viscoelastic properties. In contrast to conventional techniques based on property changes in the solid or solution phase, the proposed QCM technique simultaneously exploits property changes in both the solid and solution phases, such as the solid mass and liquid viscosity. It has the ability to analyse the crystallization processes, the induction time of nucleation, the type of adsorption pattern that the wax particles exhibit and the mechanism of formation of the first wax layer. Most importantly, it is can measure the viscoelastic properties of the wax layer formed on a metal surface *in situ* in real time.

In the literature, few studies have been considering the QCM for wax deposition studies. Paso et al.[53] investigated the properties of incipient wax layers at the solid-liquid interface between

stainless steel and model petroleum fluids using a QCM at isothermal conditions. Monitored changes in resonance frequency and energy dissipation of the quartz crystal resonator immersed in the model fluids at different wax concentrations confirm that no continual deposition of paraffin components occurs at isothermal conditions. Solid paraffin crystals dispersed in solution show no adherence to the stainless-steel surface. Liu et al.[214] developed an isothermal QCM for the in-situ analysis of the cooling crystallisation processes of a model solution at supersaturation, induction point of crystal nucleation and crystal growth. The observation and the results show that QCM response followed a monotonically shifting path that depended on the viscosity change when cooling the solution. However, the frequency and resistant varied significantly at the induction point of crystal nucleation as the viscous liquid film on the sensor suddenly shifts to an elastic solid phase. Thereafter, the QCM responses are mainly controlled by the suspension viscosity due to simultaneous crystal nucleation and growth with further cooling. Burgass et al.[215, 216] have developed a small volume testing facility based on QCM for measuring wax phase equilibria and optimising inhibitor deployment. The QCM was locally cooled to create a temperature gradient between bulk fluid and the surface of the QCM, simulating pipeline wall cooling effect. The developed device needs 35 ml of fluid and can work at high pressure conditions, simulating the effect of pressure and dissolved gas on wax phase behaviour and adhesion tendencies. Burgass used the QCM to determine WAT/WDT with and without inhibitors at atmospheric and high pressure by measuring changes in resonance frequencies with temperature reduced continuously to find the WAT and by step-heating or continuous heating at a slow rate to determine WDT.

The present research investigation stems from the need to understand the mechanism by which wax deposits initially adhere to solid surfaces in petroleum systems. A new QCM with heat transfer (HT-QCM) is developed for studying wax deposition, and promises to provide new insight into the role of surface chemistry in the formation of incipient wax deposits. The current study presents

a new QCM technique in which a temperature gradient is imposed in the direction normal to the deposition surface. The deposition chamber used in the experiments is also designed to accommodate a continuous flow of fluid across the crystal surface, qualitatively emulating the heat, mass, and momentum transfer conditions associated with wax deposition in oil pipelines. The new QCM technique is applied to investigate the physical nature of incipient wax deposits formed on gold sensor surface to study the crystallisation/deposition behaviour of the wax under heat transfer conditions and to induce the viscoelastic properties of the wax layer *in situ* at varying temperature conditions[209].

7.3 QCM Instrument Development and Theory

7.3.1 QCM Instrument Development

A QCM200 probe (Stanford Research Systems, USA) housing a 25.4 mm, 5 MHz gold-coated sensor was modified and used for wax deposition studies. A special fluid chamber was designed with the capability to impose a temperature gradient in the fluid regions above the piezoelectric quartz crystal. The fluid chamber is positioned between a lower thermal block and an upper thermal block, such that an applied temperature difference between the upper and lower blocks results in a temperature gradient in the vertical direction.

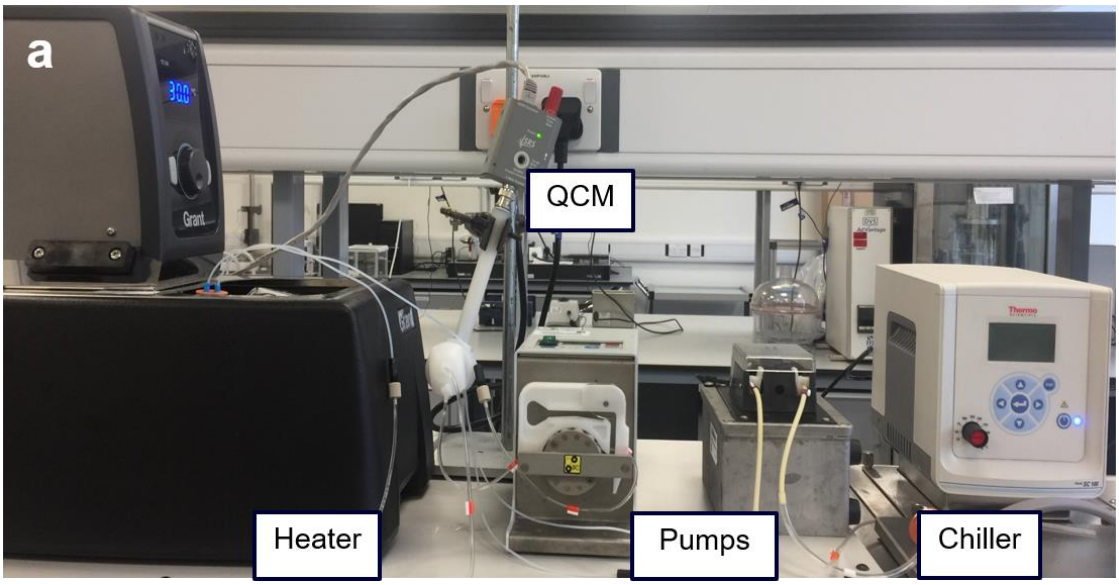

Figure 7.1. Modified QCM set up to provide cooling on the sensor surface and heating of the continuously flowed waxy solution.

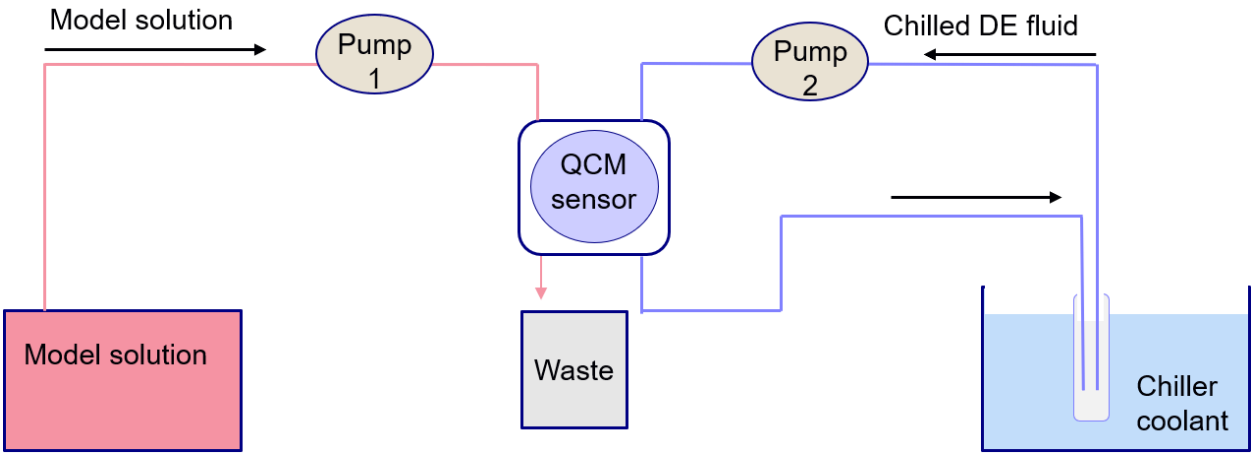

Figure 7.2. Modified QCM Flow diagram.

The lower thermal block, which is the air chamber just below the QCM sensor, is filled with cooling liquid. The cooling liquid is a dielectric fluid (DE), a type of non-conductive liquid to avoid shortcut current between detectors on both sides of the QCM surface. Galden DE, low

molecular weight Perfluoropolyether (PFPE) was chosen due to its high thermal stability up to 290 ^{o}C, very good dielectric strength, excellent chemical inertness and good compatibility with metals, plastics and elastomers[217]. The filling process of the lower thermal block is managed by digging two holes in the back of QCM holder (cf. **Figure 7.3**a) and connect it via a set of tubing (ISMATEC PhthalateFree PVC pump tubes 95625-22 0.64mm ID) and peristaltic pumps (ISMATEC Reglo Digital) to a DE tube immersed into a Chiller bath (Thermo Scientific™ ARCTIC A10B Refrigerated Circulators). All the process is very well sealed to minimise both DE vaporisation and thermal loss.

The upper chamber block, is a Flow Cell Adapter (SRS Part# O100FC) attached to the crystal holder and filled with the model solution heated to a desired temperature. The flow cell is connected via a set of tubing (ISMATEC PhthalateFree PVC pump tubes 95625-22 0.64mm ID) and peristaltic pumps (ISMATEC Reglo Digital) to the model solution flask at the inlet port and to a waste flask at the outlet port. The model solution flask is immersed into a heating bath (Grant, Optima T100 Heated Circulating Bath) to control its temperature. A cross sectional view of the Axial Flow Cell, including a schematic representation of the flow in the Flow Cell, are shown in **Figure 7.3**.

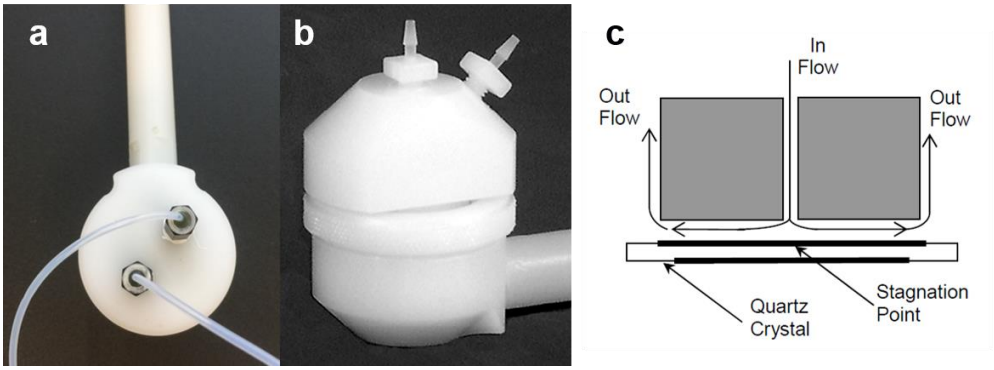

Figure 7.3. a) Close up of modified HT- QCM holder where the cooling fluid circulate **b)** the axial flow cell adapter mounted on a crystal holder **c)** Schematic representation of the liquid flow pattern in the Axial Flow cell taken Stanford QCM200 manual[218].

In the axial flow cell, the sample flows radially outward from the input port at the centre of the cell to the exit channel at the edge of the cell, in a volume of about 150 µl. The sample solution is perpendicularly injected towards the flat surface of the QCM crystal. A stagnation point is located at the centre of the crystal electrode, overlapping the area of highest sensitivity of the flat QCM oscillator. The hydrodynamics associated with stagnation point flow are well understood. At the stagnation point there is zero hydrodynamic flow - i.e. without surface shear forces. While the injected solution flows about the stagnation point, any exchange with the surface of the crystal is diffusion limited. Thus, the rate of adsorption of the sample molecules (or particles) to the crystal surface is diffusion limited as well. The stagnation point flow cell was specifically designed for the study of adsorption kinetics of particles, micelles and chemical and biological molecules at solid-liquid interfaces, under well-controlled hydrodynamic conditions[218].

7.3.2 QCM Theory

A quartz crystal microbalance (QCM) is an instrument that monitors very small changes in mass and viscosity with respect to the presence or state of a given system in real-time. This facility

can be used to monitor thin film deposition rates, molecular presence/weight or molecule to surface affinity kinetics in chemical or biological systems. QCM uses the piezo-electric effect of a thin quartz crystal between two electrodes. When a mechanical strain is applied to a piezo-electric material, this results in the generation of an electrical potential across that material. Resonance of the system is highly sensitive to the thickness of the crystal/electrode system and the acoustic frequency. The fundamental frequency of the QCM will therefore decrease with increasing mass deposited on the crystal, as there is a consequent increase in the piezo-electrode system thickness. The change of mass per unit area at the crystal surface caused by adsorption or deposition of a material, can then be mathematically related to the resultant change in frequency according to the Sauerbrey relationship as follows [219].

$$\Delta F = \frac{-2\Delta m n f_0^2}{\left(A\sqrt{\mu_q \rho_q}\right)} \qquad \text{Eq. 7.1}$$

where ΔF = change in frequency of oscillation, Δm = change in mass of the system, n = overtone number, f_0 = fundamental mode oscillation frequency, A = contact unit area, μ_q = shear modulus of quartz ($2.947.10^{11}$ g/cm.s^2) and ρ_q = density of quartz (2.648 g/cm^3).

The main assumption from this relationship is that the mass that is added onto the crystal surface experiences no shear deformation during oscillation[220]. The film must be completely rigid meaning that any changes in motional resistance or other dampening processes are zero by definition. The film does not have to be uniform for its area-averaged mass per unit area to be measured accurately, however entrainment of a bulk medium may be a concern for heterogeneous films since it may add to the detected QCM mass and therefore introduce frequency shifts that do not accurately reflect the mass per unit area of the deposited film[221, 222]. Non-rigid films such as point contact loads from particle adsorption or viscoelastic materials behaving create dampening processes in

addition to a shift in resonance frequency. Different methods are used to measure these dampening processes, with the primary three being dissipation factor (*D*), half-band-half-width (Γ) and motional resistance (*R1*)[222].

Until fairly recently, it was believed that excessive viscous loading would prohibit the use of the QCM in liquids. In fact, operation in liquids is indeed possible[223], and the response of the QCM is still extremely sensitive to mass changes at the crystal-solution interface. For many years, QCMs have been used in direct contact with liquids and/or viscoelastic films to assess changes in mass and viscoelastic properties during chemical and electrochemical surface processes. When the QCM comes in contact with a solution, there is a decrease in frequency that is dependent upon the viscosity and the density of the solution. A quantitative understanding of the resonator behavior is a prerequisite for proper interpretation of experimental results under total liquid immersion. This problem was first treated by Glassford[224], and later by Kanazawa and Gordon[225].

Kanazawa and co-workers [226] derived an experssion used to determine the frequency change when the crystal has been submerged into a nonadsorbing fluid. This expression is expressed as the equation below:

$$\Delta F = -f_0^{\frac{3}{2}} \left({\eta_s \rho_s}/{\pi \mu_q \rho_q} \right)^{\frac{1}{2}} \qquad \text{Eq. 7.2}$$

where η_s = viscosity of the solution and ρ_s = density of the solution.

7.4 Materials and Experimental methods

A model waxy oil composed of 0.5 wt% n-alkane wax-in-dodecane (WAT= 12 ^{o}C) composed of low (C_{20}-C_{40} [manufacturer quoted distribution, Merck, UK], melting point 58-62°C) and high (melting point 65-71°C, Fisher Scientific, UK) molecular weight solid n-alkane waxes, and dodecane (Acros Organics, UK) with a boiling point of 170-195°C and density of 0.751 g/cm^3 was used throughout the study. All chemicals were acquired from Sigma-Aldrich and used without further purification.

7.4.1 Methodology

All the QCM experiments were performed on a basis of some identical operating conditions; First, before starting any experiment, every component was thoroughly checked and cleaned with acetone, the QCM sensor was cleaned with a solution of DIwater:Acetone = 4:1 v/v, and dried with a nitrogen flow and left in a UV-Ozone cleaner (Bioforce Nanoscience, USA) for 3h to remove any contamination. Besides, all the deposition experiments were set at an identical pumps' flow. The flow rates were set to 15 ml/min.

In each experiment, resonance frequencies and resistance are monitored for the 1st (fundamental) overtone. Capacitance cancellation was checked and readjusted every time the environment around the crystal is changed. For instance, when transitioning from air to DE, from DE to dodecane and from dodecane to n-alkane wax-in-dodecane solution. For operation with flow cell, special attention when filling the flow chamber for the first time so that no air bubbles get trapped in the measurement volume. The reproducibility of tests was assessed by repeating each experiment 3 times.

7.4.2 WAT measured by Light Transmission

The WAT of 0.5 wt% n-paraffin-in-dodecane (composed of 1:1 mass basis for low and high molecular weight waxes) was measured by turbidity performed at different cooling rates using the Crystal 16 apparatus (Technobis). The Crystal 16 comprises of sixteen sample wells split into four blocks. Each block is independently temperature-controlled and enables a range of cooling rates to be studied simultaneously. Samples were added to 1 mL glass vials. The solution turbidity (transmission %) was measured as a function of temperature. Each test began by heating the samples to 60°C and held at temperature for 30 min to ensure thermal equilibrium. Then the samples were cooled at 0.5 °C /min to 0°C while stirred using a magnetic flea. The WAT was taken to be the temperature at a light transmission value of 90% (fully transparent sample = 100%).

7.4.3 HT-QCM Test

Before deposition experiments, the functionality of the HT-QCM was first tested with a preliminary test. The test aims to measure the frequency shift of air-water with and without the presence of the DE fluid both at room temperature and compare it to the theoretical shift calculated by Kanazawa. To this end, the QCM was first filled with water at room temperature and the resonance frequency measured until a baseline was established. The experiment was then repeated with a calibration in DE-air first until a stable baseline line was achieved, then the capacitance was cancelled and the QCM probe filled with water until the resonance frequency measured reached a new baseline. Air-water frequencies shifts with and without DE are plot in **Figure 7.4**. The same experiment of water was repeated with dodecane set at 45^{o}C and the results are shown in **Figure 7.5**.

7.4.4 Wax Deposition Experiment

The deposition of wax onto a gold surface was studied using 0.5 w% n-alkane wax-in-dodecane model solution. In an initial experiment, both the DE fluid and the dodecane solution were first injected into the measurement chamber at the desirable operating conditions, and baseline frequency values were recorded. After stable resonance frequency values were observed, the capacitance was cancelled and a continuous flow of the 0.5 wt% n-alkane wax solution was pumped to the flow cell chamber.

Both the R-F and the resistance were recorded and plot in **Figure 7.6**.

7.5 Results and Discussion

Figure 7.4 compares the shift in the fundamental resonance frequency (5 MHz) when the QCM is transitioned from resonating in air (room temperature) to resonating in water (room temperature), with the back-face of the gold sensor either in air (without DE) or contacting the DE fluid.

The air-to-water transition without DE (**Figure 7.4**a) shows a good repeatability with a frequency shift of ~750 Hz. The frequency shift under total immersion in a nonadsorbing fluid depends on the change in the solution properties i.e. viscosity and the density of the fluid in contact with the QCM sensor, as demonstrated by Kanazawa equations. The theoretical frequency shift calculated by Kanazawa (density of water = 0.9982 g/cm^3, viscosity of water = 0.010016 g/cm.s both at 20 ^{o}C)[227], was 715 Hz for an air-to-water transition at 20°C, assuming the electrode capacitance has been cancelled.

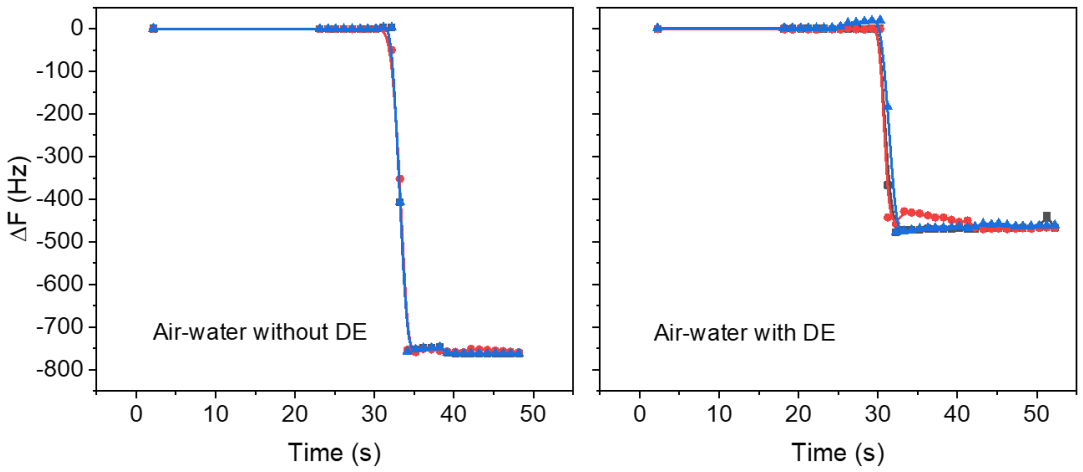

Figure 7.4. QCM resonance frequency shift from air-to-water **a)** without DE and **b)** with DE at room temperature. Repeat measurements are shown by the different coloured symbols.

The experimental result shows a slight deviation from the theoretically calculated value (difference of ~35 Hz), and maybe due to a slight difference in the fluid temperature and/or a slight variation induced by the clamping mechanism of the sensor in the QCM holder. However, it worth noting that the discrepancy in the frequency shift is small compared to the shifts measured during wax deposition, hence the slight variation can be considered negligible. Figure 4b shows the air-to-water frequency shift in the presence of DE fluid. The frequency shift is lower (~450 Hz) and results from a reduction in sensitivity due to the dampening of the QCM resonance frequency by the DE fluid. While these experiments are not common, the data in **Figure 7.4**b confirms that a stable resonance frequency can be maintained with the back-face of the QCM sensor is contacted with the DE fluid and the front-face of the QCM sensor is contacted with another liquid. Thus, the setup is suitable to study wax deposition.

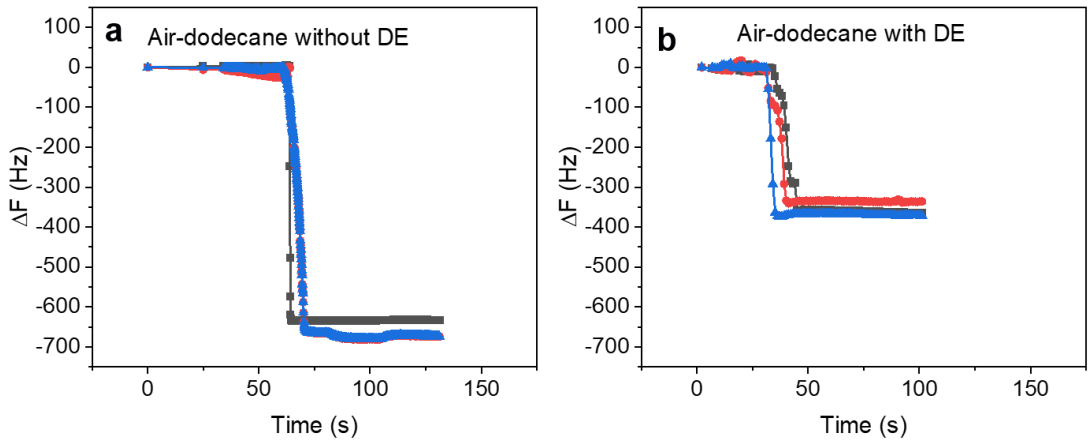

Figure 7.5. QCM frequency shift from air-to-dodecane **a)** without DE and **b)** with DE. The dodecane and the DE fluid were pumped into the QCM measurement cell at room temperature. Repeat measurements are shown by the different coloured symbols.

Figure 7.5 shows the air-to-dodecane frequency shifts with and without the DE flowing in the lower thermal chamber (sensor back-face). **Figure 7.5** shows a similar behaviour to the results in **Figure 7.4**. The flow of dodecane through the measuring chamber induces a decrease in the frequency shift due to changes in the density and viscosity of the fluid in contact with the QCM sensor. Comparing the experimental frequency shift (~680 Hz) to the theoretical frequency shift (716 Hz) (density of dodecane = 0.751 g/cm^3, viscosity of dodecane = 1.34 mPa.s both at 22^{o}C)[228], the difference again can be considered negligible, with the slight variation resulting of the points previously mentioned. In the presence of the DE fluid (**Figure 7.5**b), the decrease in the resonance frequency is ~350 Hz, highlighting the reduced sensitivity.

7.5.1 Wax Deposition Experiments

Using a 0.5 wt% n-alkane wax-in-dodecane solution, wax deposition was studied at non-isothermal conditions using the HT-QCM, with the temperature of the flowing oil maintained at

room temperature (> WAT), and the surface of the QCM sensor chilled to 10, 0, -10 and -20 °C. Both the frequency shift and the resistance were recorded with time. **Figure 7.6** shows the frequency shifts for the different temperatures, along with repeats (3 × repeat) at all measurement conditions. Time, t = 0 s corresponds to the initial time when the waxy fluid is pumped from feed vessel which was maintained at room temperature.

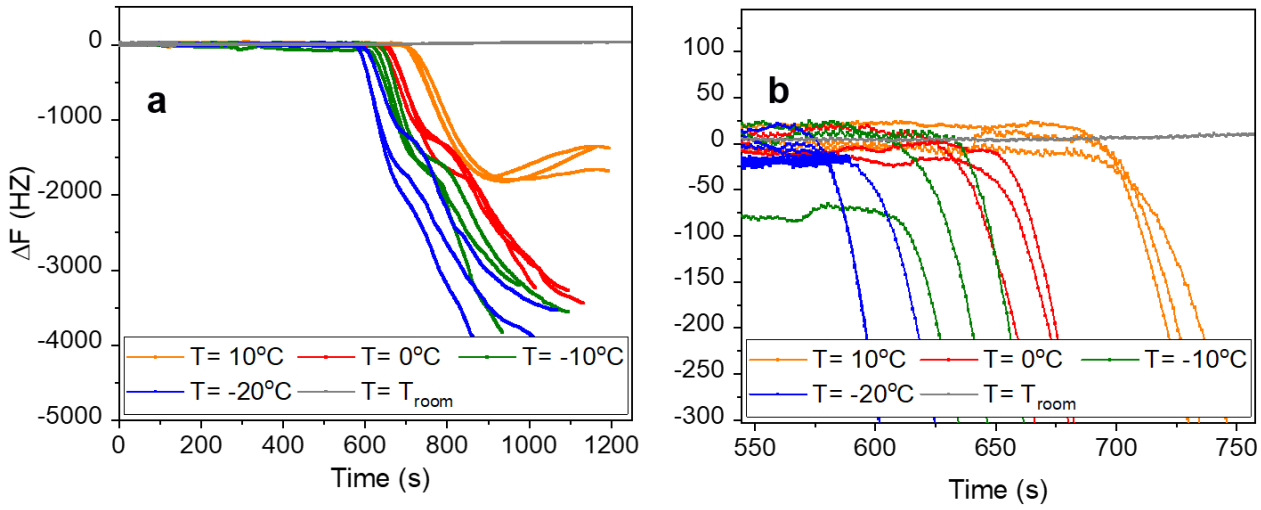

Figure 7.6. a) QCM frequency shifts from a baseline of pure dodecane to 0.5 wt% n-alkane wax-dodecane (WAT = 12°C) with the waxy fluid at room temperature (T_{room}) and the flowing DE fluid at $T_{chiller}$ = T_{room} 10, 0, -10, -20 °C, **b)** close-up of figure a.

The data in **Figure 7.6** shows that when $T_{chiller}$ > WAT (T = T_{room}), the frequency of the QCM sensor remains unchanged. However, when $T_{chiller}$ < WAT the resonance frequency of the QCM changes and shows two behaviours with respect to time. Initially, the resonance frequency is approximately stable with a constant baseline response. However, at a critical time the resonance frequency begins to drop sharply by -10^3 orders of magnitude. Such large shifts in resonance frequency relate to the crystallisation of alkane waxes onto the sensor cold surface. Depending on

the cold-side temperature, the frequency shifts can be in the order of 4000-5000 Hz, as such, the resonance of the QCM is sufficiently damped that it can no longer oscillate.

It is believed that the frequency shift resulted from the injection of the n-alkane wax-in-dodecane solution in the QCM chamber is mainly due to either the wax crystallisation in the bulk solution of dodecane inducing a higher viscosity or deposition of wax on the QCM surface as a viscoselastic film. The QCM was already stabilised at DE-dodecane conditions before the n-alkane wax-in-dodecane solution was injected, and the change in density and viscosity between the dodecane and n-alkane wax-in-dodecane mixture (without any wax crystallisation) is believed to cause a negligible frequency shift that is within the experimental error.

Figure 7.6 shows that the frequency shifts at $T_{chiller}$= 0, -10 and -20^{o}C didn't reach a steady and the wax kept crystallising on the QCM sensor until the frequency shift went outside the range. However, the frequency shift at $T_{chiller}$= 10 ^{o}C stabilised at ΔF between -1700 and -1500 HZ. It is believed that the at $T_{chiller}$= 10 ^{o}C, the system reached its steady state and the interfacial temperature between the wax crystals and the oil is within the WAT limits. At steady state, there is a thermodynamic equilibrium that induces consecutive dissolution and crystallisation of the wax crystals. This can be seen clearly from the fluctuance in the frequency shift with a range of 200 HZ, reaching a minimum at ~-1700 HZ, then increasing slightly to -1500 Hz, then starting back to decrease.

The change in resonance frequency can be used to determine an apparent mass of wax deposited using the Sauerbrey equation, see **Figure 7.7**a. The QCM sensor resonates as a standing plane wave with antinodes across the surface. When a thin, rigid film is deposited onto the sensor, the

mass acts as an extension to the thickness of the sensor, increasing the wavelength and decreasing the frequency of the standing shear wave. Since the acoustic properties of the deposited layer may differ from the resonator, a more detailed analysis was made by Günter Sauerbrey[53] showing that the reduction in the frequency is proportional to the mass per unit area of the deposited film.

It should be noted that the conversion of the frequency shift to mass using the Sauerbrey equation does not necessarily provide a true mass measurement, unless the criteria of the Sauerbrey equation are met which include because Sauerbrey is used for rigid films while wax films are viscoelastic, and the frequency shift is believed to be damped by the presence of the DE at the back of the sensor which reduces the response of the sensor. Hence, the mass is referred to as an apparent mass.

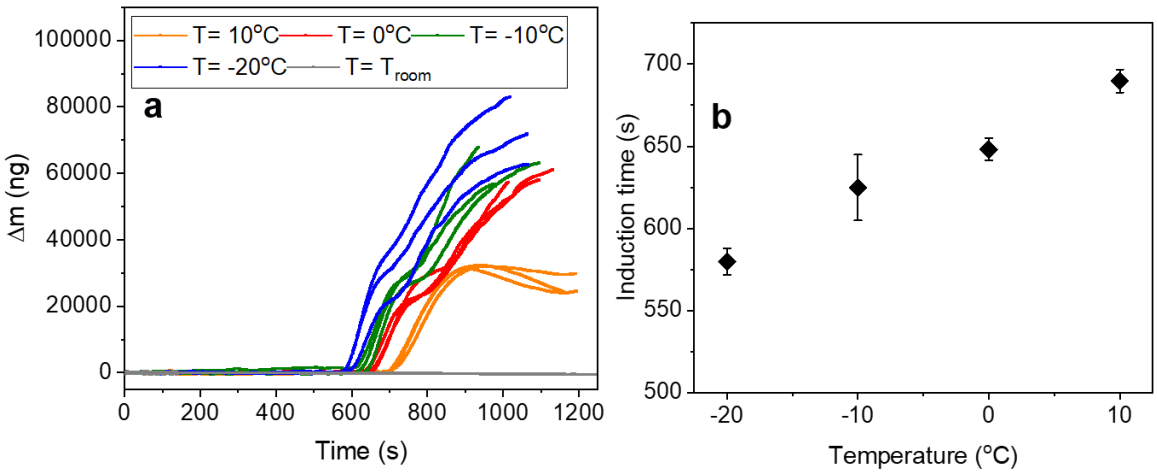

Figure 7.7. a) The mass deposited calculated by Sauerbrey equation corresponding to the frequency shift from dodecane to 0.5 wt% n-alkane wax-dodecane (WAT= 12°C) both at T_{room} with DE flowing at $T_{chiller}$ = 10, 0, -10, -20 °C, **b)** Induction time of frequency shift depending on $T_{chiller}$.

Figure 7.7a shows no wax deposited over time when the probe is at room temperature > WAT, whereas when the probe temperature is reduced to <WAT, the rate of wax deposition increases significantly. The solids may be from two sources, new solids forming in the oil near/on the cold QCM surface and solids moving from the bulk oil to the QCM surface and adhering there, potentially adhering to other microcrystalline wax[216], more investigations are needed to understand this phenomena. The curve shows as well difference in the slope of the mass deposited curve. A higher slope is observed for lower cold temperature indicating a higher rate of deposition. As the temperature decreases, the heat transfer between the hot fluid and the cold surface increases and hence, the concentration gradient decreases and wax deposition rate drops.

The delineating time between the stable initial baseline and the sudden drop in frequency is called the induction point for wax crystallisation. It is generally defined as a period of time where the solution is supersaturated forming a stable nucleus, but no crystallization is detected. The lag time depends among others on the level of supersaturation[229]. In our case, all the experiments are operating at similar flow rate, then the time for the n-alkane wax-in-dodecane solution to migrate from the solution flask to the QCM sensor is similar for all experiments and the induction time varies solely due to the time required for wax to crystallise and deposit on the QCM surface depending on the specific operating conditions i.e temperature of the QCM sensor.

Figure 7.7b shows the induction time as a function of the cooling temperature. When increasing the cooling rate, the crystal nucleation was induced at a higher critical supersaturation, resulting in a faster rate of nucleation and a shorter induction time[230]. The state of supersaturation is an essential stage to form the nucleation in order to start the crystallisation process. The critical radius of nucleus assumed as a 3-D sphere can be calculated based on the equation below:

$$r_c = \frac{2\gamma\omega}{kTln(1+\sigma)} \quad \text{Eq. 7.3}$$

where, γ is the surface energy, ω is the molecular volume, k is the Boltzmann constant, σ is the supersaturation[231]. The radius of the nucleus is decreased with the increase of supersaturation which means the high supersaturation will make the nucleation easier due to smaller size being needed.

7.5.2 Frequency−Resistance Diagram Analysis

Further analysis of the QCM responses were performed by plotting F-R diagram as presented in **Figure 7.8**. The F−R diagram model converts the QCM responses on a time scale to a plot of the resonant Frequency-Resistance and it is used to infer the phase changes in the film inherent to the sensor surface. The analysis of the F-R diagram can be summarised as follows:

- An elastic behaviour is manifested as an increase in the frequency shift. The frequency shift is directly related to a rigid mass deposited on the QCM sensor as suggested earlier by Sauerbrey equation.

- A viscous behaviour is manifested as an increase in series resonance shift. The resistance shift ΔR is directly related to the half-bandwidth ΔΓ using the following equation:

$$\Delta R + i\Delta f = \frac{A}{4\emptyset^4}\widetilde{Z_L} = -i\frac{\pi}{16}\frac{Z_q^3}{Ae_{26}^2\rho_q^2 f_0^3}(\Delta f + i\Delta\Gamma) \quad \text{Eq. 7.4}$$

Where, where A is the active sensor area (m^2), Z_q the acoustic wave impedance (8.8× 106 $kgm^{-2}\ s^{-1}$), e_{26} the piezoelectric stress coefficient (9.65 × 10^{-2} cm^{-2}), ρ_q the density of crystalline quartz (2.65 $g.cm^{-3}$) and f_0 the fundamental resonance frequency (5 MHz). Solving Eq. 7.4 leads to a simple conversion of $\Delta\Gamma \sim 2\Delta R$[232, 233].

The apparent differential loss tangent $\frac{\Delta\Gamma}{\Delta F}$ is proportional to $\frac{\Delta R}{\Delta F}$ with $\Delta\Gamma$ or ΔR measures losses, while ΔF measures stiffness. This relationship implicates a more lossy mass at a higher apparent differential loss tangent and a stiffer mass with a lower apparent differential loss tangent.

The theoretical F-R diagram in **Figure 7.8**a summarises the potential behaviour of both frequency and resistance shift to the change in the QCM crystal environment[216]. Point "a" corresponds to the original state of the undisturbed bare sensor in air, and the shift from point "a" to point "b" results from the change in viscosity when the QCM is immersed in new medium. The shifting path b-c-d is an extension of a-b and indicates an increase in the viscosity of the liquid film inherent to the sensor without an elasticity change. The response shift b-e-f however is due to an increase in the elasticity due to a rigid mass deposition on the sensor[53].

Figure 7.8b presents the experimental F-R diagram obtained while flowing pure dodecane and n-alkane wax-in-dodecane in the QCM cell at different DE temperatures.

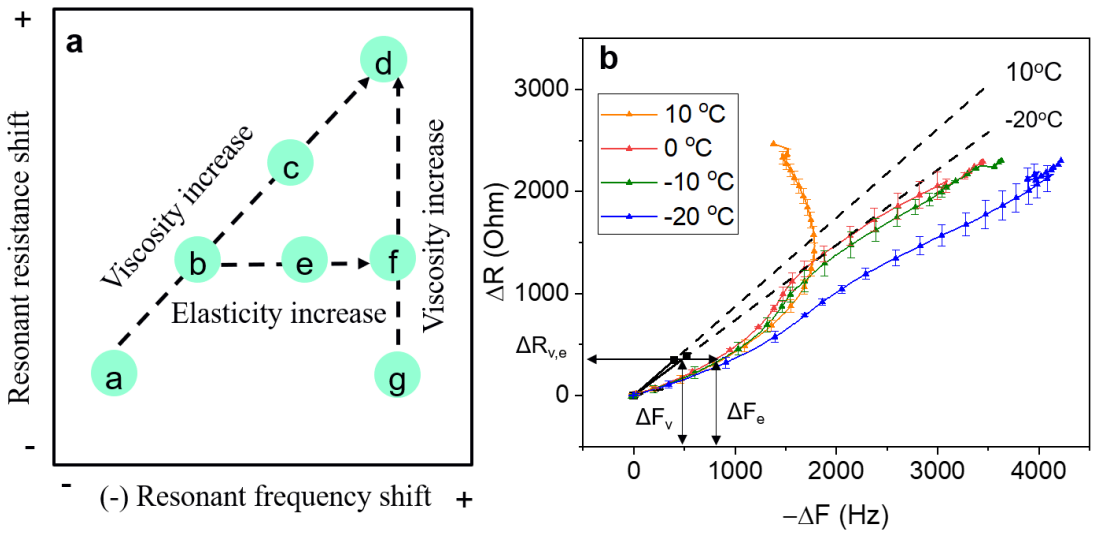

Figure 7.8. a) Explanation of interface viscosity and elasticity variation patterns using the F-R model adopted from Liu et al.[214], **b)** F-R plot of the QCM responses during the flow of 0.5 wt% n-alkane wax-dodecane (WAT= 12°C) at T_{room} with DE flowing at $T_{chiller}$ = 10, 0, -10, -20 °C with black lines representing dodecane at 10 and 20 °C. The subscripts "v" and "e" correspond to viscous for dodecane and elastic for alkane respectively.

For pure dodecane, solid black line and symbols corresponding to (ΔF = 0 Hz, ΔR = 0Ω) and (ΔF = -399 Hz, ΔR = 347.68Ω) are the experimental resistance and frequency change for pure dodecane with DE at 10 °C and the solid black line and symbols corresponding to (ΔF = 0 Hz, ΔR = 0Ω) and (ΔF = -524 Hz, ΔR = 386.48 Ω) are those of dodecane with DE at -20 °C. The dash lines are an extrapolation of the F-R behaviour of pure dodecane and serve as a reference to indicate any viscous behaviour resulting from a change in the viscosity and density of the solution due to temperature drop between 10 and -20 °C. These two dash lines are to be benchmarked against the lines and symbols graphs corresponding to the F-R diagram of 0.5 wt% n-alkane wax-in-dodecane mixture in the presence of DE at 10, 0, -10 and -20 °C.

Figure 7.8b shows that the 0.5 wt% n-alkane wax-in-dodecane solution exhibits a different behaviour then the pure dodecane (viscous dash lines). The viscous F-R behaviour is linear as stated by Kanazawa, while the non-viscous behaviour is not linear and involve a relatively higher frequency shift (elastic behaviour) than the resistance shift (dampening). Comparing the frequency shift between pure dodecane and n-alkane wax-in-dodecane at the same resonance frequency $\Delta R_{v,e}$, the frequency shift for pure dodecane decreases to $-\Delta F_v$ of ~ 399 and 524 Hz for 10 and -20 ^oC respectively while $-\Delta F_e$ reaches an average ~ 900 Hz for the n-alkane wax-in-dodecane solution at the DE temperatures of 10, 0, -10 and -20 ^oC. The large difference in the frequency shift between dodecane and n-alkane wax-in-dodecane is related to the mass of n-alkane loading on the sensor resulting from wax crystallisation on the cold surface. A calculation of $\Delta R/-\Delta F$ (proportional to the apparent differential loss tangent $\Delta\Gamma/-\Delta F$) gives $\Delta R/-\Delta F \sim 0.8\ \Omega/Hz$ for pure dodecane and an average of ~0.4 Ω/Hz for n-alkane wax-in-dodecane mixture. This drastic decrease in the resistance to frequency ratio with n-alkane wax-in-dodecane mixture implicates a much stiffer mass loading on the QCM sensor resulting from n-alkane crystals load rather than just a decrease in the viscosity of the solution.

After the designated $\Delta R_{v,e}$, n-alkane wax-in-dodecane mixture exhibit different behaviour depending on the temperature of the DE fluid. To help analysing each behaviour, separated F-R diagrams for each cooling rate are plotted in **Figure 7.9** and **Figure 7.10**.

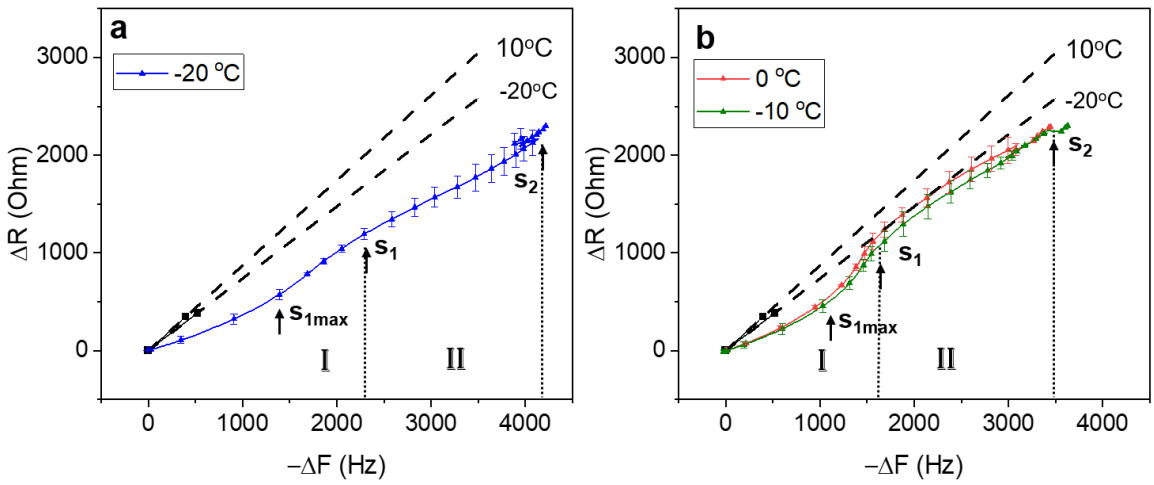

Figure 7.9. F-R plot analysis of the QCM responses during the flow of 0.5 wt% n-alkane wax-dodecane (WAT= 12°C) at T_{room} with DE flowing at **a)** $T_{chiller}$ = -20°C **b)** $T_{chiller}$ = 0 & -10°C. Stage I is delimitated between 0 and S_1 with a peak on S_{1max} and stage II is delimitated between S_1 and S_2.

Figure 7.9a shows that the n-alkane wax-in-dodecane mixture with DE at -20, -10 and 0 °C exhibits a deviation from the viscous behaviour towards an elastic behaviour and the trend can be seen as two stages I and II delimitated by the round dot lines at S_1 and S_2. S_1 was identified visually with the F-R diagram exhibiting an initial drastic elastic behaviour from zero to S_{1max}, (corresponding to the crystallisation of the alkane on the cold surface) then the resistance frequency increases rapidly after until it reaches the dot line S_1 (with the oil being incorporated into the formed wax matrix creating a higher dampening in the deposited wax layer). After the point S_1, a second stage S_2 (S_2-S_1) is identified with a behaviour depending on the DE temperature.

Table 7-1 below compares **Figure 7.9**a and b where the frequency shift and ΔR/-ΔF are presented at points S_{1max}, S_1 and S_2.

Table 7-1. Comparison of S_{1max}, S_1 and S_2 for 0, -10 and -20 ^oC.

	-20 ^oC		**0 and -10 ^oC**	
	-ΔF (Hz)	ΔR/-ΔF (Ω/Hz)	-ΔF (Hz)	ΔR/-ΔF (Ω/Hz)
S_{1max}	1400	0.41	1050	0.44
S_1	2300	0.52	1600	0.71
S_2	4200	0.54	3500	0.66

Comparing stage I and stage II for both graphs, **Table 7-1** shows that decreasing the temperature of the chiller induces a large frequency shift that is proportional to the magnitude of temperature difference between the model solution and DE; for instance -ΔF measured at DE = -20 ^oC is larger than -ΔF measured at DE = -10 and 0 ^oC by ~ 25% at S_{1max}, ~30% at S_1 and by ~15% at S_2. The larger decrease in the frequency shift means a larger amount of n-alkane wax crystallising on the cold sensor. On the other hand, ΔR/-ΔF measured at DE = -20 ^oC is lower compared to ΔR/-ΔF measured at DE = -10 and 0 ^oC by ~ 7% at S_{1max}, ~35% at S_1 and ~20% at S_2. A lower ΔR/-ΔF indicates a stiffer layer, probably including less dodecane oil trapped in the wax crystal matrix.

At DE = -20 ^oC, stage I and II are comparable in trends, however, S_2 has a lower frequency shift (S_2-S_1 = 1900 Hz compared to 0-S1= 2300 Hz) and a slightly higher ΔR/-ΔF indicating less n-alkane wax depositing and a softer wax layer resulting either from more dodecane incorporating into the wax layer or the increase in the temperature at the deposition surface due to the insulation effect of the already wax deposited.

At DE = -10 and 0°C, while stage I is elastic driven, stage II is more viscous driven as the film inherent to the sensor behaves mostly as a viscous layer approaching and mimicking the viscous dash line of the pure dodecane. In stage II, the viscosity and density are increasing within the solution itself with no wax depositing on the sensor surface. After a first stage of wax deposition, the temperature on the surface of the cold sensor increased due to insulation effect of wax crystals, hence, the model solution is cooled down from room temperature but doesn't reach yet the critical temperature (WAT) for wax crystallisation. The deposition rate is slowed down and the n-alkane wax-in-dodecane solution behaves as a viscous fluid until the end of S_2 where a new elastic behaviour seems to appear. With the elastic behaviour appearing at the end, the viscous behaviour may then be regarded as a supersaturation process where the solution increase in viscosity and density due to the formation of small cluster of nuclei. The supersaturation is very low that the induction time for wax crystallisation is large, just at the end of the stage II.

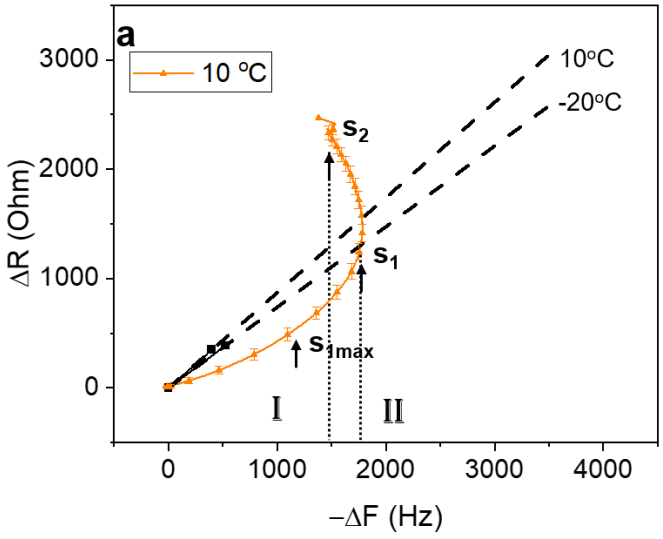

Figure 7.10. F-R plot analysis of the QCM responses during the flow of 0.5 wt% n-alkane wax-dodecane (WAT= 12°C) at T_{room} with DE flowing at $T_{chiller}$ = 10°C. Stage I is delimitated between 0 and S_1 with a peak on S_{1max} and stage II is delimitated between S_1 and S_2.

At a lower cooling rate with $T_{chiller}$ = 10 ^{o}C, **Figure 7.10** shows an interesting behaviour. Two stages S_1 and S_2 are also identified; For stage I, S_{1max} has -ΔF~1110 Hz and ΔR/-ΔF ~ 0.45 Ω/Hz, S_1 has a frequency shift of 1750 Hz and ΔR/-ΔF of 0.71 Ω/Hz, with very similar trend to the mixture flowing at T= 0 and 10 ^{o}C. This first stage corresponds to the deposition of a wax layer on the cold sensor. However, stage II shows a very exotic behaviour, with the frequency shift increasing again to 1500 Hz and the resistance increasing significantly with ΔR/-ΔF of 1.56 Ω/Hz. This behaviour may be explained by the melting of the wax layer after its formation and the incorporation of a high amount of dodecane in the wax matrix. A slow cooling rate induces the formation of large wax crystals able to incorporate a larger amount of oil in their matrix.

7.1 Conclusions

A HT- QCM technique was shown to be applicable to analyse wax deposition on cold surfaces. During wax deposition, the vibrational frequency (F) and resistance (R) of the quartz crystal sensor clearly responded to property changes in the solution and on the sensor. That is, when cooling the solution below its WAT, the viscous friction of the solution on the sensor increased, thereby decreasing the resonant frequency (F) and increasing the resonant resistance. At the induction of crystal nucleation, the resonant frequency and resonant resistance changed rapidly and significantly due to the increased viscosity and mass loading on the sensor.

Although the adherence of a gel deposit unto a quartz crystal surface is evidenced by a decrease in the frequency shift, however, it was challenging measuring accurately the thickness of soft gel deposits with QCM techniques. HT-QCM serves instead as a unique tool for investigating the mechanism of the first deposited wax layers formed on the sensor surface.

The mechanism of wax deposition was investigated by plotting F-R diagram and comparing both the magnitude of the frequency shift ΔF with ΔR/-ΔF proportional to the apparent differential loss tangent ΔΓ/-ΔF. The F-R diagram shows the model solution to change in 2 stages; In the first stage, the model solution behaviour is comparable for all the DE temperatures with a significant shift towards elastic behaviour, a decrease in the frequency shift and a low ΔR/-ΔF indicating a stiff mass layer of n-alkane depositing on the sensor cold surface. However, the magnitudes of ΔF (and therefore the amount of n-alkane depositing) and ΔR/-ΔF were proportional to the magnitude of temperature difference between the model solution and DE. The second stage however shows different behaviour of the model solution depending on the DE temperature. At DE = - 20 ^{o}C, stage II was similar to stage I indicating another layer of n-alkane crystallising, however, due to the insulating effect of the first wax layer, the second elastic stage is smaller. At DE = 0 and -10 ^{o}C, stage II was mostly viscous with the F-R diagram following the trend of a viscous layer suggesting no further wax to deposit on the cold sensor also due to the insulating effect of the already deposited wax. At DE = 10 ^{o}C, stage 2 showed an infinite increase in the resistance due to either the melting of the wax layer or the incorporation of large amount of oil in the wax matrix.

Chapter 8 Conclusions and Future work

8.1 Synopsis

In this project, the effect of physical and chemical environment on wax deposition under flow regime was studied experimentally and modelled mathematically. Systematic investigations were carried out to determine the driving force of wax deposition in dynamic flow and two regimes were identified and modelled: a thermally driven regime where the change in the temperature of the bulk oil decrease the heat transfer driving force for wax deposition, and a sloughing driven regime where the heat transfer change with CRF rotational speed is insignificant and the wax deposition is governed by the wall shear stress applied by the shearing fluid on the wax deposit.

The following conclusions are drawn from this research works:

8.2 Experimental and Theoretical Assessment of the Role of Flow Rate on Wax Deposition using the CRF

The CRF, as Couette flow device, with an inner chilled rotating cylinder allowed the study of wax deposition in the region of high wall shear stress. The removable wax deposition sample allowed a precise gravimetric measurement and the transparent outer cylinder permit the visualization of wax deposition. To assess the effect of flow on wax deposition, the CRF was set at controlled operating conditions with the rotational speed varying from static up to 700 rpm. Wax deposition rates and pseudo-steady state deposit mass values were shown to depend strongly on the CRF rotational speed. Relative to the static test (0 rpm), the wax deposit mass decreased with increasing rotational speed and temperature measurements of the bulk showed a decrease in the

bulk temperature with rotational speed up to 400 rpm only with no noticeable variation of the steady state temperature above 400 rpm. Videos shows wax layers to be stripped out of the deposit at rotational speed above 400 rpm as well. Analysing all the data together, a conclusion was made about the effect of the rotational speeds on wax deposition; At low rotational speeds, the reduction in deposited wax corresponded to changes in the bulk oil (T_{oil}) temperature with increasing CRF rotational speed, decreasing therefore the thermal driving force between the T_{cold} and T_{oil}. The change in heat transfer governed the mass deposited, with wax deposition described by a thermally-driven process. However, at high rotational speeds, the reduction in mass is attributed to sloughing caused by the wall shear stress overcoming the wax network cohesive forces with wax deposition described as sloughing driven process.

Such conclusions were assessed theoretically by deriving a mathematical model based on molecular diffusion to predict the mass deposit on the CRF in dynamic conditions. The model described the temperature profile in the boundary layer by considering the heat transfer coefficient as a function of the CRF rotational speed. Mass transfer was described by Fick's law assuming a linear solubility with temperature, and constant diffusivity. The model succeeds to fit the experimental data up to 400 rpm, however, above 400 rpm, the molecular diffusion model could not accurately describe the wax deposit mass and was modified to include a sloughing term, $\dot{S}(t)$, described mainly in terms of the wall shear stress. With inclusion of the sloughing term, wax deposition kinetics could be predicted at higher CRF rotational speeds.

The diffusion model can be further improved by incorporating the experimental solubility curve rather than assuming the solubility a linear function of temperature. The sloughing model can be improved by including the experimental viscosity curve as a function of temperature.

8.3 Evaluation of the Role of Chemical Environment on Wax Management in the Identified Wax Deposition Regimes

The chemical environment was also studied by evaluating the role of biodegradable wax inhibitors in wax management in the identified thermally driven and mechanically driven wax deposition regimes. To this end, 4 eythlcellulose inhibitors were synthesized with different degree of substitution and two alkyl pendant chain lengths (C18 and C22). A model oil of dodecane and toluene (1:1) was chosen with 5wt% n-alkane wax content. The inhibitors were then tested on the CRF for 30 minutes test, at two concentrations (50 and 500 ppm) and three flow regimes: static regime (0 rpm), thermally driven regime (100 rpm) and shear driven regime (400 rpm). The inhibitors show their efficiency in reducing the amount of wax deposit. The efficiency was a function of the degree of substitution first, where the higher DS implies a higher mass reduction, and the length of the pendant alkyl chain, where the longer alkyl chain C22 shows a better performance than C18. These results are directly related to the mechanism of inhibition based on the interaction between the inhibitor and the n-alkane wax molecules; the higher the interaction, the better the efficiency. The inhibitors show higher performance at static conditions than dynamic conditions (for both thermally driven and sloughing regimes) and the chemical composition of the wax deposit shows that this behavior is related to the change in the chemical composition of the wax deposit with the change of flow. The inhibitor is mainly functional for LMW n-alkane molecules due to the high similarity between them and the alkyl pendant chain and it is less efficient for HMW n-alkane molecules due to the large discrepancy in chain length. At higher CRF rotational speeds, the wax deposit composition shift towards HMW n-alkane wax molecules, the role of inhibitor is therefore limited to a small amount of LMW molecules that may deposit.

Besides, the incorporation of ethylcellulose in the wax deposit will make it stiffer and less affected by the wall shear stress at its surface.

The work can be taken for further to investigate the efficiency of the EC inhibitors as pour point depressant. It was found that the presence of EC-1 reduces significantly the viscosity of the waxy solution, therefore, a more systematic study of the rheology of the model solution in the presence of the synthesized inhibitors is required. A measure of the viscosity change with temperature, and the yield stress of the waxy solution at different temperatures are necessary to determine both the functionality of the inhibitors and their temperature range of use.

8.4 An Insight into the Mechanism of Incipient Wax Deposit Formation using the QCM Technique

To provide an insight into the mechanism of incipient wax deposit formation, a QCM technique, complementary to the CRF, was elaborated and tested for wax deposition studies. Using a model waxy oil of 0.5 wt% n-alkane wax-in-dodecane, both resonance frequencies and resistance were monitored for the 1st (fundamental) overtone. The adherence of a gel deposit unto a quartz crystal surface was evidenced by a response from the vibrational frequency (F) and resistance (R) of the quartz crystal sensor to property changes in the solution and on the sensor. The large decrease in frequency shift with respect to viscous curve was an indication of mass loading on the sensor due to n-alkane wax crystallising on the old surface. This crystallization is followed by oil incorporation in the wax deposit matrix shown by further increase in the resistance. The QCM method holds promise in investigating how incipient deposit formation is influenced by factors such as paraffin composition, and the presence of inhibitors.

8.5 Initial Investigations and Future Work

This project investigates the effect of hydrodynamics on the wax deposition using the CRF where two flow regimes were identified: a flow regime of low rotational speed where wax deposition is governed by heat transfer, and where the temperature of the bulk is a great function of the rotational speed; and a flow regime of high rotational speed where wax deposition is governed by sloughing, and it is independent of the heat transfer. Temperature measurement of the bulk oil and visual observations of the wax deposit were coupled with a gravimetric study at different times and CRF rotational speed from 0 to 60 minutes to delimitate the two flow regimes. however, the study couldn't quantify the sloughing effect by measuring accurately the decrease in the wax deposit thickness, nor the sloughing starting and end points. Besides, the sloughing was proven to be a function of the temperature. The temperature affects both the wax deposit hardness and composition as well as the shear rate at the deposition interface, it may induce dissolution instead of mechanical sloughing. Giving the complexity and the reciprocal effect of the heat transfer and hydrodynamic on the wax deposition, the project may carry on by aiming to decouple the thermal and the hydrodynamic effect on wax deposition.

On the other hand, oil composition is believed to be having a substantial effect on wax precipitation and deposition processes, physical properties of waxy mixtures are being identified as key factors driving the effect of temperature and hydrodynamics on wax deposition. The term oil composition includes the type, quantity and molecular weight of the n-alkane wax, and the presence of other non-alkane paraffinic components. In industry, waxy crude oils have been classified into "clean waxy crudes" and "regular waxy crudes"; the clean crude is defined as "a crude oil in which there exist only hydrocarbons and paraffins as its only heavy organic constituent", and the regular crude , which is the wide spread in the world, contains clean crude

and other heavy organics such as naphthene, asphaltene, and resin[234]. While the oil composition in terms of n-alkane wax content has been extensively investigated in the literature and in this project, the effect of other constituents, such as asphaltene, on wax deposition is poorly demonstrated and mostly contradictory; therefore, a comprehensive investigation of such species on wax deposition phenomenon is highly recommended by various researchers, as it provides valuable information about what to consider including in wax deposition modelling, if such species are present[235, 236]. In a future project, the effect of different species shall be assessed on the degree of molecular interaction with paraffin molecules, wax deposition and sloughing rates, and physical properties. **Figure 8.1** is a chart that shows a plan of a future experimental work.

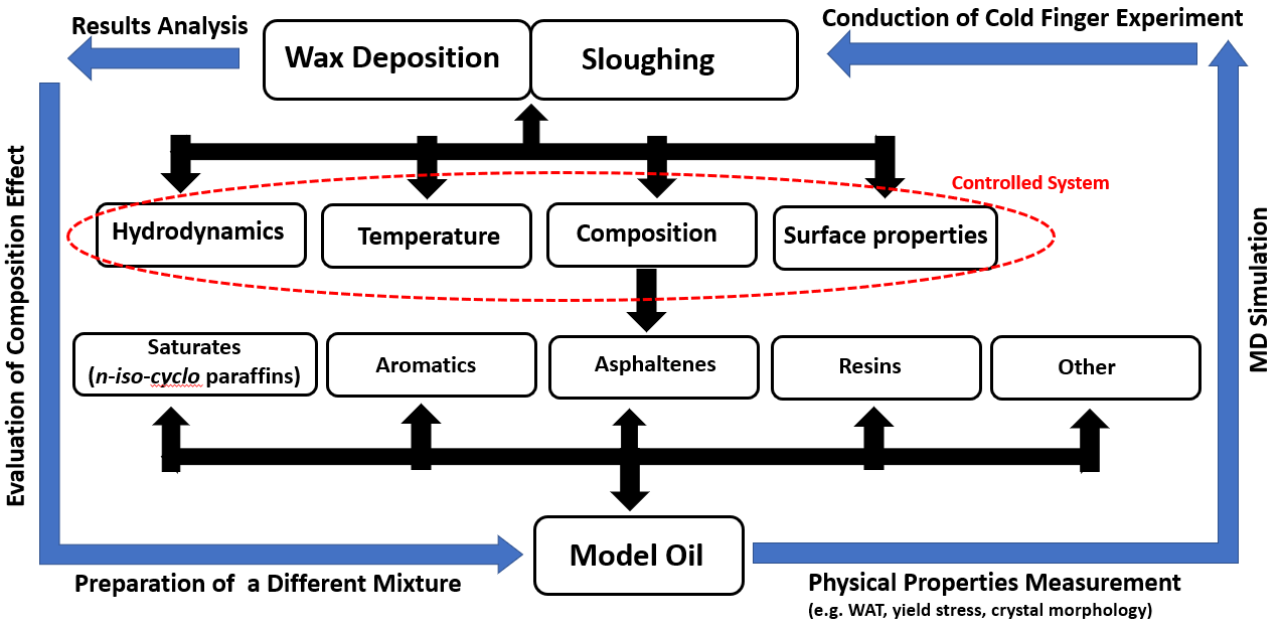

Figure 8.1. A flow chart illustrating the plan of the future experimental work.

8.5.1 Initial Experiments and Results

In order to approach the effect of flow in terms of sloughing and the effect of impurities such as asphaltene on wax deposition, several techniques have been designed and developed. The Cold Rotating Finger (CRF) was further modified and developed to separate the thermal and hydrodynamic effects for a better quantification of the sloughing process. The CRF is equipped with a newly constructed online wax deposit thickness measurement tool along with a manipulatable moving temperature probe. **Figure 8.2** below shows the modification of the CRF to be an optical visualising rig b implementing a CS235MU-Kiralux 2.3 Megapixel Monochrome CMOS camera (THORLABS Ltd), light polariser and 1x converter lens (Lambda Photo), a high-power LED lamp (Photron Ltd.) to deliver the light required for visualisation.

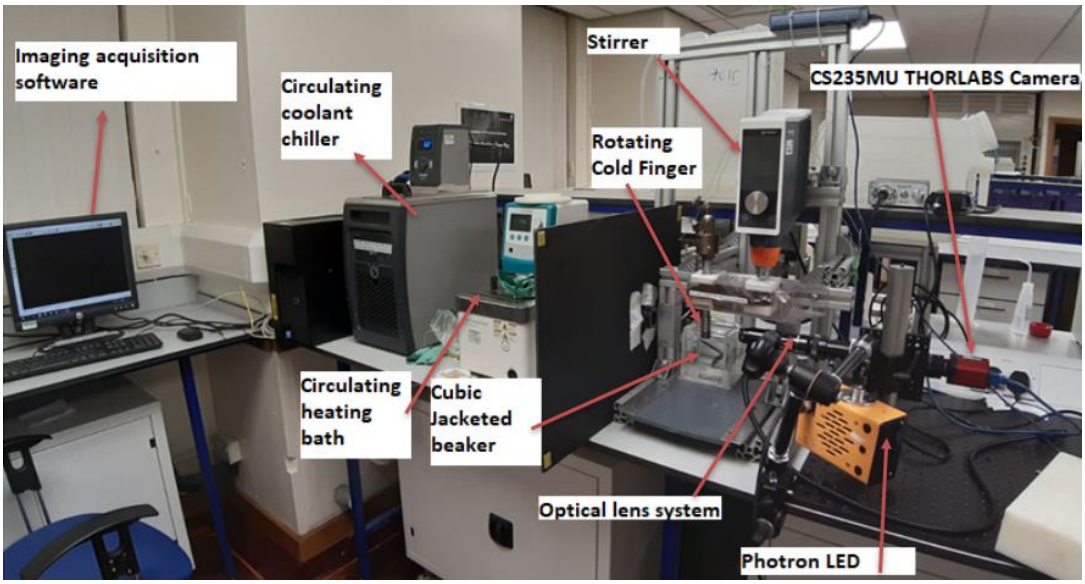

Figure 8.2. CRF apparatus with the new visualization rig.

The new CRF is capable of measuring wax deposition thickness in-situ online while deposition is taking place at different CRF rotating speeds. In processing the data, Image Segmentation was

implemented by adopting a threshold method to delineate the wax deposit edges and subsequently produces a binary image of black and white colours.

8.5.2 Effect of Asphaltene on Wax Deposition

The second objective is about studying the physical properties of waxy mixtures such as wax appearance temperature (WAT), and yield stress when various petroleum species are used. This will be conducted by adopting best practice procedure of using some analytical techniques, such as hybrid rheometer, Crystal 16, Gas Chromatography (GC) and micro-spectroscopy. Thirdly, the degree of molecular interaction between different petroleum fractions and waxes will be modelled and simulated using a Molecular Dynamics (MD) simulation software. This would be a valuable tool for validating the effect of the petroleum fractions on the physical properties of the waxy mixtures as well as deposition and sloughing rates.

8.5.3 Further investigations: mechanistic modelling for wax deposition

Investigations show that existing wax deposition models cannot accurately predict deposition in field conditions due to the elimination or approximation of some of the possible mechanisms and parameters contributing to wax deposition[237]. The development of fit-for-purpose models, such as the CRF model or other pioneer's group models such a Tulsa or MWP[11, 13, 115], is based on the preferential selection of some dominant mechanism over others. For instance, the CRF model is based on the molecular diffusion as a solely mechanism responsible for wax deposition and the wall shear stress was also approximated by major fitting parameters. The model lack of mechanistic understanding in wax deposition process i.e. the effect of the cold surface properties, such as free energy, roughness and materials, the chemical composition of the wax deposit was also neglected, the supersaturation in the boundary layer was not taken into account neither the

precipitation kinetic etc. This deficiency impedes the scalability of such a model and trial and errors are often needed to fine tune the model for a given operating condition.

This drawback in predictive tools necessitate the investigation of a holistic model that include and analyse all the possible mechanisms behind the deposition phenomena at once. The current advances in simulation i.e Computational Fluid Dynamics CFD is a prominent opportunity for such an investigation and would be an advanced step in future work[238].

Appendix

9.1 Appendix for Chapter 4

9.1.1 Taguchi Method: Key Concepts and Terms

Taguchi methods is a type of "Design of experiment DOE" developed by an engineer called Taguchi in 1951 in Japan. Taguchi Methods aims to replace the "full factorial" design experiment or "1 factor at a time" experiment with an "Orthogonal Array OA" design. OA design is an extreme design matrix where only main parameters affecting a process are assessed with the minimum experiments number. Below is a definition of an OA and a steps guide through Taguchi methods[239, 240].

9.1.1.1 Orthogonality and Orthogonal Array

Taguchi's design uses orthogonal arrays to reach the optimum results with minimum trials at minimum cost. Orthogonality is represented as $\sum x_i . x_j = 0$, for all the pair of levels, where i, and j represent high and low (+1, -1) levels. In an Orthogonal Array, each factor has equal weights and hence, it is balanced design. An example of orthogonal array is shown below:

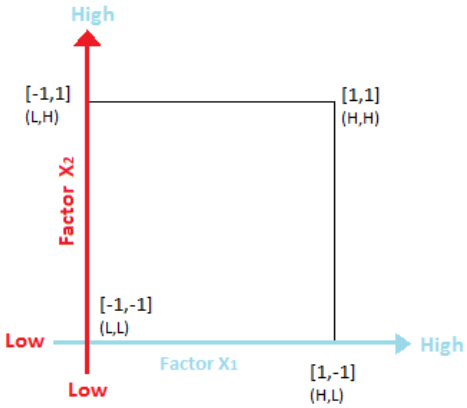

Figure 9.1. An orthogonal array adapted from Sigmaquotient[241].

Table 9-1. An example of an orthogonal array adapted from Sigmaquotient[241].

Experiment No	**Factor $X_1 - x_i$**	**Factor $X_2 - x_j$**	**$x_i.x_j$**
1	1	1	1
2	1	-1	-1
3	-1	1	-1
4	-1	-1	1
$\sum x_i . x_j$			0

The advantage of this orthogonality is that each factor can be evaluated independently, without influence from others. Therefore, factors do not affect each other during estimation.

Taguchi represents an Orthogonal Array as:

$$L_N\ (S^k) \qquad \text{Eq. 9.1}$$

where,

S = number of levels for each factor;

K = maximum number of factors whose effects can be estimated without interaction;

N= total number of trials during experimentation;

Example: $L_8\ (2^7)$ – 8 experimental runs, 7 factors with 2 levels.

9.1.1.2 Standard Orthogonal Array (OA) Table

Taguchi designed Standard OA; for each OA, he predefines the number of runs, the maximum number of factors that can be studied and the levels of each factor. Taguchi's standard OA table is shown below and here are examples to help read the table:

Ex1: L8 (2^7) – 8 experiments, 7 factors and 2 levels.

Ex2: L9(3^4) – 9 experiments, 4 factors and 3 levels.

Table 9-2. Standard orthogonal array table – Taguchi Method taken from Sigmaquotient[241].

Orthogonal Array	No. Runs	Max. Factors	Max. of columns at these levels			
			2-level	3-level	4-level	5-level
L4	4	3	3			
L8	8	7	7			
L9	9	4		4		
L12	12	11	11			
L16	16	15	15			
L'16	16	5			5	
L18	18	8	1	7		
L25	25	6				6
L27	27	13		13		
L32	32	31	31			
L'32	32	10	1		9	
L36	36	23	11	12		
L'36	36	16	3	13		
L50	50	12	1			11
L54	54	26	1	25		
L64	64	63	63			
L'64	64	21			21	
L81	81	40		40		

9.1.2 System design: Determine the Number of Experimental Runs required and the Relevant OA

Taguchi's designs use the Degree of Freedom [DoF] method to determine the number of experimental runs. DoF refers to the number of ways a system can independently vary when a constraint is imposed. The Degrees of Freedom for a Factor is given by: [No of levels -1]. The total DoF is summation of DoF for all factors. The total Degrees of Freedom is denoted as:

$$\sum_{i=1}^{k}(S_k - 1) \qquad \text{Eq. 9.2}$$

where, K = Number of Factors and S represents Levels.

In our case study, the table of factors/levels is presented below:

Table 9-3. Taguchi experimental matrix of factors affecting wax deposition.

Factors	Level 1	Level 2	Level 3	Level 4
T_{cold} (◦C)	5	10	15	20
T_{hot} (◦C)	40	45	50	55
Wax (wt %)	4.7	9	13	16.6
RPM	0	50	100	150

Therefore, the DoF can be calculated as follows:

Table 9-4. Degree of Freedom calculation for wax deposition experimental matrix.

Factors	Levels (S)	Degrees of Freedom (DoF = S-1)
T_{CRF} (◦C)	4	3
T_{bulk} (◦C)	4	3
Wax (wt %)	4	3
RPM	4	3
Total DoF		**12**

The total number of experiments $T_{experiments} = 1 + \sum_{i=1}^{k}[S_k - 1] = 1 + 12 =$ 13 experiments.

Referring to the Standard OA table, the OA that has a number of runs ≥ 13 and a suitable number of factors and levels is selected. For our case, referring to table 6, L'16 is selected because it has 16 runs for 5 factors at level 4 each.

Table 9-5. Orthogonal Array of L'16

L'16 (4^5)					
Runs	**Column 1**	**Column 2**	**Column 3**	**Column 4**	**Column 5**
1	1	1	1	1	1
2	1	2	2	2	2
3	1	3	3	3	3
4	1	4	4	4	4
5	2	1	2	3	4
6	2	2	1	4	3
7	2	3	4	1	2
8	2	4	3	2	1
9	3	1	3	4	2
10	3	2	4	3	1
11	3	3	1	2	4
12	3	4	2	1	3
13	4	1	4	2	3
14	4	2	3	1	4
15	4	3	2	4	1
16	4	4	1	3	2

Columns refer to factors and 1, 2, 3 and 4 refers to the levels of each factor.

9.1.3 Allocating Factors to Columns and Constructing the Final Experimental Matrix

In preparation to determine the experimental layout, factors are allocated to the columns of OA. This can be done as shown below:

Table 9-6. Allocating Factors to the columns of L'16 OA

Factors	Column/Nodes
T_{CRF} (◦C)	1
T_{bulk} (◦C)	2
Wax (wt %)	3
RPM	4

The final experimental matrix is shown as:

Table 9-7. Taguchi experimental matrix of wax deposition using CRF.

Run	T_{cold} (°C)	T_{hot} (°C)	Wax wt%	RPM
1	5	40	4.7	0
2	5	45	9	50
3	5	50	13	100
4	5	55	16.6	150
5	10	40	9	100
6	10	45	4.7	150
7	10	50	16.6	0
8	10	55	13	50
9	15	40	13	150
10	15	45	16.6	100
11	15	50	4.7	50
12	15	55	9	0
13	20	40	16.6	50
14	20	45	13	0
15	20	50	9	150
16	20	55	4.7	100

The experimental matrix presents a total of 16 experiments. Each row of the matrix represents a run (or an experiment) at a specified operating condition. After getting the results of all experimental runs, the mean value of wax deposit for each factor and each level are calculated along with a standard deviation.

9.2 Appendix for Chapter 5

9.2.1 Wax Deposition Modelling: Full Description

A mathematical model was developed to predict wax deposition in the CRF. The model was based on the molecular diffusion mechanism occurring in the thermal boundary layer adjacent to the deposit. The diffusion rate was determined by writing the heat and mass balances, and optimum configurations of the adjustable parameters were identified. The following assumptions were considered: i) all the main variables depend only on the radial coordinate r and on time t, and variations along the longitudinal coordinate z (CRF axis) are negligible; ii) the wax solubility was derived from an empirical equation developed by Singh et al.[19]; iii) hydrodynamics calculations were based on empirical equations fitted to the 100 rpm experimental data; iv) wax was treated as a single component; v) wax diffusivity was considered a constant tuning parameter; vi) the latent heat of crystallization was neglected; vii) the oil and wax were taken to have the same density, 800 kg/m^3; viii) the wax deposit was formed by wax and oil with the wax fraction assumed independent of time; and viii) the lateral external wall of the outer cylinder is adiabatic (zero heat flux).

Table 9-8. Operating conditions and oil properties.

Operating conditions	
T_b (ºC)	45
T_s (ºC)	7
RPM	0-700

Oil properties	
ρ (kg/m^3)	759.978
μ (Pa.s)	0.00119
Cp (J/g.K)	2.5
K_o (W/m.K)	0.137
Wax content (wt%)	13
WAT (ºC)	40.4

$$\frac{dm}{dt} = D\frac{\partial C}{\partial r}\Big|_{R_i} = D\frac{dC}{dT}.\frac{\partial T}{\partial r}\Big|_{R_i} \quad \text{Eq. 9.3}$$

where *m* is the mass deposited, *D* the wax diffusivity (D = 1.48. 10^{-10} m^2/s), *C* the concentration of dissolved wax in the boundary layer, *r* the radial coordinate and R_i the wax deposit layer thickness. The steady state temperature in the three zones is given by:

Wax deposit (D_p):

$$T(r,t) = T_s + \frac{T_i(t)-T_s}{\ln\left({}^{R_i}/_{R_s}\right)}\ln\left(\frac{r}{R_s}\right) \quad \text{Eq. 9.4}$$

Boundary layer (BL):

$$T(r,t) = T_i(t) + \frac{T_b(t)-T_i(t)}{\ln\left({}^{R_b}/_{R_i}\right)}\ln\left(\frac{r}{R_i}\right) \quad \text{Eq. 9.5}$$

Bulk oil (B):

$$T(r,t) = T_b(t) \quad \text{Eq. 9.6}$$

where, t is the time, T_s, T_i, T_b are the temperatures of the CRF surface, wax deposit-oil interface and boundary layer-bulk oil interface, respectively. R_s and R_b are the radii of the CRF and the boundary layer, respectively.

Imposing thermal flux balance at the interface R_i:

$$k_d \frac{T_i(t)-T_s}{\ln\left({}^{R_i}/_{R_s}\right)}\frac{1}{R_i} = k_o \frac{T_b(t)-T_i(t)}{\ln\left({}^{R_b}/_{R_i}\right)}\frac{1}{R_i} \quad \text{Eq. 9.7}$$

where k_d and k_o are the thermal conductivities of the wax deposit and oil, respectively. The heat flux at the interface R_d is assumed to be proportional to the temperature drop in the boundary layer so that:

$$2\pi R_d H k_d \frac{(T_i - T_s)}{\ln(\frac{R_i}{R_s})} \frac{1}{R_i} = h\,(T_b - T_i).\,2\pi R_d H \qquad \text{Eq. 9.8}$$

Where, *H* is the height of the CRF deposition sample and *h* is the heat transfer. Hence,

$$k_d \frac{(T_i - T_s)}{\ln(\frac{R_i}{R_s})} \frac{1}{R_i} = h\,(T_b - T_i) \qquad \text{Eq. 9.9}$$

$$T_i = \frac{T_b \alpha + T_s}{1+\alpha} \qquad \text{Eq. 9.10}$$

$$\alpha(t) = \frac{hR_i(t)}{k_d} \ln\left(\frac{R_i(t)}{R_s}\right) \qquad \text{Eq. 9.11}$$

Equation of ***α(t):***

Setting *M*(t) total mass of deposit as a function of time,

$$M(t) = \pi(R_i^2 - R_s^2)H\rho \qquad \text{Eq. 9.12}$$

$$R_i^2 = \frac{M(t)}{\pi H \rho} + R_s^2 \qquad \text{Eq. 9.13}$$

$R_i(t) = \sqrt{\frac{M(t)}{\rho \pi H}} + R_s^2$ (increasing function of time)

If $R_i(t)$ is known, $\alpha(t)$ is known then.

Thermal balance at $r = R_b$ yields:

$$\frac{d}{dt}\int_{R_b}^{R_o}\rho c_p T_b dr = -k_o \left.\frac{\partial T}{\partial r}\right|_{R_b} \quad \text{Eq. 9.14}$$

where R_o is the radius of the CRF outer cylinder, c_p the heat capacity of oil and ρ the density of the oil. Assuming the variation in the thickness of the wax deposit plus the boundary layer is negligible ($R_s \approx R_i \approx R_b$):

$$\rho c_p \dot{T}_b (R_o - R_s) = -k_o \frac{(T_b - T_i)}{\ln\left({}^{R_b}/_{R_i}\right)} \frac{1}{R_i} \quad \text{Eq. 9.15}$$

Or equivalently

$$\dot{T_b} = -\frac{h}{\rho c_p \Delta R}(T_b - T_i) \quad \text{Eq. 9.16}$$

where $\Delta R = R_o - R_s$ is constant. Zero flux is assumed at $r = R_o$.

Recall that:

$$T_i = \frac{(\alpha T_b + T_s)}{(1+\alpha)} \quad \text{Eq. 9.17}$$

so that

$$(T_b - T_i) = \frac{(T_b - T_s)}{(1+\alpha)} \quad \text{Eq. 9.18}$$

Combining Eqs. (1), (5), (7):

$$\dot{T_b} = -\frac{h}{\rho c_p \Delta R}\frac{(T_b - T_s)}{(1+\alpha)} = -C_1 (T_b - T_s)\frac{1}{(1+\alpha)} \quad \text{Eq. 9.19}$$

With,

$$C_1 = \frac{h}{\Delta R \rho c_p} \quad \text{Eq. 9.20}$$

Therefore

$$\dot{T_b} = -C_1 \frac{(T_b - T_s)}{(1+\alpha)} \qquad \text{Eq. 9.21}$$

Integration of the above with $T_b(0) = T_h$ (the constant temperature of the circulating hot fluid) provides:

$$T_b(t) = T_s + (T_h - T_s)\exp\{-C_1 g(t)\} \qquad \text{Eq. 9.22}$$

where,

$$g(t) = \int_0^t \frac{1}{1+\alpha(t)}\,dt \qquad \text{Eq. 9.23}$$

hence,

$$\frac{\partial T_b}{\partial t} = -(T_h - T_s)\exp\left\{-\frac{h}{\Delta R \rho c_p}\int_o^t \frac{1}{1+\alpha}\,dt\right\}\frac{1}{1+\alpha(t;h)}\frac{h}{\Delta R \rho c_p} < 0 \qquad \text{Eq. 9.24}$$

proving that T_b decreases with time. Also,

$$\frac{\partial T_b}{\partial h} = (T_h - T_s)\exp\left\{-\frac{h}{\Delta R \rho c_p}\int_o^t \frac{1}{1+\alpha}\,dt\right\}\frac{\partial}{\partial h}\left\{-\frac{h}{\Delta R \rho c_p}\int_0^t \frac{1}{1+\alpha}\,dt\right\} < 0 \quad \text{Eq. 9.25}$$

Details of the integration:

$$\frac{\partial T_b}{\partial h} = (T_h - T_s)\exp\left\{-\frac{h}{\Delta R \rho c_p}\int_o^t \frac{1}{1+\alpha}\,dt\right\}\frac{\partial}{\partial h}\left\{-\frac{h}{\Delta R \rho c_p}\int_0^t \frac{1}{1+\alpha}\,dt\right\} \qquad \text{Eq. 9.26}$$

Hence, this derivative must be evaluated: $\frac{\partial}{\partial h}\left\{-\frac{h}{\Delta R \rho c_p}\int_0^t \frac{1}{1+\alpha}\,dt\right\}$

$$\frac{\partial}{\partial h}\left\{-\frac{h}{\Delta R \rho c_p}\int_0^t \frac{1}{1+\alpha}\,dt\right\} = \frac{\partial}{\partial h}\left\{-\frac{h}{\Delta R \rho c_p}\right\}\int_0^t \frac{1}{1+\alpha(t;h)}\,dt - \frac{h}{\Delta R \rho c_p}\int_0^t \frac{\partial}{\partial h}\left[\frac{1}{1+\alpha(t;h)}\right]dt =$$

$$-\frac{1}{\Delta R \rho c_p}\int_0^t \frac{1}{1+\alpha(t;h)}\,dt - \frac{h}{\Delta R \rho c_p}\int_0^t -\frac{1}{(1+\alpha(t;h))^2}\frac{\partial \alpha}{\partial h}\,dt = -\frac{1}{\Delta R \rho c_p}\int_0^t \left[\frac{1}{1+\alpha(t;h)} - \frac{\partial \alpha}{\partial h}\frac{h}{(1+\alpha(t;h))^2}\right]dt = A$$

Eq. 9.27

Now, from the definition of α it is easy to check that:

$$\frac{\partial \alpha}{\partial h} = \frac{\alpha}{h} \qquad \text{Eq. 9.28}$$

Hence,

$$A = -\frac{1}{\Delta R \rho c_p} \int_0^t \left[\frac{1}{1+\alpha((t;h))^2}\right] dt \qquad \text{Eq. 9.29}$$

Finally,

$$\frac{\partial T_b}{\partial h} = (T_h - T_s) \exp\left\{-\frac{h}{\Delta R \rho c_p} \int_o^t \frac{1}{1+\alpha} dt\right\} . \left\{-\frac{1}{\Delta R \rho c_p} \int_0^t \left[\frac{1}{(1+\alpha(t;h))^2}\right] dt\right\} < 0$$

since:

$(T_h - T_s) \exp\left\{-\frac{h}{\Delta R \rho c_p} \int_o^t \frac{1}{1+\alpha} dt\right\} > 0$

$\left\{-\frac{1}{\Delta R \rho c_p} \int_0^t \left[\frac{1}{(1+\alpha(t;h))^2}\right] dt\right\} < 0$

implying that T_b decreases as the heat transfer (and hence the CRF rotational speed) increases. Following Singh et al.,[19] the solubility gradient is supposed constant and given by the empirical relation:

$$\frac{dC}{dT} = \beta = ab(T_s + 17.8)^{(d^{-1})} \qquad \text{Eq. 9.30}$$

where, a, b and d are constants and equal to $4.9.10^{-7}$, 297.95 and 5.98 respectively. Recalling Eq. 1, the mass growth rate is expressed as:

$$\frac{dm}{dt} = \frac{D\beta h}{k_o}\left(T_b(t) - T_i(t)\right) \qquad \text{Eq. 9.31}$$

where $T_b(t), T_i(t)$ are given by Eqs. (8) and (20).

The heat transfer coefficient is calculated using the Nusselt number:

$$Nu = LR_e^m P_r^n = \frac{hR_o}{k_o} \quad \text{Eq. 9.32}$$

where, Re is the Reynolds number ($Re = \frac{\rho\omega R_s^2}{\mu}$), Pr the Prandtl number ($Pr = \frac{\mu c_p}{k_o}$), with constants L, m and n determined by fitting the wax deposition data at 100 rpm.

Contribution of Sloughing:

In order to account for sloughing, the model was modified to include a sloughing term $\dot{S}(t)$ as follows:

$$\dot{m}(t) = \dot{D}(t) - \dot{S}(t) \quad \text{Eq. 9.33}$$

where, $\dot{D}(t)$ is the deposition rate (Eq. 29) and $\dot{S}(t)$ is the sloughing rate:

$$\dot{S}(t) = -\theta|\tau|_{R_i}R_i \quad \text{Eq. 9.34}$$

where θ is a fitting parameter describing the sloughing intensity, $|\tau|$ the wall shear stress ($|\tau| = (\frac{2\mu R_o^2\omega}{R_o^2 - R_i^2})$, with ω the angular velocity), and R_i the radius of the wax deposit.

$$m(t) = \int_0^t \dot{D}(\delta)d\delta - \int_0^t \frac{2R_o^2}{R_o^2 - R_i^2}\,[\theta\mu(T_i(\delta)).w.R_i]d\delta \quad \text{Eq. 9.35}$$

where the viscosity, $\mu = \mu(T)$, and is a decreasing function of temperature (with γ being a constant):

$$\mu = \frac{\gamma}{T_i(t)} \qquad \text{Eq. 9.36}$$

So that,

$$m(t) = \int_0^t \dot{D}(\delta)d\delta - \int_o^t \left(\frac{2R_o^2 w}{R_o^2 - R_i^2}\right)\frac{\theta\gamma R_i}{T_i(\tau)}d\delta \qquad \text{Eq. 9.37}$$

$$m(t) = \int_0^t \dot{D}(\delta)d\delta - \int_o^t C_2 \frac{wR_i}{T_i(t)}d\delta \qquad \text{Eq. 9.38}$$

where,

$$C_2 = \theta\gamma\left(\frac{2R_o^2}{R_o^2 - R_i^2}\right) \qquad \text{Eq. 9.39}$$

C_2 and is a fitting parameter

9.2.2 Matlab Codes

9.2.2.1 Matlab Codes: Create a Fit for Mass Function

```
function [fitresult, gof] = createFit(ts, Ms)
%CREATEFIT1(TS,MS)
%  Create a fit.
%
%  Data for 'untitled fit 1' fit:
%      X Input : ts
%      Y Output: Ms
%  Output:
%      fitresult : a fit object representing the fit.
%      gof : structure with goodness-of fit info.
```

```
%
%  See also FIT, CFIT, SFIT.

%  Auto-generated by MATLAB on 25-Sep-2019 12:17:01


%% Fit: 'untitled fit 1'.
[xData, yData] = prepareCurveData( ts, Ms );

% Set up fittype and options.
ft = fittype( 'rat22' );
opts = fitoptions( 'Method', 'NonlinearLeastSquares' );
opts.Display = 'Off';
opts.StartPoint     =     [0.0461713906311539     0.0971317812358475
0.823457828327293 0.694828622975817 0.317099480060861];

% Fit model to data.
[fitresult, gof] = fit( xData, yData, ft, opts );

% % Plot fit with data.
% figure( 'Name', 'untitled fit 1' );
% h = plot( fitresult, xData, yData );
% legend( h, 'Ms vs. ts', 'untitled fit 1', 'Location', 'NorthEast'
);
% % Label axes
% xlabel ts
% ylabel Ms
% grid on
```

9.2.2.2 Matlab Codes: Create a Fit for “Phi” Function

```
function [fitresult, gof] = createFit3(t_phi, phi)
%CREATEFIT3(T_PHI,PHI)
%  Create a fit.
%
%  Data for 'untitled fit 1' fit:
%      X Input : t_phi
%      Y Output: phi
%  Output:
%      fitresult : a fit object representing the fit.
%      gof : structure with goodness-of fit info.
%
%  See also FIT, CFIT, SFIT.

%  Auto-generated by MATLAB on 04-Oct-2019 11:01:44


%% Fit: 'untitled fit 1'.
[xData, yData] = prepareCurveData( t_phi, phi );

% Set up fittype and options.
```

```
ft = fittype( 'poly1' );
opts = fitoptions( 'Method', 'LinearLeastSquares' );
opts.Robust = 'LAR';

% Fit model to data.
[fitresult, gof] = fit( xData, yData, ft, opts );

% % Plot fit with data.
% figure( 'Name', 'untitled fit 1' );
% h = plot( fitresult, xData, yData );
% legend( h, 'phi vs. t_phi', 'untitled fit 1', 'Location', 'NorthEast'
);
% % Label axes
% xlabel t_phi
% ylabel phi
% grid on
```

9.2.2.3 Matlab Codes: Deposition Model- Example of 100 rpm

```
clear all

no=400;

Ms=[0 2.1606 3.1247 3.3882 3.3697 3.5475 3.7045 3.71167 3.97285]'; %gr
ts=[0 1 5 10 15 20 25 30 60]'; % min
t=linspace(0,60,no);

%%%%%%%%%%% parameters %%%%%%%%%%%%%%%%%%%%%%

%%%%%%%%%%%%%%%%%%%%%%%%%%%%%%%%%%%%%%%%%%%%%%

H=2.976; % cm
rho=0.795978; %%%% . gr/cm^3;
Rs=1.998;  %%%%   cm;
Ro=5;    %%%%  cm
DR=Ro-Rs;  %%%%  cm
Ts=7;
Th=45;
ko=0.137;%%%% W/m*K;
w=100;  %%%%% rpm
q=0.98;
mu=1.19e-03 ; %% viscosity Pa*sec
cp=2.5;  %%%% J/g*K

%%%%% b,D,h,ko from fogler %%%%%%

a=4.9e-7;
b=297.95;
d=5.98;
beta=a*b*(Ts+17.8)^(d-1); %g/(cm^3*K);
```

```
D=1.48e-06; %cm^2/sec

%%%%% heat transfer coefficient %%%%%%

Re=(rho*w*Rs^2/mu)*(1/600); %%%% Reynolds

Pr=(mu*cp/ko)*1e+03;   %%%%%%%%%% . Prandtl

h=(ko/(Ro))*0.048*Re^(4/5)*Pr^(1/3);  %%%%%%%% . W/(m*cm)*K

h=h/100; %w/cm^2*K
ko=ko/100; %w/cm*K

Rit=sqrt(Mt/(rho*pi*H)+Rs^2); %%% cm

ms=Mt./(2*pi*H*Rit); %%% experimental mass p.u. surface


%%%%%%%%%%% parameters %%%%%%%%%%%%%%%%%%%%%%%

[fitresult, gof]=createFit(ts, Rit);


Ri=fitresult(t);
Mt=rho*pi*(Ri.^2-Rs^2)*H;

%%%%%%% coefficient of the model %%%%%%%%%%%%%

C1=(h/(DR*rho*cp))*3600;
C2=(h*Rs/ko);
C3=(D*beta*h/ko);

a=C2*(Ri/Rs).*log(Ri/Rs);


%%%%%%%%%%%%% creation of the function g(t). %%%%%%%%%%%%%%%%%%%%%%%

g=zeros(length(t),1);

for i=2:length(t)

    g(i)=trapz(t(1:i),1./(1+a(1:i)));

end

%%%%%%%%%%%%%%%%%% . creation of the function Tb %%%%%%%%%%%%%%%%%%%

Tb=Ts+(Th-Ts)*exp(-C1*g);

Ti= Tb-((Th-Ts)*exp(-C1*g))./(1+a);

%%%%%%%%%%%%%%%%% . creation of the function m %%%%%%%%%%%%%%%%%%%%
```

```
m=zeros(length(t),1);

for i=2:length(t)

    int=C3*(Tb(1:i)-Ts)./(1+a(1:i));

    m(i)=trapz(t(1:i),int);

end

MM=2*pi*Ri*H.*m;

phi=MM./M;

%%%%%%%%%% fitting of phi %%%%%%%%%%%%%%%%%%%%%%


phi=[phi(100) phi(200) phi(300) phi(350) phi(400)];
t_phi=[t(100) t(200) t(300) t(350) t(400)];

[fitresult3, gof3]=createFit3(t_phi, phi);

phi=fitresult3(t);

const=mean(phi)/0.083;
%
phi=phi./const;
%%%%%%%%%%%%%%%%%%%%%%%%%%%%%%%%%%%%%%%%%%%%%%%%%%%

plot(ts,Ms,'*')
hold on
plot(t,MM./phi)


function dmdt=funzode(t,m,beta,D,h,ko,kd,Ts,Rs,rho,DT)

l=m/(rho*phi)

Ri=(l+sqrt(l^2+Rs^2));  %%%%% cm

alpha=(Ri*h/(kd*100))*log(Ri/Rs);

dmdt=(D*beta*h*DT/(ko*100))/(1+alpha);

end
```

9.2.2.4 Matlab Codes: Deposition Model – Example of 200 rpm

```
clear all
```

```
no=400;

Ms=[0 1.485 2.037 2.3052 2.5341 2.5572 2.631 2.6849 2.809]'; %gr
ts=[0 1 5 10 15 20 25 30 60]'; % min
t=linspace(0,60,no);

%%%%%%%%%%% parameters %%%%%%%%%%%%%%%%%%%%%%

%%%%%%%%%%%%%%%%%%%%%%%%%%%%%%%%%%%%%%%%%%%%%%

H=2.976; % cm
rho=0.795978; %%%% . gr/cm^3;
Rs=1.998;  %%%%   cm;
Ro=5;    %%%%  cm
DR=Ro-Rs;  %%%%  cm
Ts=7;
Th=45;
ko=0.137;%%%% W/m*K;
w=200;  %%%%% rpm
q=0.98;
mu=1.19e-03 ; %% viscosity Pa*sec
cp=2.5;  %%%% J/g*K

%%%%% b,D,h,ko from fogler %%%%%%

a=4.9e-7;
b=297.95;
d=5.98;
beta=a*b*(Ts+17.8)^(d-1); %g/(cm^3*K);
D=1.48e-06; %cm^2/sec

%%%%% heat transfer coefficient %%%%%%

Re=(rho*w*Rs^2/mu)*(1/600); %%%% Reynolds

Pr=(mu*cp/ko)*1e+03;   %%%%%%%%%% . Prandtl

h=(ko/(Ro))*0.048*Re^(4/5)*Pr^(1/3);  %%%%%%%% . W/(m*cm)*K

h=h/100; %w/cm^2*K
ko=ko/100; %w/cm*K

Rit=sqrt(Mt/(rho*pi*H)+Rs^2); %%% cm

ms=Mt./(2*pi*H*Rit); %%% experimental mass p.u. surface


%%%%%%%%%%% parameters %%%%%%%%%%%%%%%%%%%%%%

[fitresult, gof]=createFit(ts, Rit);


Ri=fitresult(t);
```

```
Mt=rho*pi*(Ri.^2-Rs^2)*H;

%%%%%%% coefficient of the model %%%%%%%%%%%%%

C1=(h/(DR*rho*cp))*3600;
C2=(h*Rs/ko);
C3=(D*beta*h/ko);

a=C2*(Ri/Rs).*log(Ri/Rs);


%%%%%%%%%%%%% creation of the function g(t). %%%%%%%%%%%%%%%%%%%%%%

g=zeros(length(t),1);

for i=2:length(t)

    g(i)=trapz(t(1:i),1./(1+a(1:i)));

end

%%%%%%%%%%%%%%%%% . creation of the function Tb %%%%%%%%%%%%%%%%%%%

Tb=Ts+(Th-Ts)*exp(-C1*g);

Ti= Tb-((Th-Ts)*exp(-C1*g))./(1+a);

%%%%%%%%%%%%%%%%% . creation of the function m %%%%%%%%%%%%%%%%%%%%

m=zeros(length(t),1);

for i=2:length(t)

    int=C3*(Tb(1:i)-Ts)./(1+a(1:i));

    m(i)=trapz(t(1:i),int);

end

MM=2*pi*Ri*H.*m;

phi=MM./M;

%%%%%%%%%% fitting of phi %%%%%%%%%%%%%%%%%%%%%%


phi=[phi(100) phi(200) phi(300) phi(350) phi(400)];
t_phi=[t(100) t(200) t(300) t(350) t(400)];

[fitresult3, gof3]=createFit3(t_phi, phi);

phi=fitresult3(t);
```

```
const=mean(phi)/0.115;
%
phi=phi./const;
%%%%%%%%%%%%%%%%%%%%%%%%%%%%%%%%%%%%%%%%%%%%%%%%%%%%%%%%

plot(ts,Ms,'*')
hold on
plot(t,MM./phi)


function dmdt=funzode(t,m,beta,D,h,ko,kd,Ts,Rs,rho,DT)

l=m/(rho*phi)

Ri=(l+sqrt(l^2+Rs^2));  %%%%% cm

alpha=(Ri*h/(kd*100))*log(Ri/Rs);

dmdt=(D*beta*h*DT/(ko*100))/(1+alpha);

end
```

9.2.2.5 Matlab Codes: Sloughing Model – Example of 400 rpm

```
clear all

no=400;

Ms=[0 0.706 1.1947 1.3562 1.4695 1.5049 1.5893 1.5902 1.80343]'; %gr
ts=[0 1 5 10 15 20 25 30 60]'; % min
t=linspace(0,60,no);

%%%%%%%%%%% parameters %%%%%%%%%%%%%%%%%%%%%%%

%%%%%%%%%%%%%%%%%%%%%%%%%%%%%%%%%%%%%%%%%%%%%%%%%%%%%%%%

H=2.976; % cm
rho=0.795978; %%%% . gr/cm^3;
Rs=1.998;  %%%%   cm;
Ro=5;    %%%%  cm
DR=Ro-Rs;  %%%%  cm
Ts=7;
Th=45;
ko=0.137;%%%% W/m*K;
w=400;  %%%%% rpm
q=0.98;
mu=1.19e-03 ; %% viscosity Pa*sec
cp=2.5;  %%%% J/g*K
```

```
%%%%% b,D,h,ko from fogler %%%%%%

a=4.9e-7;
b=297.95;
d=5.98;
beta=a*b*(Ts+17.8)^(d-1); %g/(cm^3*K);
D=1.48e-06; %cm^2/sec

%%%%% heat transfer coefficient %%%%%%

Re=(rho*w*Rs^2/mu)*(1/600); %%%% Reynolds

Pr=(mu*cp/ko)*1e+03;   %%%%%%%%%% . Prandtl

h=(ko/(Ro))*0.048*Re^(4/5)*Pr^(1/3);  %%%%%%%% . W/(m*cm)*K

h=h/100; %w/cm^2*K
ko=ko/100; %w/cm*K

Rit=sqrt(Mt/(rho*pi*H)+Rs^2); %%% cm

ms=Mt./(2*pi*H*Rit); %%% experimental mass p.u. surface


%%%%%%%%%%% parameters %%%%%%%%%%%%%%%%%%%%%%%

[fitresult, gof]=createFit(ts, Rit);


Ri=fitresult(t);
Mt=rho*pi*(Ri.^2-Rs^2)*H;

%%%%%%% coefficient of the model %%%%%%%%%%%%%

C1=(h/(DR*rho*cp))*3600;
C2=(h*Rs/ko);
C3=(D*beta*h/ko);

a=C2*(Ri/Rs).*log(Ri/Rs);


%%%%%%%%%%%%% creation of the function g(t). %%%%%%%%%%%%%%%%%%%%%%%

g=zeros(length(t),1);

for i=2:length(t)

    g(i)=trapz(t(1:i),1./(1+a(1:i)));

end

%%%%%%%%%%%%%%%%% . creation of the function Tb %%%%%%%%%%%%%%%%%%%
```

```
Tb=Ts+(Th-Ts)*exp(-C1*g);

Ti= Tb-((Th-Ts)*exp(-C1*g))./(1+a);

%%%%%%%%%%%%%%%%%% . creation of the function m %%%%%%%%%%%%%%%%%%%%

m=zeros(length(t),1);

for i=2:length(t)

    int=C3*(Tb(1:i)-Ts)./(1+a(1:i));

    m(i)=trapz(t(1:i),int);

    d=3e-07;

    intsl=d*w*Rd(1:i)./(Ts(1:i));

    m(i)=m(i)-trapz(t(1:i),intsl);  % sloughing


end

MM=2*pi*Ri*H.*m;

phi=MM./M;

%%%%%%%%%% fitting of phi %%%%%%%%%%%%%%%%%%%%%%


phi=[phi(100) phi(200) phi(300) phi(350) phi(400)];
t_phi=[t(100) t(200) t(300) t(350) t(400)];

[fitresult3, gof3]=createFit3(t_phi, phi);

phi=fitresult3(t);

const=mean(phi)/0.145;

phi=phi./const;
%%%%%%%%%%%%%%%%%%%%%%%%%%%%%%%%%%%%%%%%%%%%%%%%%%%%%%%%%%%%%%%%

plot(ts,Ms,'*')
hold on
plot(t,MM./phi)


function dmdt=funzode(t,m,beta,D,h,ko,kd,Ts,Rs,rho,DT)

l=m/(rho*phi)

Ri=(l+sqrt(l^2+Rs^2));  %%%%% cm
```

```
alpha=(Ri*h/(kd*100))*log(Ri/Rs);

dmdt=(D*beta*h*DT/(ko*100))/(1+alpha);

end
```

9.2.2.6 Matlab Codes: Sloughing model – Example of 700 rpm

```
clear all

no=400;

Ms=[0 0.6611 1.0545 1.1931 1.2172 1.3485 1.3528 1.3557 1.5446]'; %gr
ts=[0 1 5 10 15 20 25 30 60]'; % min
t=linspace(0,60,no);

%%%%%%%%%%% parameters %%%%%%%%%%%%%%%%%%%%%%

%%%%%%%%%%%%%%%%%%%%%%%%%%%%%%%%%%%%%%%%%%%%%%

H=2.976; % cm
rho=0.795978; %%%% . gr/cm^3;
Rs=1.998;  %%%%   cm;
Ro=5;    %%%%  cm
DR=Ro-Rs;  %%%%  cm
Ts=7;
Th=45;
ko=0.137;%%%% W/m*K;
w=700;  %%%%% rpm
q=0.98;
mu=1.19e-03 ; %% viscosity Pa*sec
cp=2.5;  %%%% J/g*K

%%%%% b,D,h,ko from fogler %%%%%%

a=4.9e-7;
b=297.95;
d=5.98;
beta=a*b*(Ts+17.8)^(d-1); %g/(cm^3*K);
D=1.48e-06; %cm^2/sec

%%%%% heat transfer coefficient %%%%%%

Re=(rho*w*Rs^2/mu)*(1/600); %%%% Reynolds

Pr=(mu*cp/ko)*1e+03;   %%%%%%%%%% . Prandtl

h=(ko/(Ro))*0.048*Re^(4/5)*Pr^(1/3);  %%%%%%%% . W/(m*cm)*K

h=h/100; %w/cm^2*K
```

```
ko=ko/100; %w/cm*K

Rit=sqrt(Mt/(rho*pi*H)+Rs^2); %%% cm

ms=Mt./(2*pi*H*Rit); %%% experimental mass p.u. surface


%%%%%%%%%%% parameters %%%%%%%%%%%%%%%%%%%%%%

[fitresult, gof]=createFit(ts, Rit);


Ri=fitresult(t);
Mt=rho*pi*(Ri.^2-Rs^2)*H;

%%%%%%% coefficient of the model %%%%%%%%%%%%%

C1=(h/(DR*rho*cp))*3600;
C2=(h*Rs/ko);
C3=(D*beta*h/ko);

a=C2*(Ri/Rs).*log(Ri/Rs);


%%%%%%%%%%%% creation of the function g(t). %%%%%%%%%%%%%%%%%%%%%%

g=zeros(length(t),1);

for i=2:length(t)

    g(i)=trapz(t(1:i),1./(1+a(1:i)));

end

%%%%%%%%%%%%%%%%% . creation of the function Tb %%%%%%%%%%%%%%%%%%%

Tb=Ts+(Th-Ts)*exp(-C1*g);

Ti= Tb-((Th-Ts)*exp(-C1*g))./(1+a);

%%%%%%%%%%%%%%%%% . creation of the function m %%%%%%%%%%%%%%%%%%%%

m=zeros(length(t),1);

for i=2:length(t)

    int=C3*(Tb(1:i)-Ts)./(1+a(1:i));

    m(i)=trapz(t(1:i),int);

    d=5.5e-07;

    intsl=d*w*Rd(1:i)./(Ts(1:i));
```

```
    m(i)=m(i)-trapz(t(1:i),intsl);   % sloughing

end

MM=2*pi*Ri*H.*m;

phi=MM./M;

%%%%%%%%%% fitting of phi %%%%%%%%%%%%%%%%%%%%%%


phi=[phi(100) phi(200) phi(300) phi(350) phi(400)];
t_phi=[t(100) t(200) t(300) t(350) t(400)];

[fitresult3, gof3]=createFit3(t_phi, phi);

phi=fitresult3(t);

const=mean(phi)/0.15;
%
K=phi
phi=phi./const;
%%%%%%%%%%%%%%%%%%%%%%%%%%%%%%%%%%%%%%%%%%%%%%%%%%%

plot(ts,Ms,'*')
hold on
plot(t,MM./phi)


function dmdt=funzode(t,m,beta,D,h,ko,kd,Ts,Rs,rho,DT)

l=m/(rho*phi)

Ri=(l+sqrt(l^2+Rs^2));  %%%%% cm

alpha=(Ri*h/(kd*100))*log(Ri/Rs);

dmdt=(D*beta*h*DT/(ko*100))/(1+alpha);

end
```

9.3 Appendix for Chapter 6

9.3.1 Mechanism of Williamson Ether Synthesis

The reaction of alkoxides with alkyl halides is an important general method for the preparation of ethers, and is known as the Williamson synthesis[242]. The Williamson ether synthesis is an organic reaction, forming an ether from an organohalide and a deprotonated alcohol (alkoxide). This reaction was developed by Alexander Williamson in 1850. Typically it involves the reaction of an alkoxide ion with a primary alkyl halide via an S_N2 reaction. In an S_N2 reaction mechanism there is a backside attack of an electrophile by a nucleophile and it occurs in a concerted mechanism (happens all at once). Alkoxide ion formation is important as a means of generating a strong nucleophile that will readily form C-O bonds and the halide is a strongly negative electrophile that form a good leaving group[242]. The general reaction mechanism is as follows:

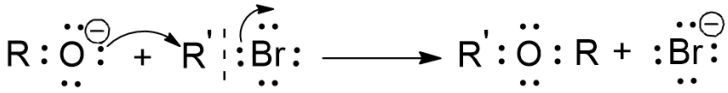

S_N2 reaction is a second order reaction with the rate dependant on the concentrations of both reactants because it is a single step reaction that involves collisions between hydroxide ions and alkylhalide molecules. Hence, the reaction rate (v) may be expressed as following:

$$v = k[RX][Y]$$

Experimentally, the rate of formation of product is found to be proportional to the concentrations of both haloalkane and hydroxide ion. Such reactions are classified as bimolecular nucleophilic substitutions because there are two reactant molecules in the transition state[242].

9.3.2 Sample of the Stoichiometric Calculation used for the Etherification of EC using Alkyl Bromide

This sample discuss the calculation for the EC-4.

The number of moles in 2 g of EC used in the reaction is calculated as follows:

$$n_{EC} = \frac{m_{EC}}{M_{EC}} = \frac{2}{209.52} = 0.00954563\ moles \qquad \text{Eq. 9.40}$$

EC has a degree of substitution of 49% ethoxy, this means that each monomer of EC has 49% of the 3 OH originally present in cellulose. Therefore, the number of OH moles in the 2 g of EC used in the reaction is calculated as follows:

$$n_{OH} = 3 \times n_{EC} \times \frac{49}{100} = 3 \times 0.00954563 \times \frac{49}{100} = 0.01431844\ moles \qquad \text{Eq. 9.41}$$

The mass of alkyl bromide ($C_{18}Br$) needed to make a stochiometric substitution of OH group by C18 group is calculated as follows:

$$m_{C_{18}Br} = n_{OH} \times M_{C_{18}Br} = 0.01431844 \times 333.39 = 4.77362543\ g \qquad \text{Eq. 9.42}$$

As the alkyl bromide is introduced to the reaction solution in liquid state, therefore, the volume of alkyl bromide needed is calculated as follows:

$$V_{C_{18}Br} = \frac{m_{C_{18}Br}}{\rho_{C_{18}Br}} = \frac{4.77362543}{0.976} = 4.89\ mL \qquad \text{Eq. 9.43}$$

References

1. Khatib, H., IEA World Energy Outlook 2011—A comment. *Energy Policy* **2012,** *48*, 737-743.
2. Huc, A.-Y., *Heavy Crude Oils in the Perspective of World Oil Demand*. Editions Technip: 2011; p 2-2.
3. Schobert, H., *Fuels and the Global Carbon Cycle*. Cambridge University Press: 2013; p 1-8.
4. Stratiev, D.; Shishkova, I.; Nedelchev, A.; Kirilov, K.; Nikolaychuk, E.; Ivanov, A.; Sharafutdinov, I.; Veli, A.; Mitkova, M.; Tsaneva, T.; Petkova, N.; Sharpe, R.; Yordanov, D.; Belchev, Z.; Nenov, S.; Rudnev, N.; Atanassova, V.; Sotirova, E.; Sotirov, S.; Atanassov, K., Investigation of Relationships between Petroleum Properties and Their Impact on Crude Oil Compatibility. *Energy & Fuels* **2015,** *29* (12), 7836-7854.
5. Khan, M. I.; Islam, M. R., *The New Management Guidelines*. Gulf Publishing Company: 2007; p 1-1.
6. Bai, Q.; Bai, Y., *Subsea engineering handbook*. Gulf Professional Publishing: Waltham, MA, 2012.
7. Research and Markets: OECD Green Growth Studies: Energy. Normans Media Ltd: Coventry, 2011.
8. (EIA)., U. S. E. I. A. EIA forecasts U.S. crude oil production will keep growing through 2021, but more slowly. https://www.eia.gov/todayinenergy/detail.php?id=42615#.
9. Azevedo, L. F. A.; Teixeira, A. M., A Critical Review of the Modeling of Wax Deposition Mechanisms. *Petroleum Science and Technology* **2003,** *21* (3-4), 393-408.
10. Bai, Y.; Bai, Q., *Overview of Subsea Engineering*. Elsevier: 2012; p 2-2.
11. Huang, Z.; Zheng, S.; Fogler, H. S., *Wax Deposition*. 1 ed.; CRC Press: 2016.
12. *Offshore pipelines design, installation, and maintenance*. 2nd ed. ed.; Gulf Professional Publishing: Waltham, Mass, 2014.
13. Huang, Z.; Senra, M.; Kapoor, R.; Fogler, H. S., Wax deposition modeling of oil/water stratified channel flow. *AIChE Journal* **2011,** *57* (4), 841-851.
14. Group, T. E. C. Gulf of Mexico Oil and Gas Industry: Deepwater Focus. http://www.energy-cg.com/GOM/GOM_OilGas_Overview.html.
15. Hennessy, A.; Neville, A.; Roberts, K. J., In-situ SAXS/WAXS and turbidity studies of the structure and composition of multihomologous n-alkane waxes crystallized in the absence and presence of flow improving additive species. *Crystal Growth and Design* **2004,** *4* (5), 1069-1078.
16. Wang, P.; Wang, W.; Gong, J.; Zhou, Y.; Yang, W.; Zhang, Y., Effect of pour point on wax deposition under static cooling conditions. *Asia-Pacific Journal of Chemical Engineering* **2013,** *8* (5).
17. Zhu, T.; Walker, J. A.; Liang, J. *Evaluation of Wax Deposition and Its Control During Production of Alaska North Slope Oils*; ; University of Alaska: 2008; p Medium: ED.
18. Gluyas, J. G.; Underhill, J. R., The Staffa Field, Block 3/8b, UK North Sea. *Geological Society Memoir* **2003,** *20* (1), 327-333.
19. Singh, P.; Venkatesan, R.; Fogler, H. S.; Nagarajan, N., Formation and aging of incipient thin film wax-oil gels. *AIChE Journal* **2000,** *46* (5), 1059-1074.
20. Wu, C. H.; Wang, K. S.; Shuler, P. J.; Tang, Y.; Creek, J. L.; Carlson, R. M.; Cheung, S., Measurement of wax deposition in paraffin solutions. *AIChE Journal* **2002,** *48* (9), 2107-2110.

21. Mahir, L. H. A.; Vilas Bôas Fávero, C.; Ketjuntiwa, T.; Fogler, H. S.; Larson, R. G., Mechanism of Wax Deposition on Cold Surfaces: Gelation and Deposit Aging. *Energy & Fuels* **2019,** *33* (5), 3776-3786.
22. Paso, K.; Kompalla, T.; Aske, N.; Rønningsen, H. P.; Øye, G.; Sjöblom, J., Novel Surfaces with Applicability for Preventing Wax Deposition: A Review. *Journal of Dispersion Science and Technology* **2009,** *30* (6), 757-781.
23. Dwivedi, G.; Sharma, M. P., Impact of cold flow properties of biodiesel on engine performance. *Renewable and Sustainable Energy Reviews* **2014,** *31*, 650-656.
24. Xu, B., Influencing factors governing paraffin wax deposition of heavy oil and research on wellbore paraffin remover. *Petroleum Science and Technology* **2018,** *36* (20), 1635-1641.
25. Biorefineries - Industrial Processes and Products, 2 vols bound together. *Focus on catalysts* **2010,** *2010* (11), 8-8.
26. Deffense, E., Milk fat fractionation today: A review. *Journal of the American Oil Chemists' Society* **1993,** *70* (12), 1193-1201.
27. Hartel, R. W., Crystallization in Foods. In *Handbook of Industrial Crystallization*, 3 ed.; Lee, A. Y.; Myerson, A. S.; Erdemir, D., Eds. Cambridge University Press: Cambridge, 2019; pp 460-478.
28. Zhu, H.; Li, C.; Xiu, Z.; Zhao, Z.; Mu, K.; Dai, H.; Wang, F.; Yang, F.; Yao, B., Effect of Ethylene-Vinyl Acetate Copolymer/Amino-Functionalized Polymethylsilsesquioxane Composite Wax Inhibitor on the Rheological and Wax Depositing Characteristics of Waxy Crude Oil. *Energy & Fuels* **2020,** *34* (7), 8120-8128.
29. Janamatti, A.; Lu, Y.; Ravichandran, S.; Sarica, C.; Daraboina, N., Influence of operating temperatures on long-duration wax deposition in flow lines. *Journal of Petroleum Science and Engineering* **2019,** *183*, 106373.
30. Kané, M.; Djabourov, M.; Volle, J.-L.; Lechaire, J.-P.; Frebourg, G., Morphology of paraffin crystals in waxy crude oils cooled in quiescent conditions and under flow. *Fuel* **2003,** *82* (2), 127-135.
31. Singh, P.; Venkatesan, R.; Fogler, H. S.; Nagarajan, N. R., Morphological evolution of thick wax deposits during aging. *AIChE Journal* **2001,** *47* (1), 6-18.
32. Singh, P.; Fogler, H. S.; Nagarajan, N., Prediction of the wax content of the incipient wax-oil gel in a pipeline: An application of the controlled-stress rheometer. *Journal of Rheology* **1999,** *43* (6), 1437-1459.
33. Billy, L.; Hikmat Said Ak, S.; Norida, R., A review of the mechanism and role of wax inhibitors in the wax deposition and precipitation. Unpublished: 2018.
34. Ganeeva, Y.; Yusupova, T.; Romanov, G., Waxes in asphaltenes of crude oils and wax deposits. *Petroleum Science* **2016,** *13* (4), 737-745.
35. Musser, B. J.; Kilpatrick, P. K., Molecular characterization of wax isolated from a variety of crude oils. *Energy and Fuels* **1998,** *12* (4), 715-725.
36. Ronningsen, H. P.; Bjorndal, B.; Hansen, A. B.; Pedersen, W. B., Wax Precipitation from North Sea Crude Oils. 1. Crystallization and Dissolution Temperatures, and Newtonian and Non-Newtonian Flow Properties. *Energy and Fuels* **1991,** *5* (6), 895-908.
37. Yang, F.; Li, C.; Li, C.; Wang, D., Scaling of Structural Characteristics of Gelled Model Waxy Oils. *Energy & Fuels* **2013,** *27* (7), 3718-3724-3718-3724.
38. Burger, E. D.; Perkins, T. K.; Striegler, J. H., STUDIES OF WAX DEPOSITION IN THE TRANS ALASKA PIPELINE. *JPT, Journal of Petroleum Technology* **1981,** *33* (6), 1075-1086.
39. Liu, Z.; Li, Y.; Wang, W.; Song, G.; Lu, Z.; Ning, Y., Wax and Wax–Hydrate Deposition Characteristics in Single-, Two-, and Three-Phase Pipelines: A Review. *Energy & Fuels* **2020,** *34* (11), 13350-13368.

40. Jennings, D. W.; Weispfennig, K., Effect of Shear on the Performance of Paraffin Inhibitors: Coldfinger Investigation with Gulf of Mexico Crude Oils. *Energy & fuels* **2006,** *20* (6), 2457-2464.
41. Dos Santos, J. D. S. T.; Fernandes, A. C.; Giulietti, M., Study of the paraffin deposit formation using the cold finger methodology for Brazilian crude oils. *Journal of Petroleum Science and Engineering* **2004,** *45* (1-2), 47-60.
42. Kasumu, A. S.; Mehrotra, A. K., Solids deposition from wax-solvent-water "waxy" mixtures using a cold finger apparatus. *Energy and Fuels* **2015,** *29* (2), 501-511.
43. Zougari, M.; Jacobs, S.; Ratulowski, J.; Hammami, A.; Broze, G.; Flannery, M.; Stankiewicz, A.; Karan, K., Novel organic solids deposition and control device for live-oils: Design and applications. *Energy & Fuels* **2006,** *20* (4), 1656-1663.
44. Zougari, M. I., Shear driven crude oil wax deposition evaluation. *Journal of Petroleum Science and Engineering* **2010,** *70* (1), 28-34.
45. Bidmus, H.; Mehrotra, A. K., Measurement of the liquid-deposit interface temperature during solids deposition from wax-solvent mixtures under sheared cooling. *Energy and Fuels* **2008,** *22* (6), 4039-4048.
46. Jennings, D. W.; Weispfennig, K., Effects of shear and temperature on wax deposition: Coldfinger investigation with a Gulf of Mexico crude oil. *Energy and Fuels* **2005,** *19* (4), 1376-1386.
47. Lu, Y.; Huang, Z.; Hoffmann, R.; Amundsen, L.; Fogler, H. S., Counterintuitive effects of the oil flow rate on wax deposition. *Energy and Fuels* **2012,** *26* (7), 4091-4097.
48. Creek, J. L.; Lund, H. J.; Brill, J. P.; Volk, M., Wax deposition in single phase flow. *Fluid Phase Equilibria* **1999,** *158-160*, 801-811.
49. Bott, T.; Gudmundsson, J., Deposition of Paraffin Wax From Kerosene in Cooled Heat Exchanger Tubes. *Canadian Journal of Chemical Engineering* **1977,** *55* (4), 381-385.
50. Lee, H.; Singh, P.; Thomason, W.; Fogler, H., Waxy oil gel breaking mechanisms: Adhesive versus cohesive failure. *Energy & Fuels* **2008,** *22* (1), 480-487.
51. Sinha, C., Investigation of 'Sloughing Behaviour' of Wax Deposit from Paraffin mIxtures in Pipe Flow. University of, C.; University of, C.; Mehrotra, A. K., Eds. University of Calgary: 2016.
52. Tinsley, J. F.; Prud'homme, R. K.; Guo, X.; Adamson, D. H.; Callahan, S.; Amin, D.; Shao, S.; Kriegel, R. M.; Saini, R., Novel laboratory cell for fundamental studies of the effect of polymer additives on wax deposition from model crude oils. *Energy and Fuels* **2007,** *21* (3), 1301-1308.
53. Paso, K.; Kompalla, T.; Aske, N.; Sjöblom, J., A Quartz Crystal Microbalance Characterization of Metal-Oil Interfaces and Interactions with Wax Molecules. *Journal of Dispersion Science and Technology* **2008,** *29* (5), 775-782.
54. Yang, J.; Lu, Y.; Daraboina, N.; Sarica, C., Wax deposition mechanisms: Is the current description sufficient? *Fuel* **2020,** *275*, 117937.
55. Giacchetta, G.; Marchetti, B.; Leporini, M.; Terenzi, A.; Dall'Acqua, D.; Capece, L.; Cocci Grifoni, R., Pipeline wax deposition modeling: A sensitivity study on two commercial software. *Petroleum* **2019,** *5* (2), 206-213.
56. Ehsani, S.; Haj-Shafiei, S.; Mehrotra, A. K., Experiments and modeling for investigating the effect of suspended wax crystals on deposition from 'waxy' mixtures under cold flow conditions. *Fuel* **2019,** *243*, 610-621.
57. Ehsani, S.; Mehrotra, A. K., Validating Heat-Transfer-Based Modeling Approach for Wax Deposition from Paraffinic Mixtures: An Analogy with Ice Deposition. *Energy & fuels* **2019,** *33* (3), 1859-1868.

58. Alnaimat, F.; Ziauddin, M., Wax deposition and prediction in petroleum pipelines. *Journal of petroleum science & engineering* **2020,** *184*, 106385.
59. Harun, A.; Khairul Irfan Nik Ab Lah, N.; Husin, H.; Hassan, Z., An Overview of Wax Crystallization, Deposition Mechanism and Effect of Temperature & Shear. IEEE: 2016; pp 1-5.
60. Struchkov, I.; Rogachev, M., Wax precipitation in multicomponent hydrocarbon system. *Journal of Petroleum Exploration and Production Technology* **2017,** *7* (2), 543-553.
61. Venkatesan, R.; Singh, P.; Fogler, H., Delineating the pour point and gelation temperature of waxy crude oils. *Spe Journal* **2002,** *7* (4), 349-352.
62. Huang, Z.; Lu, Y.; Hoffmann, R.; Amundsen, L.; Fogler, H., The Effect of Operating Temperatures on Wax Deposition. *Energy & Fuels* **2011,** *25* (11), 5180-5188-5180-5188.
63. Agrawal, K. M.; Khan, H. U.; Surianarayanan, M.; Joshi, G. C., Wax deposition of Bombay high crude oil under flowing conditions. *Fuel* **1990,** *69* (6), 794-796.
64. Bidmus, H. O.; Mehrotra, A. K., Solids deposition during "cold flow" of wax-solvent mixtures in a flow-loop apparatus with heat transfer. *Energy and Fuels* **2009,** *23* (6), 3184-3194.
65. Ridzuan, N.; Adam, F.; Yaacob, Z., Screening of factor influencing wax deposition using full factorial experimental design. *Petroleum Science and Technology* **2016,** *34* (1), 84-90.
66. Lashkarbolooki, M.; Esmaeilzadeh, F.; Mowla, D., Mitigation of Wax Deposition by Wax-Crystal Modifier for Kermanshah Crude Oil. *Journal of Dispersion Science and Technology* **2011,** *32* (7), 975-985.
67. Paso, K. G.; Fogler, H. S., Bulk stabilization in wax deposition systems. *Energy and Fuels* **2004,** *18* (4), 1005-1013.
68. Pan, S.; Zhu, J.; Zhang, D.; Razouki, A.; Talbot, M.; Wierzchowski, S., Case Studies on Simulation of Wax Deposition in Pipelines. *Society of Petroleum Engineers - International Petroleum Technology Conference 2009, IPTC 2009* **2009,** *2*.
69. Ridzuan, N.; Adam, F.; Yaacob, Z., Effects of Shear Rate and Inhibitors on Wax Deposition of Malaysian Crude Oil. *Oriental Journal of Chemistry* **2015,** *31*, 1999-2004.
70. Fong, N.; Mehrotra, A. K., Deposition under turbulent flow of wax-solvent mixtures in a bench-scale flow-loop apparatus with heat transfer. *Energy and Fuels* **2007,** *21* (3), 1263-1276.
71. Parthasarathi, P.; Mehrotra, A., Solids Deposition from Multicomponent Wax-Solvent Mixtures in a Benchscale Flow-Loop Apparatus with Heat Transfer. *Energy & Fuels* **2005,** *19* (4), 1387-1398.
72. Valinejad, R.; Solaimany Nazar, A. R., An experimental design approach for investigating the effects of operating factors on the wax deposition in pipelines. *Fuel* **2013,** *106*, 843-850.
73. Hu, Z.; Meng, D.; Liu, Y.; Dai, Z.; Jiang, N.; Zhuang, Z., Study of wax deposition law by cold finger device. *Petroleum Science and Technology* **2019,** *37* (15), 1846-1853.
74. Quan, Q.; Gong, J.; Wang, W.; Gao, G., Study on the aging and critical carbon number of wax deposition with temperature for crude oils. *Journal of Petroleum Science and Engineering* **2015,** *130*, 1-5.
75. Quan, Q.; Gong, J.; Wang, W.; Wang, P., The Influence of Operating Temperatures on Wax Deposition During Cold Flow and Hot Flow of Crude Oil. *Petroleum Science and Technology* **2015,** *33* (3), 272-277.
76. Merino-Garcia, D.; Correra, S., Cold Flow: A Review of a Technology to Avoid Wax Deposition. *Petroleum Science and Technology* **2008,** *26* (4), 446-459.
77. Bidmus, H. O.; Mehrotra, A. K., Solids Deposition during “Cold Flow” of Wax−Solvent Mixtures in a Flow-loop Apparatus with Heat Transfer. *Energy & fuels* **2009,** *23* (6), 3184-3194.
78. Quan, Q.; Gong, J.; Wang, W.; Gao, G. J. J. o. P. S.; Engineering, Study on the aging and critical carbon number of wax deposition with temperature for crude oils. **2015,** *130*, 1-5.

79. Wang, W.; Huang, Q.; Wang, C.; Li, S.; Qu, W.; Zhao, J.; He, M. J. J. o. T. A.; Calorimetry, Effect of operating conditions on wax deposition in a laboratory flow loop characterized with DSC technique. **2015,** *119* (1), 471-485.
80. Lashkarbolooki, M.; Seyfaee, A.; Esmaeilzadeh, F.; Mowla, D. J. E.; fuels, Experimental investigation of wax deposition in Kermanshah crude oil through a monitored flow loop apparatus. **2010,** *24* (2), 1234-1241.
81. Creek, J.; Lund, H. J.; Brill, J. P.; Volk, M., Wax deposition in single phase flow. *Fluid Phase Equilibria* **1999,** *158*, 801-811.
82. Huang, Z.; Lu, Y.; Hoffmann, R.; Amundsen, L.; Fogler, H. S. J. E.; Fuels, The effect of operating temperatures on wax deposition. **2011,** *25* (11), 5180-5188.
83. Parthasarathi, P.; Mehrotra, A. K., Solids deposition from multicomponent wax− solvent mixtures in a benchscale flow-loop apparatus with heat transfer. *Energy & fuels* **2005,** *19* (4), 1387-1398.
84. Sanjay, M.; Simanta, B.; Kulwant, S. J. S. P.; Facilities, Paraffin problems in crude oil production and transportation: a review. **1995,** *10* (01), 50-54.
85. Theyab, M., Wax deposition process: Mechanisms, affecting factors and mitigation methods. *Open Access J. Sci* **2018,** *2*, 112-118.
86. Soedarmo, A. A.; Daraboina, N.; Lee, H. S.; Sarica, C. J. E.; Fuels, Microscopic Study of Wax Precipitation Static Conditions. **2016,** *30* (2), 954-961.
87. Zhao, Y., Shut in and Restart of Waxy Crude Oil Pipelines: Gelation, Rheology Model Development, and Application of Polymer/Ionic Liquid Based Additive. Norges Teknisk-Naturvitenskapelige Universitet, F. f. N. O. T. I. f. K. P., Ed. Norges teknisk-naturvitenskapelige universitet, Fakultet for naturvitenskap og teknologi, Institutt for kjemisk prosessteknologi: 2013.
88. Venkatesan, R.; Nagarajan, N. R.; Paso, K.; Yi, Y. B.; Sastry, A. M.; Fogler, H. S., The strength of paraffin gels formed under static and flow conditions. *Chemical Engineering Science* **2005,** *60* (13), 3587-3598.
89. Chang, C.; Boger, D. V.; Nguyen, Q. D., Influence of thermal history on the waxy structure of statically cooled waxy crude oil. *SPE Journal* **2000,** *5* (2), 148-157.
90. Guo, X.; Pethica, B. A.; Huang, J.; Adamson, D.; Prud'Homme, R., Effect of cooling rate on crystallization of model waxy oils with microcrystalline poly(ethylene butene). *Energy & Fuels* **2006,** *20* (1), 250-256.
91. Soedarmo, A.; Daraboina, N.; Lee, H.; Sarica, C., Microscopic Study of Wax Precipitation-Static Conditions. *Energy & Fuels* **2016,** *30* (2), 954-961.
92. Sun-Young Jung, P.-S. K., Jong-Se Lim, An experimental study on the effects of internal tubular coatings on mitigating wax deposition in offshore oil production. *Journal of the Korean Society of Marine Engineering* **2014,** *38* (10), 7.
93. Guo, Y.; Li, W.; Zhu, L.; Liu, H., An excellent non-wax-stick coating prepared by chemical conversion treatment. *Materials letters* **2012,** *72*, 125-127.
94. Carteau, D.; Vallée-Réhel, K.; Linossier, I.; Quiniou, F.; Davy, R.; Compère, C.; Delbury, M.; Faÿ, F., Development of environmentally friendly antifouling paints using biodegradable polymer and lower toxic substances. *Progress in organic coatings* **2014,** *77* (2), 485-493.
95. Zhang, X.; Tian, J.; Wang, L.; Zhou, Z., Wettability effect of coatings on drag reduction and paraffin deposition prevention in oil. *Journal of Petroleum Science and Engineering* **2002,** *36* (1), 87-95.
96. Brady, R. F., A fracture mechanical analysis of fouling release from nontoxic antifouling coatings. *Progress in Organic Coatings* **2001,** *43* (1), 188-192.

97. Patton, C. C.; Casad, B. M., Paraffin Deposition from Refined Wax-Solvent Systems. *Society of Petroleum Engineers journal* **1970,** *10* (1), 17-24.
98. Liang, W.; Zhu, L.; Xu, C.; Li, W.; Liu, H., Ecologically friendly conversion coatings with special wetting behaviors for wax prevention. *RSC advances* **2016,** *6* (31), 26045-26054.
99. Brown, T.; Niesen, V.; Erickson, D. D., MEASUREMENT AND PREDICTION OF THE KINETICS OF PARAFFIN DEPOSITION. *Journal Of Petroleum Technology* **1995,** *47* (4), 328-329.
100. Mansourpoor, M.; Azin, R.; Osfouri, S.; Izadpanah, A. A., Experimental investigation of wax deposition from waxy oil mixtures. *Applied petrochemical research* **2019,** *9* (2), 77-90.
101. Li, R.; Huang, Q.; Huo, F.; Fan, K.; Li, W.; Zhang, D., Effect of shear on the thickness of wax deposit under laminar flow regime. *Journal of Petroleum Science and Engineering* **2019,** *181*, 106212.
102. Hamouda, A.; Davidsen, S. In *An approach for simulation of paraffin deposition in pipelines as a function of flow characteristics with a reference to Teesside oil pipeline*, SPE International Symposium on Oilfield Chemistry, Society of Petroleum Engineers: 1995.
103. Hsu, J.; Brubaker, J. In *Wax deposition measurement and scale-up modeling for waxy live crudes under turbulent flow conditions*, International Meeting on Petroleum Engineering, Society of Petroleum Engineers: 1995.
104. Montalvo, P. Modeling of Wax Deposition in a Crude Oil Carrying Pipeline. Department of Chemical Engineering, University of Utah, 2012.
105. Lu, Y.; Huang, Z.; Hoffmann, R.; Amundsen, L.; Fogler, H. S., Counterintuitive effects of the oil flow rate on wax deposition. *Energy & Fuels* **2012,** *26* (7), 4091-4097.
106. Jennings, D. W.; Weispfennig, K., Effects of shear and temperature on wax deposition: Coldfinger investigation with a Gulf of Mexico crude oil. *Energy & fuels* **2005,** *19* (4), 1376-1386.
107. Hoffmann, R.; Amundsen, L., Single-Phase Wax Deposition Experiments. *Energy & Fuels* **2010,** *24* (2), 1069-1080.
108. Hsu, J. J. C.; Brubaker, J. P., Wax Deposition Measurement and Scale-Up Modeling for Waxy Live Crudes under Turbulent Flow Conditions. In *International Meeting on Petroleum Engineering*, Society of Petroleum Engineers: Beijing, China, 1995; p 10.
109. Tiwary, R.; Mehrotra, A. K., Deposition from wax-solvent mixtures under turbulent flow: Effects of shear rate and time on deposit properties. *Energy and Fuels* **2009,** *23* (3), 1299-1310.
110. Bidmus, H. O.; Mehrotra, A. K., Heat-Transfer Analogy for Wax Deposition from Paraffinic Mixtures. *Industrial and Engineering Chemistry Research* **2004,** *43* (3), 791-803.
111. Hernandez, O. C.; Hensley, H.; Sarica, C.; Brill, J. P.; Volk, M.; Delle-Case, E., Improvements in single-phase paraffin deposition modeling. *Spe Production & Facilities* **2004,** *19* (4), 237-244.
112. Nazar, A. R. S.; Dabir, B.; Islam, M. R., Experimental and Mathematical Modeling of Wax Deposition and Propagation in Pipes Transporting Crude Oil. *Energy Sources* **2005,** *27* (1-2), 185-207.
113. Roehner, R. M.; Fletcher, J. V.; Hanson, F. V.; Dahdah, N. F., Comparative compositional study of crude oil solids from the Trans Alaska Pipeline System using high-temperature gas chromatography. *Energy and Fuels* **2002,** *16* (1), 211-217.
114. Venkatesan, R.; Fogler, H. S., Comments on analogies for correlated heat and mass transfer in turbulent flow. *AIChE Journal* **2004,** *50* (7), 1623-1626.
115. Huang, Z.; Lee, H. S.; Senra, M.; Scott Fogler, H., A fundamental model of wax deposition in subsea oil pipelines. *AIChE Journal* **2011,** *57* (11), 2955-2964.
116. Paso, K.; Senra, M.; Yi, Y.; Sastry, A. M.; Fogler, H. S., Paraffin polydispersity facilitates mechanical gelation. *Industrial and Engineering Chemistry Research* **2005,** *44* (18), 7242-7254.

117. Müller-Steinhagen, H., Heat transfer fouling: 50 years after the Kern and Seaton model. *Heat Transfer Engineering* **2011,** *32* (1), 1-13.
118. Nazar, A. S.; Dabir, B.; Islam, M., Experimental and mathematical modeling of wax deposition and propagation in pipes transporting crude oil. *Energy sources* **2005,** *27* (1-2), 185-207.
119. Hernandez, O.; Hensley, H.; Sarica, C.; Brill, J.; Volk, M.; Delle-Case, E. In *Improvements in single-phase paraffin deposition modeling*, SPE Annual Technical Conference and Exhibition, Society of Petroleum Engineers: 2003.
120. Edmonds, B.; Moorwood, T.; Szczepanski, R.; Zhang, X., Simulating wax deposition in pipelines for flow assurance. *Energy & Fuels* **2007,** *22* (2), 729-741.
121. Venkatesan, R. The deposition and rheology of organic gels. University of Michigan, 2004.
122. Pan, S.; Zhu, J.; Zhang, D.; Razouki, A.; Talbot, M.; Wierzchowski, S. In *Case studies on simulation of wax deposition in pipelines*, International Petroleum Technology Conference, International Petroleum Technology Conference: 2009.
123. Wang, W.; Huang, Q., Prediction for wax deposition in oil pipelines validated by field pigging. *Journal Of The Energy Institute* **2014,** *87* (3), 196-207.
124. Wang, W.; Huang, Q.; Wang, C.; Li, S.; Qu, W.; Zhao, J.; He, M., Effect of operating conditions on wax deposition in a laboratory flow loop characterized with DSC technique. *Journal of Thermal Analysis and Calorimetry* **2015,** *119* (1), 471-485.
125. Sarmento, R. C.; Ribbe, G. A. S.; Azevedo, L. F. A., Wax Blockage Removal by Inductive Heating of Subsea Pipelines. *Heat Transfer Engineering* **2004,** *25* (7), 2-12.
126. Yang, F.; Zhao, Y.; Sjöblom, J.; Li, C.; Paso, K. G., Polymeric Wax Inhibitors and Pour Point Depressants for Waxy Crude Oils: A Critical Review. *Journal of Dispersion Science and Technology* **2015,** *36* (2), 213-225.
127. Ashbaugh, H. S.; Guo, X.; Schwahn, D.; Prud'homme, R. K.; Richter, D.; Fetters, L. J., Interaction of paraffin wax gels with ethylene/vinyl acetate co-polymers. *Energy and Fuels* **2005,** *19* (1), 138-144.
128. Machado, A. L. C.; Lucas, E. F.; González, G., Poly(ethylene-co-vinyl acetate) (EVA) as wax inhibitor of a Brazilian crude oil: oil viscosity, pour point and phase behavior of organic solutions. *Journal of Petroleum Science and Engineering* **2001,** *32* (2-4), 159-165.
129. Machado, A. L. d. C.; Lucas, E. F., POLY(ETHYLENE-CO-VINYL ACETATE) (EVA) COPOLYMERS AS MODIFIERS OF OIL WAX CRYSTALLIZATION. *Petroleum Science and Technology* **1999,** *17* (9-10), 1029-1041.
130. Ridzuan, N.; Adam, F.; Yaacob, Z., Molecular Recognition of Wax Inhibitor Through Pour Point Depressant Type Inhibitor. In *International Petroleum Technology Conference*, International Petroleum Technology Conference: Kuala Lumpur, Malaysia, 2014; p 9.
131. Al-Sabagh, A. M.; El-Kafrawy, A. F.; Khidr, T. T.; El-Ghazawy, R. A.; Mishrif, M. R., Synthesis and Evaluation of Some Novel Polymeric Surfactants Based on Aromatic Amines Used as Wax Dispersant for Waxy Gas Oil. *Journal of Dispersion Science and Technology* **2007,** *28* (6), 976-983.
132. Radulescu, A.; Fetters, L.; Richter, D., Polymer-driven wax crystal control using partially crystalline polymeric materials. *Wax Crystal Control: Nanocomposites, Stimuli-Responsive Polymers* **2008,** *210* (1), 1-100.
133. Zhang, J.; Wu, C.; Li, W.; Wang, Y.; Cao, H., DFT and MM calculation: the performance mechanism of pour point depressants study. *Fuel* **2004,** *83* (3), 315-326.
134. Soni, H. P.; Kiranbala, D. P.; Bharambe, D. P., Performance-based designing of wax crystal growth inhibitors. *Energy and Fuels* **2008,** *22* (6), 3930-3938.

135. Wu, C.; Zhang, J.-L.; Li, W.; Wu, N., Molecular dynamics simulation guiding the improvement of EVA-type pour point depressant. *Fuel* **2005,** *84* (16), 2039-2047.
136. Leube, W.; Monkenbusch, M.; Schneiders, D.; Richter, D.; Adamson, D.; Fetters, L.; Dounis, P.; Lovegrove, R., Wax-crystal modification for fuel oils by self-aggregating partially crystallizable hydrocarbon block copolymers. *Energy and Fuels* **2000,** *14* (2), 419-430.
137. Al-Sabagh, A. M.; Noor El-Din, M. R.; Morsi, R. E.; Elsabee, M. Z., Styrene-maleic anhydride copolymer esters as flow improvers of waxy crude oil. *Journal of Petroleum Science and Engineering* **2009,** *65* (3), 139-146.
138. Li, L.; Xu, J.; Tinsley, J.; Adamson, D. H.; Pethica, B. A.; Huang, J. S.; Prud' Homme, R. K.; Guo, X., Improvement of oil flowability by assembly of comb-type copolymers with paraffin and asphaltene. *AIChE Journal* **2012,** *58* (7), 2254-2261.
139. Soldi, R. A.; Oliveira, A. R. S.; Barbosa, R. V.; César-Oliveira, M. A. F., Polymethacrylates: Pour point depressants in diesel oil. *European Polymer Journal* **2007,** *43* (8), 3671-3678.
140. Wang, K.-S.; Wu, C.-H.; Creek, J. L.; Shuler, P. J.; Tang, Y., Evaluation of Effects of Selected Wax Inhibitors on Paraffin Deposition. *Petroleum Science and Technology* **2003,** *21* (3-4), 369-379.
141. Xu, J.; Zhang, X.; Sun, J.; Li, L.; Guo, X., How comb-type poly(maleic acid alkylamide-co -α-olefin) assemble in waxy oils and improve flowing ability. *Asia-Pacific Journal of Chemical Engineering* **2009,** *4* (5), 551-556.
142. Al-Sabagh, A. M.; El-Hamouly, S. H.; Khidr, T. T.; El-Ghazawy, R. A.; Higazy, S. A., Preparation the Esters of Oleic Acid-Maleic Anhydride Copolymer and Their Evaluation as Flow Improvers for Waxy Crude Oil. *Journal of Dispersion Science and Technology* **2013,** *34* (11), 1585-1596.
143. Jafari Behbahani, T.; Miranbeigi, A.; Sharifi, K., A new experimental investigation on upgrading of waxy crude oils by methacrylate polymers. *Petroleum Chemistry* **2017,** *57* (10), 874-880.
144. Yang, F.; Li, C. X.; Lin, M. Z.; Li, Z. Y.; Yu, T., Depressive effect of polyacrylate (PA) pour point depressant on waxy crude oils. *Shiyou Huagong Gaodeng Xuexiao Xuebao/Journal of Petrochemical Universities* **2009,** *22*, 20-25.
145. Chen, W.; Zhao, Z.; Yin, C., The interaction of waxes with pour point depressants. *Fuel* **2010,** *89* (5), 1127-1132.
146. Pedersen, K. S.; Rønningsen, H. P., Influence of wax inhibitors on wax appearance temperature, pour point, and viscosity of waxy crude oils. *Energy and Fuels* **2003,** *17* (2), 321-328.
147. Ashbaugh, H. S.; Fetters, L. J.; Adamson, D. H.; Prud'homme, R. K., Flow improvement of waxy oils mediated by self-aggregating partially crystallizable diblock copolymers. *Journal of Rheology* **2002,** *46* (4), 763-776.
148. Monkenbusch, M.; Schneiders, D.; Richter, D.; Willner, L.; Leube, W.; Fetters, L. J.; Huang, J. S.; Lin, M., Aggregation behaviour of PE–PEP copolymers and the winterization of diesel fuel. *Physica B: Physics of Condensed Matter* **2000,** *276-278* (C), 941-943.
149. Lim, Z.; Al Salim, H.; Ridzuan, N.; Nguele, R.; Sasaki, K., Effect of surfactants and their blend with silica nanoparticles on wax deposition in a Malaysian crude oil. *Petroleum Science* **2018,** *15* (3), 577-590.
150. Al-Yaari, M., Paraffin Wax Deposition: Mitigation and Removal Techniques. In *SPE Saudi Arabia section Young Professionals Technical Symposium*, Society of Petroleum Engineers: Dhahran, Saudi Arabia, 2011; p 10.

151. Radulescu, A.; Schwahn, D.; Stellbrink, J.; Kentzinger, E.; Heiderich, M.; Richter, D.; Fetters, L. J., Wax crystallization from solution in hierarchical morphology templated by random poly(ethylene-co-butene) self-assemblies. *Macromolecules* **2006,** *39* (18), 6142-6151.
152. Jafari Ansaroudi, H. R.; Vafaie-Sefti, M.; Masoudi, S.; Behbahani, T. J.; Jafari, H., Study of the Morphology of Wax Crystals in the Presence of Ethylene-co-vinyl Acetate Copolymer. *Petroleum Science and Technology* **2013,** *31* (6), 643-651.
153. Ashbaugh, H. S.; Radulescu, A.; Prud'homme, R. K.; Schwahn, D.; Richter, D.; Fetters, L. J., Interaction of paraffin was gels with random crystalline/amorphous hydrocarbon copolymers. *Macromolecules* **2002,** *35* (18), 7044-7053.
154. Cao, K.; Wei, X.-X.; Li, B.-J.; Zhang, J.-S.; Yao, Z., Study of the Influence of Imidization Degree of Poly(styrene-co-octadecyl maleimide) as Waxy Crude Oil Flow Improvers. *Energy & Fuels* **2013,** *27* (2), 640-645-640-645.
155. Duffy †, D. M.; Moon, C.; Rodger, P. M., Computer-assisted design of oil additives: hydrate and wax inhibitors. *Molecular Physics* **2004,** *102* (2), 203-210.
156. Duffy, D. M.; Rodger, P., Wax inhibition with poly(octadecyl acrylate). *Physical Chemistry Chemical Physics* **2002,** *4* (2), 328-334.
157. Technobis crystallization systems Crystal 16. https://www.crystallizationsystems.com/crystal16.
158. Eh, *BS EN 12619:1999 - Stationary source emissions. Determination of the mass concentration of total gaseous organic carbon at low concentrations in flue gases. Continuous flame ionization detector method*. 1999.
159. Sun, Y., *Detection technologies for chemical warfare agents and toxic vapors*. CRC Press: Boca Raton, 2005.
160. Barnes, H. A., *An introduction to rheology*. Elsevier: Amsterdam ;, 1989.
161. Mezger, T. G., *The rheology handbook : for users of rotational and oscillatory rheometers*. 4th edition. ed.; Vincentz Network: Hanover, 2014.
162. TA instruments Discovery hybrid rheometers. https://www.tainstruments.com/products/rheology/discovery-hybrid-rheometers/.
163. Thermofisher Advantages of a Fourier Transform Infrared Spectrometer. https://tools.thermofisher.com/content/sfs/brochures/TN50674-E-0215M-FT-IR-Advantages.pdf.
164. Taha, L.; Ashton, K.; Davis, C.; Dawson, T.; Martin, F., Spectrochemical differentiation of meningioma tumours based on attenuated total reflection Fourier-transform infrared (ATR-FTIR) spectroscopy. *Analytical and Bioanalytical Chemistry* **2020,** *412* (5), 1077-1086.
165. Inkson, B. J., 2 - Scanning electron microscopy (SEM) and transmission electron microscopy (TEM) for materials characterization. In *Materials Characterization Using Nondestructive Evaluation (NDE) Methods*, Hübschen, G.; Altpeter, I.; Tschuncky, R.; Herrmann, H.-G., Eds. Woodhead Publishing: 2016; pp 17-43.
166. Walock, M., Nanocomposite coatings based on quaternary metal-nitrogen and nanocarbon systems. Stanishevsky, A. V.; Nouveau, C.; Catledge, S.; Imhoff, L.; Martin, N.; Vohra, Y.; Weaver, M., Eds. ProQuest Dissertations Publishing: 2012.
167. Pti, *BS ISO 17247:2013 - Coal. Ultimate analysis*. 2013.
168. Pti, *BS EN ISO 16948:2015 - Solid biofuels. Determination of total content of carbon, hydrogen and nitrogen*. 2015.
169. Rennie, R.; Law, J., thermal imaging. Oxford University Press: 2019.
170. Raccuglia, M.; Heyde, C.; Lloyd, A.; Hodder, S.; Havenith, G., The use of infrared thermal imaging to measure spatial and temporal sweat retention in clothing. *International Journal of Biometeorology* **2019,** *63* (7), 885-894.

171. Stanger, L. R.; Wilkes, T.; Boone, N.; McGonigle, A.; Willmott, J., Thermal Imaging Metrology with a Smartphone Sensor. **2018**.
172. Avio https://www.infrared.avio.co.jp/en/products/ir-thermo/lineup/r300sr/index.html.
173. Nigo, R. Y.; Chew, Y. M. J.; Houghton, N. E.; Paterson, W. R.; Wilson, D. I., Experimental studies of freezing fouling of model food fat solutions using a novel spinning disc apparatus. *Energy and Fuels* **2009,** *23* (12), 6131-6145.
174. Lathrop; Fineberg; Swinney, Transition to shear-driven turbulence in Couette-Taylor flow. *Physical review. A, Atomic, molecular, and optical physics* **1992,** *46* (10), 6390-6405.
175. Akbarzadeh, K.; Zougari, M., Introduction to a novel approach for modeling wax deposition in fluid flows. 1. Taylor-couette system. *Industrial and Engineering Chemistry Research* **2008,** *47* (3), 953-963.
176. Ostilla-Mónico, R.; Verzicco, R.; Grossmann, S.; Lohse, D., The near-wall region of highly turbulent Taylor-Couette flow. *Journal of Fluid Mechanics* **2016,** *788*, 95-117.
177. Cole, R. J., and Jessen, F.W. , Paraffin deposition. *Oil Gas J.* **1960,** (58), 87-91.
178. Howell, J. N., and Jessen, F. W. , Effect of flowarate on paraffin accumulation in plastic, steel and coated pipe. *Ptrol. Trans. AIME* **1958,** (213), 80-85.
179. Seth, S.; Towler, B. F.; Mokhatab, S., The Effect of Tube Orientation and Pour Point Depressant on Paraffin Wax Deposition. *Petroleum Science and Technology* **2011,** *29* (4), 378-392.
180. Blake, A.; Marangoni, A., The Use of Cooling Rate to Engineer the Microstructure and Oil Binding Capacity of Wax Crystal Networks. *Food Biophysics* **2015,** *10* (4), 456-465.
181. Blake, A.; Marangoni, A., The Effect of Shear on the Microstructure and Oil Binding Capacity of Wax Crystal Networks. *Food Biophysics* **2015,** *10* (4), 403-415.
182. Fong, N.; Mehrotra, A., Deposition under turbulent flow of wax-solvent mixtures in a bench-scale flow-loop apparatus with heat transfer. *Energy & Fuels* **2007,** *21* (3), 1263-1276.
183. Yang, J.; Lu, Y.; Daraboina, N.; Sarica, C., Wax deposition mechanisms: Is the current description sufficient? *Fuel* **2020,** *275*.
184. Ji, Z.; Li, C.; Yang, F.; Cai, J.; Cheng, L.; Shi, Y., An experimental design approach for investigating and modeling wax deposition based on a new cylindrical Couette apparatus. *Petroleum Science and Technology* **2016,** *34* (6), 570-577.
185. Tinsley, J. F.; Prud'homme, R. K., Deposition apparatus to study the effects of polymers and asphaltenes upon wax deposition. *Journal of Petroleum Science and Engineering* **2010,** *72* (1-2), 166-174.
186. Kasumu, A. S.; Arumugam, S.; Mehrotra, A. K., Effect of cooling rate on the wax precipitation temperature of "waxy" mixtures. *Fuel* **2013,** *103*, 1144-1147.
187. Jennings, D. W.; Breitigam, J., Paraffin Inhibitor Formulations for Different Application Environments: From Heated Injection in the Desert to Extreme Cold Arctic Temperatures † Presented at the 10th International Conference on Petroleum Phase Behavior and Fouling. *Energy & Fuels* **2010,** *24* (4), 2337-2349.
188. Production Chemicals for the Oil and Gas Industry. *Chromatographia* **2010,** *72* (1), 199-199.
189. Banerjee, S.; Kumar, R.; Akhtar, A.; Bairagi, R.; Mandal, A.; Naiya, T. K., Effect of pour point depressant on wax deposition and drag reduction in horizontal pipelines. *Petroleum Science and Technology* **2017,** *35* (6), 561-569.
190. Still, I., The OSPAR Environmental Strategy beyond 2020 – A new approach to the regulation of offshore chemicals or a continuation of the existing regime? In *Chemistry in the Oil Industry XVI, New Chemistries for Old Problems*, The Royal Society of Chemistry, Speciality Chemicals Sector & EOSCA: University of Manchester, Manchester, UK, 2019.

191. Lomakin, S. M.; Rogovina, S. Z.; Grachev, A. V.; Prut, E. V.; Alexanyan, C. V., Thermal degradation of biodegradable blends of polyethylene with cellulose and ethylcellulose. *Thermochimica acta* **2011,** *521* (1-2), 66-73.
192. Yuan, W.; Yuan, J.; Zhang, F.; Xie, X., Syntheses, Characterization, and in Vitro Degradation of Ethyl Cellulose-graft-poly(ε-caprolactone)-block-poly(l-lactide) Copolymers by Sequential Ring-Opening Polymerization. *Biomacromolecules* **2007,** *8* (4), 1101-1108.
193. Hasan, A. M. A.; Abdel-Raouf, M. E., Applications of guar gum and its derivatives in petroleum industry: A review. *Egyptian Journal of Petroleum* **2018,** *27* (4), 1043-1050.
194. Dai, L.; Long, Z.; Chen, J.; An, X.; Cheng, D.; Khan, A.; Ni, Y., Robust Guar Gum/Cellulose Nanofibrils Multilayer Films with Good Barrier Properties. *ACS Applied Materials & Interfaces* **2017,** *9* (6), 5477-5485.
195. Zhao, H., Investigation of the applications of nanofibrillated cellulose in the oil industry. Nasr-El-Din, H. A.; Barrufet, M.; El-Halwagi, M.; Holditch, S., Eds. ProQuest Dissertations Publishing: 2015.
196. Feng, X.; Wang, S.; Hou, J.; Wang, L.; Cepuch, C.; Masliyah, J.; Xu, Z., Effect of hydroxyl content and molecular weight of biodegradable ethylcellulose on demulsification of water-in-diluted bitumen emulsions. *Industrial and Engineering Chemistry Research* **2011,** *50* (10), 6347-6354.
197. Trasi, N. S.; Abbou Oucherif, K.; Litster, J. D.; Taylor, L. S., Evaluating the influence of polymers on nucleation and growth in supersaturated solutions of acetaminophen. *CrystEngComm* **2015,** *118* (33), 1242-1248.
198. Morán, J. I.; Alvarez, V. A.; Cyras, V. P.; Vázquez, A., Extraction of cellulose and preparation of nanocellulose from sisal fibers. *Cellulose (London)* **2007,** *15* (1), 149-159.
199. Hagoort, J., Prediction of Wellbore Temperature in Gas Production Wells. *Journal of Petroleum Science and Engineering - J PET SCI ENGINEERING* **2005,** *49*, 22-36.
200. Wang, Z.; Yu, X.; Li, J.; Wang, J.; Zhang, L., The use of biobased surfactant obtained by enzymatic syntheses forwax deposition inhibition and drag reduction in crude oil pipelines. *Catalysts* **2016,** *6* (5).
201. Wu, Y.; Ni, G.; Yang, F.; Li, C.; Dong, G., Modified Maleic Anhydride Co-polymers as Pour-Point Depressants and Their Effects on Waxy Crude Oil Rheology. *Energy & Fuels* **2012,** *26* (2), 995-1001-995-1001.
202. Pedersen, K. S.; Rønningsen, H. P., Influence of Wax Inhibitors on Wax Appearance Temperature, Pour Point, and Viscosity of Waxy Crude Oils. *Energy & fuels* **2003,** *17* (2), 321-328.
203. Chala, G.; Sulaiman, S.; Japper-Jaafar, A., Flow start-up and transportation of waxy crude oil in pipelines-A review. *Journal of Non-Newtonian Fluid Mechanics* **2018,** *251*, 69.
204. Coto, B.; Martos, C.; Espada, J. J.; Robustillo, M. D.; Peña, J. L., Experimental study of the effect of inhibitors in wax precipitation by different techniques. *Energy Science & Engineering* **2014,** *2* (4), 196-203.
205. Ragunathan, T.; Husin, H.; Wood, C. D., Wax Formation Mechanisms, Wax Chemical Inhibitors and Factors Affecting Chemical Inhibition. *Applied sciences* **2020,** *10* (2), 479.
206. Hsu, J. J. C.; Santamaria, M. M.; Brubaker, J. P.; Hawker, P., Wax Deposition And Gel Strength Of Waxy Live Crudes. In *Offshore Technology Conference*, Offshore Technology Conference: Houston, Texas, 1994; p 8.
207. Chala, G. T.; Sulaiman, S. A.; Japper-Jaafar, A., Flow start-up and transportation of waxy crude oil in pipelines-A review. *Journal of non-Newtonian fluid mechanics* **2018,** *251*, 69-87.
208. Bae, J. H.; Kim, S. H., Alkylation of mixed micro- and nanocellulose to improve dispersion in polylactide. *Polymer International* **2015,** *64* (6), 821-827.

209. Aske, N.; Viitala, T.; Braathen, B.; Paso, K.; nningsen, H.; Sjöblom, J., Wax Deposition Investigations with Thermal Gradient Quartz Crystal Microbalance. 2008; pp 567-584.
210. Yamada, R.; Uosaki, K., Two-Dimensional Crystals of Alkanes Formed on Au(111) Surface in Neat Liquid: Structural Investigation by Scanning Tunneling Microscopy. *The Journal of Physical Chemistry B* **2000,** *104* (25), 6021-6027.
211. Groszek, A. J., Preferential Adsorption of Long-chain Normal Paraffins on MoS2, WS2 and Graphite from n-Heptane. *Nature* **1964,** *204* (4959), 680.
212. San-Miguel, M. A.; Rodger, P. M., Wax deposition onto Fe2O3 surfaces. *Physical Chemistry Chemical Physics* **2003,** *5* (3), 575-581.
213. Acharya, B.; Sidheswaran, M. A.; Yungk, R.; Krim, J., Quartz crystal microbalance apparatus for study of viscous liquids at high temperatures. *Review of Scientific Instruments* **2017,** *88* (2).
214. Liu, L.-S.; Kim, J.; Chang, S.-M.; Choi, G. J.; Kim, W.-S., Quartz Crystal Microbalance Technique for Analysis of Cooling Crystallization. *Analytical Chemistry* **2013,** *85* (9), 4790-4796.
215. Burgass, R.; Tohidi, B., Development and Validation of Small Volume Multi-Tasking Flow Assurance Tool. In *SPE Asia Pacific Oil and Gas Conference and Exhibition*, Society of Petroleum Engineers: Jakarta, Indonesia, 2011; p 10.
216. Burgass, R. W. Applications of Quartz Crystal Microbalance Technology in Petroleum Engineering Demonstrated by Studies of Wax, Asphaltenes, Hydrates, Ice, Diesel Additives and Anti deposition Coatings. Heriot Watt University, UK, 2015.
217. Solvay Galden PFPE. https://www.solvay.com/en/brands/galden-pfpe.
218. Systems, S. R., Operation and Service Manual: QCM200 Quartz Crystal Microbalance Digital Controller. Stanford Research Systems, I., Ed. 1290-C Reamwood Avenue
Sunnyvale, California 94089, USA, 2011.
219. Sauerbrey, G., Verwendung Von Schwingquarzen Zur Wagung Dunner Schichten Und Zur Mikrowagung. *Z Phys* **1959,** *155* (2), 206-222.
220. Deakin, M. R.; Buttry, D. A., Electrochemical Applications of the Quartz Crystal Microbalance. *Anal Chem* **1989,** *61* (20), A1147-&.
221. Deakin, M. R.; Buttry, D. A., Electrochemical applications of the quartz crystal microbalance. *Analytical Chemistry* **1989,** *61* (20), 1147A-1154A.
222. Botha, J. A. Application of Quartz Crystal Microbalance to Measure the Rheology of Complex Colloidal Suspensions. University of Leeds, 2018.
223. Nomura, T.; Nagamune, T., Internal electrolytic determination of silver in solution with a piezoelectric quartz crystal. *Analytica Chimica Acta* **1983,** *155* (C), 231-234.
224. Glassford, A. P. M., Response of a quartz crystal microbalance to a liquid deposit. *Journal of Vacuum Science and Technology* **1978,** *15* (6), 1836-1843.
225. Keiji Kanazawa, K.; Gordon, J. G., The oscillation frequency of a quartz resonator in contact with liquid. *Analytica Chimica Acta* **1985,** *175* (C), 99-105.
226. Kanazawa, K. K.; Gordon, J. G., Frequency of a Quartz Microbalance in Contact with Liquid. *Anal Chem* **1985,** *57* (8), 1770-1771.
227. TheEngineeringToolbox https://www.engineeringtoolbox.com/water-dynamic-kinematic-viscosity-d_596.html?vA=20&units=C#.
228. Feng, S.; Liu, Z.; Bi, Q.; Pan, H., Viscosity Measurements of n-Dodecane at Temperatures between 303 K and 693 K and Pressures up to 10 MPa. *Journal of Chemical & Engineering Data* **2018,** *63* (3), 671-678.
229. Trasi, N. S.; Abbou Oucherif, K.; Litster, J. D.; Taylor, L. S., Evaluating the influence of polymers on nucleation and growth in supersaturated solutions of acetaminophen. *CrystEngComm* **2015,** *17* (6), 1242-1248.

230. Lapidot, T.; Sedransk Campbell, K. L.; Heng, J. Y. Y., Model for Interpreting Surface Crystallization Using Quartz Crystal Microbalance: Theory and Experiments. *Analytical Chemistry* **2016,** *88* (9), 4886-4893.
231. Tang, X. Crystal structure, phase behavior and kinetics associated with the crystallisation of octadecane, hexadecane, and mixtures thereof. University of Leeds, 2017.
232. Botha, J. A.; Ding, W.; Hunter, T. N.; Biggs, S.; Mackay, G. A.; Cowley, R.; Woodbury, S. E.; Harbottle, D., Quartz crystal microbalance as a device to measure the yield stress of colloidal suspensions. **2018**.
233. Botha, J. A.; Hunter, T. N.; Ding, W.; Biggs, S.; Mackay, G. A.; Cowley, R.; Woodbury, S. E.; Harbottle, D., A Novel Technology for Complex Rheological Measurements. WM Symposia: 2016.
234. Mustaffa, N. B. M., *Oil pipeline wax deposition inhibition using chemical methods*. B. Tech. Thesis, University Malaysia Pahang, Pahang, Malaysia: 2010.
235. Hammami, A.; Ratulowski, J.; Coutinho, J. A. J. P. S.; Technology, Cloud points: can we measure or model them? **2003,** *21* (3-4), 345-358.
236. Tinsley, J. F.; Prud'homme, R. K. J. J. o. P. S.; Engineering, Deposition apparatus to study the effects of polymers and asphaltenes upon wax deposition. **2010,** *72* (1-2), 166-174.
237. Soedarmo, A. A.; Daraboina, N.; Sarica, C., Validation of wax deposition models with recent laboratory scale flow loop experimental data. *Journal of Petroleum Science and Engineering* **2017,** *149*, 351-366.
238. Soedarmo, A. A.; Daraboina, N.; Sarica, C., Microscopic Study of Wax Deposition: Mass Transfer Boundary Layer and Deposit Morphology. *Energy & Fuels* **2016,** *30* (4), 2674-2686.
239. Mori, T., *Taguchi methods benefits, impacts, mathematics, statistics, and applications*. ASME Press: New York, NY, 2011.
240. Upton, G.; Cook, I., Taguchi methods. Oxford University Press: 2014.
241. Quotient, S. Taguchi method - Introduction. http://sigmaquotient.com/.
242. Roberts, J. D., *Basic principles of organic chemistry*. Second edition. ed.; W. A. Benjamin: Menlo Park, Calif, 1977.